Analog and Digital Approaches to UWB Narrowband Interference Cancellation

Omid Abedi

Thesis submitted to the
Faculty of Graduate and Postdoctoral Studies
In partial fulfillment of the requirements
For the PhD degree in Electrical and Computer Engineering

School of Electrical Engineering and Computer Science
Faculty of Engineering
University of Ottawa

Abstract

Ultra wide band (UWB) is an extremely promising wireless technology for researchers and industrials. One of the most interesting is its high data rate and fading robustness due to selective frequency fading. However, beside such advantages, UWB system performance is highly affected by existing narrowband interference (NBI), undesired UWB signals and tone/multi-tone noises. For this reason, research about NBI cancellation is still a challenge to improve the system performance vs. receiver complexity, power consumption, linearity, etc.

In this work, the two major receiver sections, i.e., analog (radiofrequency or RF) and digital (digital signal processing or DSP), were considered and new techniques proposed to reduce circuit complexity and power consumption, while improving signal parameters.

In the RF section, different multiband UWB low-noise amplifier key design parameters were investigated like circuit configuration, input matching and desired/undesired frequency band filtering, highlighting the most suitable filtering package for efficient UWB NBI cancellation.

In the DSP section, due to pulse transmitter signals, different issues like modulation type and level, pulse variety, shape and color noise/tone noise assumptions, were addressed for efficient NBI cancelation. A comparison was performed in terms of bit-error rate, signal-to-interference ratio, signal-to-noise ratio, and channel capacity to highlight the most suitable parameters for efficient DSP design. The optimum number of filters that allows the filter bandwidth to be reduced by following the required low sampling rate and thus improving the system bit error rate was also investigated.

Acknowledgment

I would like to thank my parents Mr. Gholamali and Ms. Sharebano Abedi who have always been behind me with their warm encouragement. I appreciate my younger brother Mr. Arya Abedi for his emotional support; without him, I could not finish this thesis.

Also specific thanks for my religious brother Mr. Kambiz Najafzadeh who paving my path not only with financial support but also inspires me to continue and never be disappointed.

I would like to thank Dr. Yagoub for his availability throughout the course of this work, which includes not only giving me opportunity to study but also has a kind attention to my research abilities.

I would like also to thank Ms. Margaret Moriarty, Mr. Lafrance and Ms. Laurence from the Faculty of Graduate Studies for their support.

In the end, let me thank the great Canada that not only provides these facilities and study opportunities for me but also trust me and clear my path.

Table of Contents

List of Figures

List of Tables

List of Acronyms

AFB	Analog filter bank
AWGN	Additive white Gaussian noise
ADC	Analog to digital converter
BER	Bit error rate
BPF	Band-pass filters
CAD	Computer Aided Design
CDMA	Code division multiple access
CIR	Channel impulse response
CS	Common-source
CG	Common-gate
DSP	Digital signal processing
D-GPS	Differential Global Positioning System
DS	Direct sequence
EGC	Equal gain combining
FCC	Federal Communications Commission
FN	Number of fingers
GMF	General matched filter
HPF	High-pass filters
ICBPF	Inverse Chev Bandpass filter
IM	Intermodulation
IP	Intercept point
IIP	Input intercepts point
IPI	Inter pulse interference
ISI	Inter symbol interference
LAN	Local area network
LNA	Low noise amplifier
LPF	Low-pass filters
MBOA	Multi band OFDM alliance
MF	Matched filter

MIMO	Multiple input multiple outputs
MRC	Maximum radio combining
MUI	Multi user interference
MB	Multiband
NF	Noise figure
NBI	Narrow band interference
NLOS	Non line of sight
NB-LNA, WB-LNA	Narrowband, wideband LNA
OIP	Output intercepts point
OFDM	Orthogonal frequency-division multiplexing
OOK	On off keying modulation
PAM	Pulse amplitude modulation
PPM	Pulse position modulation
PAN	Personal area network
PDP	Power delay profile
PHY	Physical layer
PDF	Power density function
PN	Pseudo noise
PSD	Power spectral density
PA	Power amplifier
RF	Radio frequency
SIR	Signal-to-Interference Ratio
SNR	Signal-to-Noise Ratio
SBF	Stop-band filters
SER	Symbol error rate
SBA	Stop band attenuation
SBW	Stop-band bandwidth
SIR	Signal to interference ratio
SBR	Single bit rate
SER	Symbol error rate
SIMO	Single input multiple outputs

SNR	Signal to noise ratio
SS	Spread spectrum
TDMA	Time division multiple access
TH-IR	Time hopping impulse ratio
UWB	Ultra-Wide Band
WAN	Wide area network
WPAM	Wireless personal area network
WGN	White Gaussian noise

List of Symbols

$A_{\max}$	Maximum ripple amplitude
A_v	Voltage gain
B_n	Normalized bandwidth.
B_w	Signal bandwidth
C	Capacity per bit
C_{gs}	Gate-source capacitor
$D(f)$	Effect of PPM modulator time shift
E_{Rx}	Received energy per pulse
E_{Tx}	Transmitted energy per pulse
FN	Filter numbers
F_{BW}	Fractional bandwidth
f_c	Sample frequency
f_T	Transistor cut-off frequency
$F_{\min}$	Minimum noise figure
G	Power gain
g_m	Transconductance
$h(t)$	Complete link transfer function
$h_{ch}(t)$	Channel impulse response
$h_r(t)$	Receiver matched impulse response
$H(s)$	Transfer function
J_n	Bessel function
k	Boltzman's constant
K_f	Rollet's factor
$k_i(n)$	Impulse response of the i^{th} filter bank

L	Number of multi-path components
L_s	Source inductor
L_g	Gate inductor
M	M-ary communication
N_h	Length of channel duration
N_T	Number of time slots in one frame
N_R	Number of rake fingers
N_s	Number of pulses per symbol
N_p	TH-coding period (OFDM modulation)
N_f	Number of fingers (correlator)
$p(t)$	Pulse function
$\Pr_b$	Probability of error
$\Pr_s$	Symbol error rate
P_I	UWB interference power
P_L	Maximum power delivery to the load
Q	Quality Factor
Q_c	The noise covariance matrix
R_b	Bit rate
R_s	Source resistance
R_c	Code rate
R_{Sl}	Line spectral radio
R_g	Gate resistor
$R_{S,L}$	Degeneration inductor series resistor
$r_i(n)$	Receive signal at i-th filter channel.
$r_{qi}(n)$	Quantized version of $r_i(n)$
$S_i(t)$	UWB PPM-PAM symbol

SNR_z	SNR output of GMF
T	Temperature
T_G	Interval guard time
T_{sym}	Symbol duration
T_s	Frame duration, symbol period
T_c	Chip period, pulse Resolution interval
T_h	Pulse duration
T_b	Bit period
$u(n)$	AWGN channel noise
V_t	Threshold voltage
Vcc	Power supply
V_p	Pinch-off voltage
$V_{n,out}^2$	Total output noise power
v_{ip3}	Intercept point voltage
$v(n)$	NBI channel noise discrete time
W_j	Rake weighting coefficient
$w(n)$	Total channel noise in discrete time
Z	Output of the rake receiver
Z_{in}	Input impedance
Z_{out}	Output impedance

σ	Standard deviation
σ_g	Standard deviation of the channel amplitude
β	Pulse shape factor
Γ	The power decay factor for cluster
Γ_l	Load reflection coefficient

Λ	The cluster arrival rate
λ	The pulse arrival rate
γ	Power decay factor for pulses
ε	PPM time shift
Δf	Orthogonally among different transmission symbol

Chapter 1 Introduction

1.1 Motivations

Appealing features such as flexibility and robustness, as well as high-precision ranging capability, low power, low interference, and low regulation, have attracted attention and made ultra-wide band (UWB) an excellent candidate for a variety of applications [1]-[2]. UWB is emerging as a particularly appealing transmission technique for applications requiring either high bit rates over short ranges or low bit rates over large ranges.

Historically, UWB radar systems were developed mainly as a military tool. However, UWB technology has been recently focused on consumer electronics and communications. Ideal UWB systems are considered to have low power, low cost, high data rates, precise positioning capability and extremely low interference. Also the UWB technology is different from conventional narrow-band wireless transmission technology. UWB spreads signals across a very wide range of frequencies.

Researchers often see UWB as a promising technology. In fact, UWB is currently moving in new directions, such as automobile collision avoidance, positioning systems and indoor high data rates communications [3]. Note that if the dominant technique of wireless communication is currently based on sinusoidal waves, the first communication systems were in fact pulse-based.

However, beside such advantages, there are some issues and challenges in UWB technology, which are mostly correlated with the receiver design involving both major receiver sections, i.e., analog (Radio Frequency or RF) and digital (Digital Signal Processing or DSP) in which different signal transmission design methods have to be applied, such as carrier or pulse shape.

In fact, receiver complexity is not only related to the transmitter modulation, modulation level, and receiver signal power, but also to the system requirements because of Federal Communications Commission (FCC) regulations.

Indeed, since other applications have to share parts of the UWB frequency range, UWB system performance is highly affected by existing narrowband interferences (NBI), undesired UWB signals and multi-tone noises [4]. For this reason, further research about NBI cancellation becomes crucial to enhance UWB system performance.

In this work, UWB receiver design issues have been identified and new solutions have been proposed and successfully compared with existing design methods in terms of Bit Error Rate (BER), Signal-to-Interference Ratio (SIR), Signal-to-Noise Ratio (SNR), power consumption and system complexity. This comparison has been achieved relatively to the two major receiver blocks namely, the analog RF section and the digital DSP section.

1.2 Advantages of the UWB technology

Because UWB waveforms have short time duration, they have some unique specifications. In communications, UWB systems can be used to provide extremely high data rate performance in multi-user network applications. On the other hand, for radar applications, they can be used for range resolution and precision distance as well as positioning measurement capacities. More recently, the differential Global Positioning System (D-GPS) has also gained interest. As known, GPS is a system that requires Line-of-Sight (LOS) propagation but in Non-Line-of-Sight (NLOS) or even Extreme Non-Line-of-Sight (ENLOS) cases like in indoor communications, combination of wideband GPS and DGSP systems is required. This combination may increase the system complexity, but the interference signal will be significantly attenuated and thus, the total system performance will be improved.

In summary, UWB presents a solution to many of the challenges that wireless communication designers have to face. These advantages include:

- Speed: The same UWB device can scale from high speed to very low speed and low power applications, e.g., in meter reading.
- Multi-channel capabilities: due to its huge bandwidth, UWB can support hundreds of channels compared to existing systems.

- Simultaneous network: UWB can be used as personal area network (PAN), local area network (LAN) or wide area network (WAN).
- Global interoperability: the RF spectrum assignments vary from one country to another. UWB operates without this limitation, thus promising global interoperability.
- High security: UWB transmission signals, coupled to noise floor, are virtually impossible to detect, making the UWB one of the most secure wireless communication technologies.
- Higher resolution in ENLOS: propagation of UWB signals has a better performance through walls and other obstacles.

However, UWB presents some disadvantages as well. For instance, for extremely high data rates (tens of Gigabits/s and higher) in point-to-point or point-to-multi-point applications, it will be difficult for UWB systems to compete with point-to-point direct LOS wireless communication systems like optical point-to-point communication systems.

Also, as observed in some mobile and indoor wireless communications, multipath cancellation can occur when a strong reflected wave (from wall, vehicle …) adds with the direct path signal, causing reduced amplitude response at the receiver.

Therefore, there should be tradeoffs as in any other RF technology, such as SNR vs. bandwidth, maximum distance vs. transmitter power, etc.

1.3 Current work and thesis objectives

As mentioned, UWB system performance is highly affected by existing narrowband interference (NBI), undesired UWB signals, and multi-tone/color noises. For this reason improving the NBI system cancellation in UWB RF receivers or UWB pulse transmitters is crucial. Thus, advanced techniques should be proposed for UWB-NBI cancellation in UWB systems without increasing overall circuit complexity or decreasing performance. In this work, to avoid high sampling rate (ADC) and color noise while improving the UWB pulse transmitters receiver SNR, techniques such as signal mapping and orthogonal methods (General matched filter, GMF and Filter bank) have been first briefly investigated, thus combined, to improve interference cancellation. As for UWB RF receivers, a new UWB multi-band low-noise amplifier (LNA) with various LC ladders has been proposed to cancel major narrow band caused by WLAN systems.

In UWB system design, most recent papers consider only white noise in their studies [5]-[14]. This assumption is not entirely valid for indoor UWB wireless communication systems that deal with color noise. Therefore, the challenge is not only how to eliminate the color noise but also how to improve the system performance in terms of complexity and power consumption. Furthermore, the above mentioned papers investigated different methods to improve the system performance but, *to the best of our knowledge*, none of them simultaneously considered key system design elements in their investigation, such as pulse shape, maximum distance, BER, SIR, SNR, channel capacity, power consumption and system complexity.

Therefore, in this work, we investigated the following aspects:

at the transmitter side (system level)

- Pulse modulation and levels and their comparison in terms of BER, SER, and channel capacity to achieve the best modulation/level signal for NBI cancellation,
- Pulse duration and power spectral density (PSD),
- Effect of pulse shape to the system performance. In fact, most widely used channel models such as 802.11.3a or 802.11.4a did not take into account the pulse shape,
- Effect of repetition pulse code (number of pulse per data) on the system complexity,
- Channel parameters in different fading scenarios,

at the receiver side (system level)

- Rake receiver performance by considering color noise,
- Number of filters to be considered for increasing the receiver performance,

at the receiver side (circuit level)

- Transistor parameters: the system performance depends highly of the transistor parameters. Optimizing his characteristics is indeed necessary.

- Comparison between different LNA configurations in terms of linearity, power consumption and S-parameters frequency responses.
- Selection of the most suitable pass-band/stop-band filters in terms of order, sharpness, element size/number, etc.
- Evaluation of noise orthogonal methods such as OFDM modulation or differential multiband LNAs in terms of layout issues caused by the differential design [8], [12].

1.4 Research contributions

Actually, if the transmitter modulation is OFDM, then the power amplifier (PA) linearity will be limited and the transmitter power consumption should be increased to satisfy the linearity. Thus, the battery life will be reduced as well [13].

At the receiver side, designing the RF section raises different issues related to design flexibility, integration level, NBI cancellation, which leads to more complex topologies [4], [14]. In this work, we tried to answer most of the raised questions. Therefore to reach our objective, i.e., narrowband interference cancellation (NBI), major contributions have been achieved:

- ✓ New multiband UWB low-noise amplifier (MB-UWB-LNA) configuration to mitigate major narrow-band interference issues [15]. In this work, an original approach for efficient MB-UWB-LNA design is presented, focusing on input matching and desired/undesired frequency bands.
- ✓ New filter design approach for NBI-UWB applications [16], [17]. We indeed investigated the performance of a variety of band-pass filters (BPF) and stop-band filters (SBF) filters in terms of frequency response, input/output matching, phase, sharpness and stop-band attenuation, maximum bandwidth and number of components. Then, we compared their performance in regard to UWB requirements.
- ✓ New narrow-band noise cancellation approach including color noise orthogonally and partial rake receiver parameters [18], [19]. A comparison was performed in terms of BER, SIR, channel capacity and optimum filter bank numbers to highlight the most suitable parameters for efficient DSP design.

1.5 Thesis outline

This thesis is organized as follows: in Chapter 2, we compared the performance of different UWB filters (both 3-7GHz band-pass filters and 5-6GHz stop-band filters). The goal was to design a multi-channel filter with higher sharpness with respect to pass-band flatness, attenuation and element size.

In Chapters 3 and 4, we used the designed filters as input matching network for core LNA and compared their performance. We used two major LNA topologies: common-source (CS) and common-gate (CG). Thus in Chapter 4, the CS topology was investigated while combined with different multi-band topologies to mitigate undesired frequency band (5-6GHz).

In chapter 5 we introduced the IR-UWB system and alternative receiver design techniques to recover the low-power UWB signal from noise.

In Chapter 6, we evaluated the possible modulation schemes used in UWB communication. The objective of this chapter was to reduce the power spectral density (PSD) of discrete components. Also, performance of pulse modulation schemes was analyzed in terms of symbol error rate (SER), complexity, data rate, maximum transmit power, maximum transfer receiver distance and channel capacity. Chapter 7 showed that pulse differentiation and width variations affect the PSD and therefore, can be used to shape the transmitted waveform. Also analysis and evaluation of different Gaussian pulse shapes for UWB systems in light of the FCC frequency emission restrictions were studied such as Gaussian, Gaussian monocycle (first derivatives), Gaussian doublet, their combination (linear, random, LSE) and Hermite pulses. Chapter 8 briefly described the performance of a single user UWB communication system with TH-PPM modulation by applying IRAKE and PRAKE filter banks through the combination of maximum ratio combining (MRC) and general matched filter receiver. These receivers have been evaluated in several scenarios, such as NLOS and ENLOS, and evaluated by BER, capacity of the channel, signal to interference ratio, and SIR parameters. Future work objectives and research perspectives were discussed in Chapter 9.

References

[1] R. Kshetrimayum, "An introduction to UWB communication systems," *IEEE J. Magazines*, pp. 9-13, 2009.

[2] Z. Xiao, C. Zhang, N. Ge, D. Jin, "Introduction of SC-UWB proposal," *IEEE Conf. Computational Problem-Solving,* pp. 698-702, 2011.

[3] R. Cardinali, L. De Nardis, M.G. Di Benedetto, P. Lombardo, "UWB ranging accuracy in high- and low-data-rate applications," *IEEE Trans. Microwave Theory Tech.,* pp. 1865-1875, 2006.

[4] O. Abedi, M.C.E. Yagoub "Efficient narrowband interference cancellation in UWB RAKE receivers," submitted to *IET J. communications*, March 2012.

[5] S. Winder, *Analog and Digital Filter Design*, Woburn, MA, Newnes, 2002.

[6] A. Ismail, A. Abidi, "A 3-10 GHz low noise amplifier with wideband LC-Ladder matching network" *IEEE J. Solid State Circuits,* Vol. 39, No. 12, 2003.

[7] A. Inami, C. Sugimoto, R. Kohno, "Performance analysis of equalization and interference cancellation by adaptive digital filter for UWB-IR system inside a vehicle," *IEEE Conf. Information Theory and its Applications,* pp. 209-214, 2010.

[8] W. Green, P. Marilynn, "adjacent frequency coding technique for decreasing mb-OFDM UWB interference to other radio services," *IEEE Sarnoff Symp.,* pp. 1-4, 2006.

[9] T.W. Fischer, B. Kelleci, S. Kai, A.I. Karsilayan, E. Serpedin, "An analog approach to suppressing in-band narrow-band interference in UWB receivers," *IEEE Trans. Circuits and Systems*, pp. 941-950, 2007.

[10] G. Cusmai, M. Brandolini, P. Rossi, F. Svelto, "A 0.18-µm CMOS selective receiver front-end for UWB applications," *J. IEEE Solid-State Circuits,* pp. 1764-1771, 2006.

[11] C. Liao, S.I. Liu, "A broadband noise-canceling CMOS LNA for 3.1-10.6-GHz UWB receiver," *IEEE Custom Integrated Circuits Conf.,* 2005.

[12] K.W. Wong, A. Arasu, W. Chan, "A 90-nm CMOS LNA for MB-OFDM UWB in QFN package" *IEEE Radio Frequency Integrated Circuits Symp.*, pp. 497-500, 2008

[13] E. Bertran, M.S. O'Droma, P.L. Gilabert, G. Montoro, “Performance analysis of power amplifier back-off levels in UWB transmitters,” *IEEE J. Consumer Electronics,* pp. 1309-1313, 2007.

[14] G. Sapone, G. Palmisano, “A 3–10-GHz low-power CMOS low-noise amplifier for ultra-wideband communication,” *IEEE Trans. Microwave Theory Tech.,* pp. 678-686, 2011.

[15] O. Abedi, M.C.E. Yagoub, “CS-UWB-LNA with inverse ICPF filter in 130nm CMOS,” submitted to *IET J. Communications*, April 2012.

[16] O. Abedi, M.C.E. Yagoub, “Efficient UWB filter performance for multi-band UWB LNAs,” submitted to *IEEE Communications*, July 2012.

[17] O. Abedi, M.C.E. Yagoub, A. Abedi, “Enhanced UWB CS-LNA with inverse filter and shunt feedback resistor in 130nm CMOS,” *IEEE Int. Conf. on Signals, Circuits and Systems*, pp. 1-6, 2009.

[18] O. Abedi, M.C.E. Yagoub, “Comparison of ultra wide-band pulse modulation scheme performance under white Gaussian noise channels,” Accepted for publication in *Int. J. of Microwave Science and Technology.*

[19] O. Abedi, M.C.E. Yagoub, “Performance comparison of UWB pulse modulation schemes under white Gaussian noise channels,” *Int. Conf. Modelling and Simulation*, pp. 1-7, 2012.

Chapter 2 Filter Design for UWB-NBI Applications

2.1 Introduction

In ultra wide-band NBI cancellation, filters play a key role in the overall system performance. For that purpose, two kinds of filters should be investigated namely, 3-7GHz band-pass filters and 5-6GHz stop-band filters. Furthermore, those filters should be multi-channel filters with high sharpness with respect to pass-band flatness, attenuation, and element size.

Because active filters need to be supplied (which can add additional noise to the system response), have low-frequency response, and are sensitive to element tolerances [1], we focused only on passive filters.

In existing works [1], the focus was made mainly on filter response, size, and sharpness rate, to design UWB filters. No deep investigation has been achieved to select the most appropriate filter for efficient wide-band NBI cancellation. Therefore, we designed in Cadence different types of passive filters and compared their performance with respect to several key design parameters such as frequency response, sharpness rate, reflection coefficient, phase linearity, group delay, element size, and circuit topology (series/parallel). We also explored different design techniques, such as the zigzag method, to reduce the number of inductors in the circuit to further decrease its size.

2.2 Filter design parameters

A filter is a frequency selective circuit. Its design objectives depend strongly on its application. For instance, in some applications, pass-band ripple is critical (such as in image filters) [2], while in other applications, sharpness and integrated space is critical, which pushes the designer to use filters with higher sharpness [3].

Radio-frequency filters can be classified into five groups: low-pass filters (LPF), high-pass filters (HPF), band-pass filters (BPF), stop-band filters (SBF), and all-pass filters (APF) [4].

There are many transfer functions that may satisfy the attenuation and/or phase requirements of a particular filter. Among them, Gaussian, Bessel, Butterworth, Chebyshev (type I -ChevI- with higher pass-band ripple or type II -ChevII- with higher stop-band ripple [5]), Hourglass, and Elliptic, are the most widely used. Comparing their performance will help us to select the most suitable for UWB systems. In UWB-NBI applications, the following criteria should be considered for efficient selection [6]:

- High pass-band flatness (Low ripple),
- High attenuation,
- High sharpness and low-pass edge overshoot with respect to stop-band attenuation (SBA) and filter order,
- High phase linearity and low group delay.

Another criterion that has to be considered for efficient UWB filter design is the amplitude/phase distortion. In this work, we focused only on the amplitude distortion which is more critical (amplitude harmonic attenuation).

Note that for filter initial design, the Filter Design software, Version-3, has been used, assuming ideal transmission-lines (no losses and infinite Q factor) for the purpose of comparison.

2.3 Filter Design Steps

Filter design can be achieved through two steps [7]: approximation and synthesis. Filter approximation usually depends on filter specifications, such as ripple, SBA, corner frequency, stop-band bandwidth (SBW), band-pass bandwidth (BPW), sharpness, filter circuit configuration (symmetry, type of source). Usually, we start with an initial design, which assumes that all passive elements are ideal (i.e., inductors and capacitors have infinite Q factor). Filter synthesis is based on a given transfer function, called $H(s)$, where $s = j\omega$ is the complex frequency. Filter design starts by designing a LPF prototype and then converting it to the required type. This well-known process is detailed in [8].

In Table 2.1, we summarized the main characteristics of the different types of filters we investigated with regard to their application as input matching network of UWB low-noise amplifiers (UWB-LNA) [3], [8], [9].

Table 2.1: 3[th] order BPF specifications for UWB-LNA input matching.

	R_S / R_L (Ω)	f_L (GHz)	f_H (GHz)	f_C (GHz)*	A_{max} (dB)	SBA (dB)
Gaussian	50 / 50	3	7	4.55	0	25
Bessel	50 / 50	3	7	4.30	0	30
Butterworth	50 / 50	3	7	4.55	0	32
ChevI	50 / 50	3	7	4.55	0.01-0.1	< 10
ChevII	50 / 50	3	7	4.58	0.01-0.1	< 10
Elliptic	50 / 50	3	7	4.58	0.01-0.1	< 10
Hourglass	50 / 50	3	7	4.55	0.5	< 10

* f_C can be different (some filters have to be optimized to meet band-pass conditions).

In this table, R_S refers to the input impedance and R_L to the load impedance. f_C is the cutoff frequency of LPF and HPF whereas f_L and f_H stand for the lower and the upper cutoff frequency of BPF and SBF, respectively. In Table 2.2, we did the same for multiband UWB low-noise amplifiers (MB-UWB-LNA). To be consistent, all filters are assumed working with voltage sources and be symmetrical. Neither delay equalization nor bias sources were considered.

Table 2.2: 1st order SPF specifications for MB-UWB-LNA input matching.

	R_S / R_L (Ω)	f_L (GHz)	f_H (GHz)	f_C (GHz)*	A_{max} (dB)	SBA (dB)
Gaussian	50 / 50	5	6	5.48	---	< 10
Bessel	50 / 50	5	6	5.50	---	< 10
Butterworth	50 / 50	5	6	5.48	---	< 10
ChevI	50 / 50	5	6	5.47	0.01- 0.1	< 15
ChevII	42 / 40	5	6	5.50	0.1**	< 10
Elliptic	45 / 40	5	6	5.50	0.1**	< 10
Hourglass	45 / 50	5	6	5.48	0.1**	< 10

* f_C can be different (some filters have to be optimized to meet band-pass conditions).
** *ChevII*: SBW = 475MHz. *Elliptic*: SBW = 473MHz and *Hourglass*: SBW = 475MHz.

2.4 Gaussian Filters

Gaussian filters are well known for their high flatness baseband, high stop-band attenuation (SBA), and low group delay [9].

Their transfer function is inversely proportional to the square root of the McLaren series expansion of e^{s^2} [10]

$$H(s) = \frac{1}{\sqrt{2\pi}\sigma} e^{\frac{-s^2}{2\sigma^2}} \tag{2.1}$$

where σ is the standard deviation of the distribution assumed with zero mean.

2.4.1 Gaussian BPF

To investigate the Gaussian BPF filter performance, we first simulated its magnitude response vs. the circuit order (Fig. 2.1). Then, the variation of the input impedance (Z_{in}) versus frequency (Fig. 2.2) shows that this parameter is almost independent of the filter order. As for the input reflection coefficient (Fig. 2.3), it shows a narrowband performance indicating lower efficiency in wideband applications.

From these results, we can see that the 3rd order Gaussian filter can be the best compromise due to its sharpness in lower orders. Its corresponding shunt/series topologies are given in Fig. 2.4. However, the Gaussian filter is not acceptable for our purpose due to inductor size.

2.4.2 Gaussian SBF

In MB-UWB-LNA applications, different stop-band filters can be considered in terms of inductor size, sharpness, and low order. As for the Gaussian BPF, we simulated the SBF response, reflection coefficient and phase for different filter orders (Figs. 2.5, 2.6 and 2.7, respectively).

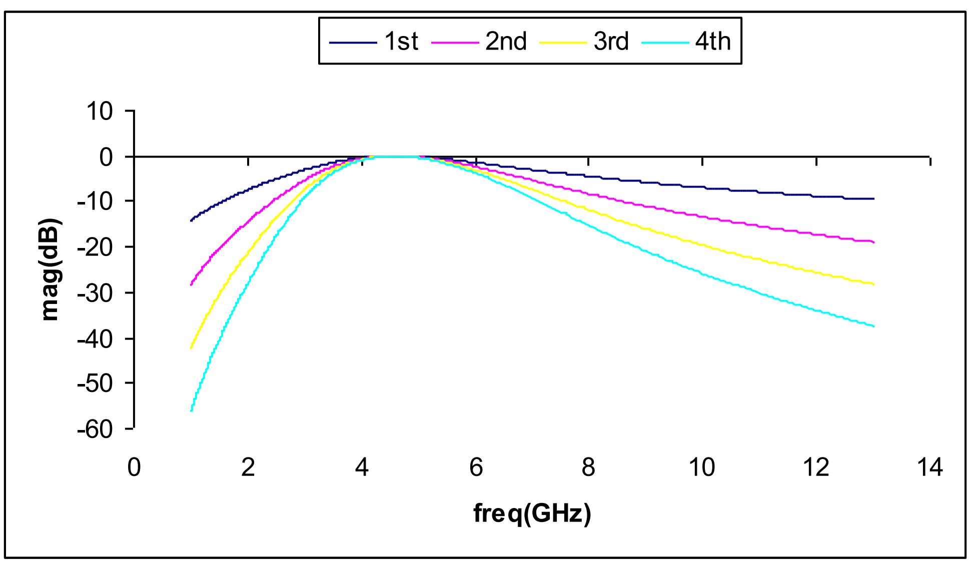

Fig. 2.1: Gaussian BPF magnitude for 1st, 2nd, 3rd, and 4th order configurations

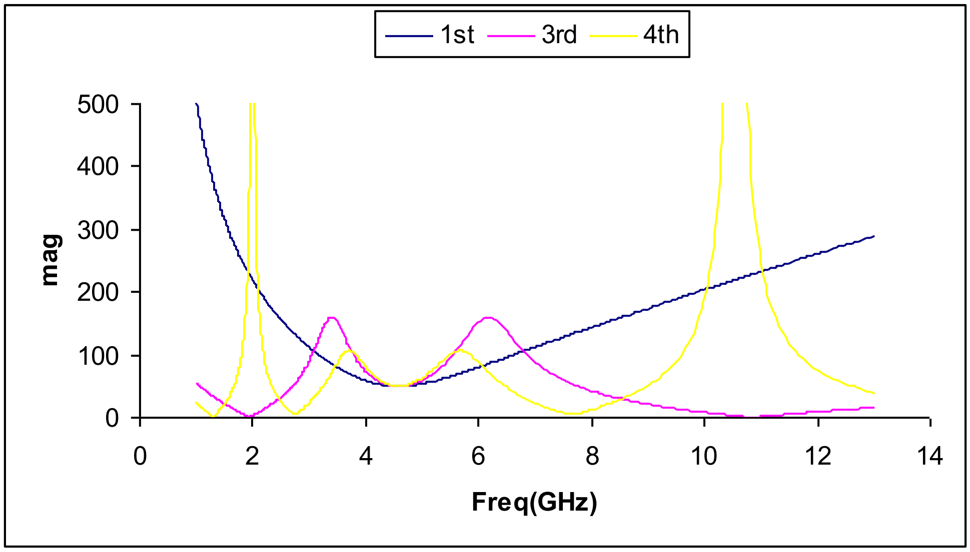

Fig. 2.2: Gaussian BPF input impedance for 1st, 3rd, and 4th order configurations.

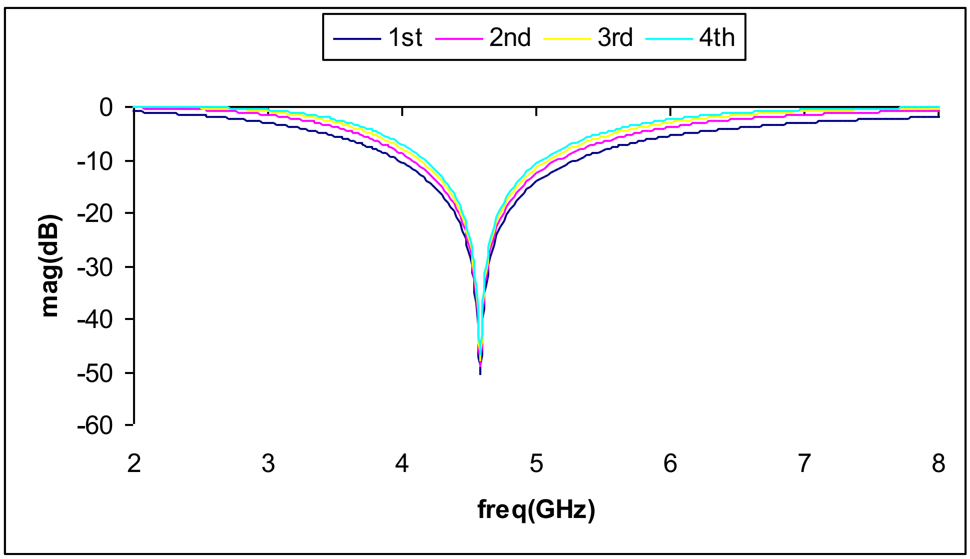

Fig. 2.3: Gaussian BPF reflection coefficient for 1st, 2nd, 3rd, and 4th order configurations.

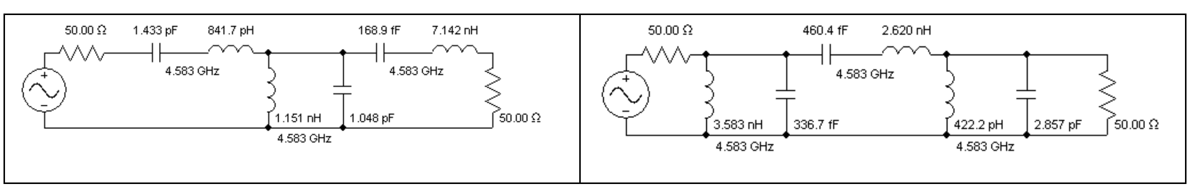

(a) (b)

Fig. 2.4: 3rd order Gaussian BPF, a) Series, b) Shunt topology.

In order to suppress the WLAN spectrum frequency band (5-6 GHz), the 1st order SBF (Fig. 2.8) could be retained because of its good attenuation and minimum number of inductors involved (the stop-band attenuation is smaller than 10dB, enough for our purpose). However, both configurations are not acceptable. In fact, the series configuration is not a good option due to its higher overshoot in the desired bandwidth (3-5GHz and 6-7GHz), while the shunt topology has indeed a better performance in terms of sharpness but with higher inductor size.

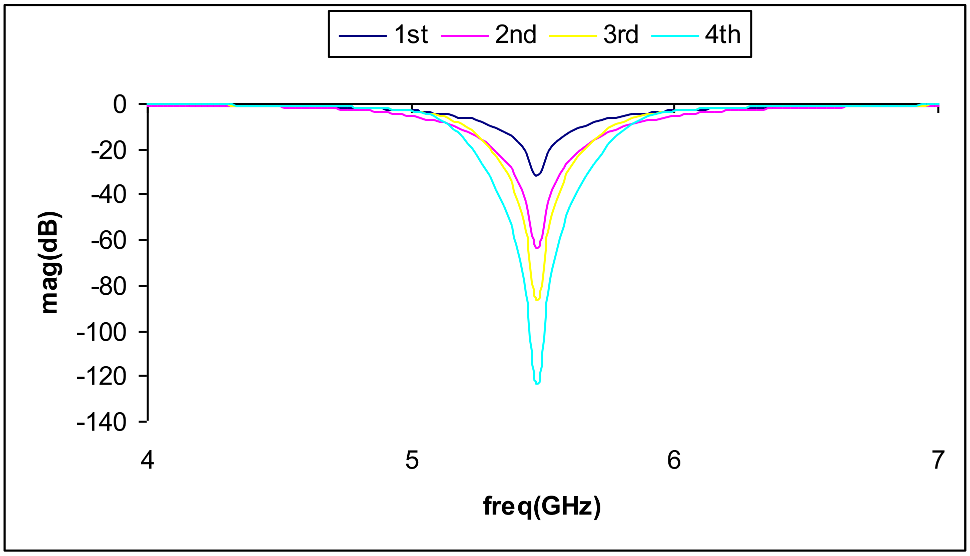

Fig. 2.5: SBF Gaussian magnitude for the 1st, 2nd, 3rd, and 4th order configurations

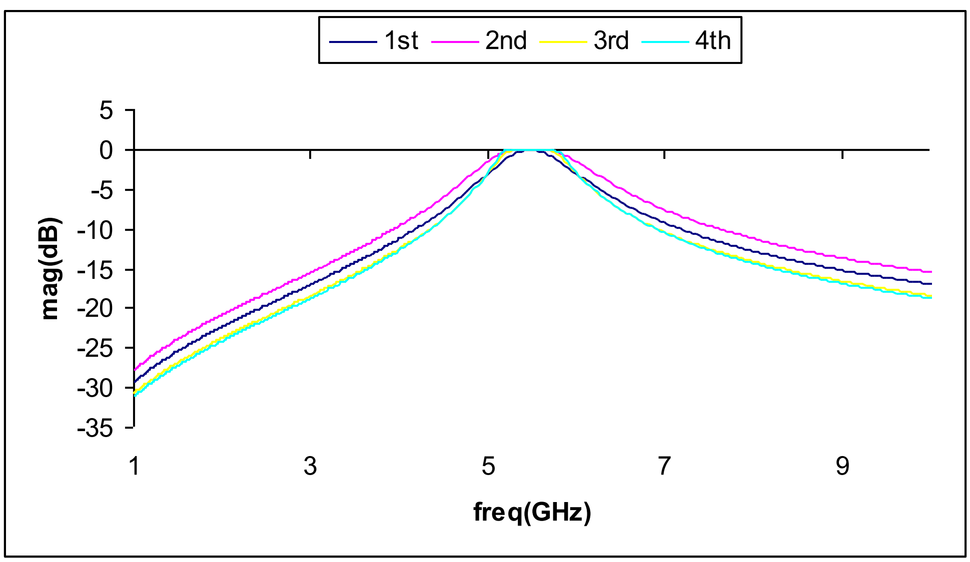

Fig. 2.6: SBF Gaussian reflection coefficient for the 1st, 2nd, 3rd, and 4th order configurations

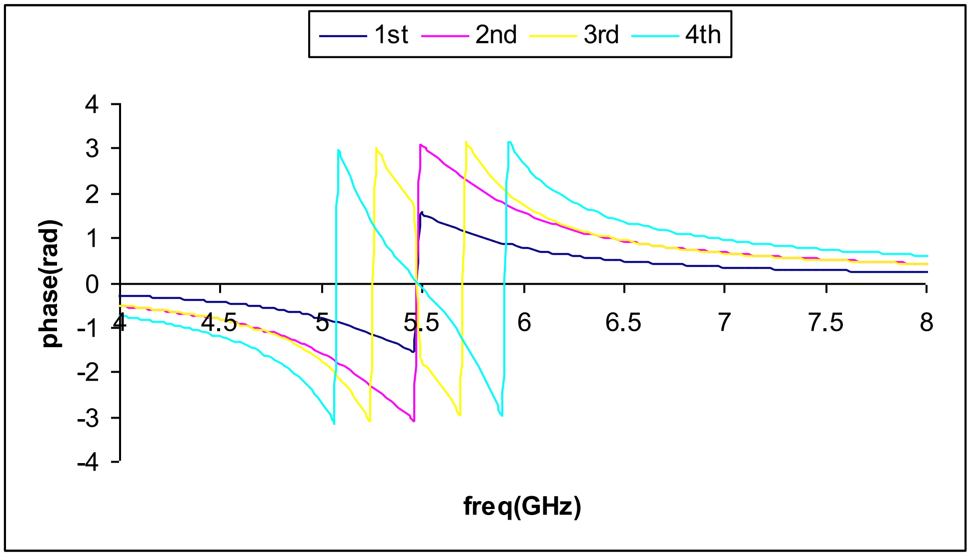

Fig. 2.7: SBF Gaussian phase for the 1st, 2nd, 3rd, and 4th order configurations

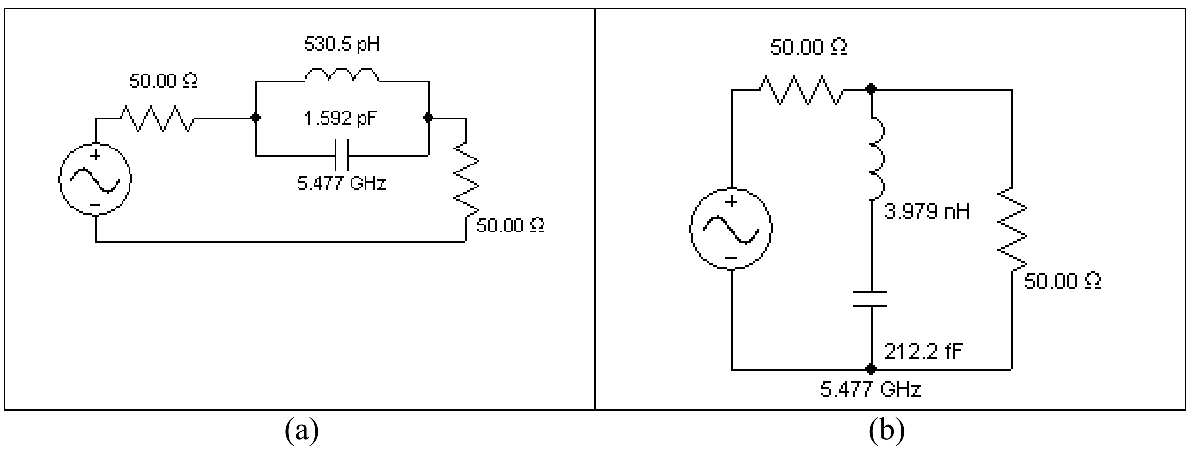

Fig. 2.8: 1st order Gaussian SBF, a) series b) shunt topology

2.5 Butterworth Filters

The Butterworth transfer function is expressed in terms of odd/even functions [11]

$$H(S)=\begin{cases}\Pi_{k=1}^{n/1}\dfrac{1}{s^2+(2\sin\theta_k)s+1} & even\quad n\\ \dfrac{1}{s+1}\Pi_{k=1}^{\frac{n-1}{2}}\dfrac{1}{s^2+(2\sin\theta_k)s+1} & odd\; n\end{cases}\qquad \theta_k=\frac{2k-1}{2n}\pi;\; k=1,2,\ldots n \qquad (2.2)$$

Because the Butterworth transfer function derivatives are zero at $\omega = 0$,

$$\frac{\partial |H_N(iw)|^2}{\partial w} = \frac{-nw^{2n-1}}{(1+w^{2n})^{3/2}} \tag{2.3}$$

This filter shows an excellent flatness in band-pass (lowest ripple). Also the filter slope rate is directly related to filer order (20*n* dB/decade) according to

$$|H_N(iw)|^2 \approx \frac{1}{w^{2n}},\ H(iw)_{dB} = -20n\log w \tag{2.4}$$

2.5.1 Butterworth BPF

Figure 2.9 shows that a Butterworth BPF gives maximum flatness in pass-band but its sharpness slope rate is worse at the highest part of the filter bandwidth (5-7GHz) compared to the lower side of the filter bandwidth (3-4GHz).

Figure 2.10 shows that the SBA is directly dependent on the filter order and thus, the 1st order Butterworth BPF is enough to meet our specifications (> 10dB in stop-band attenuation). Figure 2.11 shows the equivalent shunt/series topology of the 3rd order filter.

However, the shunt topology is not acceptable due to its higher inductor size and also because it will add a parallel capacitor to the next stage (the core LNA block).

For further investigations, we simulated the circuit with real elements and the results are shown in Fig. 2.12. From this, we can conclude that a maximum flatness has been achieved in the desired pass-band, but it is not critical in our purpose. Note that there is 6dB magnitude difference between the Cadence simulation using real elements and the ideal filter solution, which depends on the load voltage divider.

We can also conclude that the Butterworth BPF presents very low sharpness and thus is not suitable for our purpose (narrow-band interference cancellation). Also, the inductor size is larger in comparison with the other filter types.

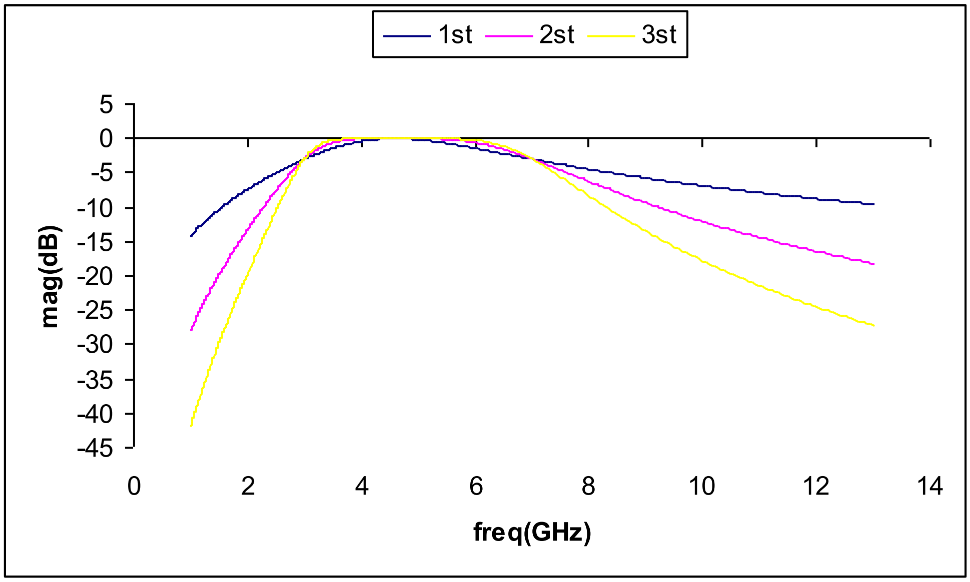

Fig. 2.9: Butterworth BPF magnitude for various filter orders

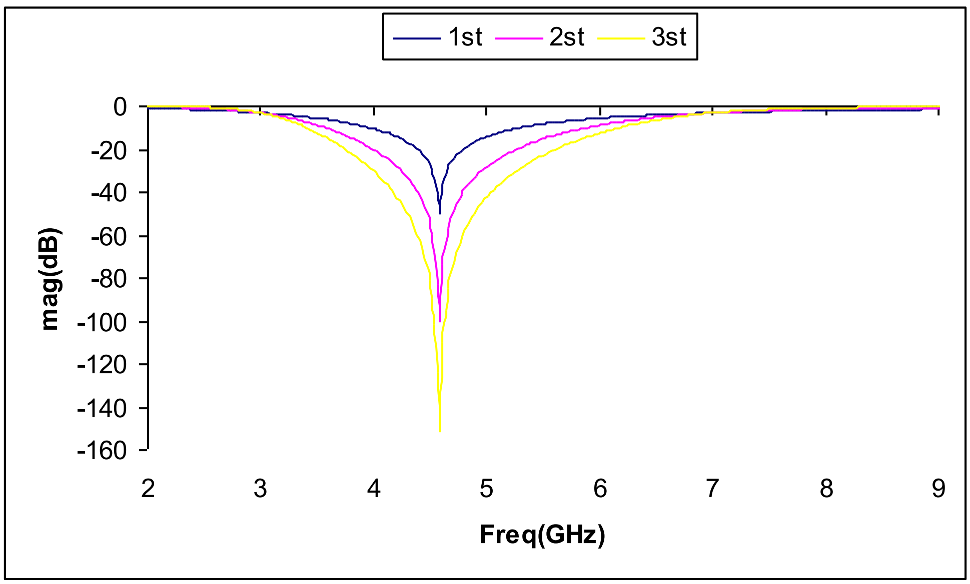

Fig. 2.10: Butterworth BPF reflection coefficient for various filter order

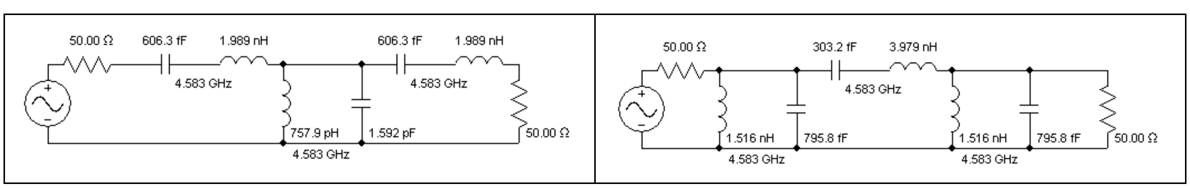

(a) (b)

Fig. 2.11: 3^{rd} order Butterworth BPF, a)Element series, b) Element shunt

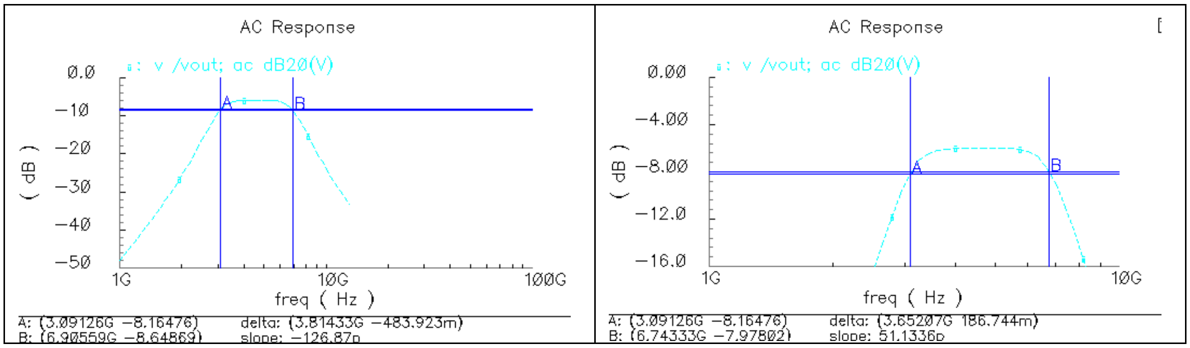

Fig. 2.12: 3rd order Butterworth BPF with real elements a) magnitude (dB), b) Zoom in the bandwidth.

2.5.2 Butterworth SBF

As for the filters we already investigated, we plot the frequency response, reflection coefficient and phase of a Butterworth SBF for various circuit orders (Figs. 2.13, 2.14 and 2.15, respectively).

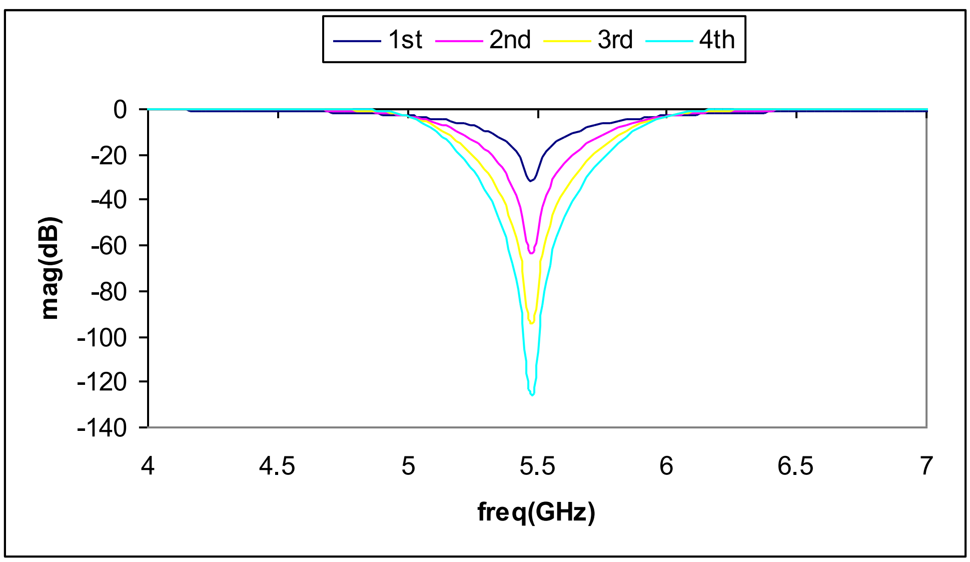

Fig. 2.13: Butterworth SBF magnitude for various filter orders.

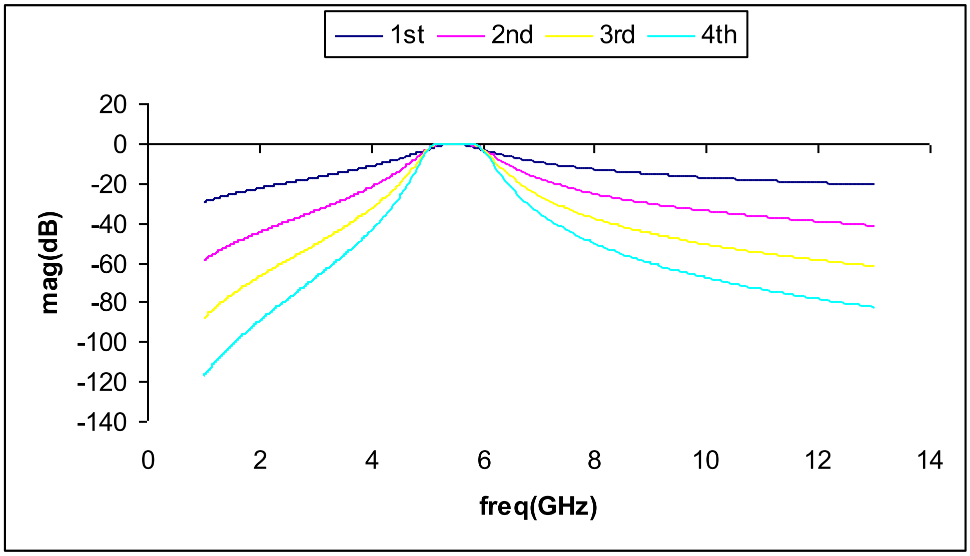

Fig. 2.14: Butterworth SBF reflection coefficient for various filter orders.

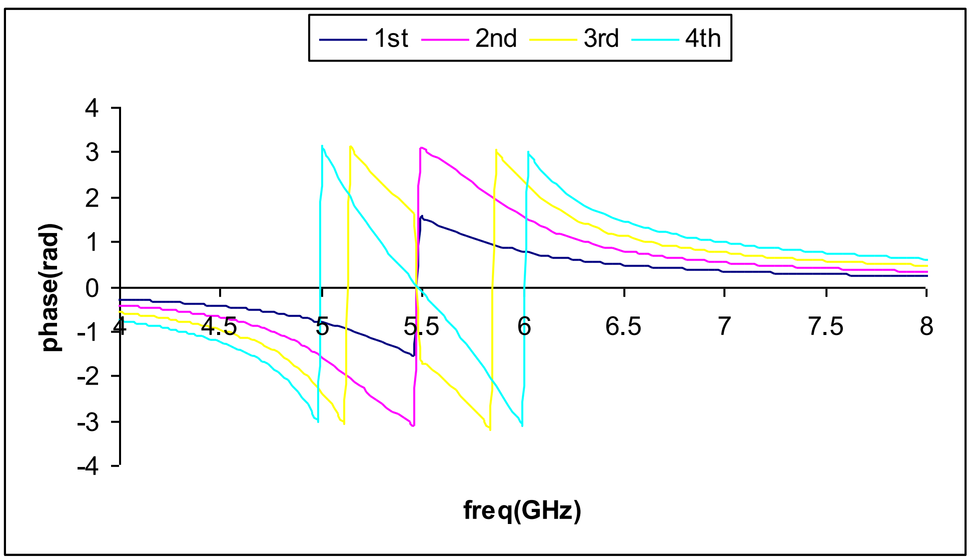

Fig. 2.15: Butterworth SBF phase for various filter orders.

From these figures, the 2^{nd} order Butterworth SBF shows excellent stop-band attenuation (its shunt/series topologies are displayed in Fig. 2.16). However, this characteristic is not critical for our application. Most important, its reflection coefficient in desired stop-band is lower compared to other filter types.

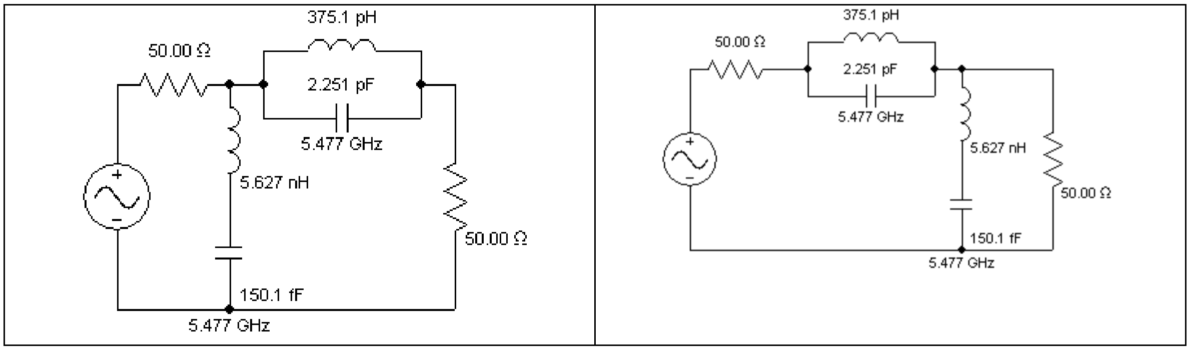

(a) (b)

Fig. 2.16: 2nd order Butterworth SBF, a) shunt b) series elements

2.6 Type I Chebyshev filters

Butterworth and Gaussian filters have indeed a maximum flatness but they do not have a high sharpness with respect to filter order. The ChevI filter suppresses this issue. Furthermore, it has an equal ripple in desired pass-band, where ripple period is directly related to the filter order. ChevI filter transfer function can be expressed as [5], [12].

$$|H(iw)|^2 = \frac{1}{1+\varepsilon^2 T_n^2(w)}, \quad A_{\max} = 10\log\left(1+\varepsilon^2\right) \tag{2.5}$$

$$T_n(w) = \cos(n\cos^{-1} w) \text{ with } \begin{cases} 0 \le T_n(w) \le 1 & 0 \le |w| \le 1 \\ T_n(w) \ge 1 & |w| > 1 \end{cases} \quad \text{n} = 1, 2 \ldots \tag{2.6}$$

where w is the normalized frequency and $A_{\max}$ the maximum ripple amplitude. There is a direct relation between stop-band attenuation (SBA), ripple amplitude, element size and filter order. By reducing the ripple, the element size will increase. Compared to other filters, ChevI has the highest sharpness with reasonable attenuation, minimum ripple and inductor size/number [13], [14], [15].

Chebyshev and Butterworth filters are known as pole filters, which do not have zeros. However, in Butterworth, the poles are placed in circular position while Chebyshev poles are placed in elliptic position. Whenever, the Chebyshev poles are closer to the imaginary axis, which indicates higher inductor size along with higher ripple amplitude (not ripple bandwidth) and sharpness.

2.6.1 ChevI BPF

We simulated the ChevI BPF response and reflection coefficient as function of the filter order and maximum ripple (Figs. 2.17, 2.18 and 2.19, respectively). As shown, the 3rd order filter with higher ripple (i.e., 0.1 dB) presents the highest sharpness and lowest attenuation. However, targeting more flatness will lead to higher inductor size.

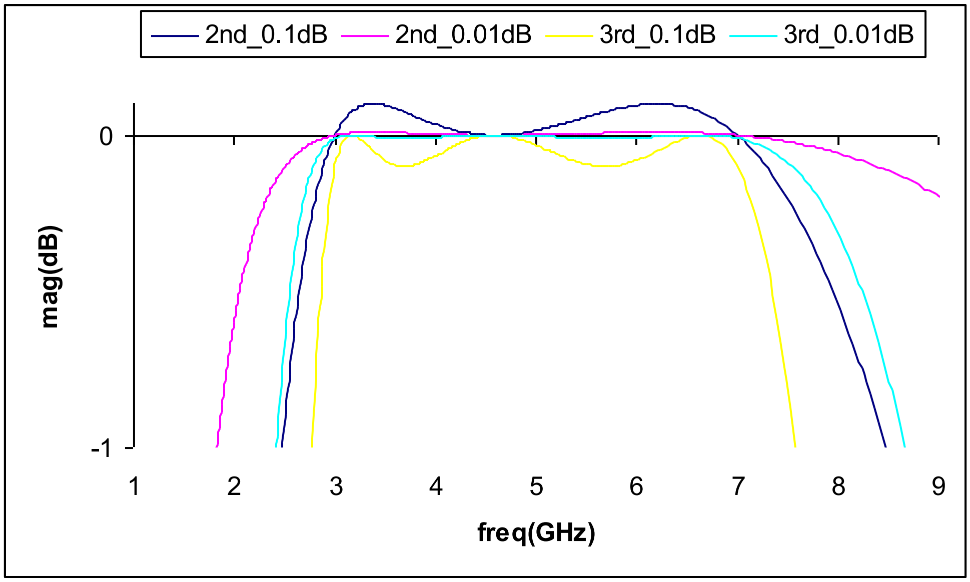

Fig. 2.17: ChevI BPF gain for various order and max ripple

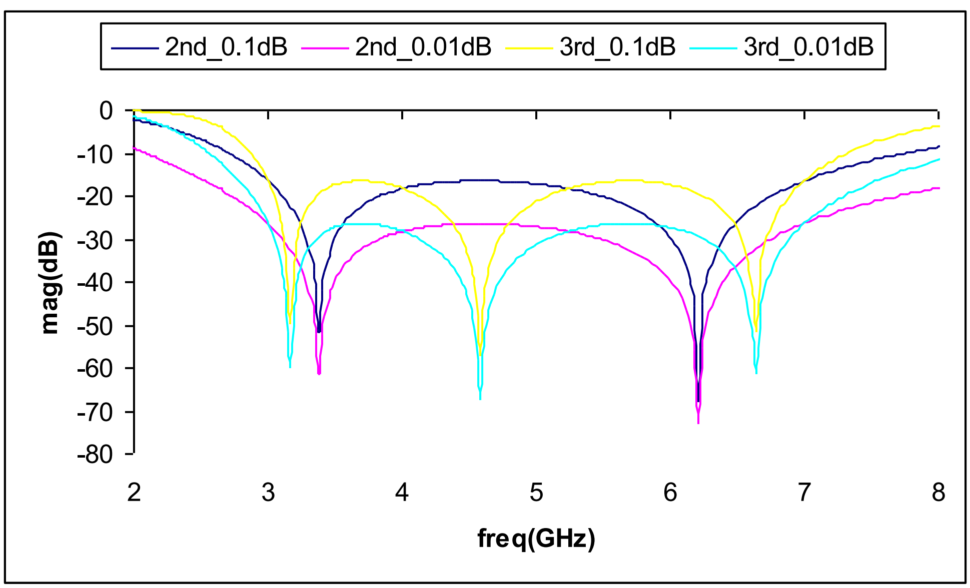

Fig. 2.18: ChevI BPF reflection coefficient for various order and max ripple.

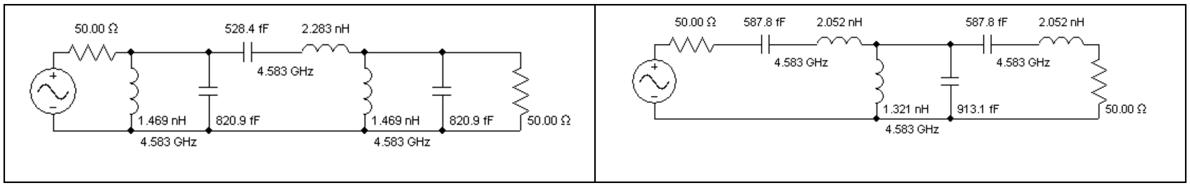

(a) (b)

Fig. 2.19: A three cell BPF chevI filter with shunt and series elements (A_{max} = 0.1dB).

2.6.2 ChevI SBF

The ChevI SBF filter shunt topology cannot be retained since the size of its inductors exceeds the circuit integration limitations (> 10nH). On the other side, ChevI SBF series topology has reasonable SBA, excellent reflection coefficient, higher stop-band response for higher orders (> 2) and good sharpness compared to other filters (Figs. 2.20 and 2.21, respectively). By reducing ripple, the inductor size decreases along with sharpness. However it adds larger capacitor to the circuit instead. Such large capacitor reactance will add more parasitic effects in IC integration processing and therefore, making simulation results quite different from layout simulations due to higher area connection. So we selected the 1st order ChevI SBF with a ripple of 0.1dB (Fig. 2.22).

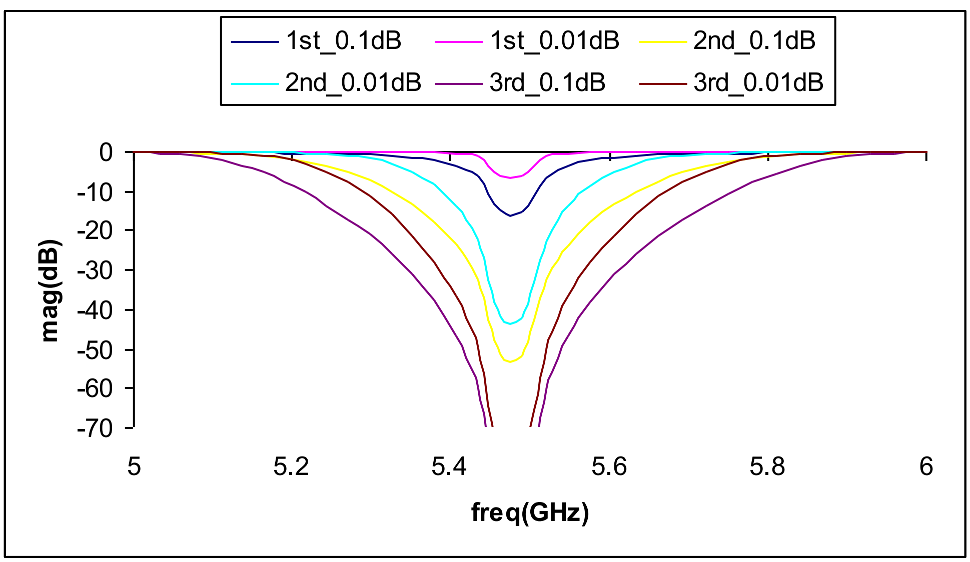

Fig. 2.20: ChevI SBF gain for various filter order and maximum ripple.

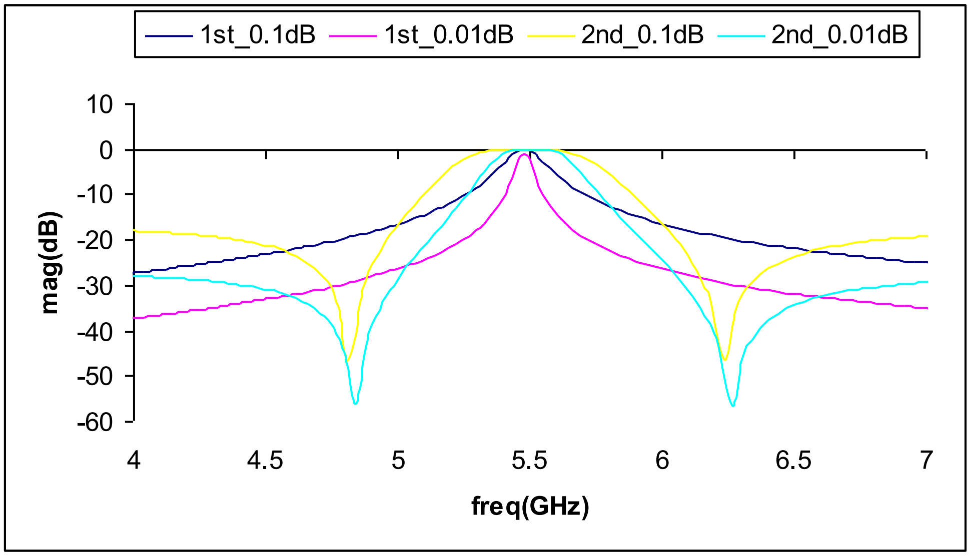

Fig. 2.21: ChevI SBF reflection coefficient for various filter order and maximum ripple.

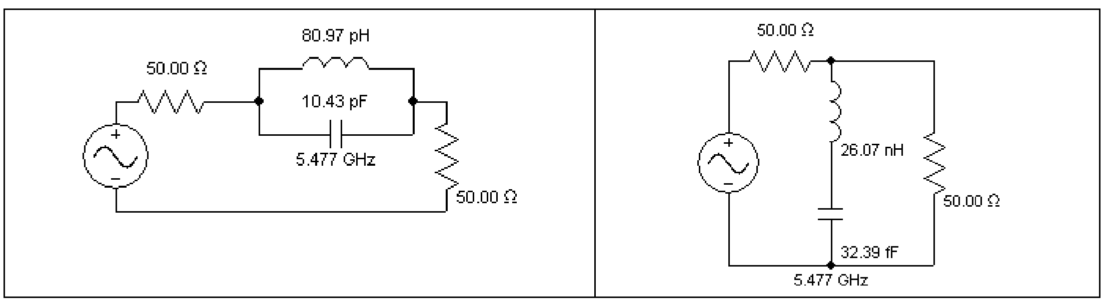

Fig. 2.22: 1st order ChevI SBF, a) series, b) shunt topology

2.7 Type II Chebyshev filters

Type I Chebyshev (or ChevI) and Butterworth filters are pole filters while Type II Chebyshev filters (or ChevII) have maximum flatness (lowest ripple) in pass-band and equal-ripple in stop-band [8]. ChevII transfer function and order can be expressed as

$$|H_{II}(iw)|^2 = \frac{\varepsilon^2 T_n^2\left(\frac{w_c}{w}\right)}{1+\varepsilon^2 T_n^2\left(\frac{w_c}{w}\right)} \tag{2.7}$$

and

$$A_{\max} = 10\log\left(1+\frac{1}{\varepsilon^2}\right)_{dB} \qquad \rightarrow \qquad n \geq \frac{\cosh^{-1}\dfrac{1}{\varepsilon\sqrt{10^{\alpha/10}-1}}}{\cosh^{-1}\left(\dfrac{w_c}{w}\right)} \tag{2.8}$$

where $w/w_c = w_n$ is the normalized frequency.

2.7.1 ChevII BPF

In ChevII BPF, there is a tradeoff between SBA, sharpness and inductor size. A preliminary investigation helped us to setup the optimized SBA value in the range of 8-10dB. According to a Monte-Carlo simulation, the inductor size increases by 10% with 50% reduction of SBA, resulting in higher flatness. Also, ChevII BPF required higher number of elements compared to other same order filters (e.g., the 3rd order needs 8 elements as in Fig. 2.23). Also the inductor size will increase. In fact by simulating the third order, we found that reducing SBA will increase the inductor size (e.g., for the lowest case SBA = 7dB, we obtained an inductor value of 5nH). In addition, it shows that SBA is more significant in the higher part of the spectrum (Fig. 2.24).

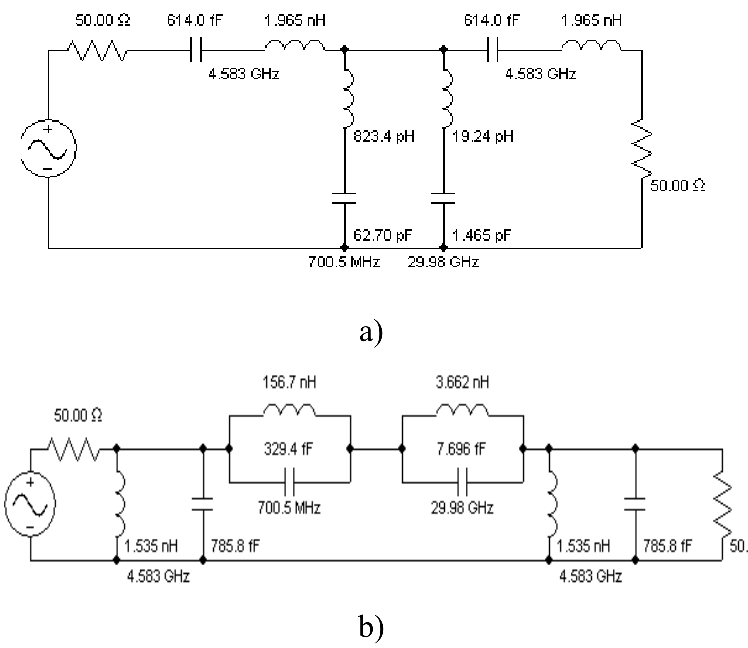

Fig. 2.23: 3rd order ChevII BPF, a) series b) shunt topology.

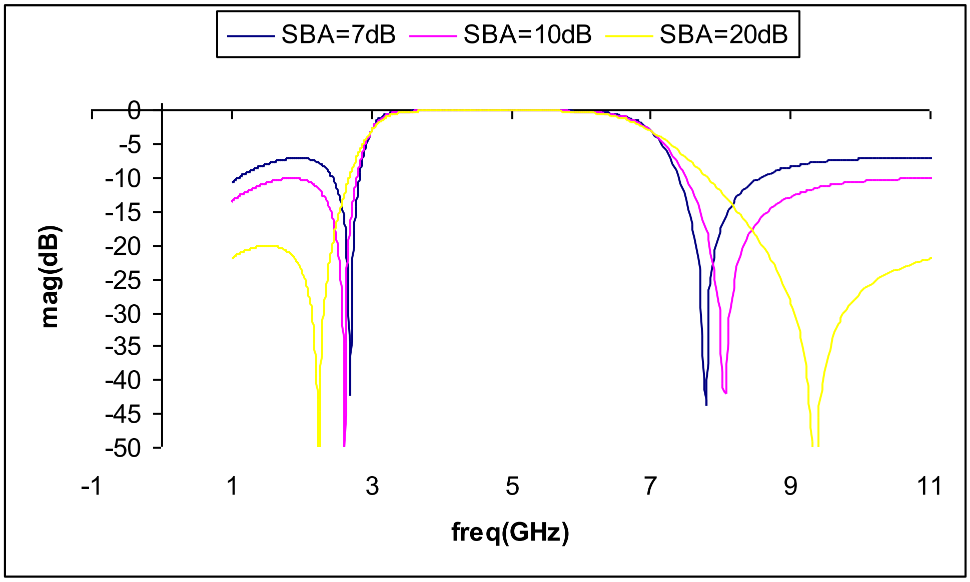

Fig. 2.24: 3rd order ChevII BPF magnitude response for various SBA

2.7.2 ChevII SBF

Satisfying the stop-band bandwidth (SBW) requirements is our main design goal in designing SBFs. First and second order stop-band ChevII filters achieved only a maximum SBW of 500MHz (Fig. 2.25), while for the 3rd order (Fig. 2.26) it increases to 900-950MHz. However, this improvement was achieved at the expense of lower attenuation (15dB), higher number of elements and higher ripple. Again, there is a trade-off between attenuation and sharpness as shown in Fig. 2.27.

2.8 Bessel filters

Bessel filters are well known as delay filters with ideal phase [2], [8]. This type of filters has some advantages, such as linear phase and excellent stop-band attenuation. However, to achieve higher sharpness, it requires higher order, which is not acceptable for our design. Furthermore, the inductor size is larger compared to similar configurations and there is an overshoot in the pass-band edge.

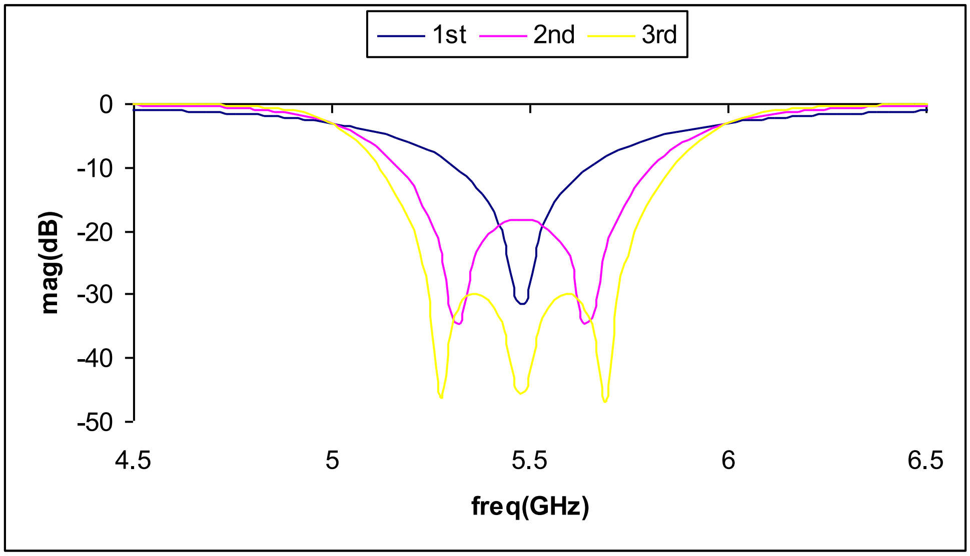

Fig. 2.25: ChevII SBF magnitude response for various filter orders.

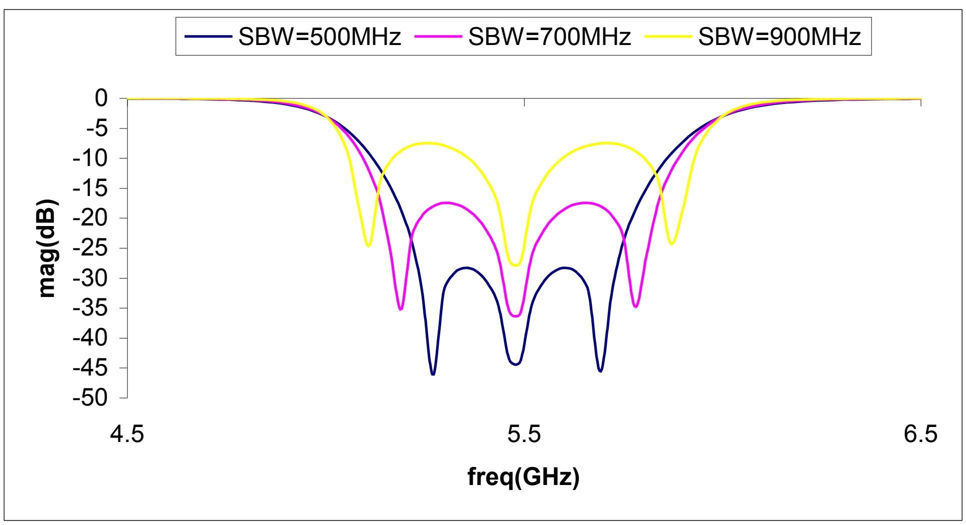

Fig. 2.26: 3rd order ChevII SBF magnitude for various stop-band bandwidths (SBW).

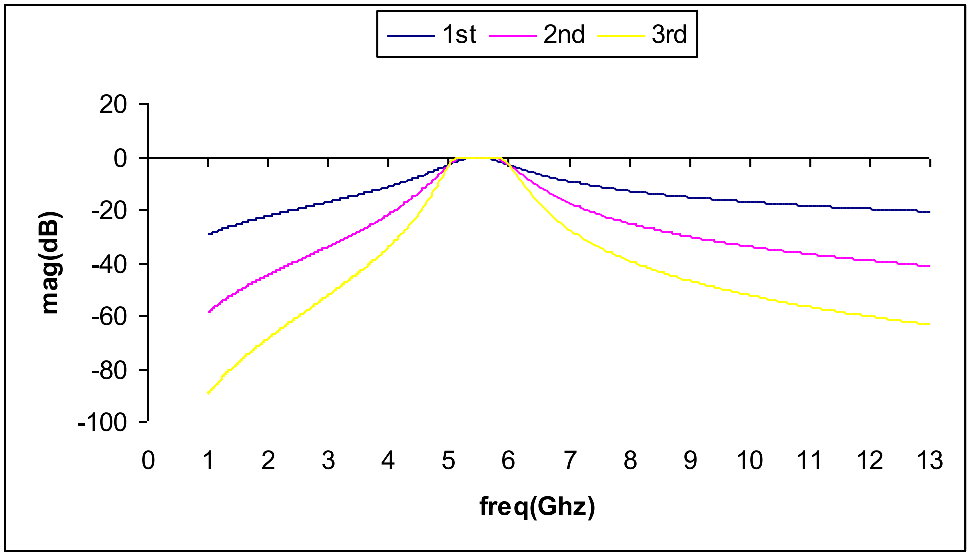

Fig. 2.27: ChevII SBF reflection coefficient for various filter orders.

2.8.1 Bessel BPF

Figures 2.28, 2.29, 2.30, and 2.31 show the Bessel BPF response, reflection coefficient phase and delay, respectively. From these figures, we can conclude that the 3rd order Bessel BPF cannot be retained. It indeed has the highest SBA, but not enough sharpness. Furthermore, its element sizes (Fig. 2.32) are higher compared to other filter types, which prove again that the Bessel BPF is not suitable for our purpose.

2.8.2 Bessel SBF

In Bessel SBF design, shunt topology is preferred due to smaller inductor size. From Figs. 2.33, 2.34, and 2.35, which show its respective response, reflection coefficient and phase, we can say that the 2nd order could be the best choice. However, simulating its schematic (Fig. 2.36) highlighted the fact that it exhibits different frequency responses for shunt and series elements. Also, the capacitor sizes are large, which is a big issue for layout.

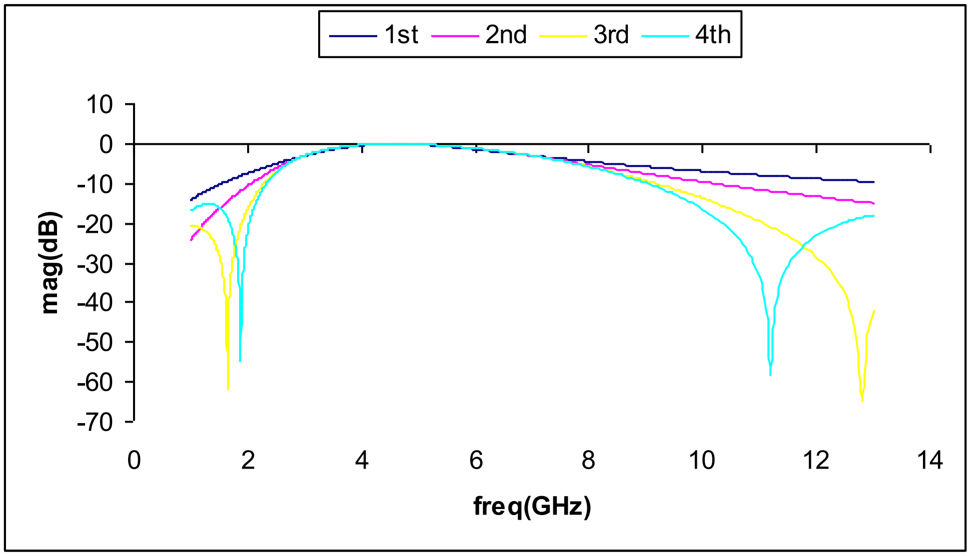

Fig. 2.28: Bessel BPF response for various orders.

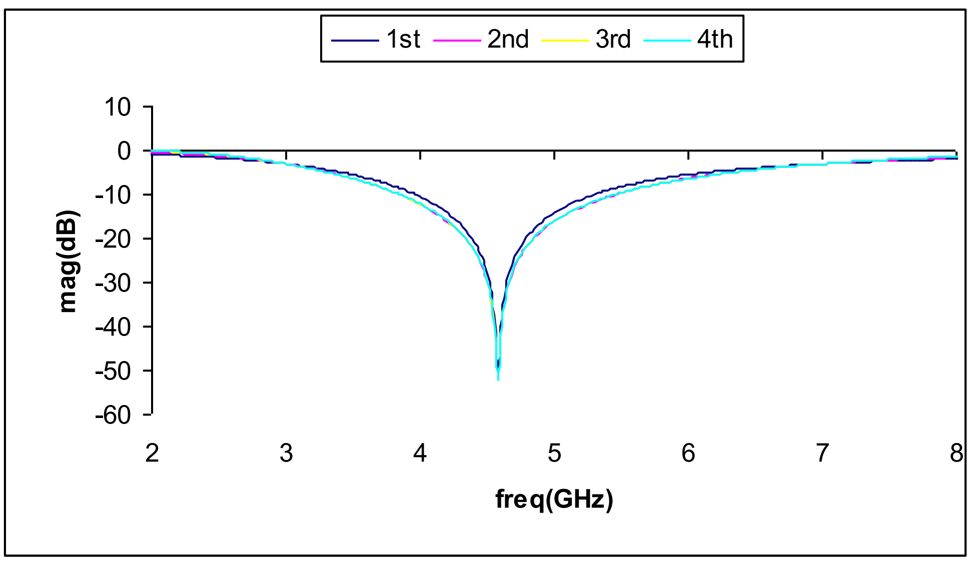

Fig. 2.29: Bessel BPF reflection coefficient for various orders.

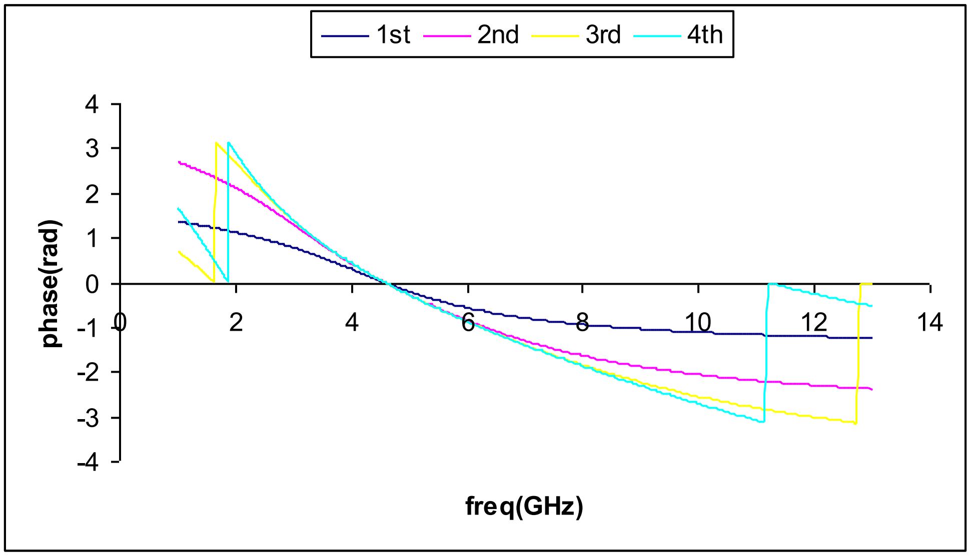

Fig. 2.30: Bessel BPF phase for various orders.

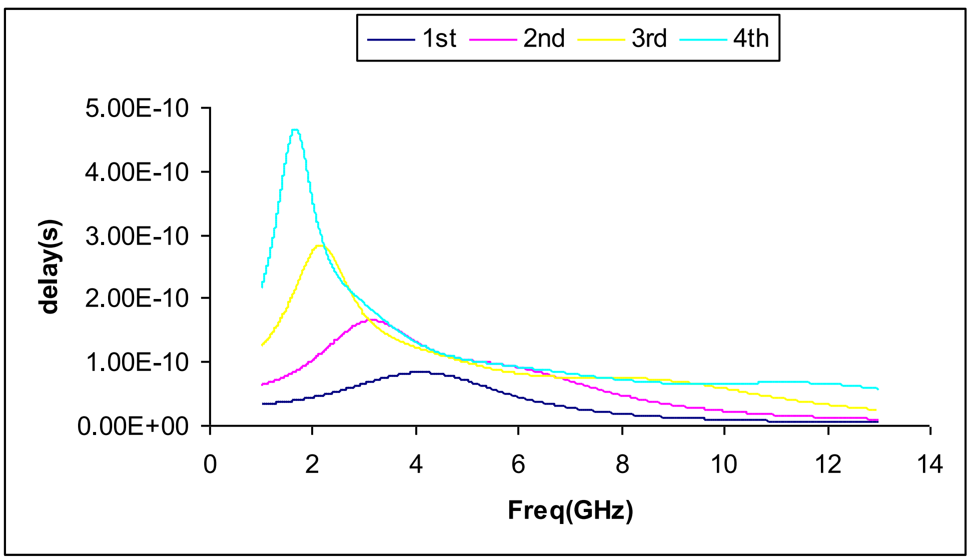

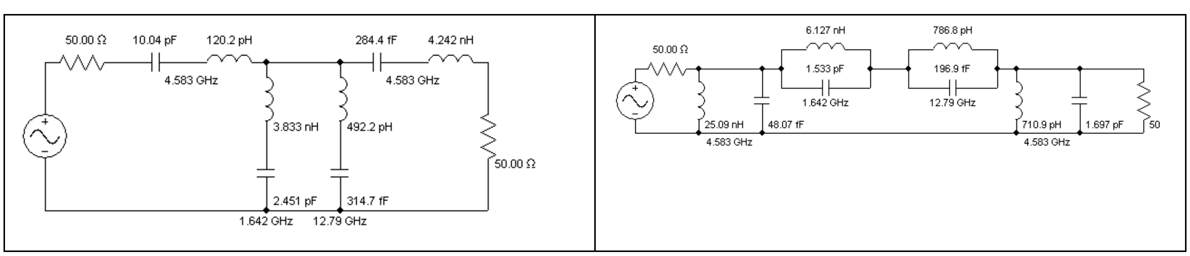

(a) (b)

Fig. 2.32: 3rd order Bessel BPF, a) series b) shunt topology

Fig. 2.31: Bessel BPF delay for various orders.

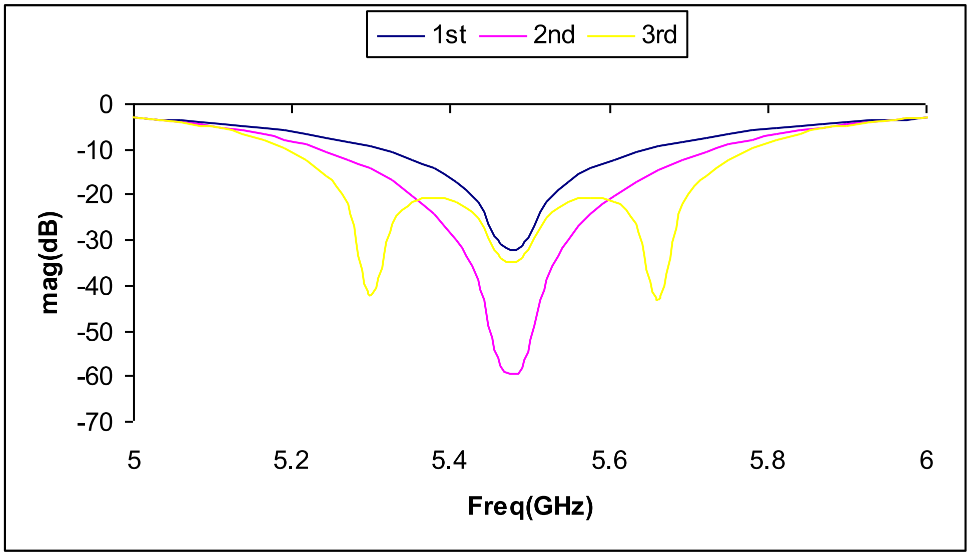

Fig. 2.33: Bessel SBF response for various orders.

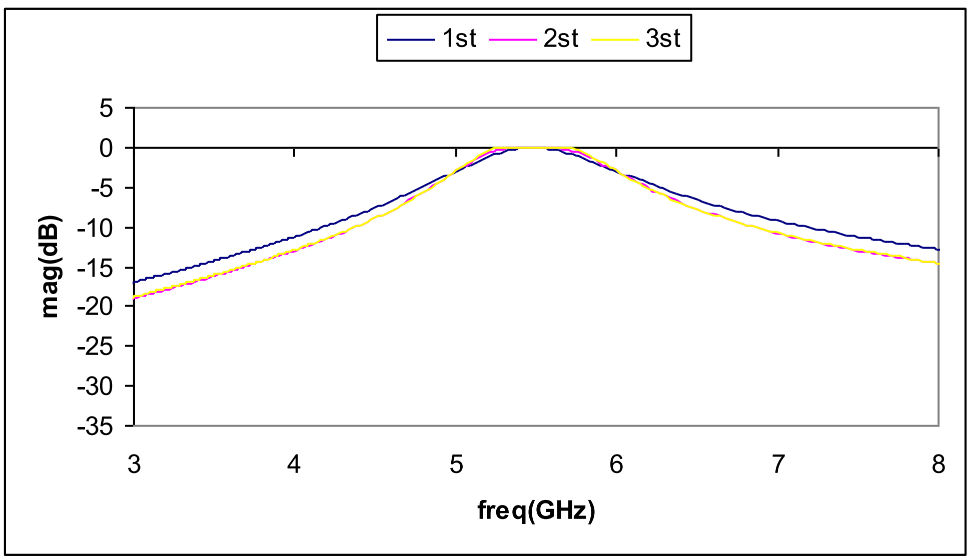

Fig. 2.34: Bessel SBF reflection response for various orders.

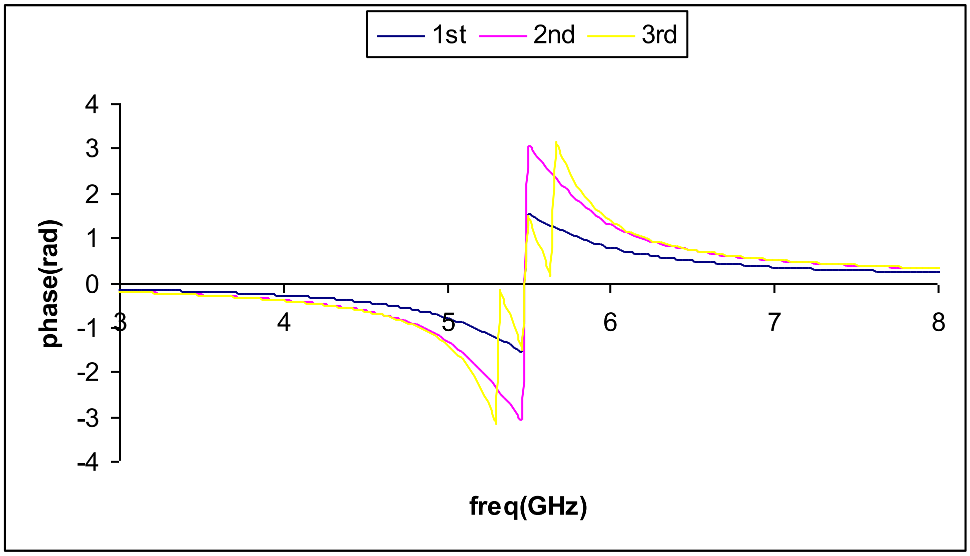

Fig. 2.35: Bessel SBF phase for various orders.

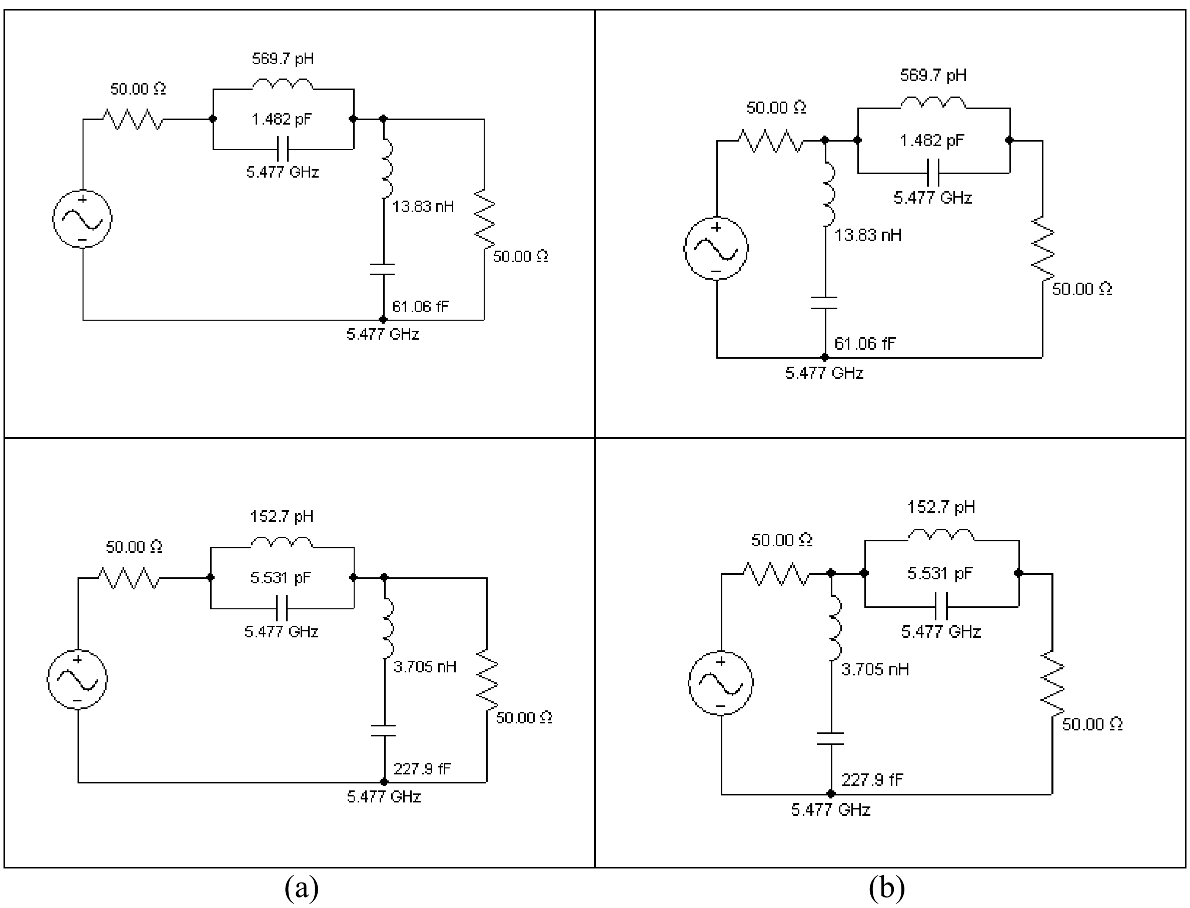

Fig. 2.36: 2[nd] order Bessel SBF, a) series b) shunt topology

2.9 Elliptic filters

The main reason for investigating the Elliptic Filter is its higher sharpness but at the price of higher inductor size. Pass-band and stop-band ChevI and ChevII filters have equal-ripples positioned inversely while the Elliptic filter is the only filter that has equal-ripple in both bands. The elliptic filter transfer function is defined as [16], [17]:

$$|H(iw)|^2 = \frac{1}{1+\varepsilon^2 R_n^2(w)}$$

$$\begin{cases} R_n(w) = \dfrac{w\left(w_1^2 - w^2\right)\left(w_2^2 - w^2\right)....\left(w_k^2 - w^2\right)}{\left(1 - w_1^2 w^2\right)\left(1 - w_2^2 w^2\right)....\left(1 - w_k^2 w^2\right)}; k = \dfrac{n-1}{2};\ odd\,(n) \\ R_n(w) = \dfrac{\left(w_1^2 - w^2\right)\left(w_2^2 - w^2\right)....\left(w_k^2 - w^2\right)}{\left(1 - w_1^2 w^2\right)\left(1 - w_2^2 w^2\right)....\left(1 - w_k^2 w^2\right)}; k = n/2;\ 0 \le w_i \le 1;\ even\ (n) \end{cases} \tag{2.9}$$

2.9.1 Elliptic BPF

For Elliptic BPFs, the shunt topology is usually preferred due to its lower inductor size. However, a small series resistor must be added to the shunt inductor to avoid simulation fatal error. First, a ripple of 0.1dB and a SBA of 10dB have been retained (Fig. 2.37). Thus, following Figs. 2.38 and 2.39, the third order circuit (Fig. 2.40) appears to be the best choice.

2.9.2 Elliptic SBF

Elliptic SBFs with even order require *n* inductors, with *n* the filter order, while odd orders require *n*-1 inductors. To avoid having so large number of inductors, we used the Zigzag method to design elliptic SBFs [17]. This approach can provide a design with only one inductor for the entire filter but by adding more capacitors to the circuit. Note that in even order circuits, the source resistor will be set to a special value (depending on the filter specifications). Also this technique is useful in applications that are not sensitive to filter sharpness [17].

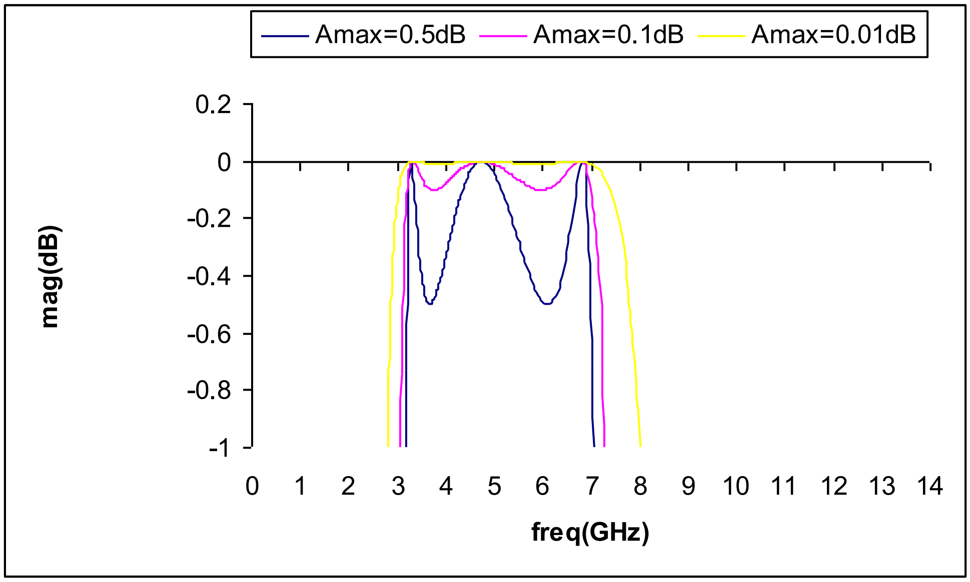

Fig. 2.37: Elliptic BPF magnitude response for various ripples with SBA = 10dB

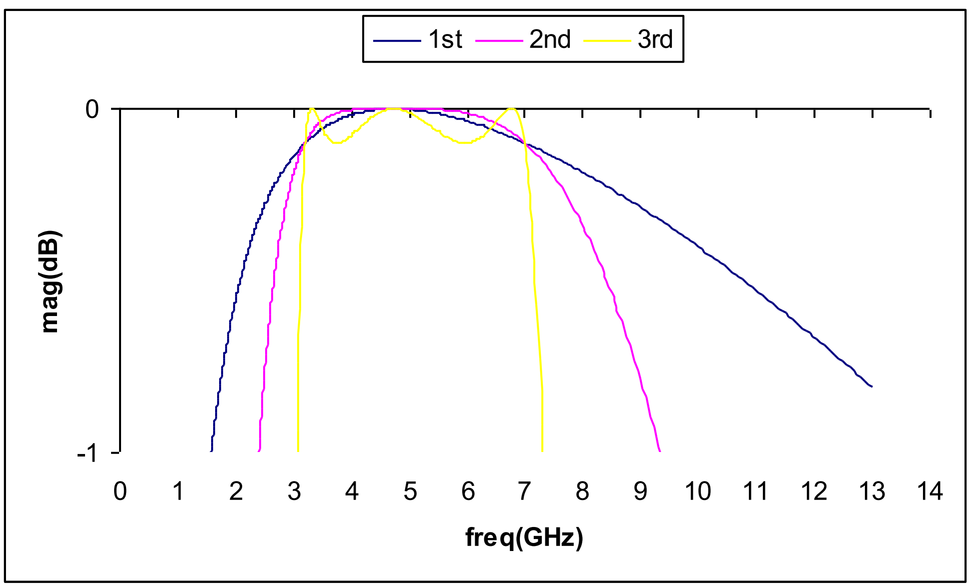

Fig. 2.38: Elliptic BPF response for various filter orders (Zoom in)

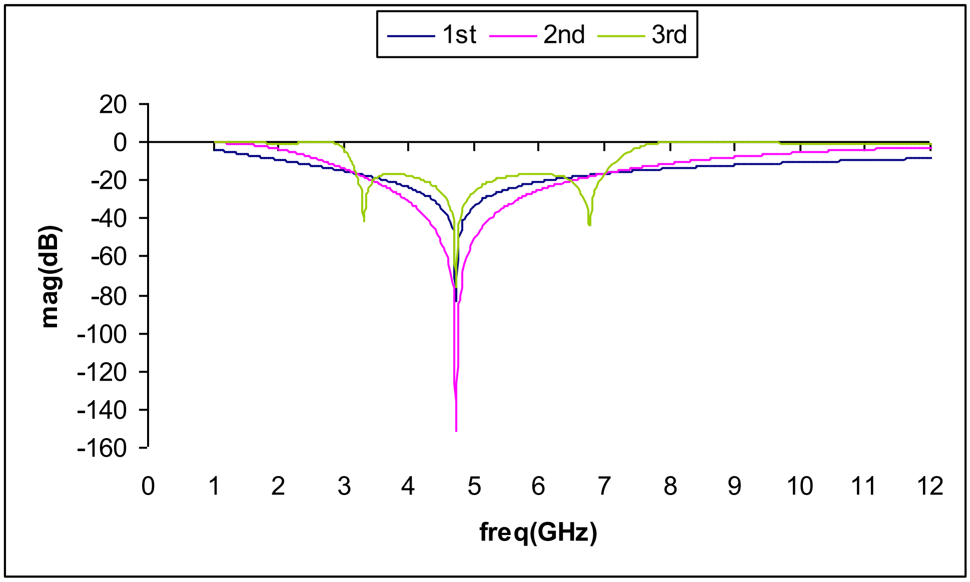

Fig. 2.39: Elliptic BPF reflection coefficient for various filter orders

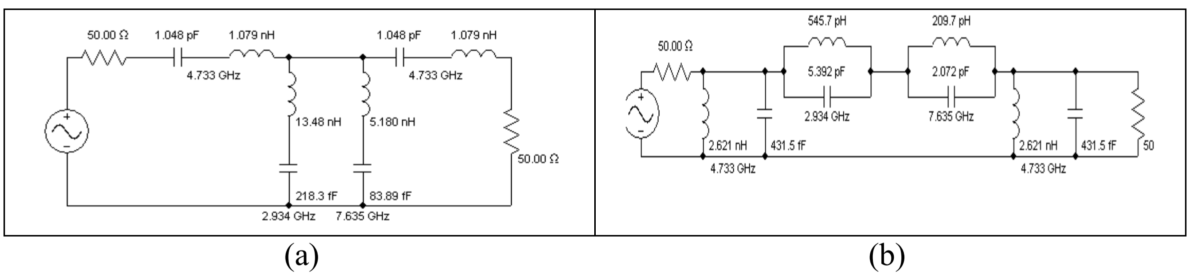

Fig. 2.40: 3rd order Elliptic BPF, a) series, b) shunt topology

Figures 2.41 and 2.42 show the filter response for different orders and ripples. By increasing the filter order, we can increase its sharpness as well as its SBW. Also, the even order filter has a higher attenuation compared to the odd order. Thus, by further obtaining the reflection coefficient at different orders (Fig. 2.43), we can make a tradeoff between SBW, sharpness, size, and attenuation. Filters with higher order have better sharpness and stop-band bandwidth (SBW) as well as higher SBA. On the other hand, lower ripple allows better bandwidth and attenuation (SBA). Therefore, 1st filter order (Fig. 2.44) can be the best compromise in terms of sharpness, integration space, element size and stop-band attenuation.

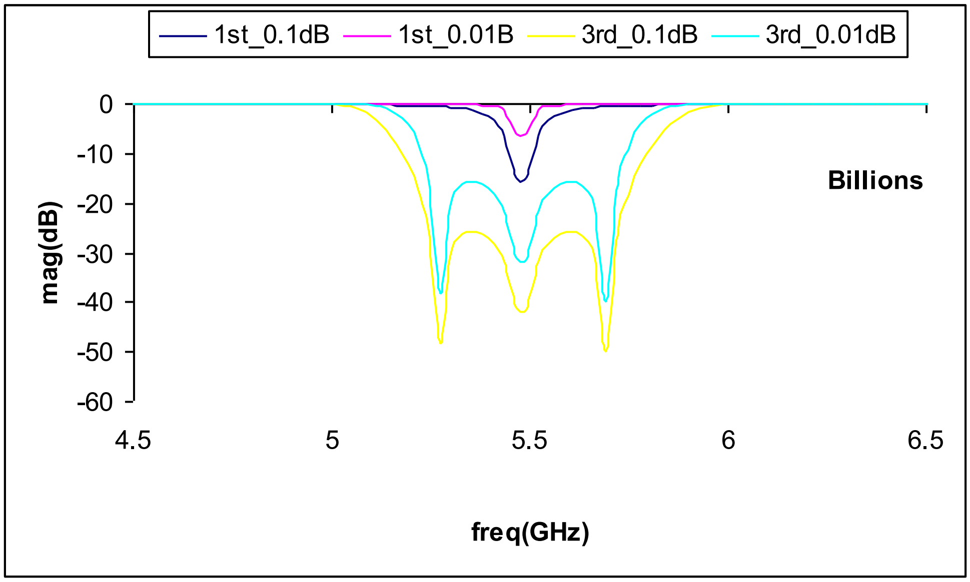

Fig. 2.41: Elliptic SBF magnitude response for various orders and ripples.

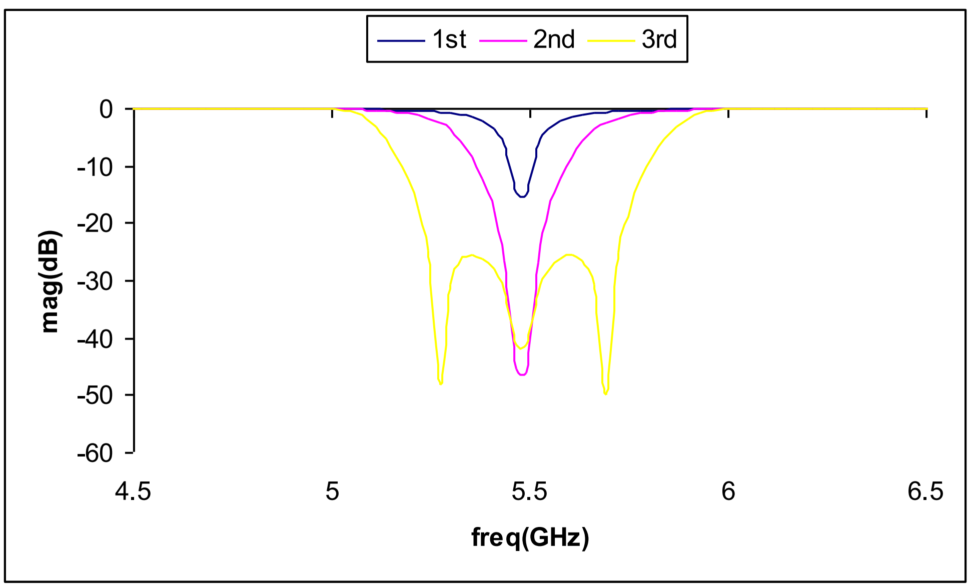

Fig. 2.42: Elliptic SBF response for various filter orders (A_{max} = 0.1dB)

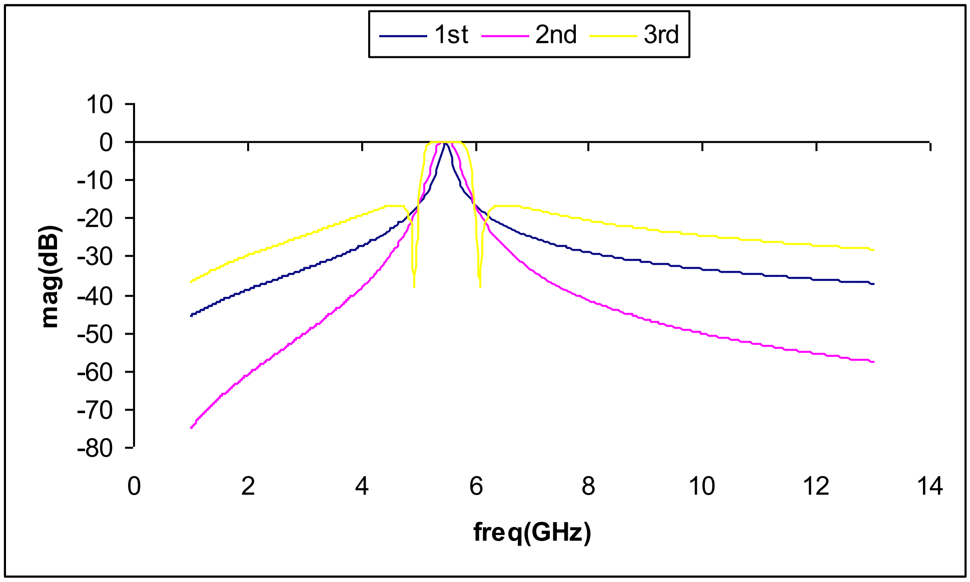

Fig. 2.43: Elliptic SBF reflection coefficient for various filter orders (A_{max} = 0.1dB)

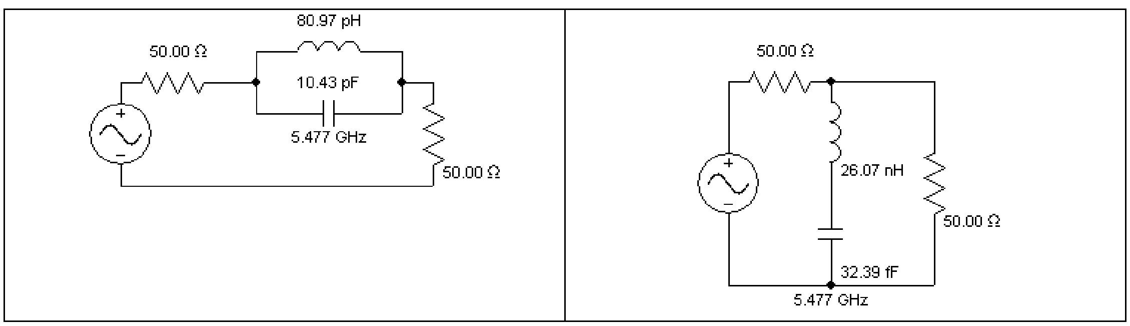

(a) (b)

Fig. 2.44: 1st order elliptic SBF, a) series b) shunt topology

2.10 Hourglass filters

Hourglass filters are very similar to ChevII and Elliptic filters [18], and can be considered as particular cases of elliptic filters with constant band-pass/stop-pass ripple (0.5dB). However, the hourglass filter presents the highest sharpness and stop-band attenuation compared to other filters with respect to the filter order and inductor size. Because of its highest sharpness, this filter can be a good candidate for NBI cancellation but on the other hand, its pass-band ripple (0.5dB) is not so low.

2.10.1 Hourglass BPF

Compared to ChevI and ChevII filters, Hourglass BPFs have larger element size but better sharpness with respect to stop-band attenuation. The 3rd order BPF response has significant improvements compared to the 1st and 2nd order, with a fixed equal-ripple of 0.5dB (Figs. 2.45 and 2.46). Its circuit is shown in Fig. 2.47.

2.10.2 3rd order hourglass BPF with zigzag method

We further investigated the 3rd order Hourglass BPF design while using the Zigzag method (Fig. 2.48). As expected, the resulting Hourglass filter has less inductors in comparison with the regular hourglass filter designed in the previous section. However, the shunt/series circuit topology is not symmetric and does not have equal source and load impedance. Similarly, lower SBA gives a higher sharpness and less phase linearity response as shown in Fig. 2.49. Finally, for a given SBA (10dB), design using the zigzag method has lower magnitude response but a fixed positive equal-ripple of 0.5dB (Fig. 2.50).

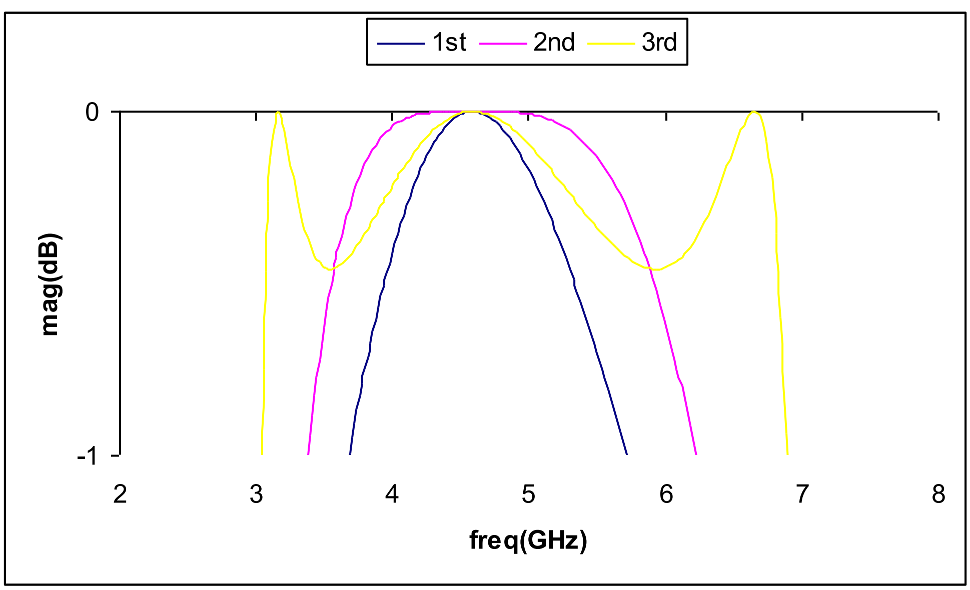

Fig. 2.45: Hourglass BPF magnitude response for various orders with a zoom in/zoom out the band of interest.

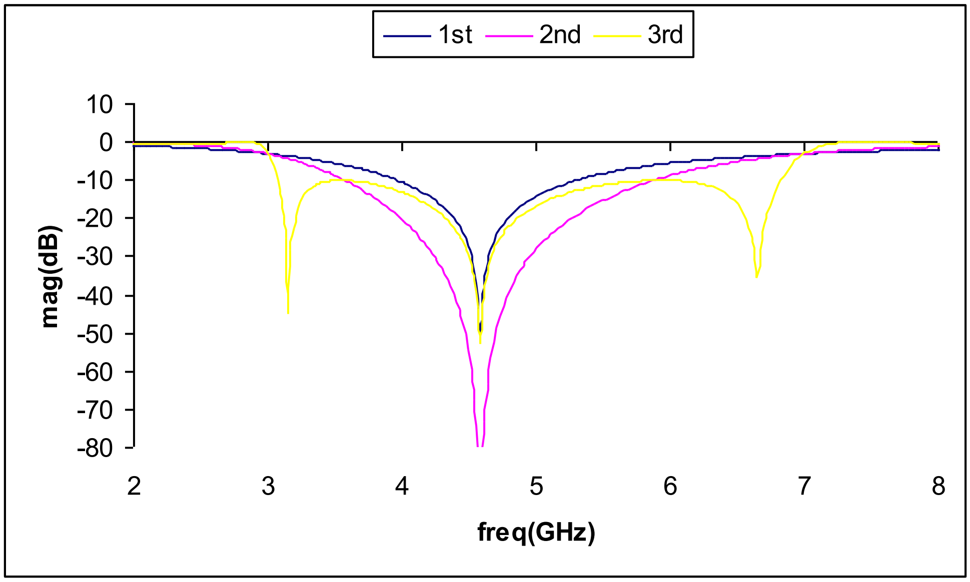

Fig. 2.46: Hourglass BPF reflection coefficient for various orders

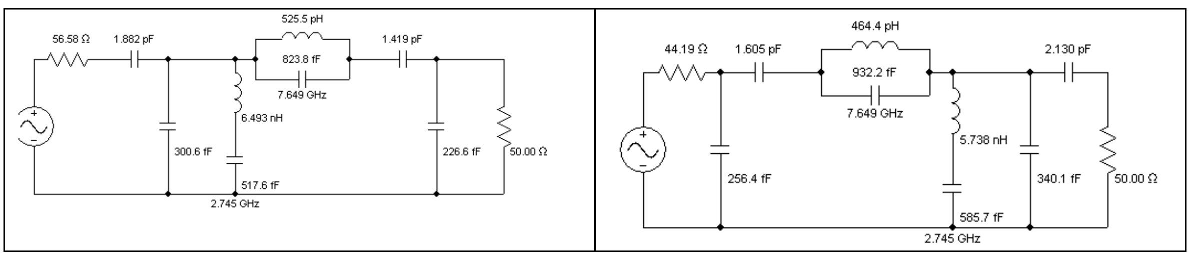

(a) (b)

Fig. 2.47: 3rd order Hourglass BPF a) series b) shunt topology (SBA=10dB).

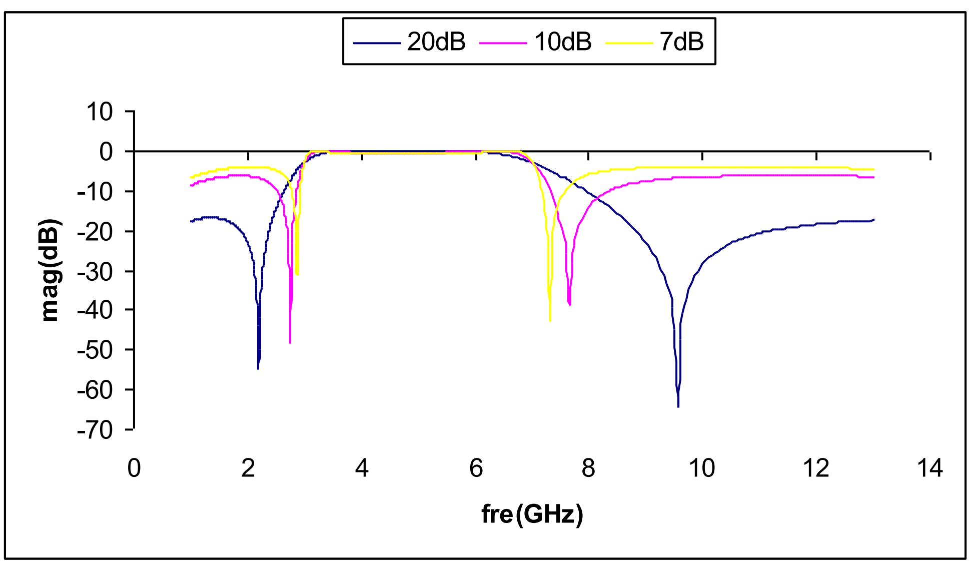

Fig. 2.48: 3rd order Hourglass BPF with the zigzag method: magnitude response for various SBA.

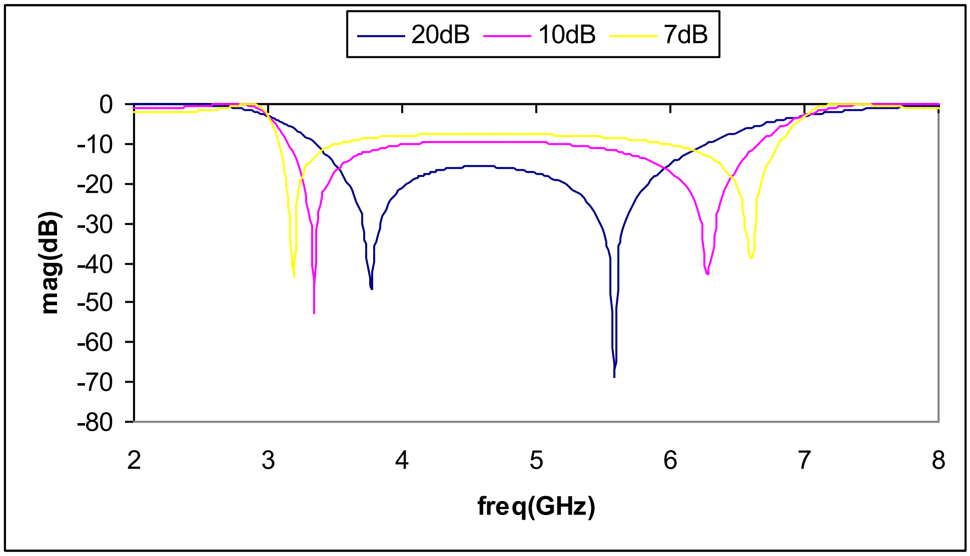

Fig. 2.49: 3rd order Hourglass BPF with the zigzag method: reflection coefficient for various SBA.

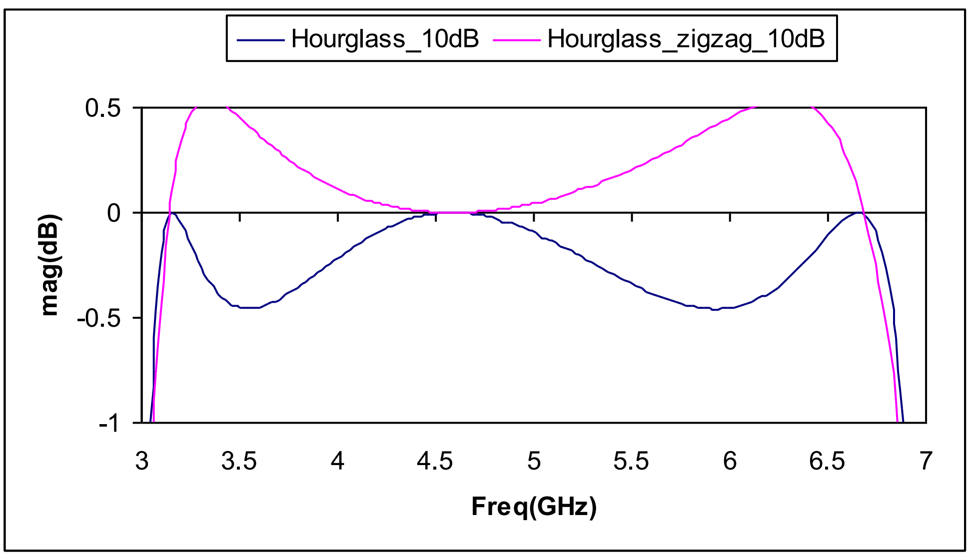

Fig. 2.50: 3rd order Hourglass BPF: comparison between the usual design approach and the approach with the zigzag method with SBA=10dB, (Zoom-in)

2.10.3 Hourglass SBF

Based on frequency response and reflection coefficient of different Hourglass SBF (Figs. 2.51 and 2.52, respectively), the 1st order Hourglass SBF (Fig. 2.53) is the most suitable over the other Hourglass SBF filters.

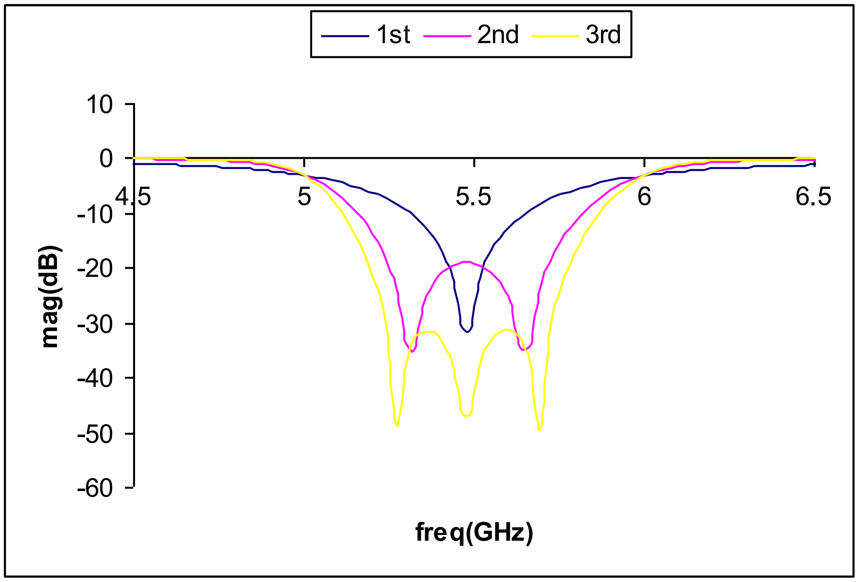

Fig. 2.51: Hourglass SBF magnitude response for various orders.

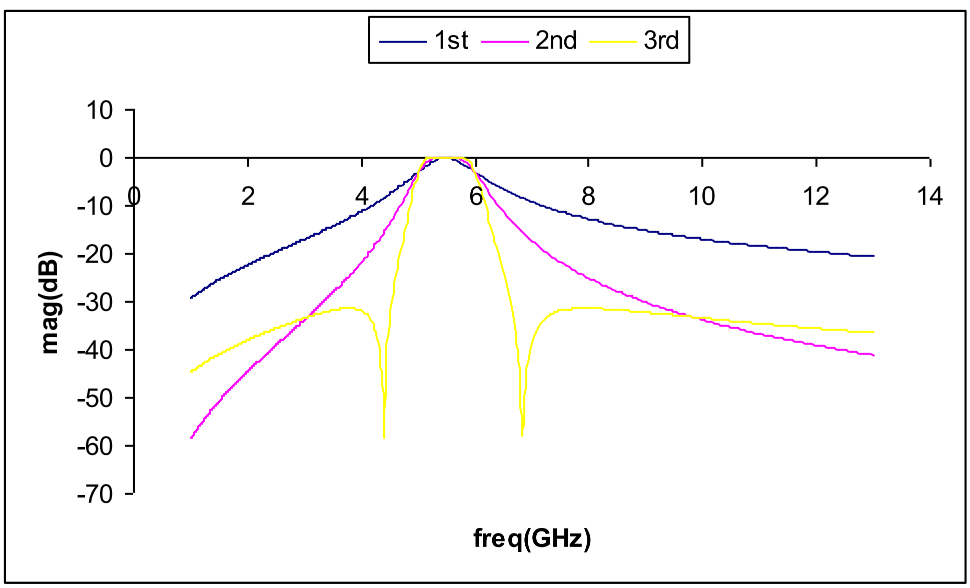

Fig. 2.52: Hourglass SBF reflection coefficient for various orders.

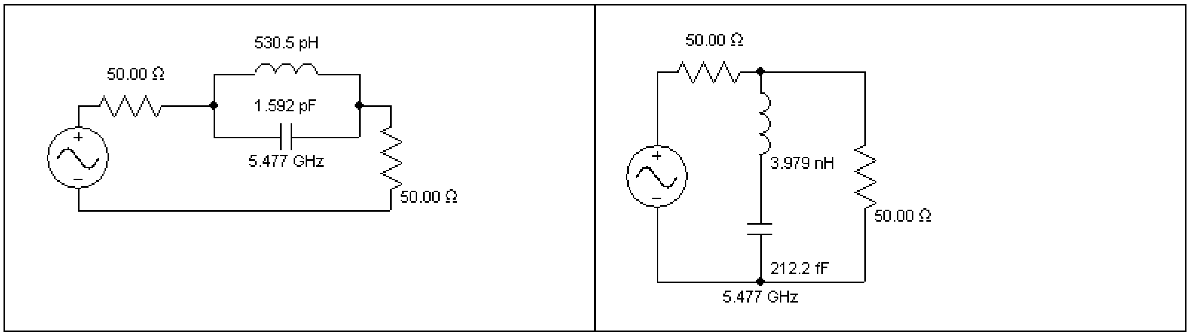

(a) (b)

Fig. 2.53: 1st order Hourglass SBF, a) series b) shunt topology

2.11 Comparison between the different filters

In this section, we compared the different responses we obtained for the filters we designed in order to select the best BPF and SBF for our application. The whole comparison should include the following specifications:

- Series/shunt topology,
- Maximum element number/size,
- Sharpness,
- Maximum SBA,
- Flatness
- Frequency response,
- Reflection coefficient,
- Phase linearity, and
- Input/output (Z_{in}/Z_{out}) impedance frequency response.

Based on Figs. 2.54 and 2.55, we can reach the following conclusions for BPF:

- In applications where element size and pass-band ripple are not critical, the Hourglass BPF is a good candidate in terms of sharpness. On the other hand, Gaussian and Bessel filters have the worst performance, while ChevII and Elliptic have almost the same performance, especially in the low frequency spectrum.

- In terms of attenuation, all filters exhibit enough stop-band attenuation. However, the Butterworth filter has the lowest reflection coefficient in center frequency.
- Gaussian, Bessel and Butterworth filters have high phase linearity (Fig. 2.56).
- ChevI, ChevII, Hourglass and Elliptic have reasonable delay group (uniform) in the desired pass-band frequency spectrum (Fig. 2.57).
- The Z_{in} input impedance frequency responses are equal due to symmetric filter design. Gaussian and Bessel have the worse input impedance frequency response (Fig. 2.58). On the other hand, ChevI, ChevII and Hourglass have the best input impedance frequency response.

Satisfying all requirements is, as expected, impossible, so tradeoffs have to be considered. Hence, it looks that ChevII and Elliptic are the best candidates to optimize such tradeoffs. Tables 2.3 and 2.4 summarize our conclusions.

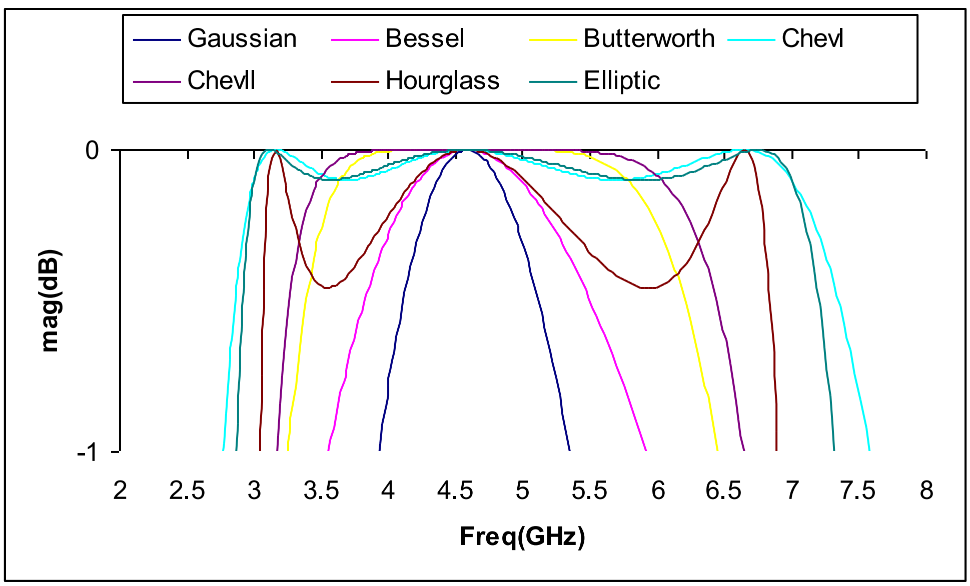

Fig. 2.54: 3rd order filter comparison in terms of frequency response with a zoom out for the band of interest (A_{max} = 0.1dB, SBA = 10dB, SBW = 4.1GHz).

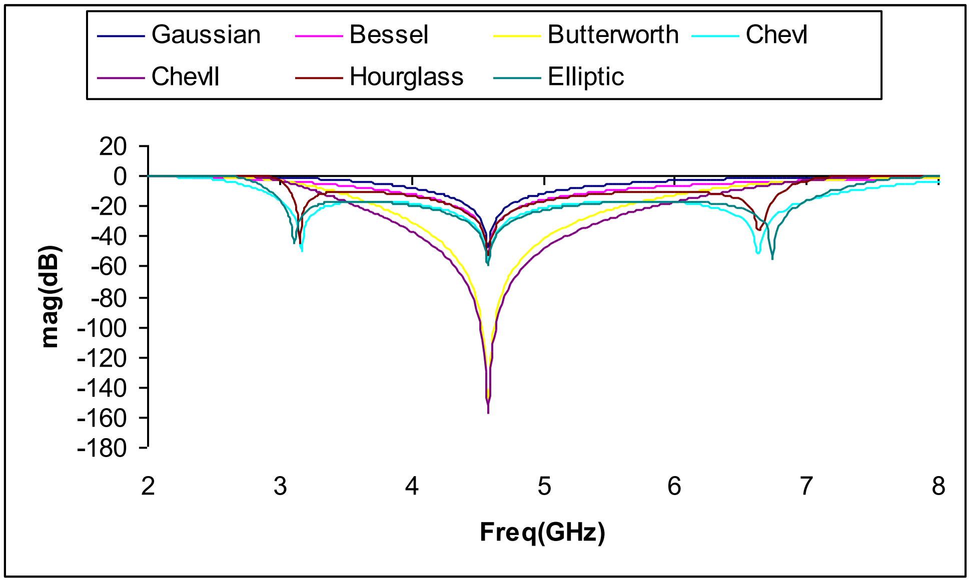

Fig. 2.55: 3rd order filter comparison in terms of reflection coefficient (A_{max} = 0.1dB, SBA = 10dB, SBW = 4.1GHz).

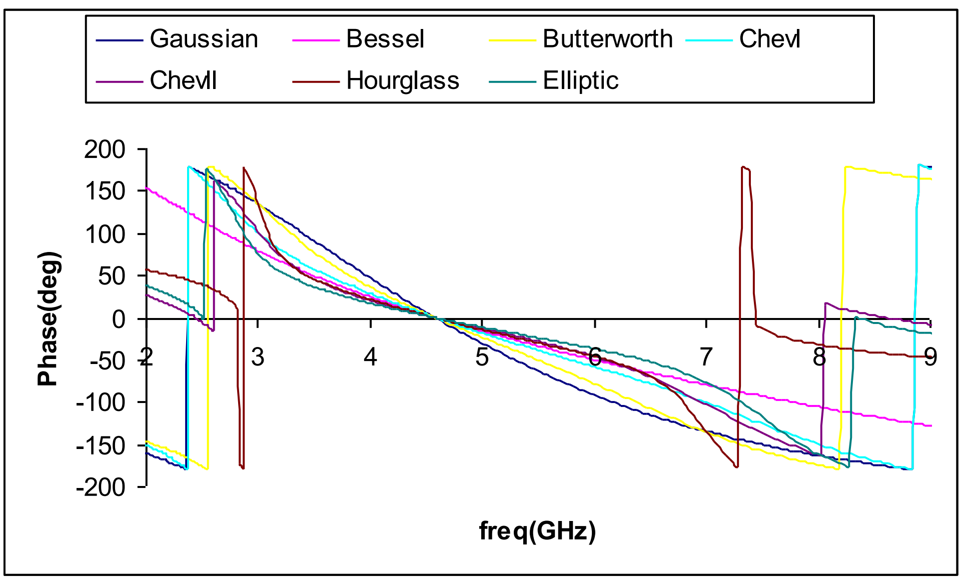

Fig. 2.56: 3rd order filter comparison in terms of phase linearity (A_{max} = 0.1dB, SBA = 10dB, SBW = 4.1GHz).

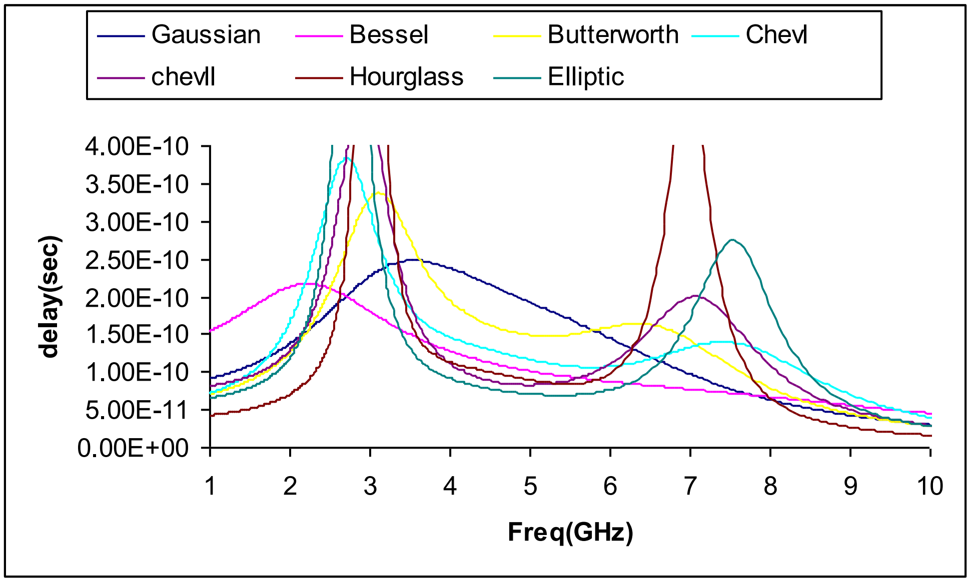

Fig. 2.57: 3rd order filter comparison in terms of group delay
(A_{max} = 0.1dB, SBA = 10dB, SBW = 4.1GHz).

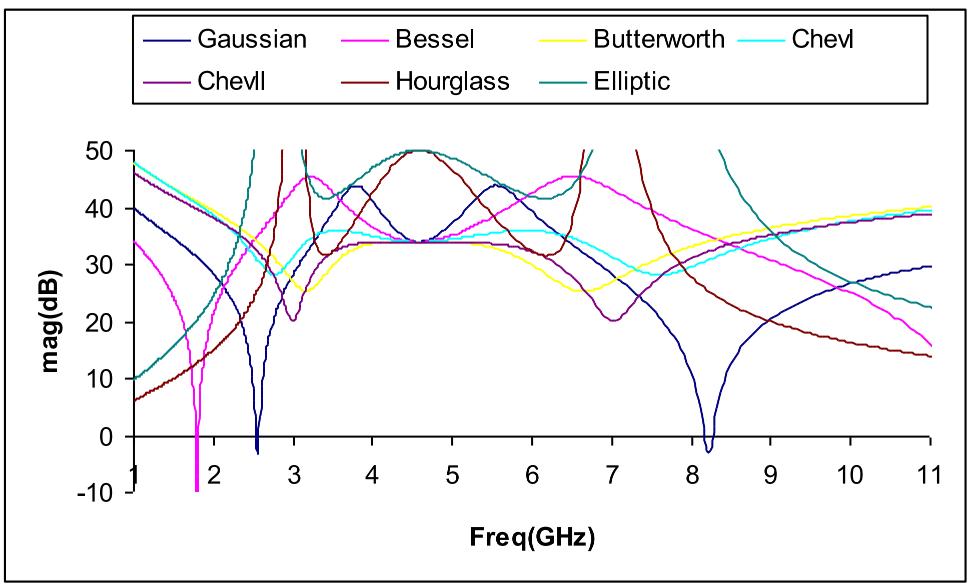

Fig. 2.58: 3rd order filter comparison in terms of input impedance
(A_{max} = 0.1dB, SBA = 10dB, SBW = 4.1GHz).

As for SBF, Gaussian, Bessel, Butterworth, and ChevII filters show the same frequency response while ChevI and Elliptic filters have similar performance. So far, the 1st order SBF Hourglass filter has the best attenuation, sharpness and SBW but with a ripple in stop-band, which is critical for our design purpose (Fig. 2.59).

Table 2.3: 3rd order BPF comparison in terms of filter elements.

	Topology	Element #	C_max	L_max
Gaussian	Shunt	6	2.8pF	2.6nH
Bessel	Series	8	10pF	4.2nH
Butterworth	Series	6	1.56pF	1.98nH
ChevI	Shunt/Series	6	913fF	2.2nH
ChevII	Shunt	6-8	1.6pF	2.7nH
Hourglass	Shunt	6-8	4.6pF	1.52nH
Elliptic	Shunt	6-8	2.8pF	2.27nH

Table 2.4: 3rd order BPF comparison in term of filter parameters.

Filter Type	Sharpness	SBA (dB/n)	Phase Linearity (deg)	Delay Frequency response	Ripple (dB)	Zin/Zout Frequency response
Gaussian	*	25-40	***	+++	0	*
Bessel	*	60-70	****	+++	0	*
Butterworth	**	30-40	*****	+	0	****
ChevI	***	40-70	*****	++	Fixed to 0.1	****
ChevII	****	40-60	***	++	0	*****
Hourglass	*****	40-80	**	++	Fixed to 0.5	*****
Elliptic	****	40-80	**	++++	Fixed to 0.1	*

* Poor, ** slightly good, *** good, **** very good, ***** excellent

+ Lowest, ++ very low, +++ low, ++++ high

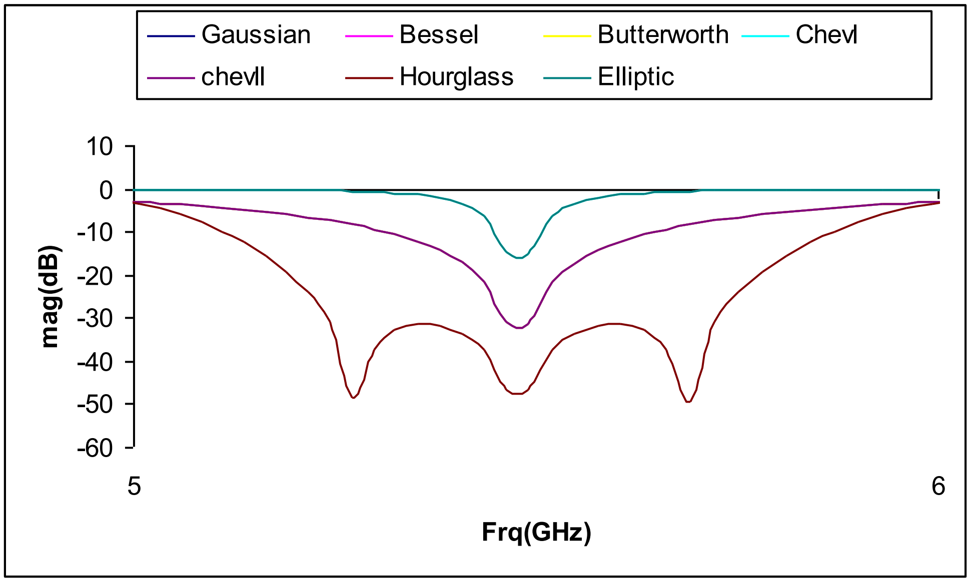

Fig. 2.59: Comparison of the frequency response of different 1rd order SBF filters
(SBW = 474MHz, A_{max} = 0.1dB, SBA = 10dB)

2.12 Conclusion

From the above simulations, it has been confirmed that reduction in inductor number (through the zigzag technique) produces more capacitors in the circuit, which causes lower frequency response and sharpness.

Also, the obtained results have shown slight differences with regard to the conclusions stated in some references we used. For instance, some references claim that Elliptic filter has the best sharpness, and therefore should be the best candidate for UWB-NBI applications. However, they did not consider its poor performance in pass-band ripple vs. element size and attenuation vs. filter order [17]-[19].

These considerations led to the fact that, in our case, the elliptic filter is indeed not the best candidate in terms of sharpness, inductor size and filter order. Finally, we have chosen the Hourglass and ChevII BPF as best candidates with respect to their high sharpness, attenuation, filter order, and inductor size. However, each one may have disadvantages such as group delay, pass-band-edge overshooting and ripple. Nevertheless, these issues are not critical in our desired application. As for stop-band filters, they will be further investigated in Multi-band UWB-LNA applications.

References

[1] R.J. Hartnett, K.C. Gross, "Innovative approaches to teaching analog and digital filter design concepts," *ASEE/IEEE Frontiers in Education Conf.*, 2009.

[2] L. Thede, *Practical Analog and Digital Filter Design*, Norwood, MA, Artech House, 2005.

[3] R. Kulkarni, J. Kim, H.J. Jeon, J. Xiao, S. Martinez, "UHF receiver front-end: Implementation and analog baseband design considerations," *IEEE Trans. J. VLSI Systems*, pp. 197-210, 2012.

[4] S. Winder, *Analog and Digital Filter Design*, Woburn, MA, Newnes, 2002.

[5] D. Budimir, L. Lalahparvar, N. Nikolic, "Design of generalized Chebyshev lumped element filters by computer optimization," *Mediterranean Electrotechnical Conf.*, pp. 475-478, 2002.

[6] O. Abedi, M.C.E. Yagoub, A. Abedi, "Enhanced UWB CS-LNA with inverse filter and shunt feedback resistor in 130nm CMOS," *IEEE Int. Conf. on Signals, Circuits and Systems*, pp. 1-6, 2009.

[7] H.R. Khodadadi, *Filter and Circuit Synthesis*, University of Imam Hossen, Iran, 2005.

[8] J. Rogers, C. Plett, *Radio Frequency Integrated Circuit Design*, Boston, MA, Artech House, 2002.

[9] G.L Matthaei, L. Young, E.M.T. Jones, *Microwave Filters, Impedance Matching networks, and Coupling Structures*, Norwood, MA, Artech House, 1980.

[10] D.M. Pozar, *Microwave Engineering*, 2nd Ed., J. Wiley & Sons, 2001.

[11] A. Williams, F. Taylor, *Electronic Filter Design Handbook: LC, Active and Digital Filters*, 2nd Ed., New-York, NY, McGraw-Hill, 1988.

[12] C.S. Yoo, J.K. Lee, D. Kim, S.D. Park, K.H. Won, N.K. Kang, K.S. Seo, W.S. Lee, "RF front-end passive circuit implementation including antenna for ZigBee applications," *IEEE Trans. Microwave Theory*, Vol. 55, pp. 906-915, 2007.

[13] R. Perrone, J. Muller, "Compact RF-filter-modules with lumped elements in LTCC for applications up to 10GHz," *ESTC Conf.*, pp. 491-496, 2008.

[14] C. Hsiang, C.Y. Chang, "Wideband chebyshev-response bandpass filter by cascading of cascadable 180^o hybrid rings," *Asia-Pacific Microwave Conf.,* pp. 151-154, 2008.

[15] A.M. Street, A.P. Jenkins, D. Abbott, "Filter design using CAD. I. Linear circuit simulation" *IEEE Colloquium conf. Effective Microwave CAD*, 2002.

[16] H.M. Lee, "Direct synthesis of transmission-line elliptic bandpass filters," *IEEE MTT-S Int. Microwave Symp*., 2011.

[17] G.S. Ching, "Design and practical implementation of a 2.4 GHz lumped element elliptic bandpass filter" *Asia-Pacific Microwave Conf*., 2002.

[18] B.J. Bennett, "A new filter synthesis technique-the hourglass," *IEEE Trans. Circuits and Systems*, pp. 1469-1477, 2002.

[19] G. Cusmai, M. Brandolini, P. Rossi, "A 0.18-μm CMOS selective receiver front-end for UWB applications," *IEEE J. Solid-State Circuits*, Vol. 41, pp. 1764-1771, 2006.

Chapter 3 UWB-LNA Configurations

3.1 Introduction

Input matching is one of the key parameters in low-noise amplifier (LNA) design. Beside noise figure and gain, it also affects linearity and power consumption. In this section, the filters designed in Chapter 2 will be used as input matching network of various UWB-LNA configurations such as common source (CS) and common gate (CG) and the performance of these combined circuits evaluated in terms of input reflection coefficient, gain, input/output isolation, noise figure, and linearity.

However, a component-level design should be first performed to adjust the active device electrical/physical parameters in the light of our design objectives.

3.2 Transistor Parameters

Since transistor parameters have a direct impact on circuit performance, the first step is to adjust such parameters for optimal LNA design. For this purpose, a 6.4GHz narrowband CS-LNA in 130nm CMOS technology was simulated. The choice of CS instead of CG is mainly based on the fact that common-source LNAs are simpler to design and can easily achieve high gain in the UWB frequency spectrum [1]-[3].

Note that we used the Cadence IBM-CMOS 130nm processing kits in our simulations.

3.2.1 Transistor size

To reach maximum gain in LNA core and buffer as well as maximum current in current mirror networks, transistors should be in saturation [4]. Find the optimal transistor size is a trade-off between power consumption and input matching. By increasing the transistor size (with fixed transistor length, i.e., by only increasing the width), the current and parasitic capacitors will increase, thus requiring higher inductor degeneration to cancel the parasitic capacitors for input matching and even increasing the power consumption (assuming that the transistor threshold voltage V_t is fixed for core LNA transistors [5], which is not true but slightly related to bias [6]. Note that a lower V_t gives better linearity but also lower gain and higher noise figure [7]).

3.2.2 Inductor degeneration for matching

Several methods have been proposed to optimize the input matching of narrowband LNAs with respect to circuit complexity, power loss and integration issues (size and number of inductors …) [5], [8]. Among them, one of the most used narrowband matching techniques is the inductor degeneration approach [9]. As shown in Fig. 3.1, this method requires two inductors, which values are obtained by

$$Z_{in} = \frac{-i}{wC_{gs}} + iwL_s + \frac{g_m L_s}{C_{gs}} + jwL_g = 50 \text{ Ohms}$$

$$\rightarrow \qquad L_s = \frac{R_s C_{gs}}{g_m};\ L_g = \frac{1}{C_{gs} w^2} - \frac{R_s C_{gs}}{g_m} \tag{3.1}$$

where R_s is the source resistance.

3.2.4 130nm transistor cut-off frequency

In transistor circuits, the transistor cut-off frequency, given by [9]

$$f_T = \frac{g_m}{2\pi C_{gs}}, \tag{3.2}$$

is usually set to a high value. To illustrate that, let us consider a generic 130nm NMOS transistor, with width of 80um, length of 120nm and 35 fingers. Moving from the 180nm to the 130nm technology will indeed increase f_T but at the same time, degrade the noise figure by almost 0.2dB [10]. So accurately evaluating f_T will give a solid base for efficient LNA design.

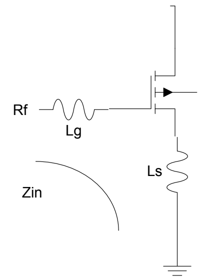

Fig. 3.1: Inductor degeneration input matching for CMOS transistors

There are different methods to evaluate f_T namely, the DC simulation, the AC simulation and the small-signal simulation (through the H_{21} parameter) [11].

$$\begin{cases} f_T = 20\log\dfrac{i_{out}}{i_{in}} = 0;\ (AC) \\ f_T = \dfrac{g_m}{2\pi C_{tot}};\ (DC) \rightarrow g_m = \sqrt{2\mu cox\dfrac{W}{L}I_d} \\ f_T = 20\log(H_{21}) = 0;\ (H21) \end{cases} \tag{3.3}$$

Note that the value of f_T obtained through DC simulation can be used as estimation. Figure 3.2 shows the result obtained by the H_{21} method, as well as the topology used to evaluate f_T. From these figures, we found f_T = 145GHz at I_d = 2mA for this particular transistor. Obviously by increasing the transistor biasing current or width, f_T will increase but with lower frequency response and higher power consumption. Table 3.1 specifies the active/passive element values used for this generic example.

3.2.5 Optimum number of transistor fingers

Minimum noise figure is strongly related to the gate resistor which is in turn directly related to the transistor width (thus to number of fingers) [12] (Fig. 3.3-a). By increasing the number of fingers (FN) from 1 to 100, the gate transistor R_g is reduced and thus the noise figure (Fig. 3.3-b). In addition, increasing the number of fingers will increase the current and the substrate effect (Figs. 3.3-c, 3.3-d, and 3.3-e).

The best way to minimize the noise figure (*NF*) is to optimize the current with a trade-off between linearity, gain, and power consumption. In fact, Fig. 3.3 shows that an optimum number of fingers in the range of 35-40 will reduce *NF*, R_g, and C_{gs}, and increase g_m and f_T.

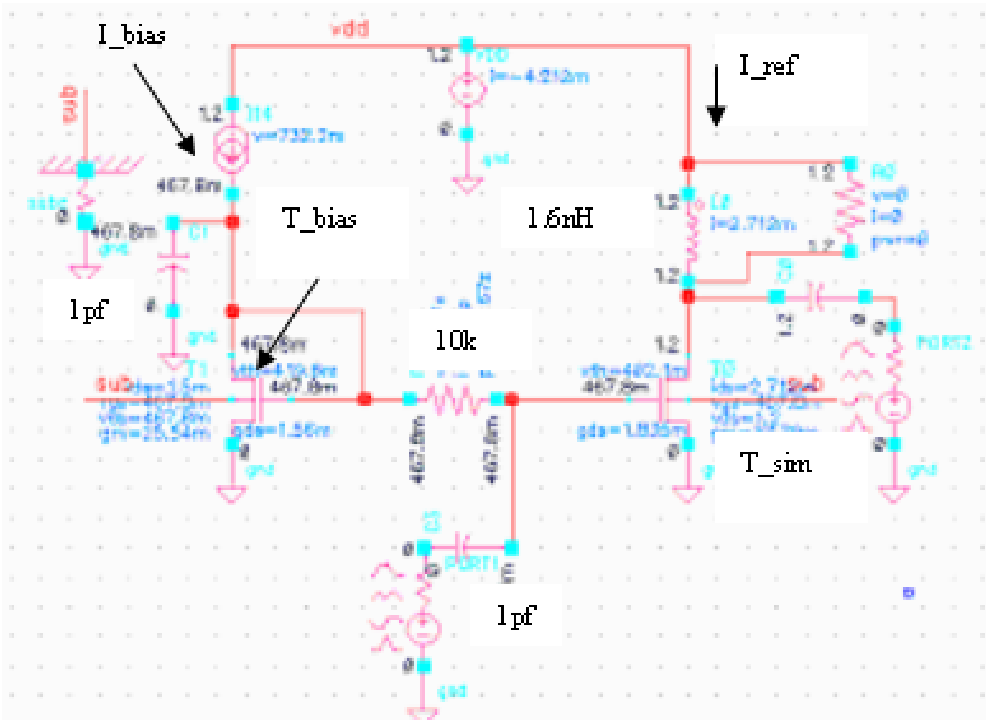

a)

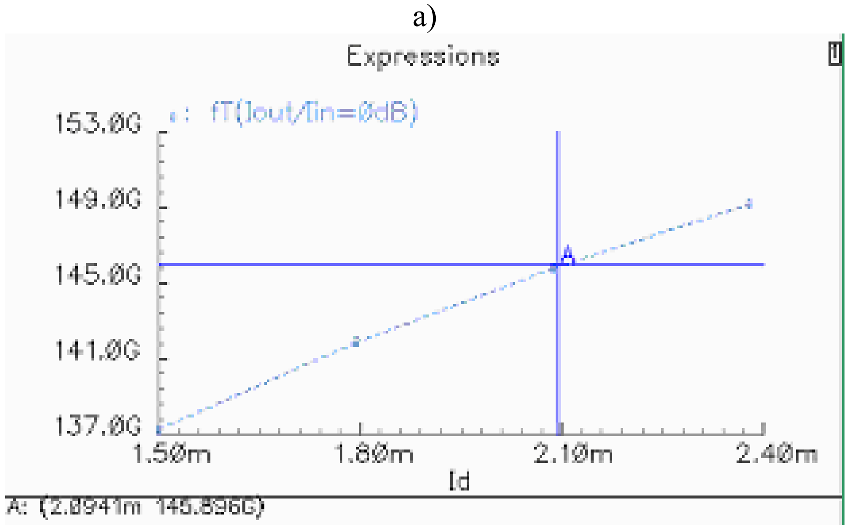

b)

Fig. 3.2: f_T calculation in a) configuration, b) H_{21} analysis

Table 3.1: Design elements used in Fig. 3.2 in 130nm technology

T_biasing	T_sim	Others
W=100um (40, 2.5um) L=120nm FN=40	W=100u (40, 2.5um) L=120nm FN=40	I_ref = 2mA Vdd=1.2 L_load=1.64nH (Q=15)

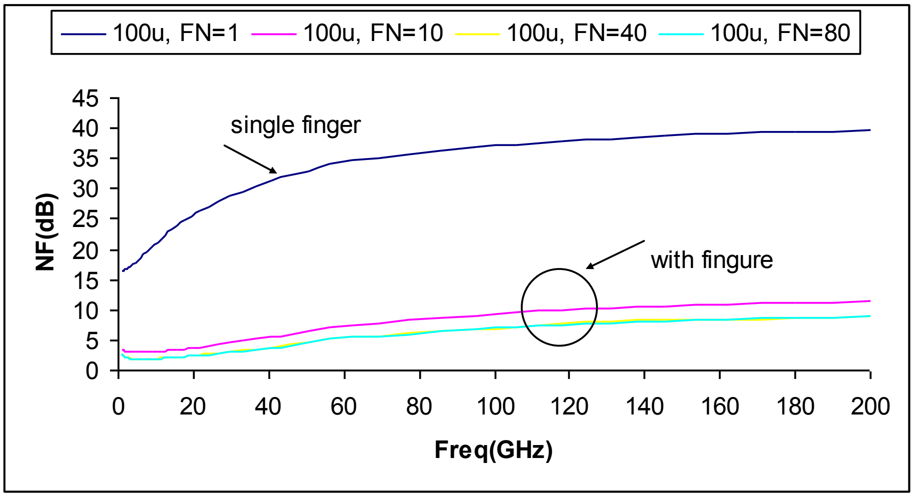

a)

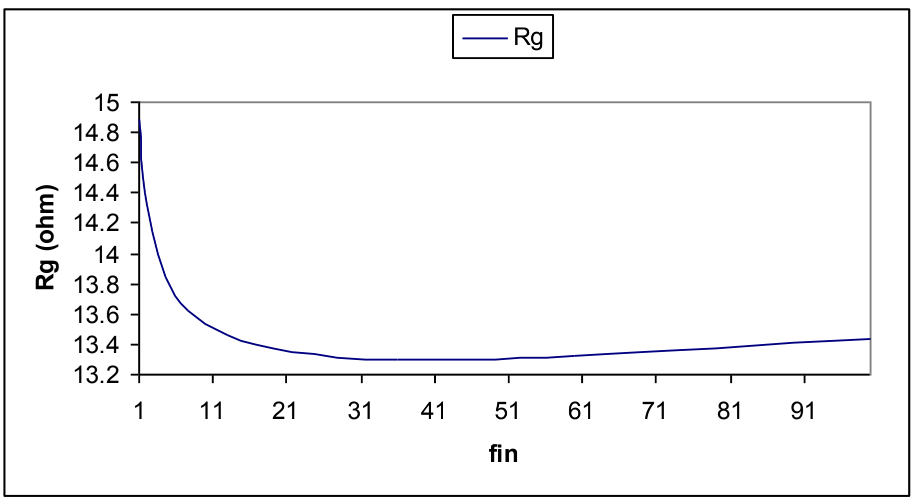

b)

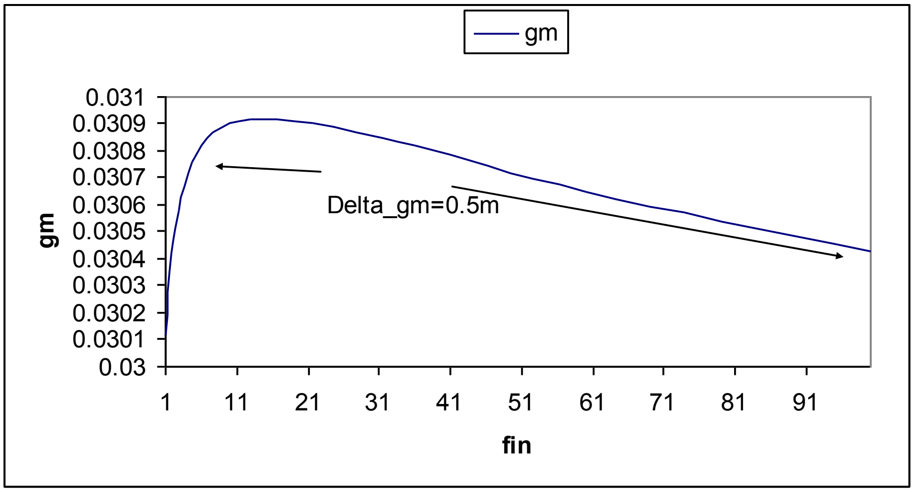

c)

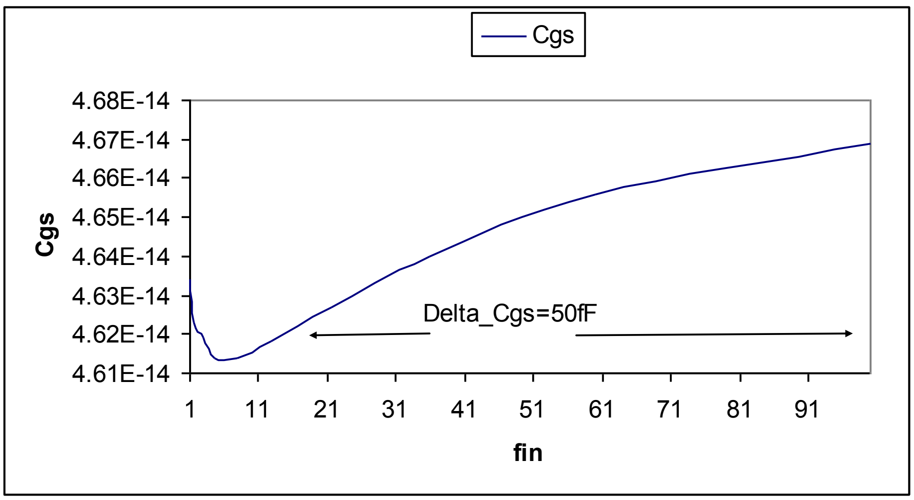

d)

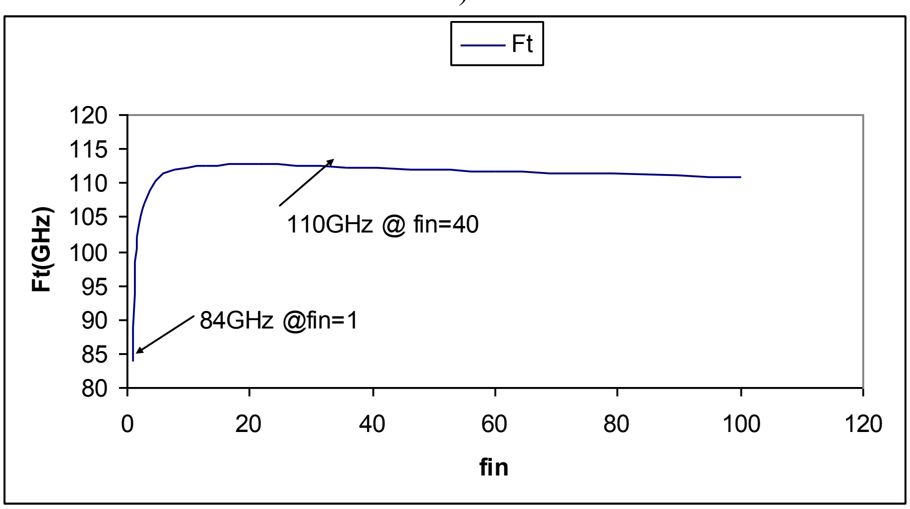

e)

Fig. 3.3: a) Noise figure, b) R_g, c) g_m, d) C_{gs} and e) f_T of a CMOS 130nm transistor with CS topology for various number of fingers (fin)

3.2.6 Maximum W/L ratio and fingers in current mirrors

The current mirror is governed by the width/length transistor ratio

$$\frac{I_1}{I_2} = \frac{W_1 / L_1}{W_2 / L_2}.$$

By choosing the same transistor length, this ratio is directly related to the transistor widths. The current mirror ratio used to provide current to cascade was 1:5.

Practically, for low noise amplifiers, this ratio could not be more than 5 and transistor number of fingers cannot exceed 25 due to shot noise.

3.2.7 Voltage distortion and DC bypass capacitor

DC bypass capacitors isolate RF from DC. The value of such capacitors should not be very large due to layout consideration. In fact, when this capacitor is large, its equivalent circuit presents some parasitic inductive effects which can degrade the input matching network performance (in the ideal case, 1-10pf range is acceptable).

Another biasing consideration is the voltage distortion capacitor [13]. In circuit simulations, this capacitor does not play a significant rule but according to [14], it could be an issue in layout simulations.

Note that a frequency selective technique was used namely, the integrated inductor characterization for tank simulation (single center frequency selection).

3.2.8 130nm Component Characterization

The cited NMOS transistor was simulated to obtain the noise figure and f_T curves. The maximum f_T occurs at approximately 40mA, while the minimum noise figure occurs at approximately 2.3mA. This results in a noise density of approximately 28uA/um. The used test bench was composed of a single transistor with a non-ideal current mirror, an RF chock connecting the transistor to the bias (V_{dd}), as well as two input/output DC blocking capacitors (Fig. 3.2).

3.3 NMOS 130nm Cascade Amplifier Characterization

In a next step, a cascade configuration was designed to increase the dominant pole frequency by adding a second transistor as load (core LNA). The cascaded transistor is chosen to have the same width as the main transistor. However this can be adjusted based on the final design requirements. Note that adding this transistor reduces the gate-drain capacitance, which can limit the circuit performance due to the Miller effect [5].

3.3.1 Transistor Width

To find the transistor width that gives the best tradeoff between input matching and noise figure, we assumed a $S_{11} < -25dB$ to match with practical UWB-LNA requirements [13]. Note that a higher S_{11} is desirable but this affects other LNA trade-offs, especially the integration space (higher filter order), circuit complexity and power loss. This was done by varying the transistor width while keeping the same current density. The width should be increased until the normalized real part of the available minimum gain, G_{min} reaches unity [15]. From Table 3.2, we can conclude that the best width would be 185um. However as mentioned, due to power consumption considerations and other design tradeoffs like linearity and noise figure, the optimum transistor width size has been found to be in the range of 100-120um.

Table 3.2: Choosing the transistor width

Width	Current	Re (G_{min})
100um	2.90mA	1.53
150um	5.20mA	1.20
175um	8.40mA	1.12
185um	9.26mA	1.06
190um	9.51mA	1.04
200um	10.10mA	0.92

3.3.2 Degeneration inductor

According to the inductor degeneration equation [9], the initial L_s and L_g values are

$$L_s = \frac{R_s C_{ds}}{g_m} = 140\text{pH} \quad \text{and} \quad L_g = \frac{1}{C_{ds} w^2} - \frac{R_s C_{ds}}{g_m} = 6.7 \text{ nH}.$$

However, those results ignore some minor parasitic effects; so it could be considered as a first approach. The simulation test bench used to find the optimal L_s was similar to the one for the cascade amplifier, with an inductor connected at the transistor source. The inductor was swept from 100pH to 2nH, step size of 1pH, and at 115pH, the input resistance is found close to 50 ohms. However, with the addition of a buffer at the output, the input reflection coefficient shifted and L_s had to be recalculated; but the variation was found negligible.

Figures 3.4 and 3.5 show the test bench for both inductors as well as the quality factor Q, tested at 6.4GHz.

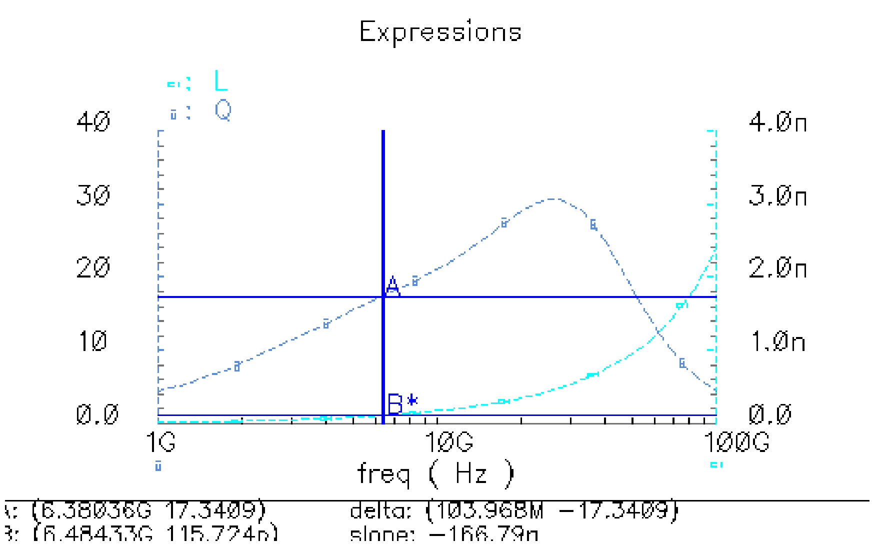

Fig. 3.4: Characterization for Ls=115pH.

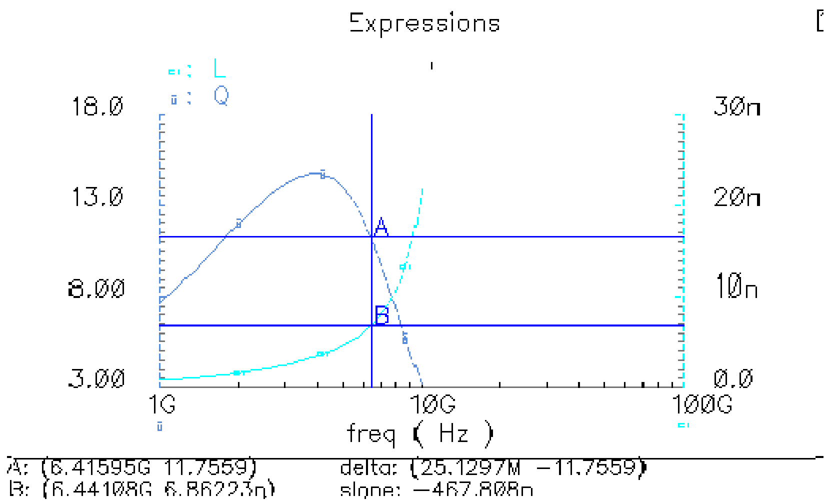

Fig. 3.5: Characterization for Lg=6.8nH

3.4 Tank Circuit

Using the following equation for the quality factor, [9]

$$Q = \frac{\mathrm{Im}(Zin)}{\mathrm{Re}(Zin)}, L = \frac{\mathrm{Im}(Zin)}{w} \quad \rightarrow \quad R_p = QwL,\ R_s \approx \frac{R_p}{Q^2} \tag{3.4}$$

a tank inductor of approximately 1.66nH was selected (Fig. 3.6). When characterizing the inductor, it is important that the maximum Q is not perfectly centered at the frequency of operation (6.4GHz). This is because Q drops significantly after reaching its peak value. The peak Q is 17 and is located at approximately 9 GHz, which is almost one and half the center frequency to increase its independence to processing variation. From Fig. 3.6, at 6.4GHz, the tank inductor has an inductance of 1.7nH and a Q of 15.3.

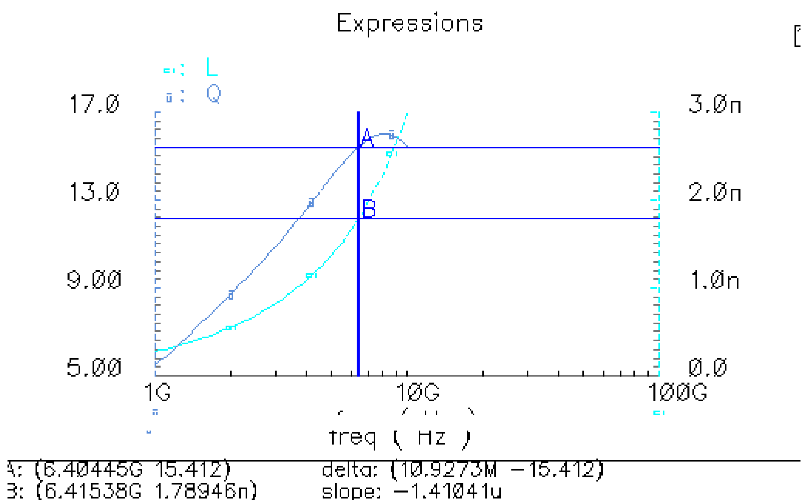

Fig. 3.6: Characterization of the 1.66nH Tank Inductor

Then, we determined the appropriate tank capacitor that oscillates at corner frequency (6.4GHz) with this inductor ($C_{\tan k} = \frac{1}{w^2 L} = 370 fF \ @ f = 6.4GHz$). Simulation showed that the required tank capacitor at 6.4GHz is 200fF. As expected, this is different from the above calculated value since the above equation is only a rough estimate and does not include the parasitic capacitance effects from both the cascade and the inductor.

3.5 Design Calculations

The initial design was optimized for minimum noise. Therefore, we expected large power consumption along with a small noise figure. This gave us some room to later improve the power consumption, while slightly worsening the noise figure and other LNA requirements. A second design was then performed to achieve a minimum possible power while still meeting most design requirements.

3.5.1 Gain

As for the gain, we assumed that the buffer has a unity gain and then, can be excluded from the gain calculation.

Note that it is practically impossible to achieve a buffer gain greater than 70%. Also, the cascade transistor has very little influence on the amplifier gain and therefore, the input transistor is the only one which conditions the gain. To find the gain, we used the following equation where R_p is the real part of the load resistor

$$A_v = \frac{g_m R_p}{R_s w_0 C_{gs}} \times \underbrace{Av \quad \times Av}_{1} \qquad\qquad R_P = QwL \tag{3.5}$$

From calculations, a 17dB gain was expected. However, we obtained a gain of approximately 13.8dB. This difference is likely due to gain reduction in other parts of the circuit that were not included in the calculation, such as buffer. For instance there is a C_{gs} at the output buffer that causes an extra parasitic parallel resistance to appear with R_P. With this gain, the linearity requirement was satisfied.

3.5.2 Noise figure

Regarding the noise figure, an assumption was made that the cascade transistor as well as the buffer do not have significant influence on the circuit noise figure [16]. Therefore, the calculation was an estimate that considers only the single transistor configuration.

Using the following noise figure equation from [17]

$$F_{\min} \approx 1 + 2.3\frac{f}{f_T} \tag{3.6}$$

we found an estimated minimum noise figure of 1.24dB, very close to the simulation result. This was expected since the minimum noise figure was calculated based on having an optimal width and number of fingers for the transistor, what we already achieved.

3.5.3 Output impedance

The output impedance Z_{out} was calculated based on the source-follower output resistance equation.

Since the current mirror transistor has a g_{ds} of 1.97mS and the buffer transistor has a g_m of 35.89mS, we obtained a real part of

$$re\left[Z_{out}\right] = \frac{1}{g_{ds\_mirr}} // \frac{1}{g_{m\_buffer}} = \frac{1}{g_{ds\_mirr} + g_{buffer}} = 26.4\,\Omega \tag{3.7}$$

while the imaginary part was much smaller and thus, neglected. The simulated output impedance was 22 Ω, so quite close to the above estimation.

3.5.4 Power Dissipation

Consummated power is a crucial design parameter since, especially in wireless devices, battery life is a key issue to consider. There are two current mirrors: one for the cascade amplifier and one for the output buffer (Fig. 3.7). The first power was calculated using the current value designed for the cascade amplifier for minimum noise figure. As for the second power dissipation, the output buffer was also designed for minimum noise, i.e., with 2.3mA current. Thus, the total power is given by:

$$Power = Vcc\left(I_{buf} + I_{mirr1} + I_{cascode} + I_{mirr2}\right)$$

$$Power = 1.2\underbrace{\left(I_{buf} + I_{mirr1} + I_{cascode} + I_{mirr2}\right)}_{3.58mA} = 4.2mW \tag{3.8}$$

The simulated power was found to be 3.4mW, close to the above theoretical value.

3.5.5 Linearity

The linearity can be calculated using [5], [18]:

$$v_{ip3} = 2\sqrt{2}v_T\left[\frac{R_{S,L} + \frac{1}{g_m}}{\frac{1}{g_m}}\right]^{\frac{3}{2}} = 2\sqrt{2}v_T\left[\frac{\sqrt{\left(2\pi wL\right)^2 + \left(\frac{2\pi wL}{Q}\right)^2} + \frac{1}{g_m}}{\frac{1}{g_m}}\right]^{\frac{3}{2}} \tag{3.9}$$

where $R_{S,L}$ represents the degeneration inductor series resistor. With g_m=17mS, L=L_s=128pH, and Q=15, we obtained v_{ip3}=-9.95dBm.

Thus, the simulated IIP3 point was found to be at -12.15dBm. The difference is likely due to the fact that some effects were not considered. In fact, linearity is affected by many factors such as tank circuit, cascade and buffer gain, and power consumption. Higher tank inductor requires higher buffer transistor width and then higher current, thus lower linearity.

3.5.6 Design Topology and Results

The final narrowband LNA (NB-LNA) circuit is shown in Fig. 3.7. The circuit shows two current mirrors: one cascade current and one buffer current. The cascade is composed of two transistors of width of 120um, built with 3um fingered transistors (FN=40), while the output buffer has been built with W=140um and 3.5um fingers (FN=40). Also a current mirror transistor with width of 100um/20um was used.

3.6 S-Parameters Design Results

3.6.1 Noise Figure

Fig. 3.8 shows the noise figure of the designed NB-LNA. We can see that the minimum attainable noise figure at 6.4GHz is 2.1dB while this design gave us a noise figure of 2.17dB. So the design has been matched to noise.

3.6.2 S_{11} and S_{21} parameters

Fig. 3.9 shows a S_{21} of 13.9dB and a S_{11} of -31.57dB. Note that we focused on minimizing the noise figure and power consumption. Fig. 3.10 shows that both S_{11} and noise figure have minima at 6.4GHz. This means that this design is simultaneously noise and power matched at the design frequency (6.4GHz).

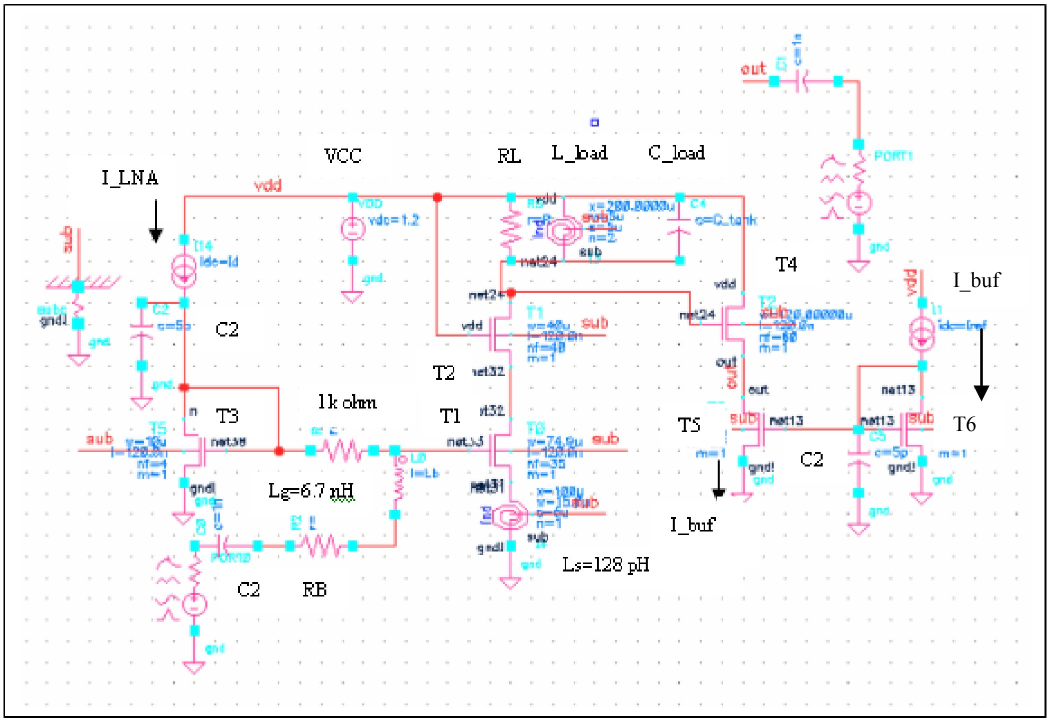

Fig. 3.7: Narrowband schematic Common source UWB LNA

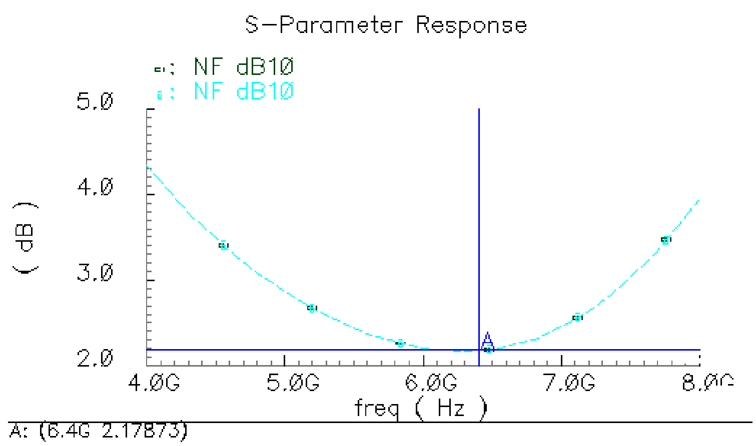

Fig. 3.8: Noise figure for narrowband LNA

Table 3.3: NB-LNA Components:

Current Mirror	Cascade AMP	RF	Buffer
T3 FN=10 W=2.5um L=120nm	T1 - FN=40 W=3um L=120nm	C2=5pf (DC blocker) RB=5Ω	RL=300Ω L_load=1.447nH C_load=256fF
I_LNA & I_buffer 100uA	T2 - FN=40 W=3um L=120nm		T6: W=10um T5 - FN=40 W=2.5um L=120nm
C2=5pf (reduce noise in current mirror) VCC=1.2v	Ls=128pH Lg=6nH	Rbias=1kΩ (biasing)	T4 - FN=40 W=2.5um L=120nm

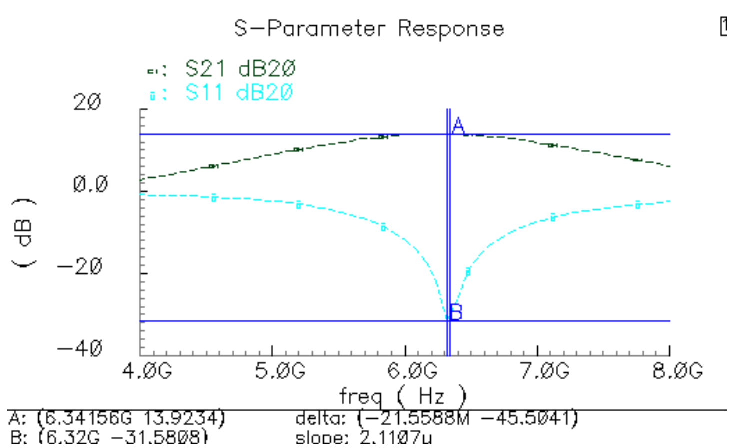

Fig. 3.9: S_{21} and S_{11} for noise optimum design.

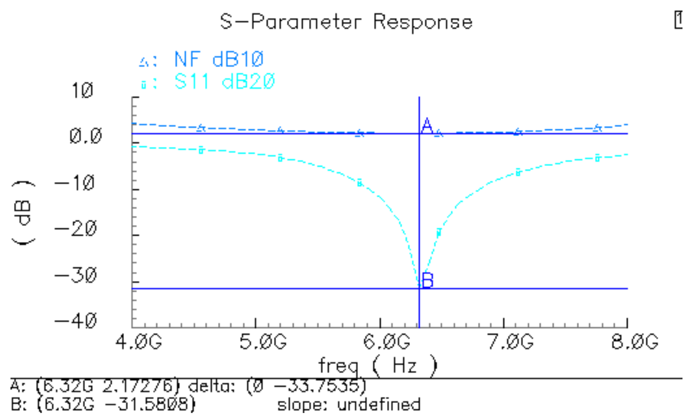

Fig. 3.10: S_{11} and noise figure, showing simultaneous noise and power matching

3.6.3 Output Impedance

From Fig. 3.11, the output impedance Z_{out} does not go above 22 ohms, meaning that the specifications for a maximum value of 30 ohm as output impedance has been met. This is due to the maximum power P_L to be delivered to the mixer [19], given by

$$P_L = \frac{1}{2}\left|V_{out}\right|^2 \frac{Z_L}{\left(Z_L + R_L\right)^2 + X_{out}^2}\ ; \quad Z_{out} = R_{out} + iX_{out}\ ; \ \Gamma_l = 0 \tag{3.10}$$

where V_{out} is the LNA output voltage and Z_L the mixer input impedance.

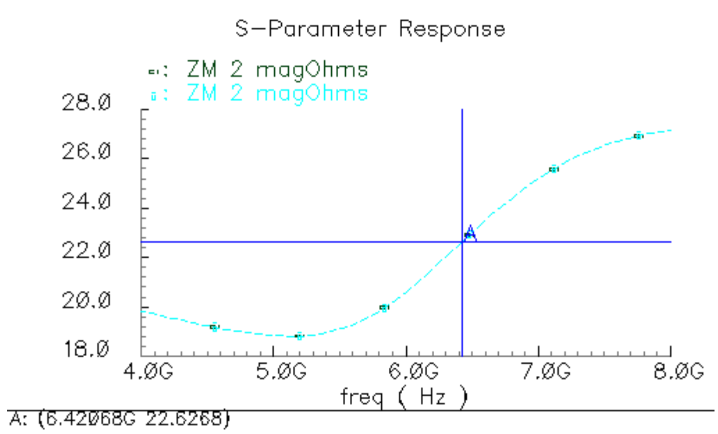

Fig. 3.11: Output impedance calculation for noise optimization

3.6.4 Stability

The Rollet's factor K_f can be used for stability analysis [9], [20]. For unconditional stability, K_f should be greater than one and B_f positive [9]

$$K_f = \frac{1-|S_{11}|^2-|S_{22}|^2+|\Delta|^2}{2|S_{12}S_{21}|} > 1, \qquad B_f = S_{11}S_{22} - S_{21}S_{12} > 0 \tag{3.11}$$

Fig. 3.12 shows that at the center frequency K_f is greater than one and B_f positive. From these plots, we can conclude that the circuit is unconditionally stable.

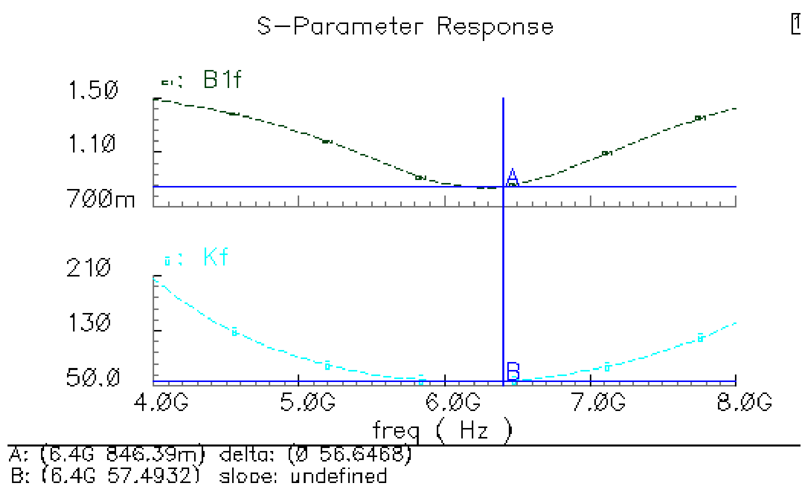

Fig. 3.12: Stability test for CS-NB-LNA

3.6.5 Linearity

Fig. 3.13 shows a 1-dB compression at -23.7dBm and a third order input inter-modulation point (IIP3) at -12.16dBm. The 1dB compression point was found by simulating harmonics with a beat frequency of 6.4GHz, while the IIP3 point was found using a 2-tone test with a primary frequency of 6.4GHz and a second tone at 6.2GHz. The inter-modulation term was ($|f_1 - 2f_2| = 6.6GHz$).

3.6.6 Specifications and achieved results

A comparison between desired specifications and achieved results is summarized in Table 3.4.

3.6.7 Monte Carlo simulation

Monte-Carlo simulations were then performed to analyze the performance of the circuit when fabrication and element tolerances have to be taken into consideration. This simulation was performed for the noise figure NF as well as the S-parameters.

From Fig. 3.14, we can conclude that S_{11} and NF are sensitive to tolerances, and corrections can be made through element and current adjustment. On the other side, S_{21}, S_{22} (Z_{out}), and S_{12} are not sensitive to tolerances.

Table 3.4: Summary of specifications and achieved results

Specifications	Design Requirements	Initial Design	Design with Optimized Power
Center frequency	6.4GHz	6.4GHz	6.4GHz
Gain	>12dB	17dB	13.8dB
Noise figure	<3dB	2.2dB	2.4dB
Output impedance	<30 Ω	26 Ω	25 Ω
1dB Compression	>-25dBm	-23.6dBm	-23.8dBm
IIP3	>-15dBm	-13.45dBm	-13.7dBm
Voltage supply	1.2V	1.2V	1.2V
Total Power	Minimized	13mW	3.2mW
Stability	Unconditionally Stable	Unconditionally Stable	Unconditionally Stable

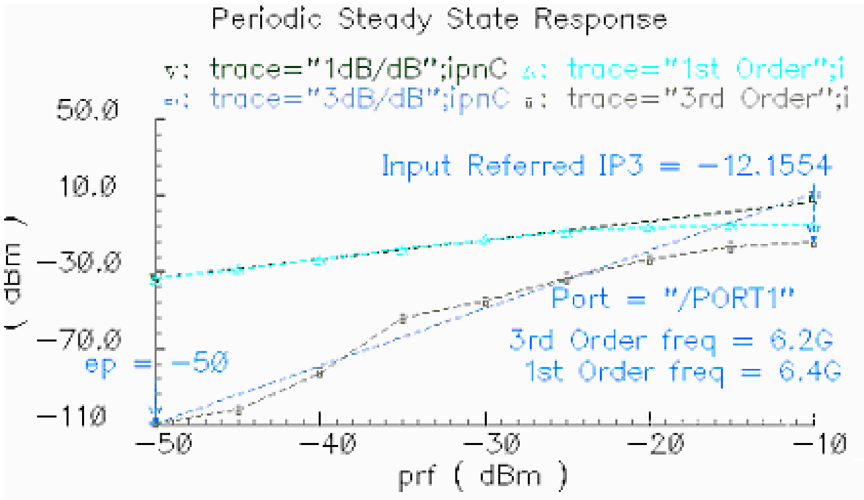

a)

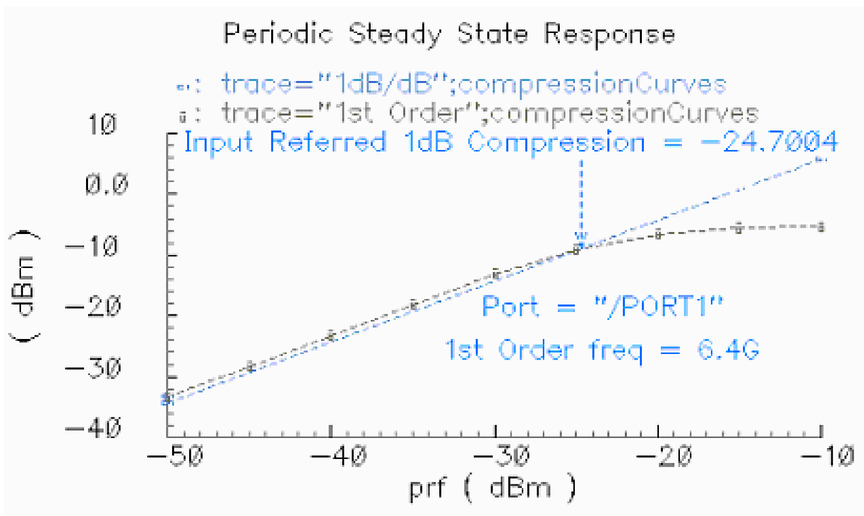

b)

Fig. 3.13: CS-NB-LNA parameters: a) 1dB compression and b) IIP3.

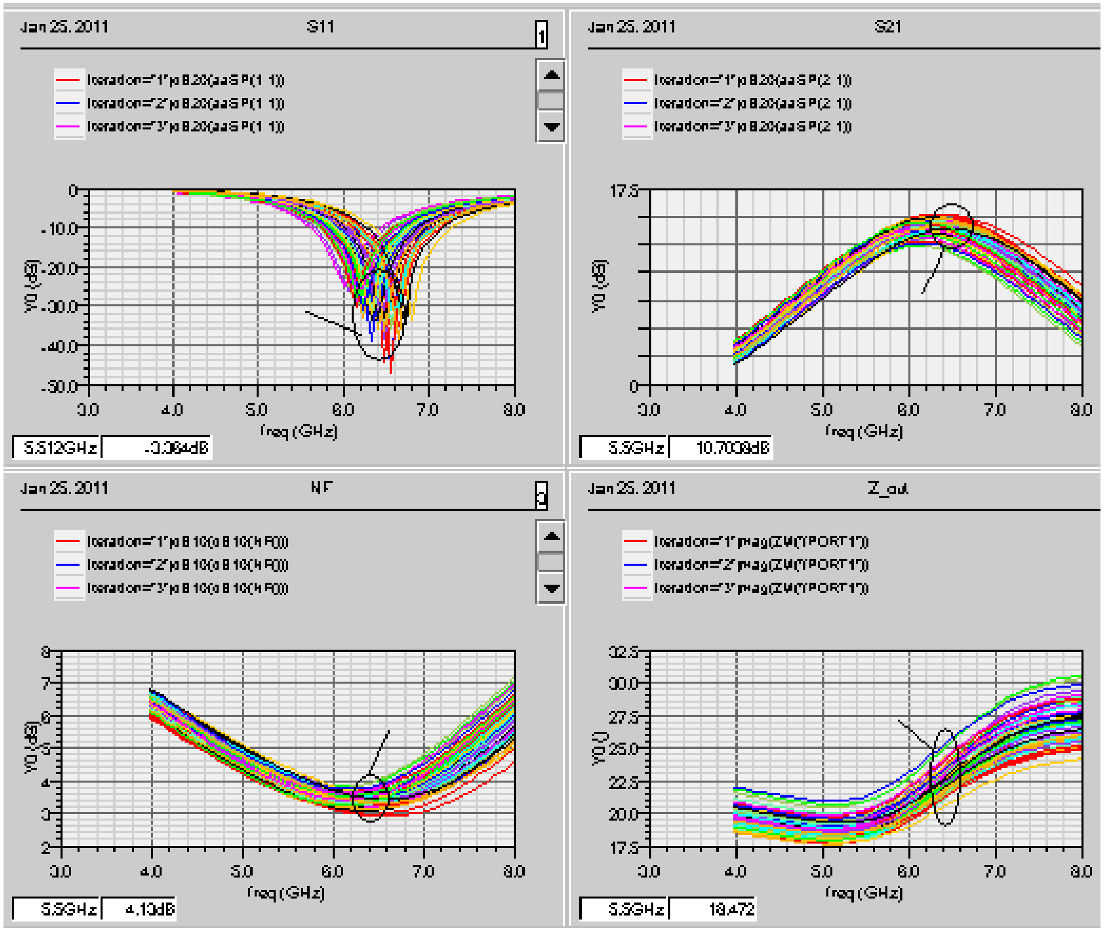
Jan 25, 2011
S11
S21
NF
Z_out
freq (GHz)

a)

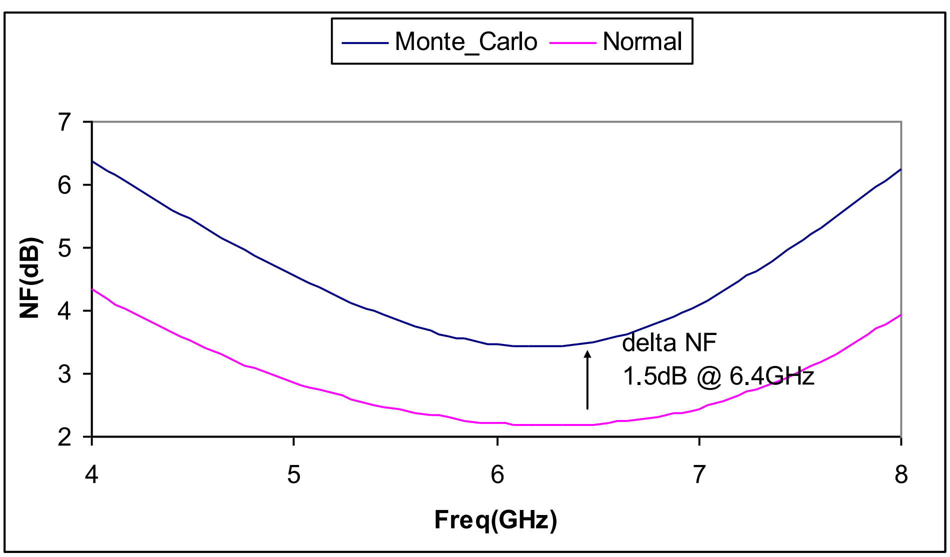
Monte_Carlo
Normal
NF(dB)
Freq(GHz)
delta NF
1.5dB @ 6.4GHz

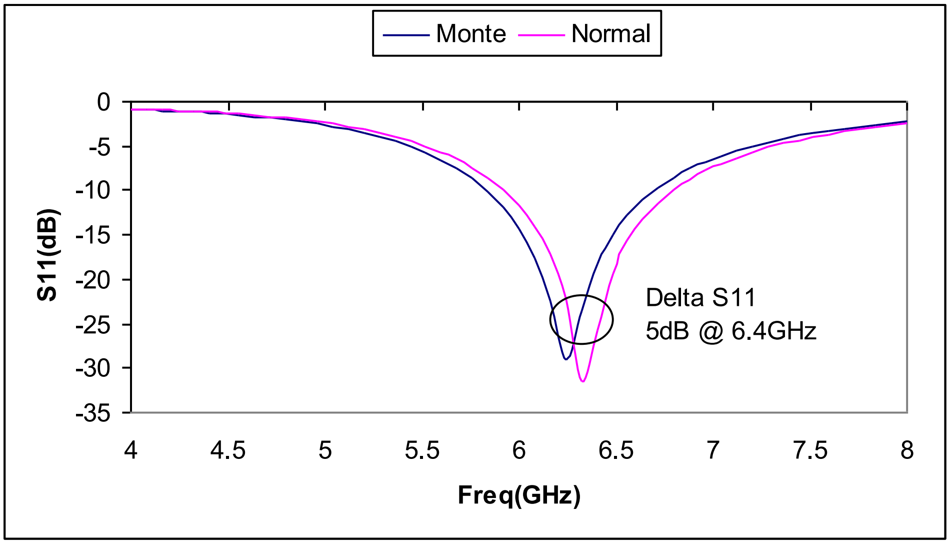
Monte
Normal
0
-5
-10
-15
-20
-25
-30
-35
S11(dB)
Delta S11
5dB @ 6.4GHz
4
4.5
5
5.5
6
6.5
7
7.5
8
Freq(GHz)

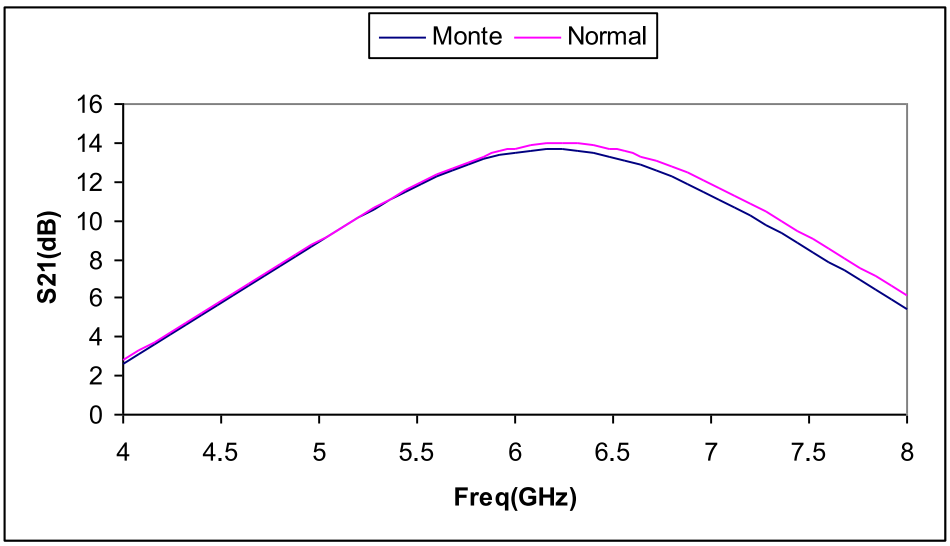
Monte
Normal
16
14
12
10
8
6
4
2
0
S21(dB)
4
4.5
5
5.5
6
6.5
7
7.5
8
Freq(GHz)

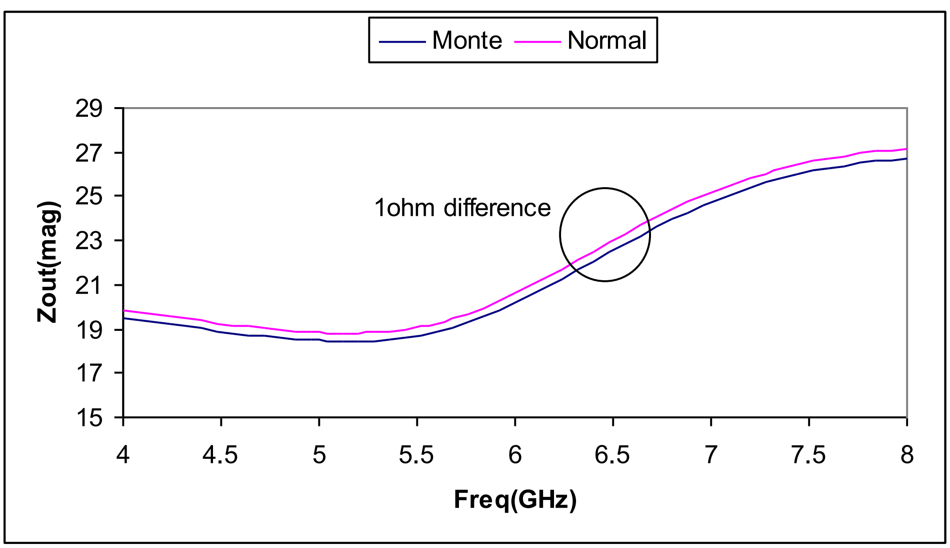
Monte
Normal
29
27
25
23
21
19
17
15
Zout(mag)
1ohm difference
4
4.5
5
5.5
6
6.5
7
7.5
8
Freq(GHz)

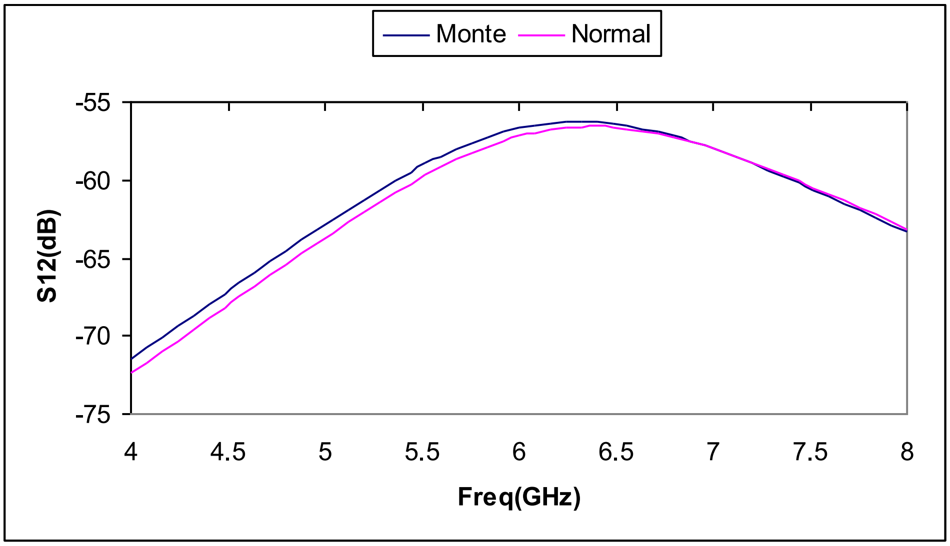

b)

Fig. 3.14: Monte-Carlo Simulation results with 100 iterations,
a) Scattering, b) Wave average (NF, S-parameters, Z_{out})

3.6.8 Conclusion

A NB-UWB-LNA was designed to operate at 5-7GHz while meeting all given specifications. Note that increasing the buffer size can reduce S_{11} and noise as well as increase gain; however it will also increase the output impedance. Therefore, the size we used was found to be optimal to meet all specifications.

A resistor was used as buffer current source to reduce the noise figure and allow the buffer to operate properly using low current. Replacing the resistor with a current mirror will require approximately 2.34mA of current, while with the resistor, 1.8mA is enough. But with the resistor, we have limited LNA linearity due to voltage issue. The current mirror ratio used to provide current to cascade was 1:5.

A small resistor was used to reduce power to the current mirror biasing transistor. The amplifier transistor was sized to meet specifications. Increasing the width and current could improve all specifications, except S_{11}. Thus, S_{11} would require degeneration inductor and gate inductor to be re-calculated to optimize noise and input matching. Similarly increasing the size of the cascade transistor improves S_{11} and S_{21} but deteriorates the output impedance and noise figure.

The DC blocking capacitor was sized such that it removed most of imaginary component of the output impedance. Therefore, when calculating the output impedance, only the real part was taken into consideration.

3.7 Convert Narrowband to wideband UWB-LNA

The final step was to convert the narrowband LNA to wideband LNA using wideband techniques (Fig. 3.15). Therefore,

- In the cascade section, instead of tank, we used a series inductor and a resistor to expand bandwidth [21]. Obviously, the resistor will add more thermal noise and limit the LNA linearity. On the other side, the external resistor will limit the voltage switching across the cascade transistor but drop the gain in the high frequency spectrum.
- We introduced a negative feedback to increase bandwidth (but with an expected negative impact on gain) [22].
- We used a BPF for input matching network [23].

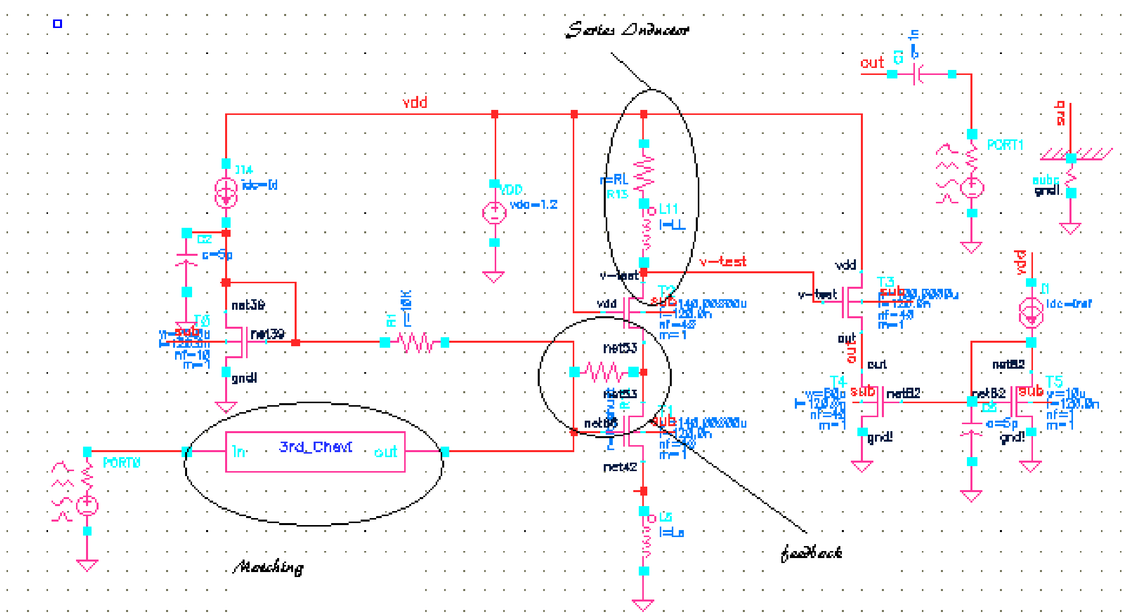

Fig. 3.15: wideband techniques in CS-UWB-LNA.

3.7.1 LNA matching

Let us consider a single stage amplifier where the matching procedure is to match the input/output impedances (Z_S, Z_L) to the characteristic impedance of coming lines, Z_o.

One approach to improve matching is to reduce the effect of the transistor S_{12} parameter either by using a cascade method (CG) or increasing isolation. However, the cascade will not only reduce the linearity [24] but also increase the NF (one more stage). Furthermore, sizing the cascade transistor could be an issue (usually, the designer chooses the same size as the LNA-core transistor to have the same current).

The input matching network can be one of the filters studied in Chapter 2. Based on the conclusions made in this chapter, we used the same specifications. As shown in Fig. 3.16 and as expected with respect to the filter order, Gaussian, Bessel and Butterworth filters present low matching performance. On the other side, ChevII, Elliptic and Hourglass filters have better matching performance. However, since all parameters are strongly dependent, the final selection will be made only after simulating the whole system (Filter + LNA).

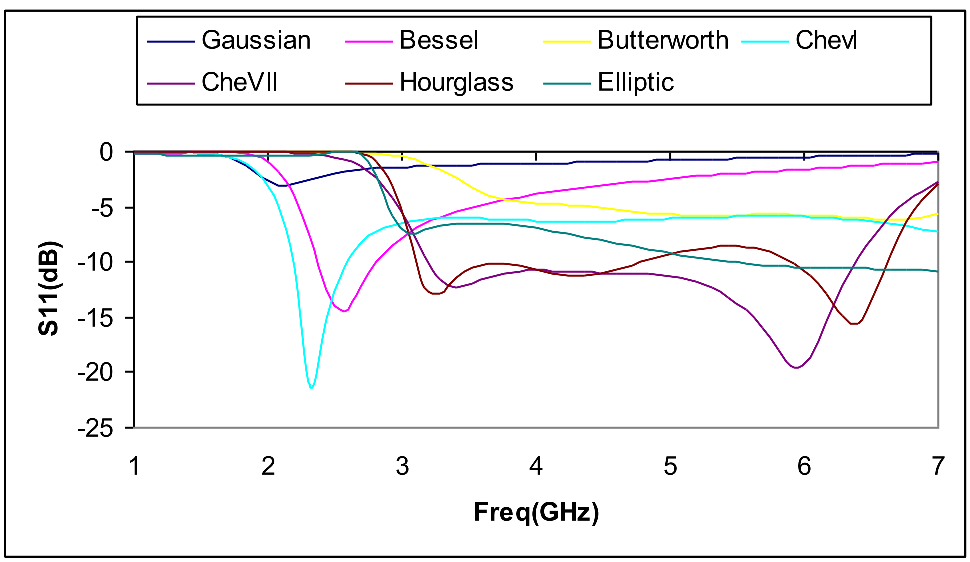

Fig. 3.16: Matching comparison in CS-UWB-LNA using different filters.

3.7.2 Gain

We thus simulated the whole system (Filter + LNA). Figure 3.17 shows the CS-UWB-LNA gain while combined with different filters used as input matching networks. Then,

- With Gaussian/Bessel/Butterworth BPFs: the system does not exhibit significant gain. Also, due to their lower sharpness, these filters allow gains in undesired frequencies (< 2GHz), leading to more interference with other wireless systems.
- With ChevI/ChevII/hourglass BPFs: the system exhibits a better gain flatness in the whole desired frequency spectrum.

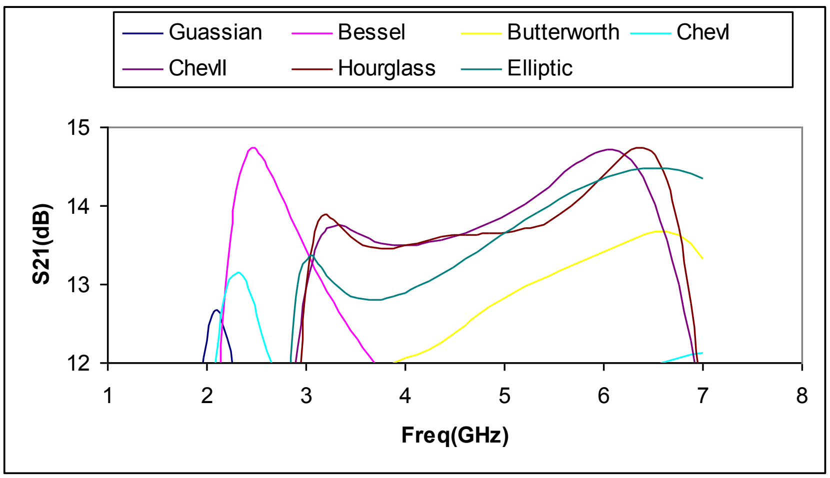

Fig. 3.17: Gain comparison in CS-UWB-LNA with different input matching filters

3.7.3 Noise figure

Let us model a noisy network by a noiseless network, moving all noise sources to the input [24] (Figs. 3.18 and 3.19). In analog circuits, the signal-to-noise ratio (SNR) is a crucial parameter to consider. In fact, in RF circuit design, the goal is to increase the SNR to better receive and detect the signal with the lowest possible bit error rate (BER).

The noise figure F can be defined as [9], [25]:

$$F = \frac{SNR_{in}}{SNR_{out}} \; ; \; NF = 10 \log F \tag{3.12}$$

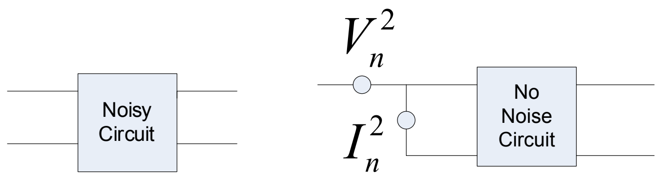

Fig. 3.18: voltage/current noise sources model.

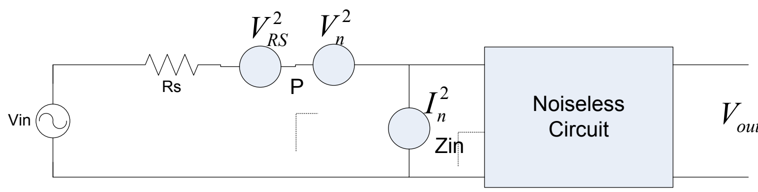

Fig. 3.19: noise figure calculation model with various noise sources.

In this equation, SNR_{in} and SNR_{out} are the input/output signal-to-noise ratios. They can be modeled as [26]

$$SNR_{in} = \frac{\alpha^2 V_{in}^2}{\alpha^2 V_{Rs}^2}; \qquad SNR_{out} = \frac{\alpha^2 A_v^2 \times V_{in}^2}{\left[V_{Rs}^2 + \left(V_n + I_n R_s\right)^2\right]\alpha^2 A_v^2} \tag{3.13}$$

where α is the gain at the 'P' plane and A_v the gain from 'P' to V_{out}. Finally, after some mathematical derivations, the noise figure can be expressed as, [25]

$$NF = 1 + \frac{\left(V_n + I_n R_s\right)^2}{V_{Rs}^2}; \qquad V_n = \sqrt{4kTB_n R_s}\ , \tag{3.14}$$

where k is the Boltzman's constant, T the temperature and B_n the normalized bandwidth (1Hz). Also, V_n and I_n are calculated in 1Hz bandwidth.

By assuming that in RF circuit design, the source and load impedances are set to 50ohms, we obtain

$$NF = \frac{V_{n,out}^2}{A^2}\frac{1}{4kTR_s}, \quad V_{n,out}^2 = A^2\left[4kTR + \left(V_n + I_n R_s\right)^2\right], \quad A = \alpha A_v \tag{3.15}$$

where $V_{n,out}^2$ is the total output noise power. Using the filters already designed, we can see that the ChevII and hourglass filters not only allow almost flat noise figure frequency response but also lower value compared to other filters (Fig. 3.20).

Furthermore, even if ChevII has slightly better performance between 5-6GHz, this slightly lower NF is insignificant when component tolerances and layout issues will be included in the optimization process.

3.7.4 Load Matching

In most design approaches, the real value of the first stage output impedance has to be less than 30ohms. However, reducing this impedance will increase the power consumption, buffer transistor size, linearity, and finally buffer biasing circuit. In our design, the first conclusion we can make is that whatever filter is used, the output impedance is almost flat, $16 < Z_{out} < 20\Omega$ (Fig. 3.21), which agrees with theory [27]

$$Z_{22} = Z_0 \frac{(1-S_{11})(1+S_{22})+S_{12}S_{21}}{(1+S_{11})(1-S_{22})-S_{12}S_{21}}, \rightarrow \frac{(1-S_{11})}{(1+S_{11})} \approx 1 \tag{3.16}$$

3.7.5 Stability

Narrowband amplifiers are usually stable while wideband amplifiers can be unstable for some particular configurations involving g_m-boosting or feedback. From (3.11), we can see that the stability can be improved by reducing the reverse gain parameter S_{12}.

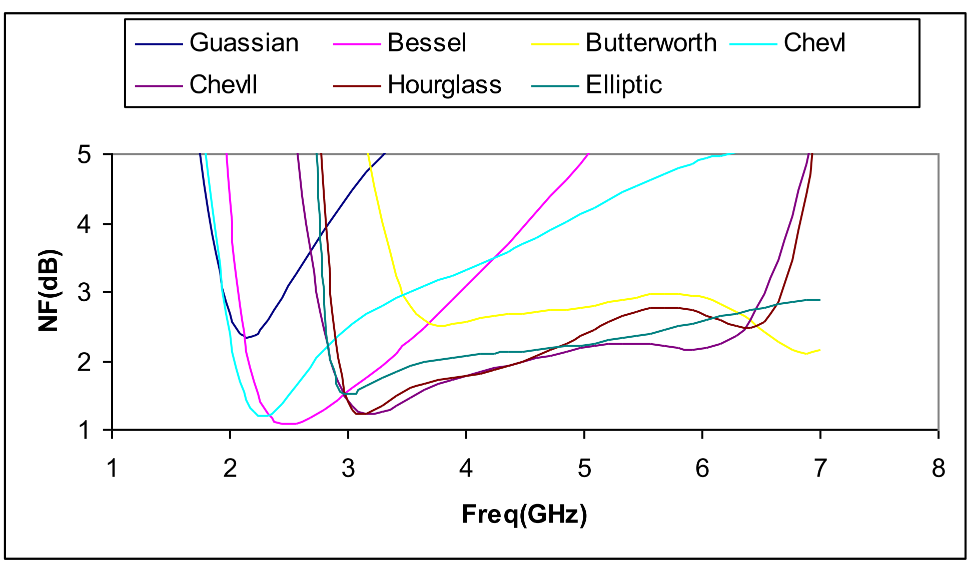

Fig. 3.20: Noise figure comparison in CS-UWB-LNA with various matching filters

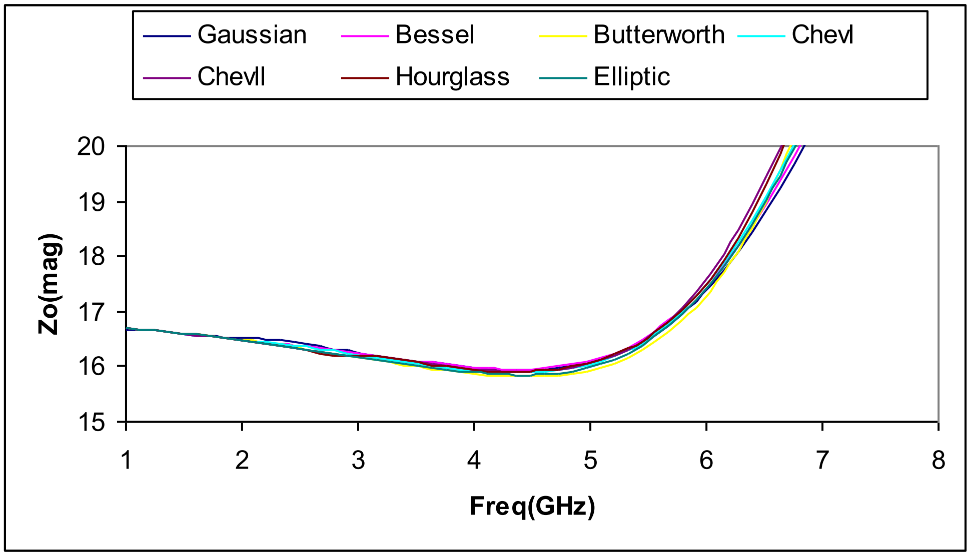

Fig. 3.21: Output impedance comparison in CS-UWB-LNA with various matching filters

There are different ways to increase the output/input isolation. We can for instance, use a cascade topology, which increases noise figure and reduces linearity, or bypass the C_{ds} component (output to input parasitic capacitance for the CS topology). Note that bypassing C_{ds} requires at least one more inductor and capacitor as resonant tank network between the output and the input. So choosing the cascade will save plenty of integration space while the bypass tank will reduce the risk of increasing the noise figure in price of power consumption, lower bandwidth, inductor radiation conflict with the RF input signal (inductor radiation distortion, layout issue), and higher space integration.

Fig. 3.22 compares the stability conditions for various input matching filters. In this figure, higher *Bf* value indicates better stability as with ChevII/Hourglass filters.

3.7.6 Linearity

First let us consider a single tone input signal received at the input of the LNA assumed to be nonlinear, as in Fig. 3.23, [1].

$$
\begin{aligned}
v_i &= v_o \cos\left(w_0 t\right) \\
v_0 &= a_0 + a_1 v_0 \cos(w_0 t) + a_2 v_o^2 \cos^2(w_o t) + a_3 v_0^3 \cos^3(w_0 t) + \ldots
\end{aligned}
\tag{3.17}
$$

The above equation can be expressed as

$$v_0 = \left(a_0 + \frac{1}{2}a_2 v_0^2\right) + \left(a_1 v_0 + \frac{3}{4}a_3 v_0^3\right)\cos(w_0 t) + \frac{1}{2}a_2 v_0^2\cos(2w_0 t) + \frac{1}{4}a_3 v_0^3\cos(3w_0 t) + \ldots \tag{3.18}$$

giving as first order approximation,

$$A_v = \left.\frac{v_0}{v_i}\right| = a_1 + \frac{3}{4}a_3 v_0^2 \tag{3.19}$$

From that, the ideal case is when $A_v = a_1$, i.e., no other higher odd harmonic. In amplifiers, the third order is defined as a negative coefficient parameter which obviously reduces the gain defined as saturation/compression gain.

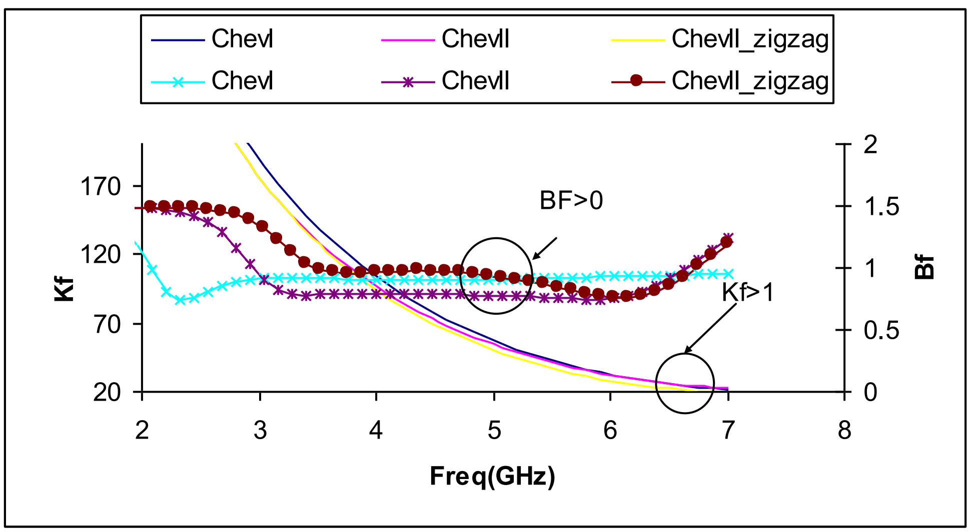

Fig. 3.22: comparison of CS-UWB-LNA stability using various input matching filters (Unconditionally stable).

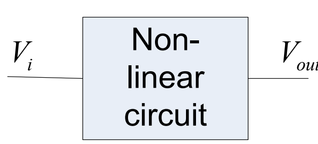

Fig. 3.23: simple nonlinear circuit topology.

- **Third order (IP3)**

One of the techniques to evaluate linearity is the third order test which applies two signals (f_1, f_2) at the system input, with equal amplitude and little frequency offset. By plotting the fundamental and third intermodulation (IM3) output powers as function of the input power, the third order intercept point (IP3) is the point where the amplitude of the intermodulation tones at $2f_1$-f_2 or $2f_2$-f_1 are equal to the amplitude of the fundamental tones at f_1, f_2 (Fig. 3.24) [9].

At this point, the corresponding input power is called IIP3 while the output is OIP3. P_1 is the fundamental output power, P_3 the third harmonic output power at IM3, P_i the input power and G the power gain. Note that in the plot, the IM3 terms have a slope of 3 and the first order terms have a slope of 1, leading to

$$\frac{OIP3-P_1}{IIP3-P_i}=1,\ \frac{OIP3-P_3}{IIP3-P_i}=3 \quad \text{and} \quad G=OIP3-IIP3=P_1-P_i \tag{3.20}$$

$$\rightarrow \qquad IIP3=P_1+\frac{1}{2}\left(P_1-P_3\right)-G=P_i+\frac{1}{2}\left(P_1-P_3\right) \tag{3.21}$$

So by increasing the input power, the linearity will increase but there are some tradeoffs that include power conception, circuit topology, gain, and voltage room (current mirror biasing).

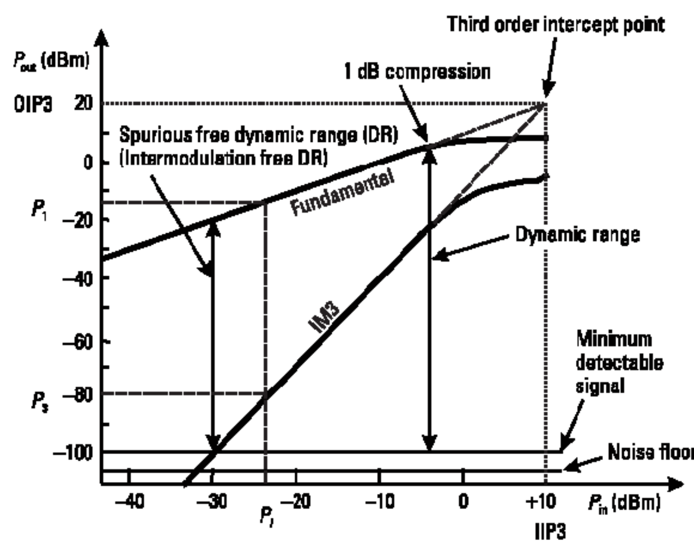

Fig. 3.24: Fundamental and IM3 output powers versus input power, [9].

- **1-dB compression**

The second linearity test is the 1-dB compression point test. This point is more accessible and requires just one tone rather than two. The 1-dB compression point is simply the input power level where the output power is 1dB less than it would be with an ideal linear device (Fig. 3.25 with different filters). It can be related to IP3 by

$$\frac{V_{IP3}}{V_{1dB}} = 3.04, \quad 20\log\left(\frac{V_{IP3}}{V_{1dB}}\right) = 9.66$$

$$\rightarrow \qquad IP3 = 1dB\_compression + 9.66(dB) \tag{3.22}$$

As expected, the Gaussian filter allows the highest linearity due to lower matching and gain (-9.66dB). Since linearity is inversely related to gain and noise figure, decreasing the gain will increase the output (transistor drain) and thus linearity will increase. The Bessel input matching filter can be the second choice in terms of linearity, while the Hourglass, Elliptic, ChevII give similar performance in terms of linearity (-16dB).

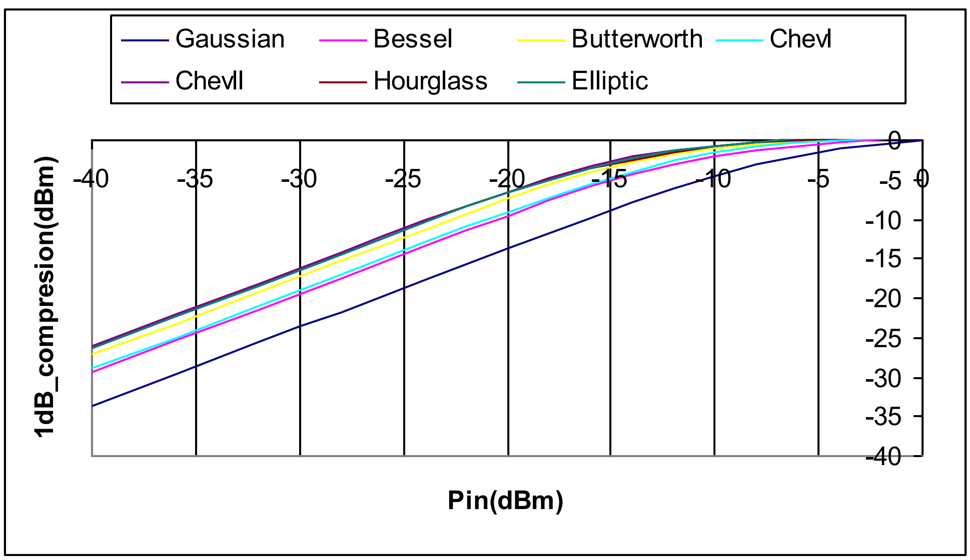

Fig. 3.25: Comparison of 1dB-compression point linearity test of the CS-UWB-LNA with various input filter matching

3.8 Regular vs. Zigzag Input Matching Filter

In this section, we will investigate and compare the Elliptic and Hourglass filter performance investigated in Chapter 2 (in both regular and zigzag topologies) while associated as matching networks to the UWB common-source LNA (CS-UWB-LNA).

3.8.1 Input matching

From Fig. 3.26, we can see that hourglass-regular and Elliptic-regular have better input matching compared to the corresponding zigzag filters. Note that to cancel the effect of the capacitor C_{gs}, a parallel capacitor filter would be preferred to a series capacitor filter. However, we will not conclude until investigating other tradeoffs like gain and noise figure performances.

3.8.2 Gain

Both regular filters have better gain and flatness than zigzag filters. This difference can be explained by using capacitor instead of inductor, since capacitor reduces the gain, Fig. 3.27. In terms of sharpness, the regular filters also satisfy this requirement.

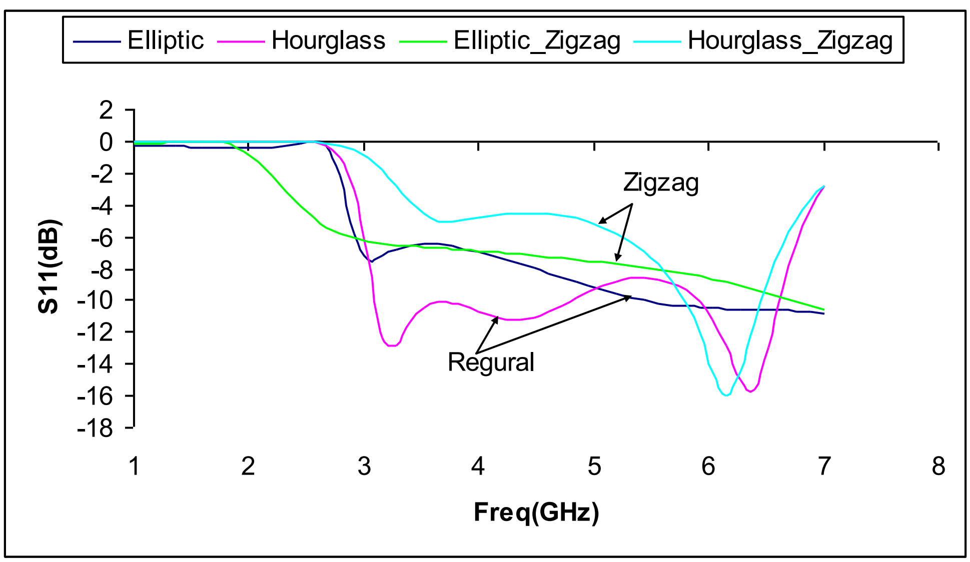

Fig. 3.26: Comparison of the input matching of CS-UWB-LNA with Elliptic and Hourglass matching filters using regular and zigzag topologies.

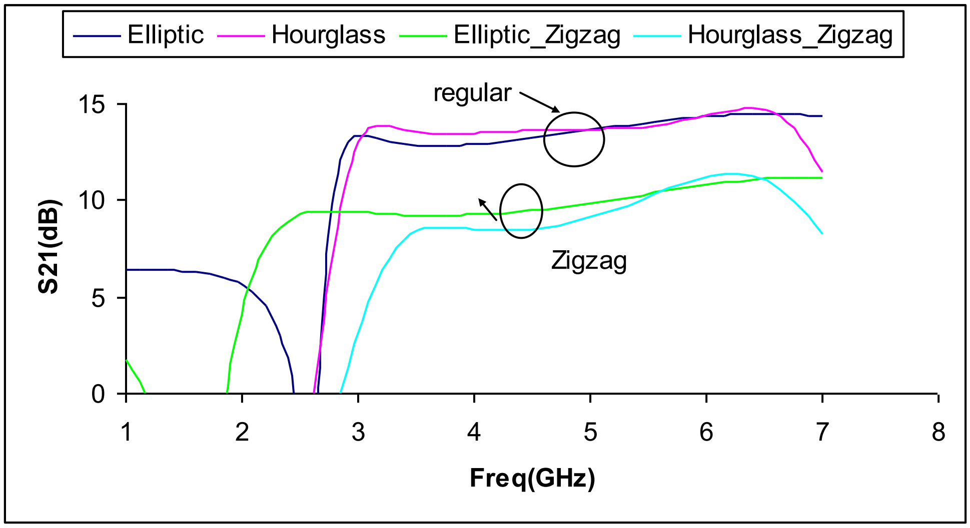

Fig. 3.27: Comparison of gain of CS-UWB-LNA with various matching filters using regular and zigzag topologies.

3.8.3 Noise figure

As expected, the regular filters act better in terms of noise due to higher matching and gain, Fig. 3.28. It is noticeable that the hourglass-regular has lower noise figure in the lower spectrum frequency part but smoothly change in high frequencies.

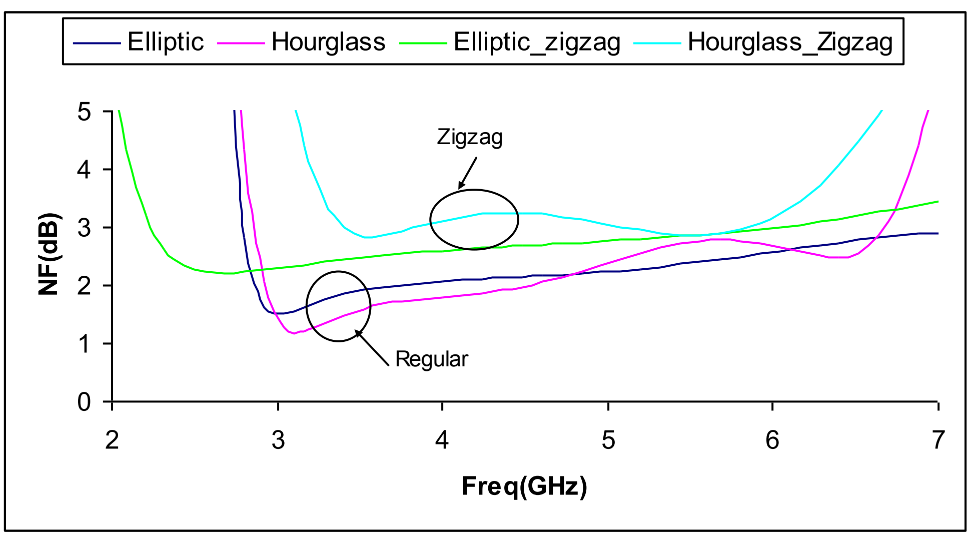

Fig. 3.28: Noise figure of CS-UWB-LNA with various third order matching filters with regular and zigzag topology.

3.8.4 Linearity

Fig. 3.29 shows that with Hourglass- and elliptic-zigzag filters, the amplifier has higher linearity or 1-dB compression point.

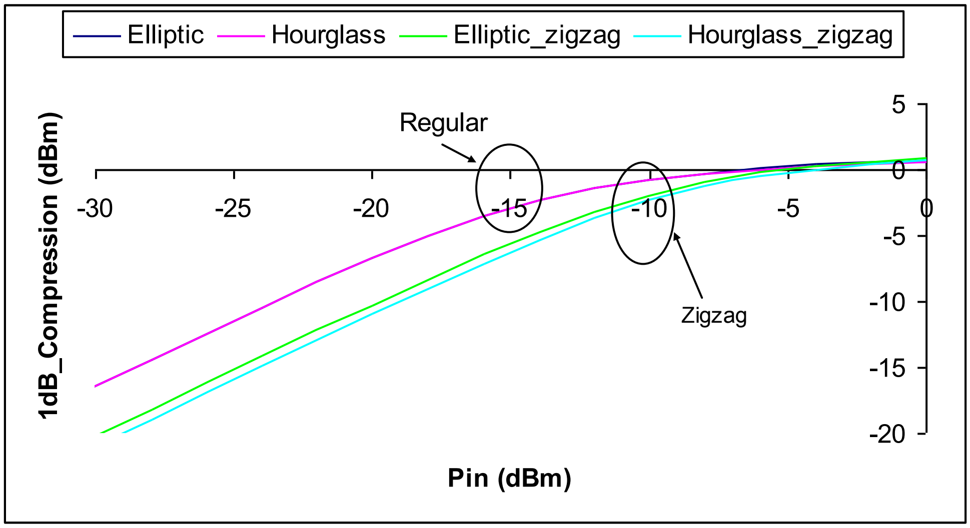

Fig. 3.29: CS-UWB-LNA linearity test with various third order matching filters with regular and zigzag topology.

3.8.5 Conclusions

Even if the hourglass-regular has low noise figure, it cannot be the best candidate (at least for common-source topology) mainly because of its higher ripple. But for other different applications not so sensitive to the gain frequency response, the hourglass zigzag may be considered as a good candidate. Table 3.5 summarizes the performances or regular/zigzag filters when associated as matching networks to common source UWB-LNA topology. However, no filter emerged as the best regarding all tradeoffs. So, let us consider the final step, the sensitivity to fabrication tolerances.

3.8.6 Tolerances

Fig. 3.30 shows the Monte-Carlo analysis with 100 iteration wave simulations for the CS-UWB-LNA with the ChevII band pass filter.

Table 3.5: performance comparison of third order regular/zigzag BPF input matching filters in CS-UWB-LNA.

	S_{11min} (dB)	S_{21max} (dB)	NF_{max} (dB)	1dB (dBm)
Elliptic-regular	-8	13.5	2.9	-16
Hourglass-regular	-9	13.6	3	-16
Elliptic-zigzag	-7	11	3.4	-9.5
Hourglass-zigzag	-9	11	3.5	-9.5

It has been proved that the design is very stable over most important parameters like noise figure, input matching, gain, and output impedance. Monte-Carlo simulation setup with 15% tolerance for all passive/active elements while the S-parameters tolerances are:

$$\Delta S_{11} = 0.8dB\,, \Delta S_{21} = 0.2dB,\ \Delta NF = 0.2dB\,, \Delta Z_{out} = 0.5\Omega\,.$$

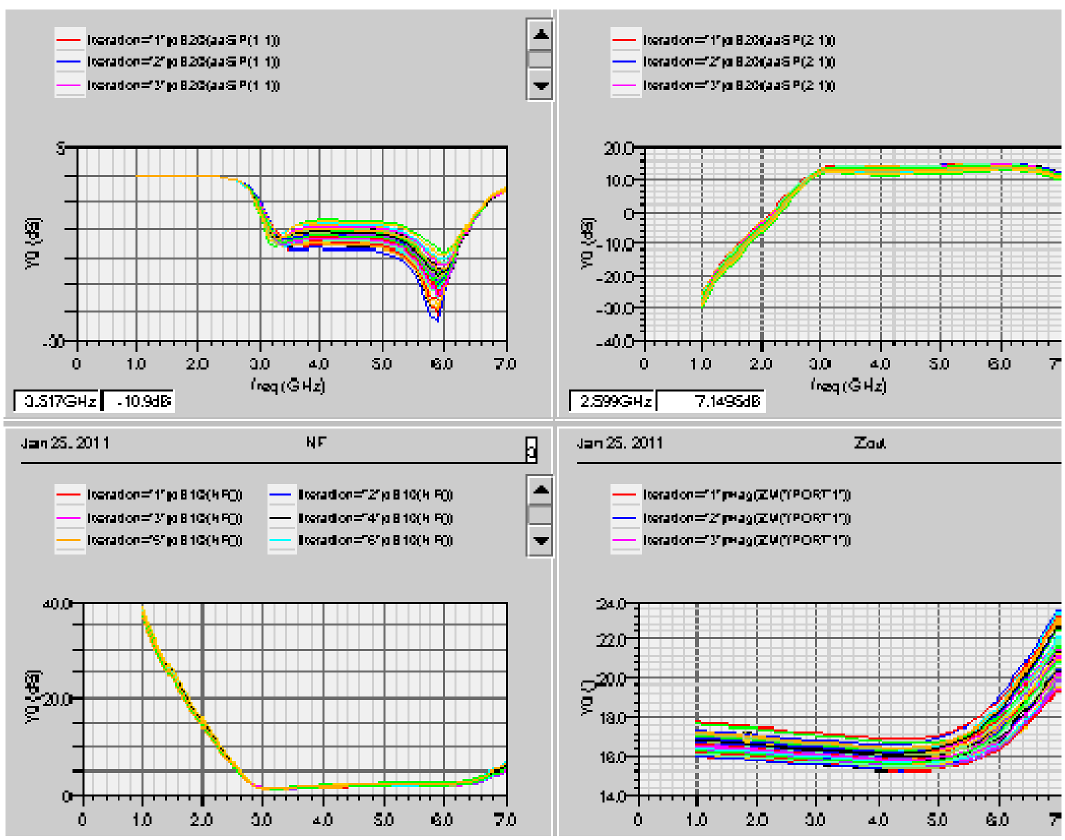

a)

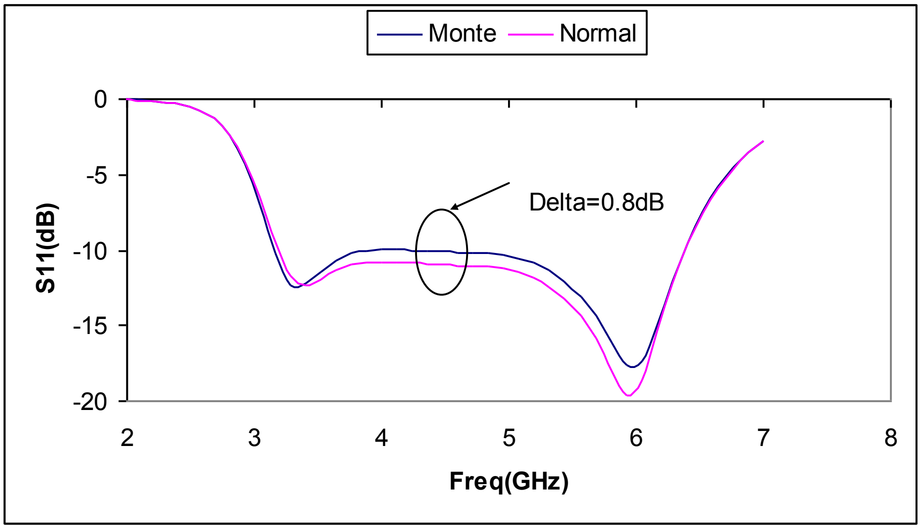

Monte
Normal
0
-5
-10
-15
-20
S11(dB)
Delta=0.8dB
2
3
4
5
6
7
8
Freq(GHz)

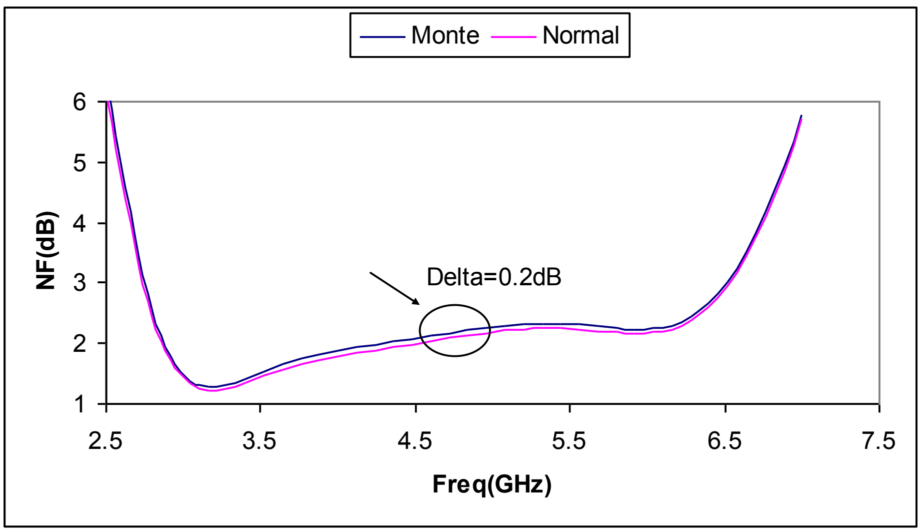

Monte
Normal
6
5
4
3
2
1
NF(dB)
Delta=0.2dB
2.5
3.5
4.5
5.5
6.5
7.5
Freq(GHz)

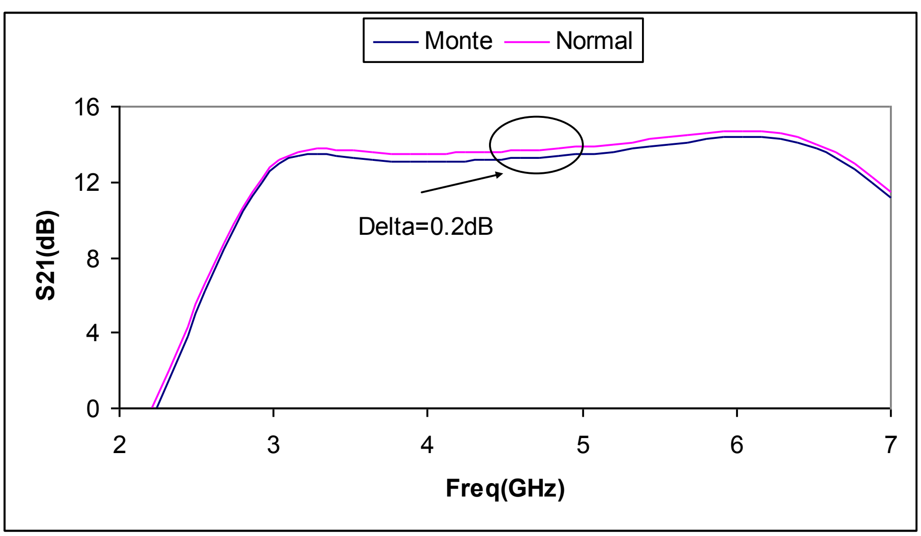

Monte
Normal
16
12
8
4
0
S21(dB)
Delta=0.2dB
2
3
4
5
6
7
Freq(GHz)

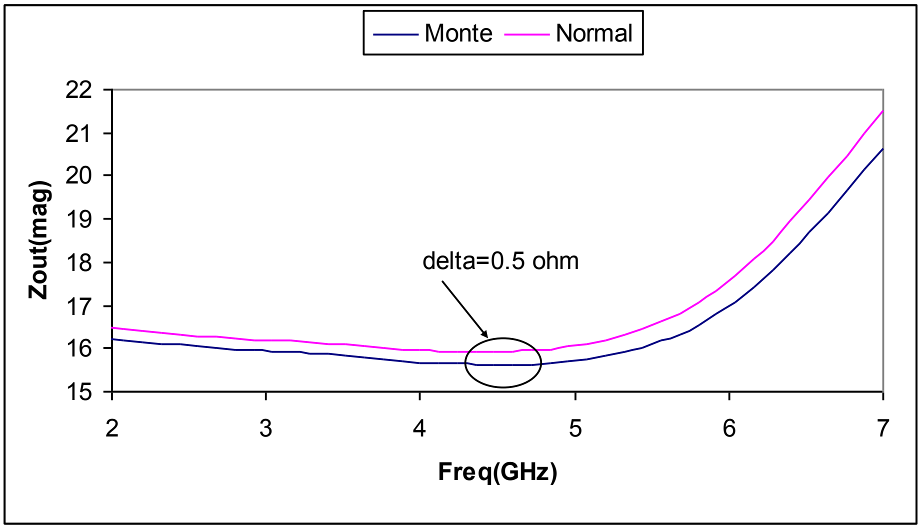

b)

Fig. 3.30: Monte-Carlo simulation results for CS-UWB-LNA_ChevII with 100 iterations, a) scattering b) average wave

3.8.7 Conclusion

The ChevII is the best candidate in terms of main tradeoffs such as reasonable input matching, desired frequency spectrum sharpness, gain, noise figure, complexity and linearity. Applying the zigzag method in special filters such as Elliptic and hourglass may have some benefits as integration space (lower inductance) and higher linearity (Figs 3.28 and 3.29) but has also slightly higher noise figure and obviously lower gain due to the nature of adding capacity.

3.9 CG-CS-UWB-LNA

We started with the CS configuration as a logical choice (most widely used configuration). However, from a designer point of view, the common-gate (CG) common-source (CS) UWB LNA (CG-CS-UWB-LNA) may be also a reasonable choice since it brings enough gain for the next receiver stage (Mixer). In fact, the CG topology has a better frequency response and requires lower-order matching filters. Also, the input matching network is simpler in CG than in CS due to the nature of the input matching, i.e., $1/g_m$, [2]. But CG also requires gain boosting system. So as in any design step, compromises need to be made.

Therefore, the next step was to test this CG-CS-UWB-LNA (Fig. 3.31) with different BPFs as input matching network and compare their performance. Note that since Gaussian, Bessel and Butterworth filters have lower performances, only ChevI, ChevII, Elliptic and hourglass filters were considered. We reported in Table 3.6 the CG-CS-UWB-LNA design parameters values.

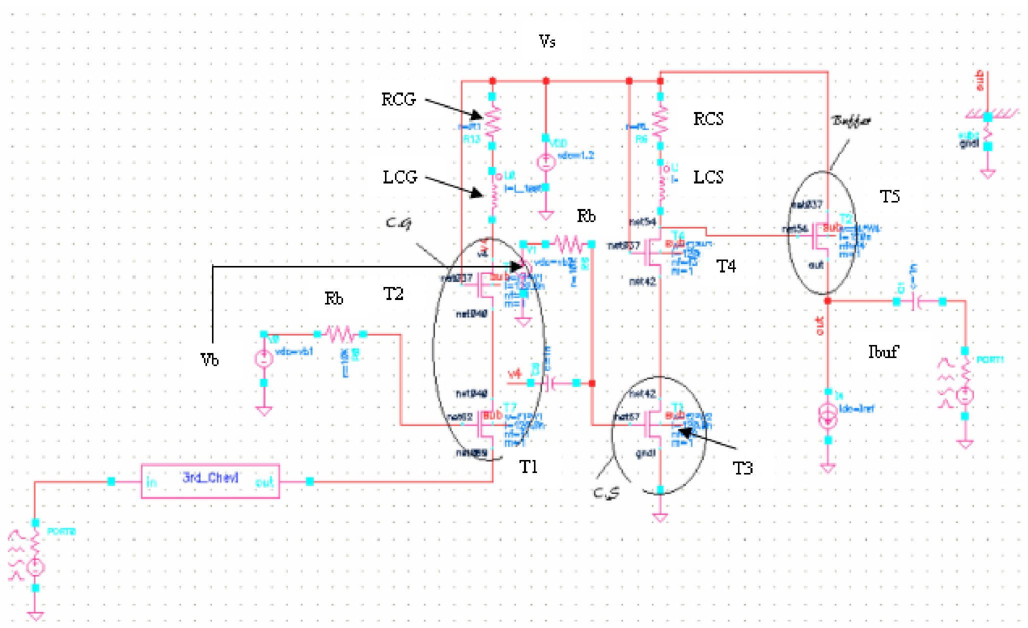

Fig. 3.31: wideband techniques in CG-CS-UWB-LNA.
*Cascade is not necessary for CG.

3.9.1 Matching

Figure 3.32 shows the input matching performance of the CG-CS-UWB-LNA with and without matching filters. As expected, the matching frequency response of the original CG topology (without matching filter) has better performance (flat) compared to the original CS. However the CS topology shows better matching performance in high frequencies compared to the CG LNA.

We cannot avoid input matching networks since some wireless systems are very sensitive to undesired signals (like GPS).

Also, the CG topology may exhibit a good matching frequency response but not enough to face the UWB-LNA matching constraint (<-6dB). As shown in the figure, the ChevII and hourglass filters give the best performance to the amplifier in terms of input matching.

In conclusion, it is clear that the CG has better matching frequency response compared to the CS topology. The input matching is highly depended on the LNA core bias, transistor parameters such as C_{gs}, and transistor technology (130nm or less).

The CG topology still requires an input matching network even if the theory claims that this configuration depends only the 1/gm biasing. ChevII and Hourglass filters are the best candidates for now.

3.9.2 Gain

Figure 3.33 shows the gain of the CG-CS-UWB-LNA configuration. Compared to the the CS topology, the CG-CS configuration has a better but lower gain response, and thus requires a boosting system such as a g_m-boosting.

Also, CG-CS UWB low-noise amplifiers with ChevII and hourglass filters exhibit the gain responses in terms of desired bandwidth matching and necessary sharpness to avoid interferences.

Table 3.6: CG-CS-UWB-LNA specifications.

<table>
<tr><td>T1-T2 (CG stage)
FN1 = 40; W = 4um; L = 120nm</td><td>T3 (CS stage)
FN3 = 40; W = 2.5um; L = 120nm</td></tr>
<tr><td>T4 (CS stage)
FN4 = 40; W = 1um; L = 120nm</td><td>T5 (Buffer)
FN5 = 40; W = 2.5um; L = 120nm</td></tr>
<tr><td colspan="2">Ibuf = 2mA; LCG = 2.5nH; RCG = 133Ω; Vs = 1.2V; Vb = 485mV; Rb = 1kΩ;
LCS = 2.5nH; RCS = 125Ω; Vbias = 485mv</td></tr>
</table>

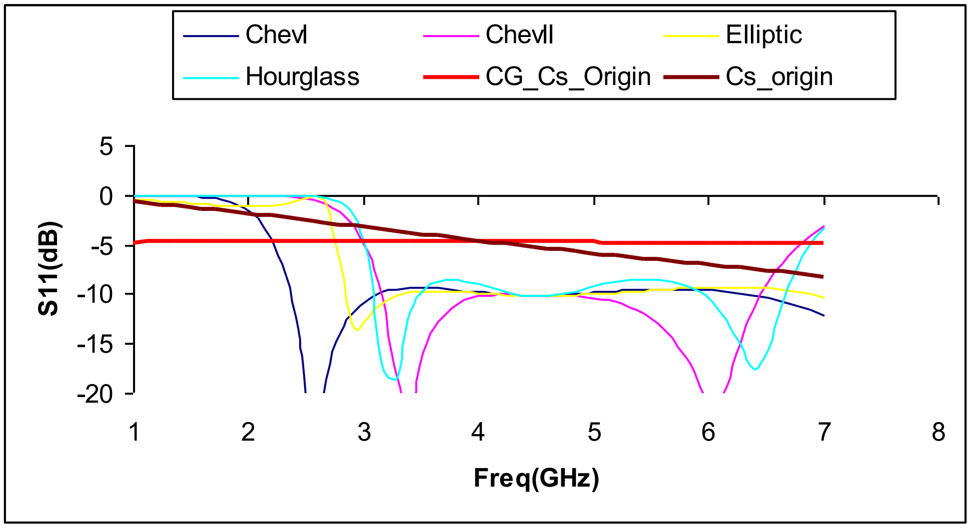

Fig. 3.32: CG-CS-UWB-LNA input matching test with various 3rd order matching filters.

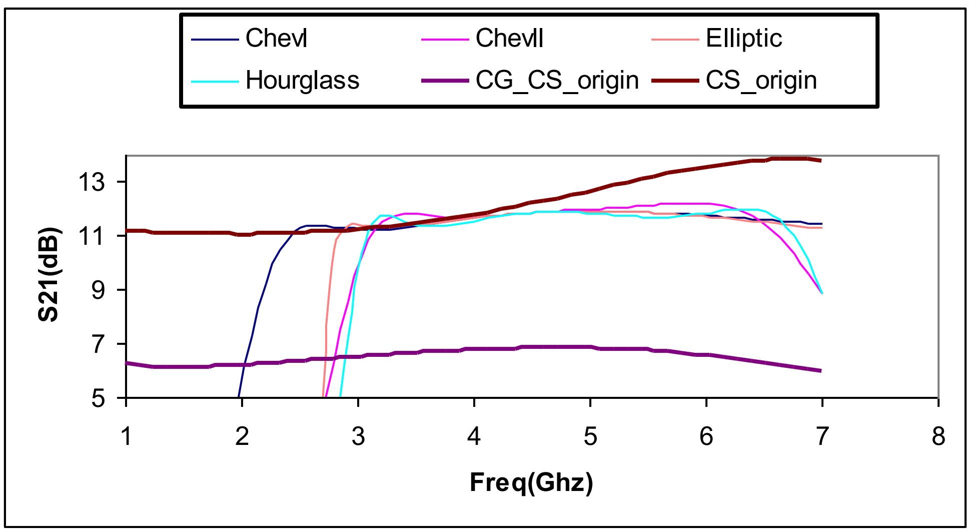

Fig. 3.33: CG-CS-UWB-LNA gain with various third order matching filters.

3.9.3 Noise figure

From Fig. 3.34, we can see that the original CG configuration (without matching network) has a higher noise figure than the CS topology (NF-CG < 10dB, NF-CS < 4dB). By adding the input matching filters, the noise figure reduces only to 5-6dB. Knowing that noise is the key parameter to consider in LNA design, the CG topology is not suitable for our application.

However, to complete our investigation, we still considered the other tradeoff results. Circuits with ChevI and Elliptic filters have better noise figure frequency response than Hourglass and ChevII, but these latter have both lower NF in the desired bandwidth and higher NF outside, making them as potential candidates.

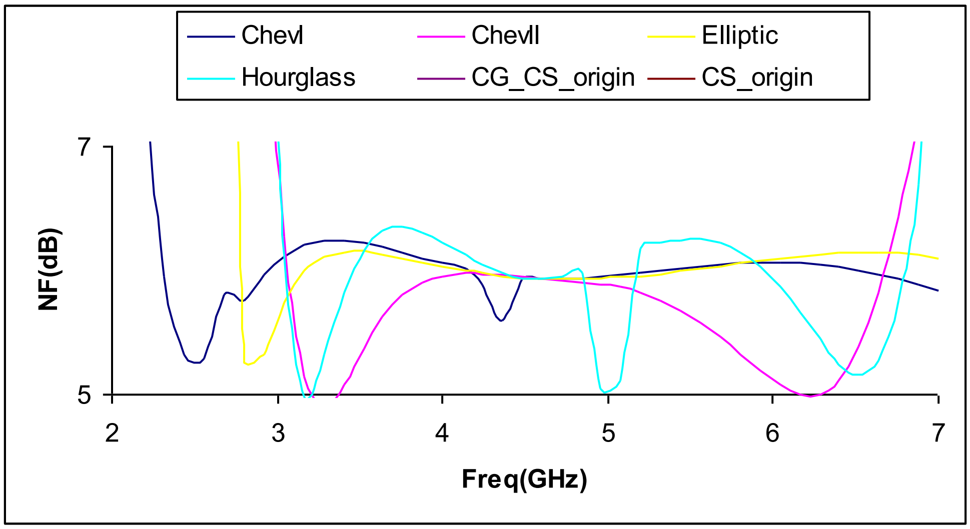

Fig. 3.34:CG-CS-UWB-LNA noise figure with various input matching filters.

3.9.4 Output matching and isolation

By increasing isolation and output matching, the input reflection will be closer to S_{11}. Most of RF LNAs try to increase these parameters in respect with linearity as well. As mentioned, adding a cascade stage in CG or/and CS configuration will increase the S_{12}, but in detriment of the voltage room for the cascade transistor, which needs to be biased. Also, as shown in Fig. 3.35, the original CG has better isolation. Also, as in Fig. 3.36, the output reflection coefficient of CG is lower than the CS one, which indicates power consumption reduction (especially in buffer section).

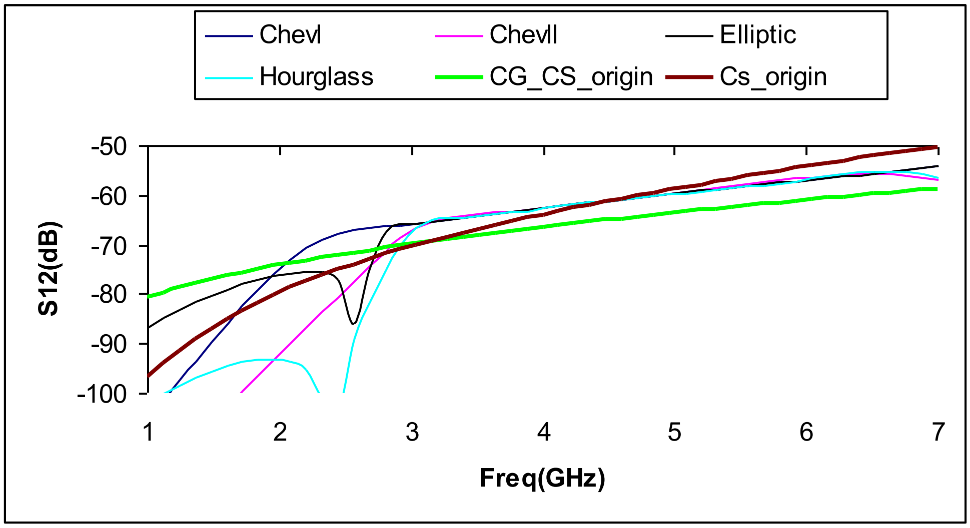

Fig. 3.35:CG-CS-UWB-LNA isolation with various input matching filters.

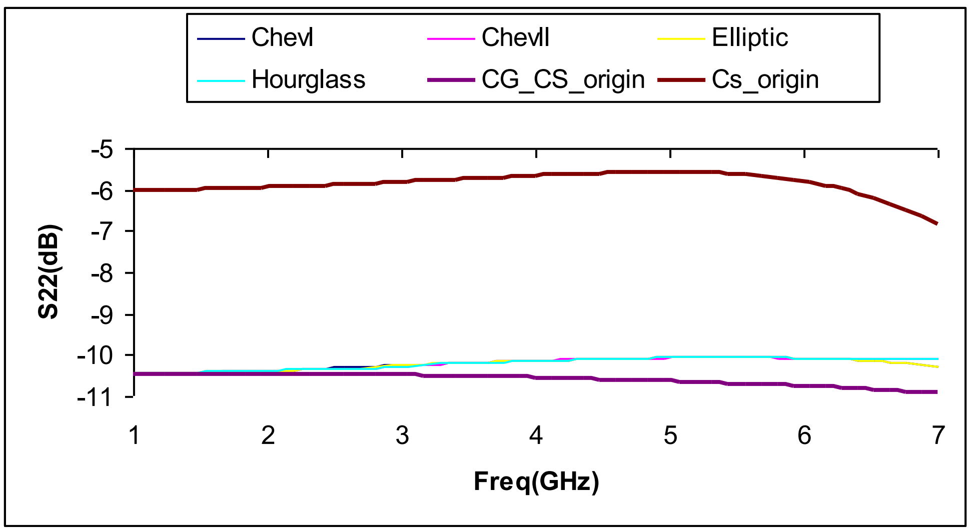

Fig. 3.36:CG-CS-UWB-LNA output matching with various input matching filters.

3.9.5 Linearity

Fig. 3.37 shows that the original CG topology has higher linearity but, as expected, by adding the input matching filters, the linearity reduces due to gain increasing. As commonly known, better matching affects linearity, gain and noise figure. However, if this statement is always true for the CS configuration, it is true for CG just for a certain matching level ($S_{11} < -10dB$) [2].

Some papers [2], [3] reviewed the CG advantages/disadvantages but forgot to highlight one of the key disadvantages namely, the high sensitivity of the CG-LNA design. In fact, since this parameter requires a perfect matching, the CG could not be as a good candidate. Also, CG-LNA stability is not included since the LNA is naturally unconditionally stable.

A summary of the LNA topologies performance with and without input matching is reported in Table 3.7.

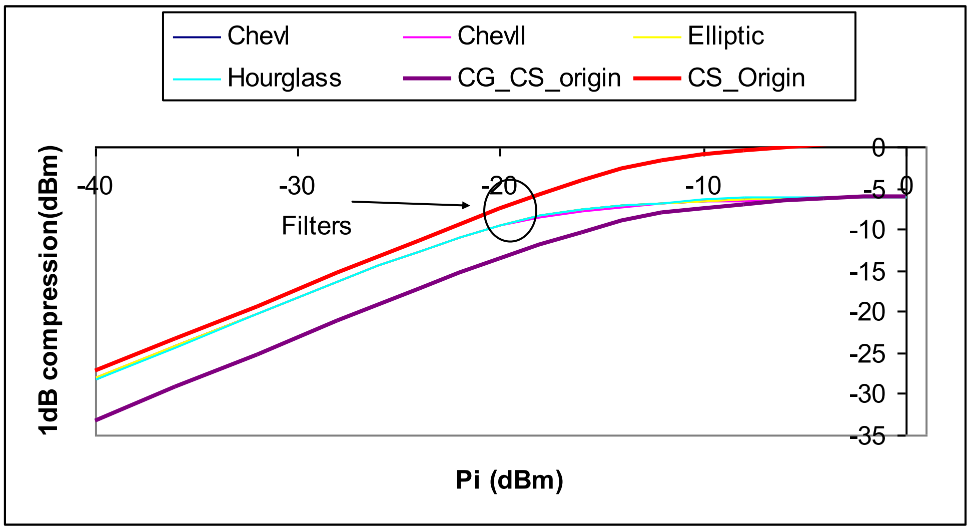

Fig. 3.37:CG-CS-UWB-LNA 1dB compression test in various input matching filters.

Table 3.7: Amplifier topologies performance with and without input matching filters.

	S_{11}(dB)	S_{21}(dB)	S_{11},S_{22} (dB)	NF(dB)	Linearity (dBm@5GHz)
ChevI (CG)	<-10.3	11.3	-10.2, -65	5-8	-21.5
ChevII (CG)	<-10	11-13	-10.5, -65	3.9-6.7	-21.7
Elliptic (CG)	<-10.2	11	-10.5, -65	5.3-5.7	-21.6
Hourglass (CG)	<-10	11-12	-10.5, -65	5.3-6	-21.5
CG_CS_original	<-5	6, 6.5	-10.5, -65	9.4-10	-17
CS original	-2, -8	11-14	-6, -50	2.3-2.8	-15

3.9.6 Monte-Carlo Analysis

Fig. 3.38 shows the Monte-Carlo analysis of the CG-CS-UWB-LNA with 100 iterations using the ChevII band-pass filter. It was setup for a 15% tolerance for all passive/active elements and with ΔS_{11}=0.2dB, ΔS_{21}=0.31dB, ΔNF=0.2dB, ΔZ_{out}=0.5Ω. As shown in the figure, NF and S_{11} are slightly better than in the CS-LNA. Also, the variations are not important vs. tolerances, confirming that the design is stable with regard to component tolerances.

3.10 Layout Configuration

In conclusion, we retained the CS-UWB-LNA topology with ChevII BPF (Inverse Chev Bandpass filter). Figures 3.39-3.44 show the layout a well as the DRC & LVC setups (Cadence).

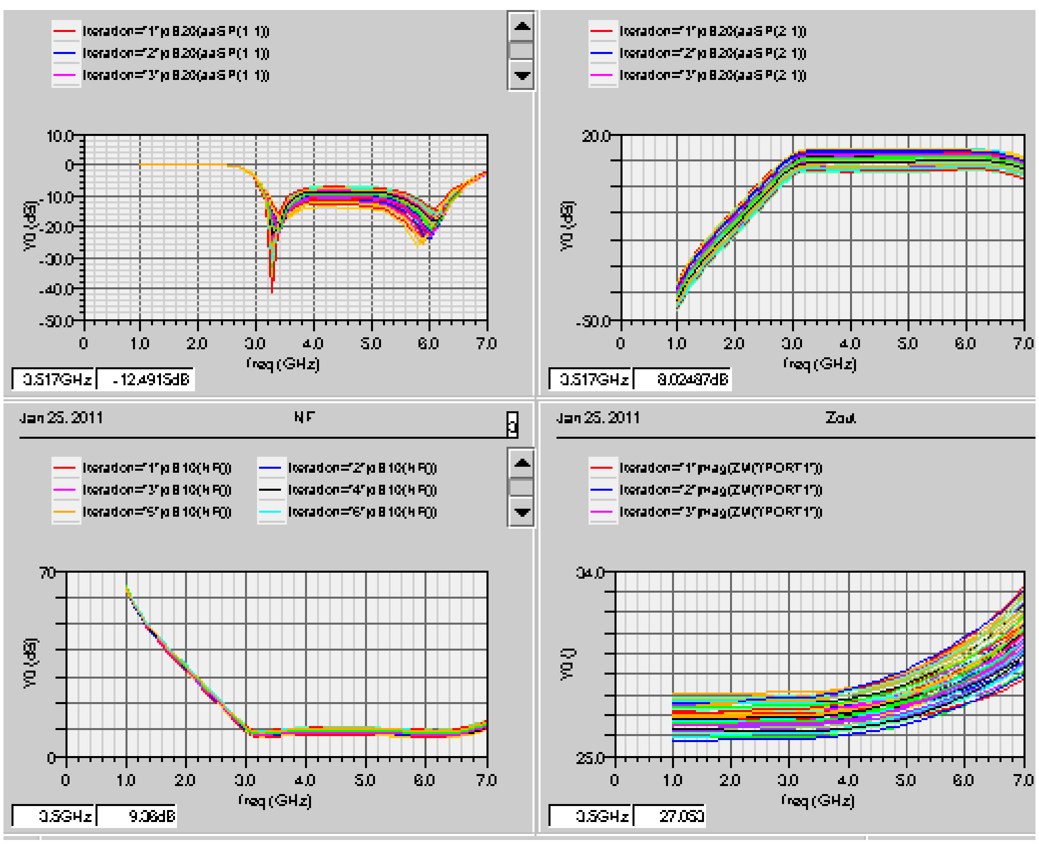

a)

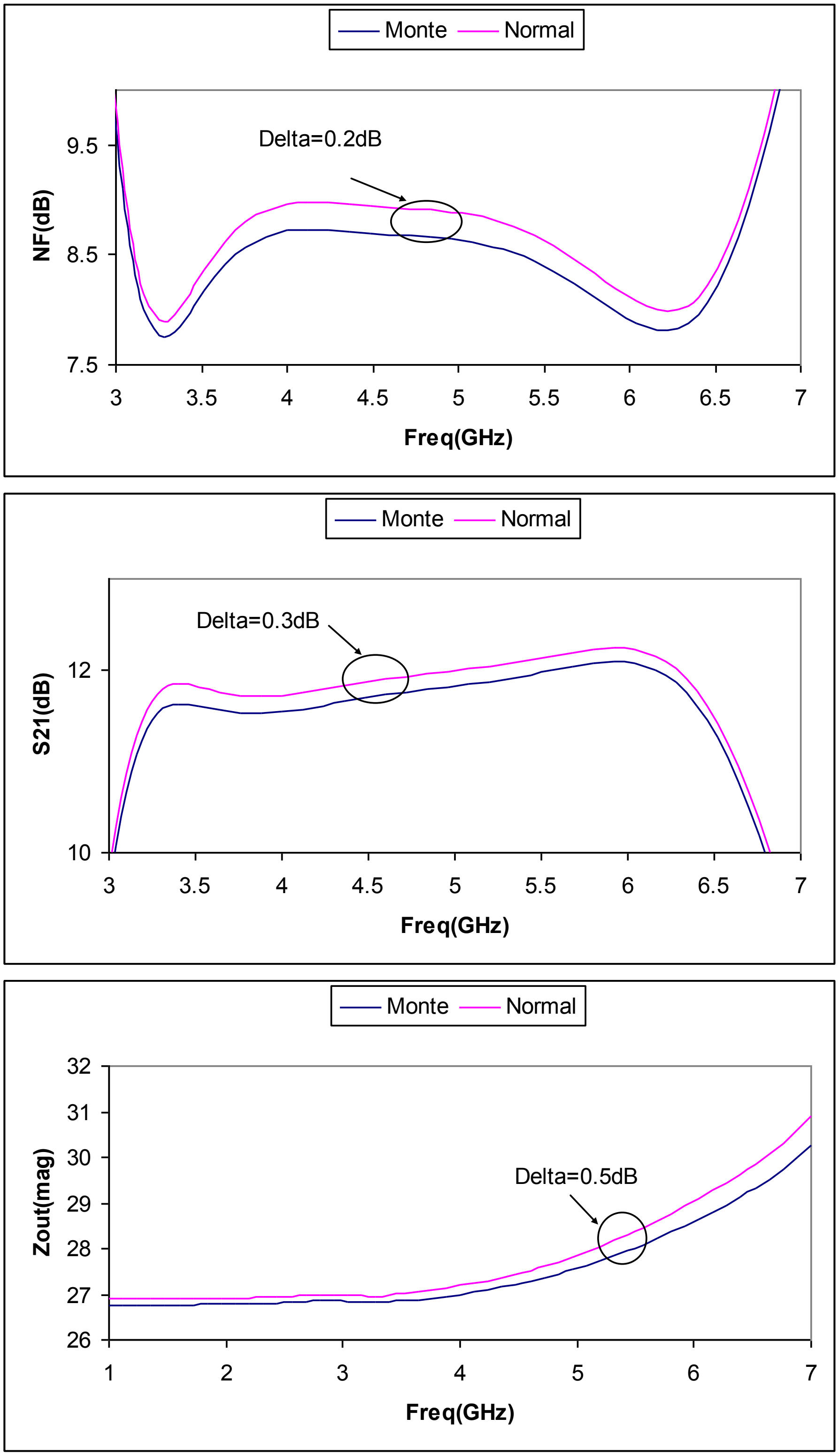

b)

Fig. 3.38: Monte-Carlo simulation results for CG-CS-UWB-LNA_ChevII with 100 iterations, a) scattering, b) average wave

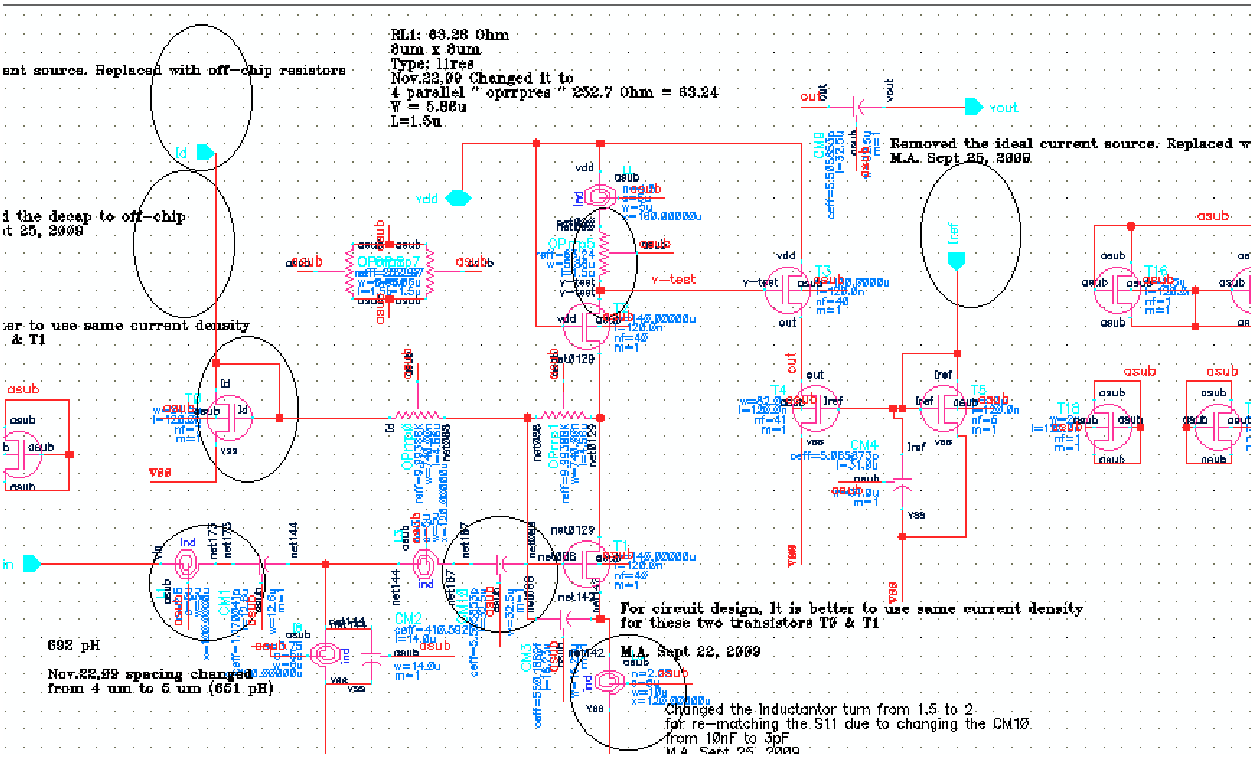

Fig. 3.39: Off/in chip schematic view (whole design)

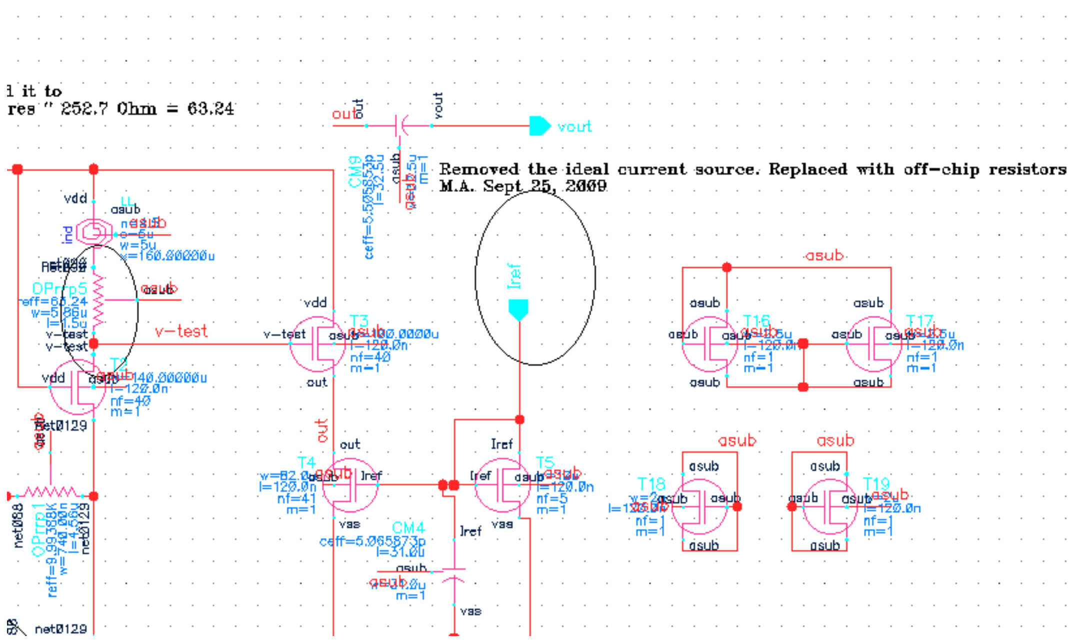

Fig. 3.40: Off chip elements view (current mirror, buffer)

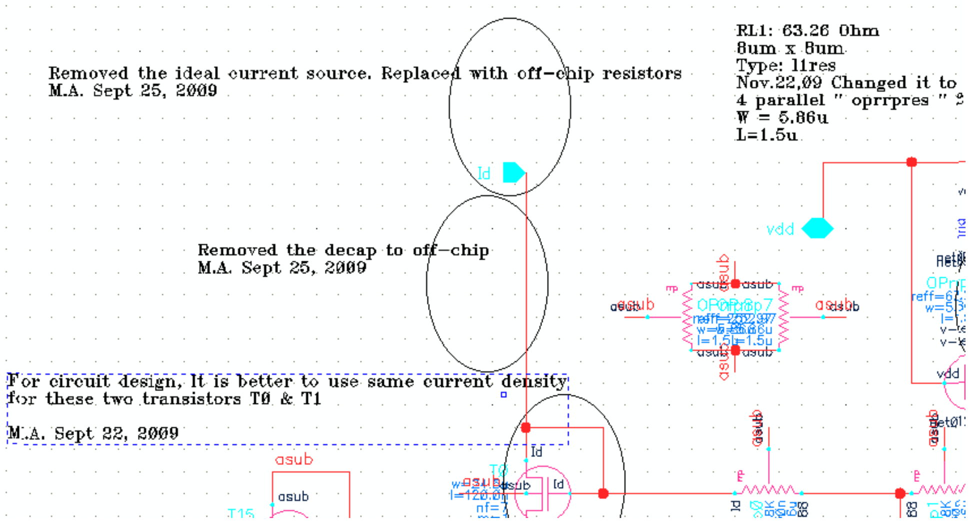

Fig. 3.41: Off chip schematic (low thermal noise resistor biasing design)
*note that small resistor is made by large parallel resistors because of noise reduction.

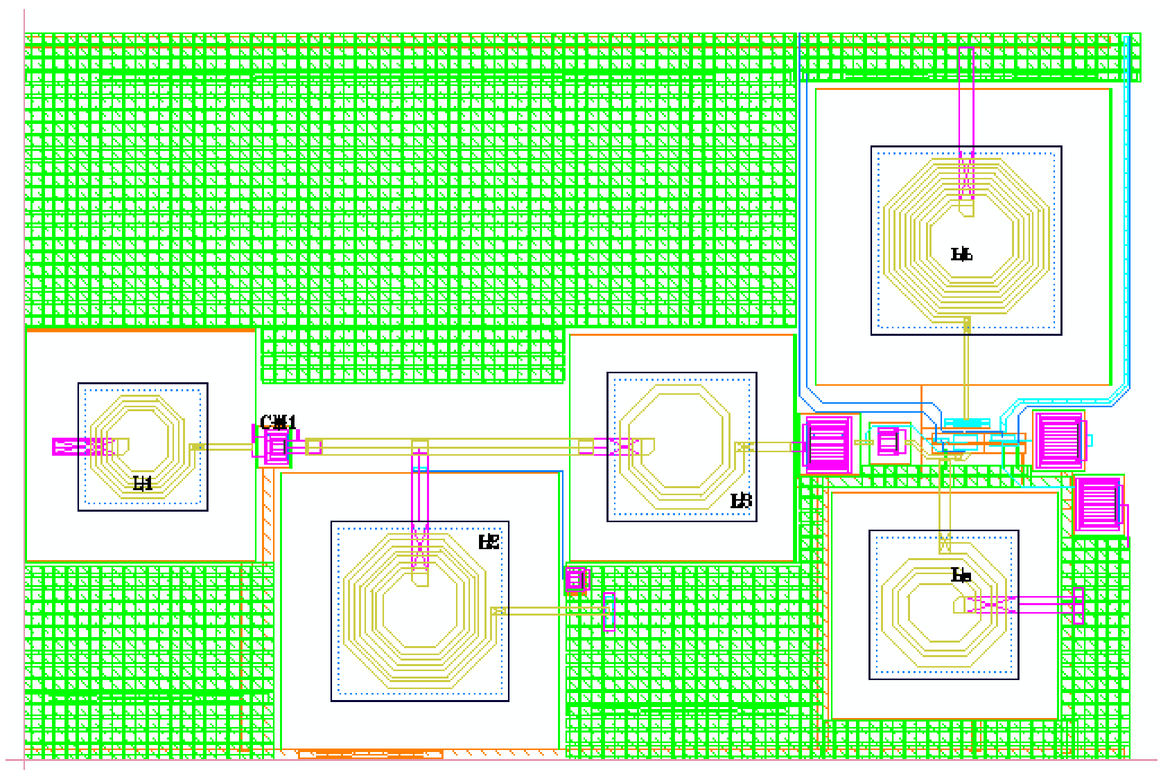

Fig. 3.42: ICBPF UWB_LNA overview layout spectrum

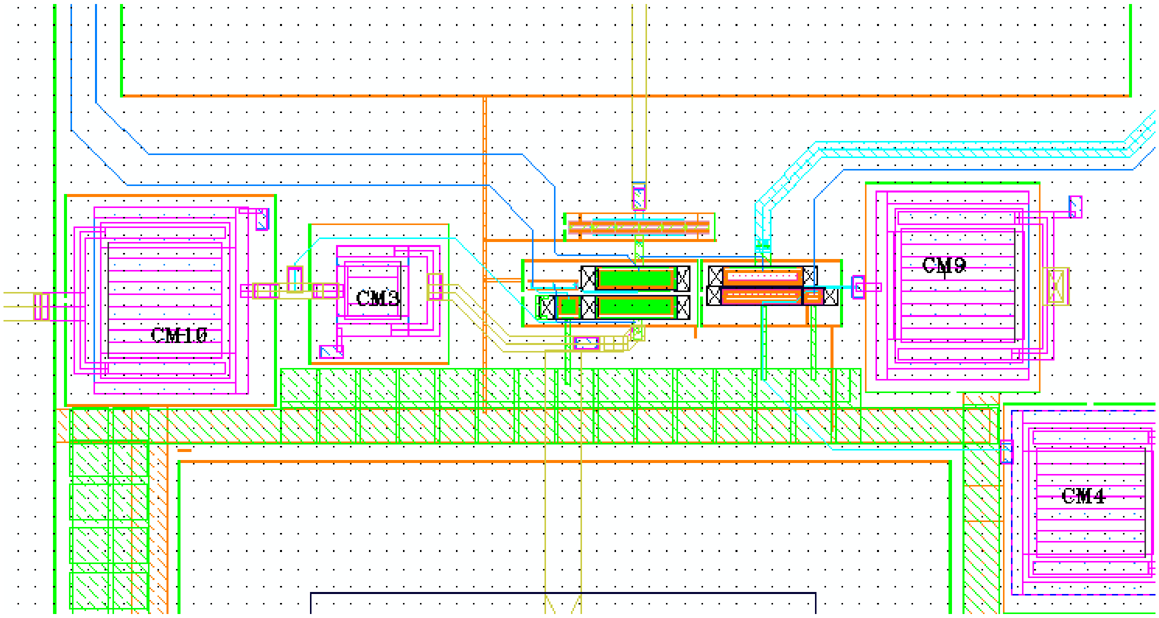

Fig3.43: Mcap (IBM-Lib) layout
*Based on noise performance, IBM-Mcap with great size has been used.

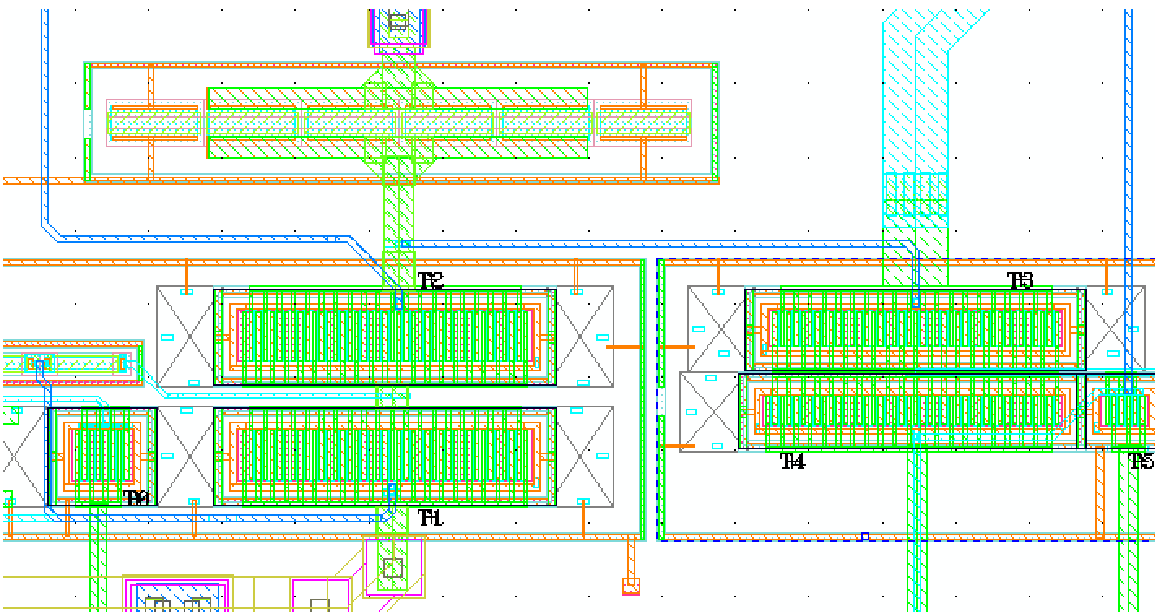

Fig. 3.44: Core- ICBF LNA transistors with corresponding fingers and layers.

3.11 General Conclusion

The CG-UWB-LNA input matching not only depends on the LNA core biasing but also still needs to meet the minimum UWB-LNA requirements. But it is very difficult to boost the gain while maintaining a reasonable noise figure. Also the biasing increases the core-LNA transistor parasitic capacitors, thus reducing the gain and increasing the noise figure even without further layout consideration. To solve this issue some boosting techniques can be used [3], [6], [7] and thus the CG-CS-UWB-LNA configuration was investigated. Further, regarding noise figure, we can deduce that there is no benefit to using the CG-CS-UWB-LNA topology for frequencies less than 10GHz. Also, its gain is lower compared to CS-UWB-LNA and needs another stage for boosting, implying even higher noise figure. In addition, the linearity was not significantly improved with the CG-CS-UWB-LNA because the linearity stage is low and the second stage gain is not so high.

On the other side, The CG-CS-UWB-LNA has better (flatter) frequency response if associated with ChevII BPF. So, the CS-UWB-LNA with ChevII BPF is finally retained. Now we need to expand our approach to multi-band UWB low-noise amplifiers.

References

[1] O. Abedi, M.C.E. Yagoub, "CS-UWB-LNA with inverse ICPF filter in 130nm CMOS," submitted to the *IET J. communications*, April 2012.

[2] Y. Shim, C.E. Kim, "Design of full band UWB common gate LNA," *IEEE Microwave and Wireless Components Lett.,* Vol. 17, No. 10, 2007.

[3] W. Zhuo, S. Shekhar, "A capacitor cross-coupled common gate low noise amplifier," *IEEE Trans. Circuits Systems*, Vol. 52, No. 12, 2005.

[4] O. Abedi, M.C.E. Yagoub, A. Abedi, "Enhanced UWB CS-LNA with inverse filter and shunt feedback resistor in 130nm CMOS," *IEEE Int. Conf. on Signals, Circuits and Systems*, pp. 1-6, 2009.

[5] H.J. Lee, D.S. Ha, S. Sang, "A 3 to 5GHz CMOS UWB LNA with input matching using miller effect," *Int. Solid-State Circuits Conf.*, 2006.

[6] P. Heydari, "Design consideration for low power ultra wideband receiver," *Int. Symp. on quality electronic design*, 2005.

[7] C. Bowick, E. Blyler, C. Ajluni, *RF Circuit Design* ,Ch. 5-6, Newnes, 2008

[8] O. Abedi, M.C.E. Yagoub, "Efficient UWB filter performance for multi-band UWB LNAs," submitted to *IEEE Communications*, July 2012.

[9] J.W.M. Rogers, C. Plett, *Radio Frequency Integrated Circuit Design*, Norwood, MA, Artech House, pp. 63-93 and pp. 141-250, 2010.

[10] C. Liao, S.I. Liu, "A broadband noise-canceling CMOS LNA for 3.1-10.6-GHz UWB receiver," *IEEE Custom Integrated Circuits Conf.,* 2005.

[11] A. Safarian, P. Heydari, *Silicon-based RF Front-End for ultra wideband radios*, Springer, pp. 3-43, 2008.

[12] B. Razavi, *RF Microelectronics,* Ch.6, pp. 185-200, 2003.

[13] G.R. Aiello, "Challenges for ultra width band (UWB) CMOS integration," *IEEE Radio Frequency Integrated Circuits Symp.*, 2003.

[14] C. Garuda, X. Cui, "A 3-5 GHz fully differential CMOS LNA with dual-gain mode for wireless UWB applications," *IEEE Int. Midwest Symp. on Circuits and Systems*, 2005.

[15] Y. Chin Lee, J. Tarng, “A low power CMOS LNA for ultra wideband wireless receiver,” *IEICE, Electronics Express,* Vol. 4, N. 9, pp. 294-299, 2007.

[16] P. Leroux, *LNA-ESD Co-Design for Fully Integrated CMOS Wireless Receivers*, Springer, Ch. 2-3, 2003.

[17] A. Ismail, A. Abidi, “A 3-10 GHz low noise amplifier with wideband LC-Ladder matching network” *IEEE J. Solid State Circuits,* Vol. 39, No. 12, 2003.

[18] A. Bevilacqua, A. Niknejad, “An ultra wideband CMOS LNA for 3.1-10.6 GHz wireless receivers” , *IEEE Int. Solid State Circuit Conf*, pp. 139-140, 2003.

[19] C. Kim, M. Kang, “An ultra-wideband CMOS low noise amplifier for 3-5-GHz UWB system,” *IEEE Journal of Solid-State Circuits*, 2005.

[20] R.C. Liu *et al*., “A 0.6-22 GHz broadband CMOS distributed amplifier,” *RFIC Symp.*, pp. 103-106, 2003.

[21] B. Chi, C. Zhang, “Bandwidth extension for ultra-wideband CMOS low-noise amplifiers,” *IEEE Int. Symp. Circuits and Systems*, 2008.

[22] M.T. Reiha, J.R. Long, “A 1.2 V reactive-feedback 3.1-10.6 GHz ultra wideband low-noise amplifier in 0.13 µm CMOS,” *IEEE Radio Frequency Integrated Circuit,* pp. 384-385, 2006

[23] Z. Hao Hsiung, W. Hui-I, “Novel wideband CMOS LNA with only an inductor as input matching network,” *TENCON,* Taipei, Taiwan, 2007.

[24] F. Bruccoleri *et al*, “Noise canceling in wideband CMOS LNA*,” Int. Solid-State Circuits Conf.*, pp. 406-407, 2002.

[25] H. Ahn, D. Allstot, “A 0.5-8.5GHz fully differential CMOS distributed amplifier,” *IEEE J. Solid State Circuits,* Vol. 37, N. 8, pp. 985-993, 2002.

[26] A. Parviz, G., Hossein “A 10GHz reconfigurable UWB LNA in 130nm CMOS” *IEEE ICSE*, pp. 751-754, 2006.

[27] B.M. Ballweber “A fully integrated 0.5-5.5 GHz CMOS distributed amplifier” *IEEE J. Solid State Circuits,* Vol. 35, pp. 231-239, 2000.

Chapter 4 Multi-Band LNA

4.1 Introduction

In the previous chapter, we evaluated different narrowband/wideband UWB-LNA topologies to find out that the CG topology is not the best candidate for frequency bands less than 10GHz due to its higher noise figure (NF) and lower gain. Thus, we proposed some approaches to improve the CG performances but with the cost of higher circuit complexity and higher power consumption. Finally, we concluded that the wideband CS-UWB-LNA configuration is the most suitable for our application.

In this chapter, we will combine this configuration with different Multiband topologies to mitigate undesired frequency bands (i.e., 5-6GHz). For this purpose we will compare different narrow-band cancellation methods to highlight the most appropriate for adequate filtering of undesired frequency bands.

4.2 NBI Cancellation Methods

4.2.1 Tunable notch filters

Tunable notch filters (Fig. 4.1) present some advantages such as second harmonic cancellation and perfect input matching but suffer from major disadvantages like:

- Higher circuit complexity due to the number of notch filters to be used for NB cancellation,
- Complex design. In fact, the differential topology makes layouts much difficult to design,
- Higher power consumption and higher noise figure due to the higher circuit complexity,
- Higher number of inductors.

Therefore, they cannot be a good candidate for our purpose. In fact, it has been demonstrated that using a bank of filters to reject the undesired bandwidths is not efficient if the noise is a white noise [1].

Figure 4.1.a shows a modified differential multi-band 3-7GHz LNA and Fig. 4.1.c shows its power gain in the desired bandwidth [1]. Note that this design was not performed for the whole UWB bandwidth but just for the first bandwidth (Orthogonal frequency-division multiplexing - OFDM - modulation purposes). Figure 4.1.b shows a modified shunt feedback of a multi-band UWB LNA (MB-UWB-LNA) for OFDM applications.

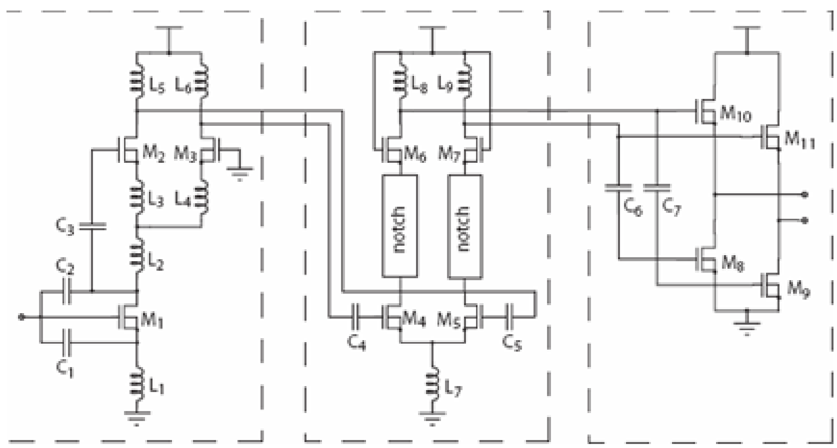

a)

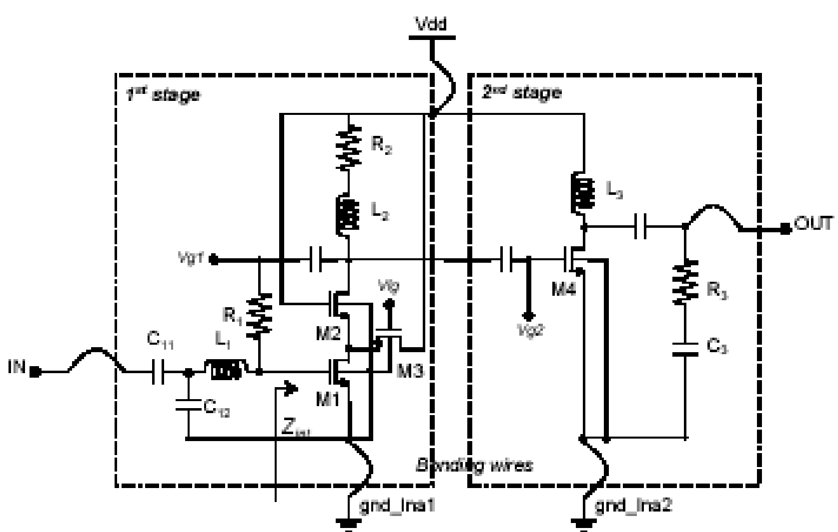

b)

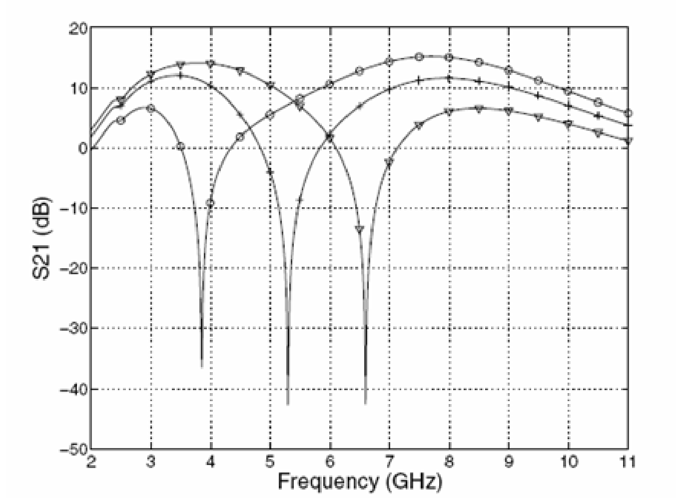

c)

Fig. 4.1: OFDM UWB-LNA, a) MB notch filter (3-7GHz) [1], b) MB modified shunt feedback [2], c) tunable notch filter gain [1]

4.2.2 Frequency Q-tunable notch filters

These filters have similar performance as bank notch filters but are not suitable for our purpose due to their circuit complexity, power consumption, and gain response [3] (Fig. 4.2).

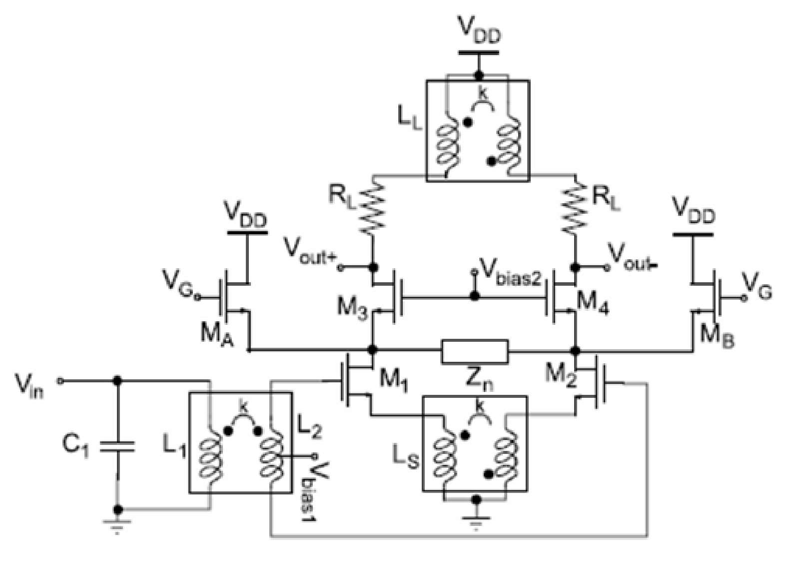

a)

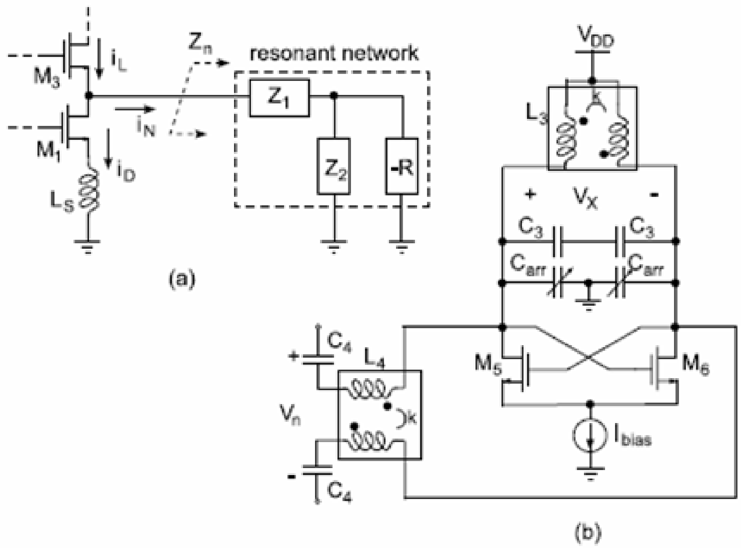

b)

Fig. 4.2: Bridge T-band and Q-tunable notch filter [3].

4.2.3 Multiband OFDM

Orthogonal frequency-division multiplexing (OFDM) is a well-known orthogonal modulation technique to improve wireless system bit error rate (BER). To achieve better performance, the multiband (MB) method should be combined with this modulation. The simplicity of this method is considerable so that it can easily mitigate undesired wide- or narrow-bands. Also this method has different possible topologies depending on bandwidth and initial requirement. In fact, if for instance the undesired bandwidth is narrowband, the design will be a simple combination of “BPF + SBF”. However, if the bandwidth is wider, a bridge T-band or notch filter along with a load tank design (parallel/series resonance) will be a better candidate (Note that the load tank design could be seen as a simple MB-OFDM approach, but the filter design flexibility will be very limited due to parasitic capacitors and power gain frequency response).

To get better frequency response and increased Q, most of existing designs use a series inductor. Note that the load inductor value is critical since it deals with signal boosting and reduces the impact of next stage parasite capacitors.

However, as shown in Fig. 4.3, the power gain frequency response is not flat. In addition, we get a higher noise figure due to the CG topology (NF > 7dB).

4.2.4 Super regeneration filters and digital filter banks

This approach, which uses analog and digital filters, not only has higher number of elements but also requires higher power consumption. In fact, all depends on the type of noise: using filter banks is inefficient in the presence of white noise but beneficial with color noise [5]. Since most commercial RF simulation tools assume white noise this approach cannot be suitable for our design. Multiband UWB approaches combine a BPF and a SBF as input matching to get both high and low reflection coefficients in desired and undesired bandwidths, respectively. Note that there exist some tunable configurations (like CS-CG LC ladder or modified shunt-feedback) that present reasonable performance [1], [6] as summarized in Tables 3.3 and 3.6.

4.3 Proposed MB-UWB-LNA

In Fig. 4.4, we propose a MB-UWB-LNA which combines a 3rd order ChevII as BPF and a 1st order SBF. As mentioned, the circuit simplicity with respect to initial requirements is the main target we considered in this design.

As shown, the SBF topology can be parallel or series (adding a serial element at the input or a parallel element before the output buffer). The next step was to investigate the performance of the proposed configuration with respect to power consumption, complexity and linearity, for both desired (3-5GHz and 6-7GHz) and undesired bandwidths (5-6GHz).

4.3.1 Input matching impedance

As shown in Fig. 4.5, the ChevII-Hourglass combination presents the better frequency response and the higher stop bandwidth as well as an excellent matching in the entire desired pass-band (3-5, 6-7 GHz).

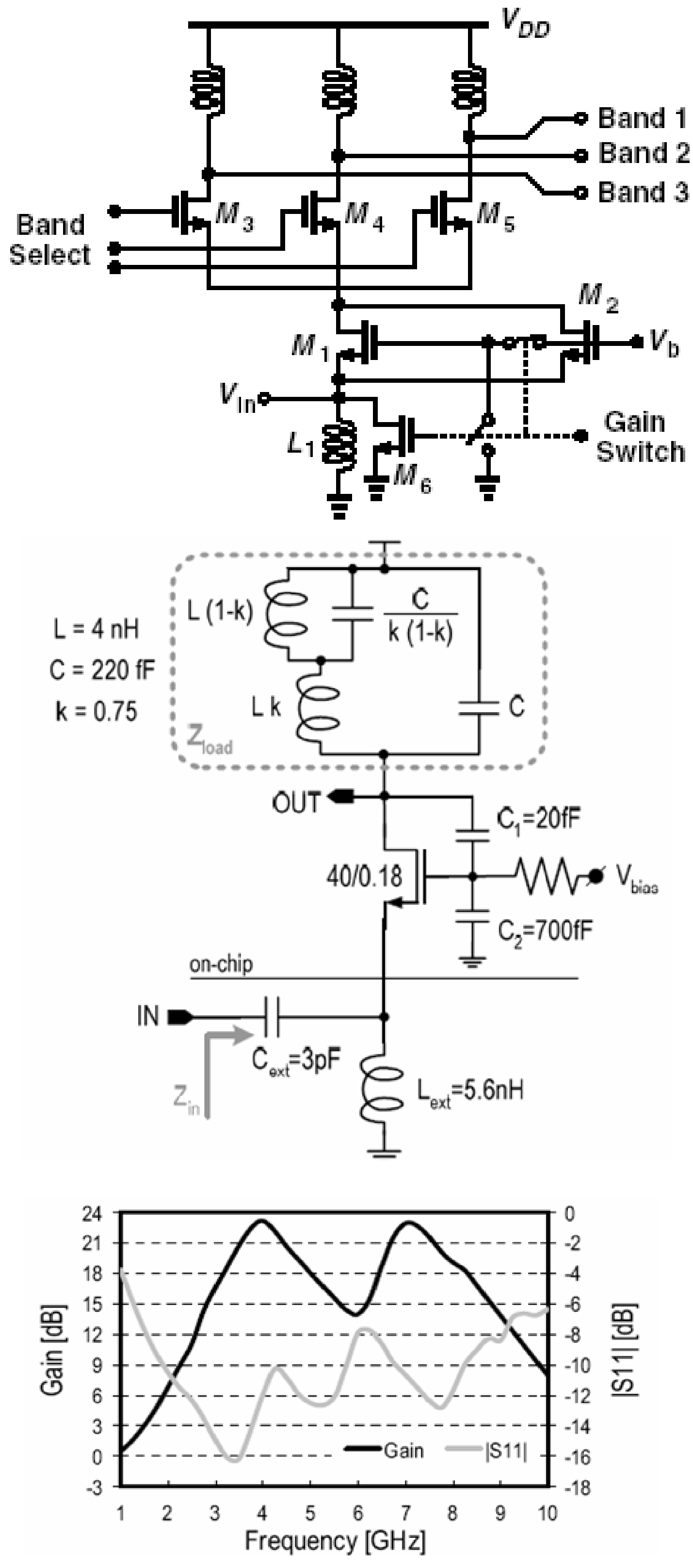

Fig. 4.3: MB-OFDM-UWB-LNA schematics with corresponding S-parameters [4]

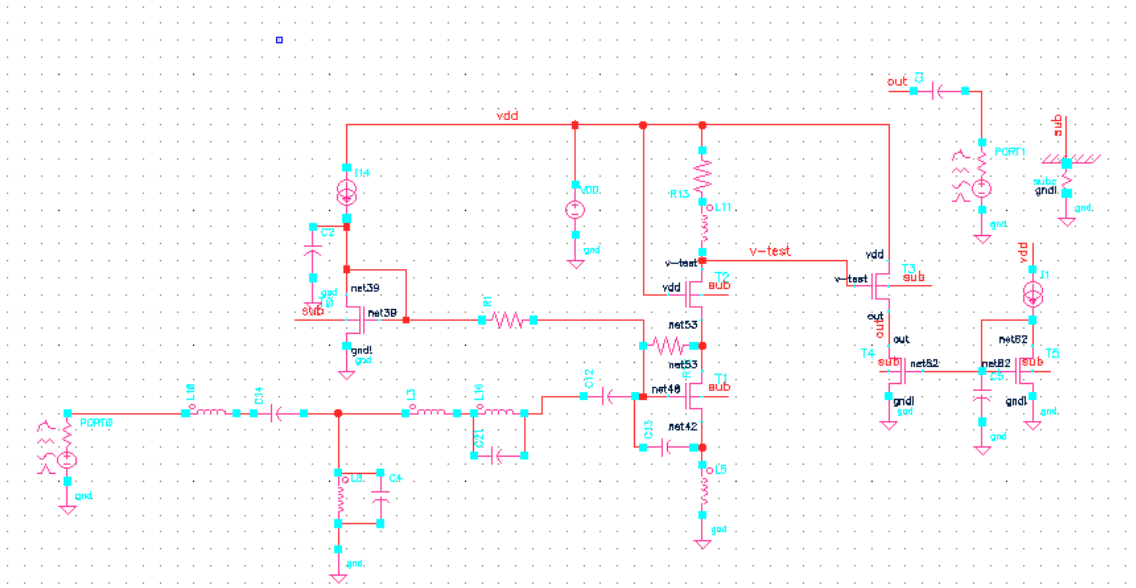

Fig. 4.4: MB-UWB-LNA with a combination of BPF ChevII and various SBF.

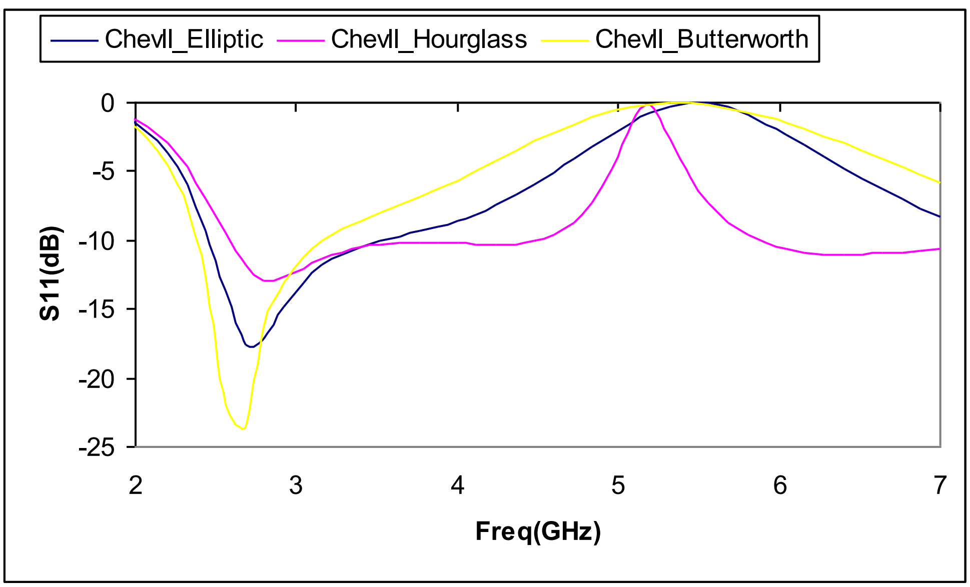

Fig. 4.5: MB-UWB input matching with combination of BPF ChevII and various SBF.

Note that the ChevII-Elliptic arrangement exhibits better matching at the lower part of the bandwidth but a poor input matching frequency response. Note also that the rest of SBFs we investigated earlier were not presented here due to their lower performance.

We have two solutions to increase the SB bandwidth: increase the filter order or use a combination of parallel/series SBF (series with the input and parallel with the buffer).

4.3.2 MB-UWB-LNA gain

Figure 4.6 shows the gain of the MB-UWB-LNA with various SBF. As expected from the matching results, the ChevII/hourglass has acceptable gain. In fact, better input matching leads to better gain frequency response. It also has maximum stop-bandwidth (SBW > 500MHz, Fig. 4.6) and reasonable stop band rejection. On the other hand, the ChevII/Butterworth has maximum SBW and highest rejection but, as we expected due to poor input matching, its gain frequency response is not acceptable. Finally, the ChevII/elliptic has an excellent frequency response but lower SBW and bandwidth rejection (<12dB) thus, does not satisfy our requirements. Again, the combination of ChevII/Hourglass is the best candidate.

4.3.3 MB-UWB-LNA noise figure

Fig. 4.7 shows the MB-UWB-LNA noise figure while combined with different SBF. In terms of performance, the Elliptic SBF exhibits the best noise figure in the whole desired frequency band (in the range of 1.5-2.6dB) but the hourglass SBF not only satisfy the NF requirement (1.5-4dB) but has also better performance in matching and gain.

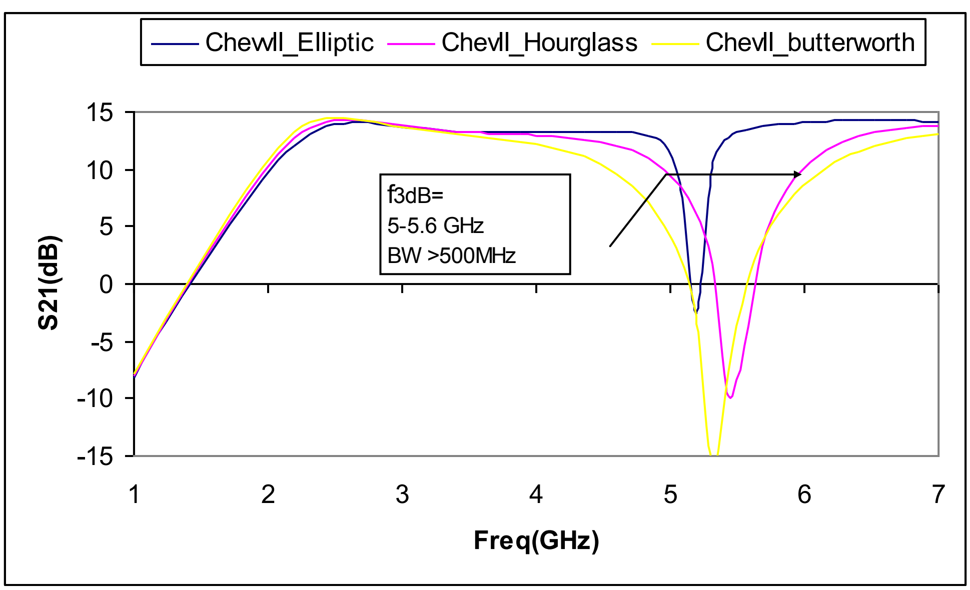

Fig. 4.6: MB-UWB gain with ChevII BPF and various SBF.

To further confirm our conclusions, we simulated the filters with higher orders and again the hourglass SBF still presents the best performance in terms of SBW and stop-band rejection.

4.3.4 MB-UWB-LNA Isolation

As expected, the isolation is almost independent to input matching due to the cascade topology, Fig. 4.8.a. Note that if the biasing is not perfectly chosen (i.e, smooth saturation) the isolation will be more sensitive to input matching [3], [7]. Also, as already explained, the output matching is not affected by any SBF combination (Fig. 4.8.b).

4.3.5 MB-UWB-LNA Linearity

Figure 4.9 shows that the ChevII/Butterworth combination presents the lowest linearity (>-20dB) while the Hourglass has a higher linearity (>-8dB). By adding the expected degradations associated to layout/fabrication, we assumed same performance for both hourglass and elliptic, i.e., >-11dB. Therefore, the combination ChevII-Hourglass will be the best candidate.

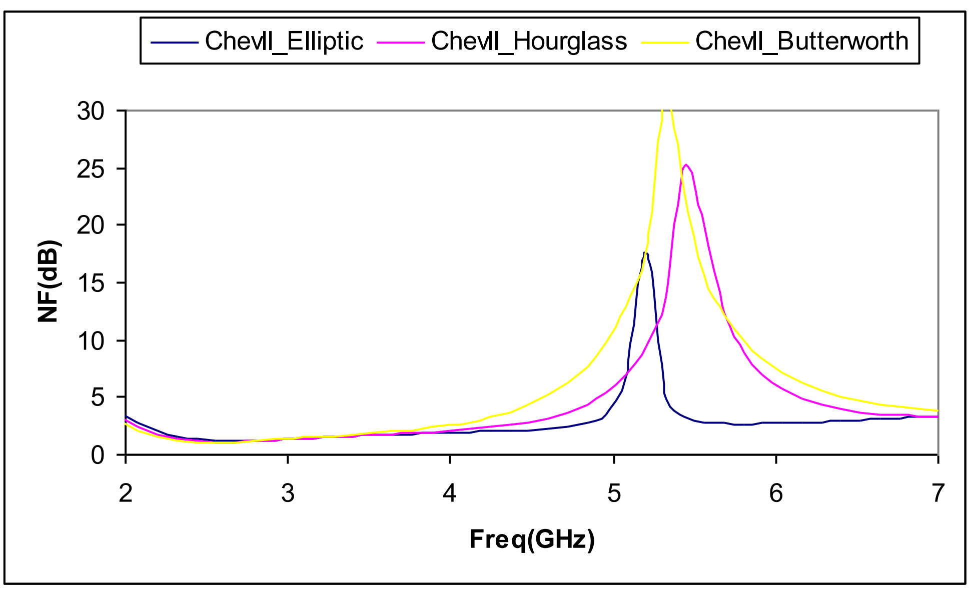

Fig. 4.7: MB-UWB noise figure comparison using various filter combination.

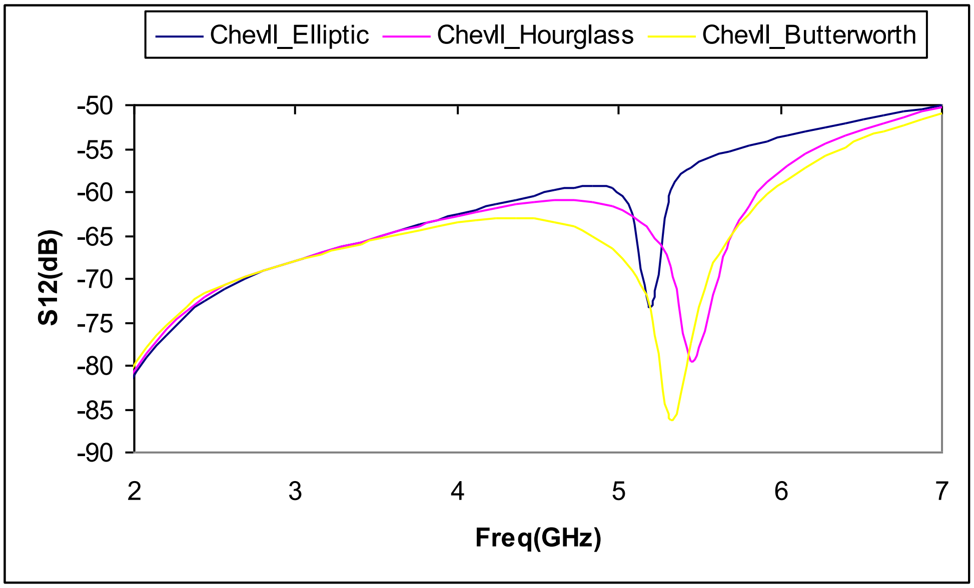

a)

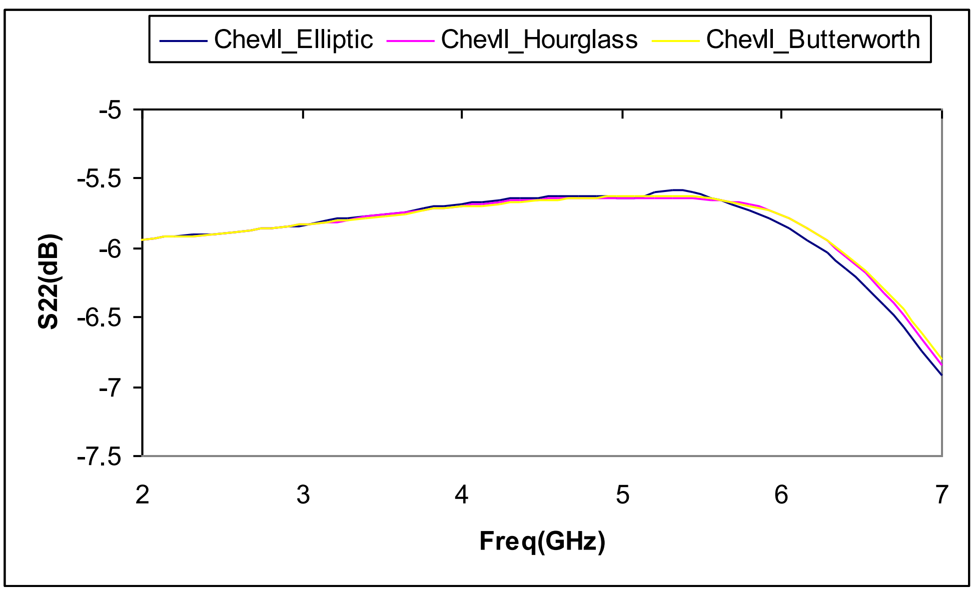

b)

Fig. 4.8: MB-UWB a) isolation, b) output matching comparison for various filter combination.

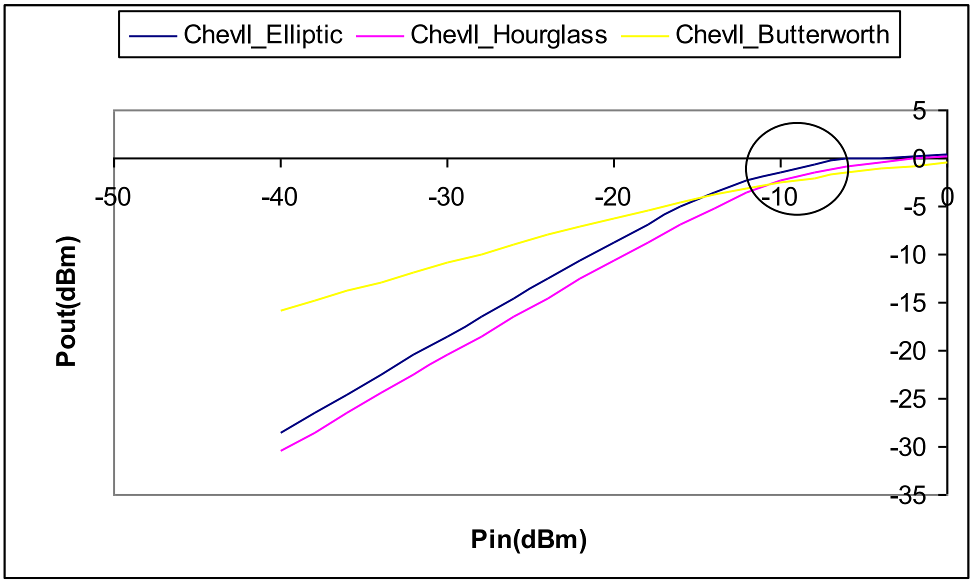

Fig. 4.9: MB-UWB linearity comparison for various filters combination.

4.3.6 Monte-Carlo simulation for MB-UWB-LNA with ChevII-Hourglass

We performed a Monte-Carlo analysis to evaluate the circuit stability vs. the parameter tolerances. Note that the Monte-Carlo simulation has been set to 20% for all active and passive parameters with a rate of 10 (average of 10 simulations).

As illustrated in Fig. 4.10, the gain, noise figure, and isolation have low sensitivity to component tolerances. Note that the performance of the CG configuration is worse than that of the CS, especially for input matching, a critical point in LNA design.

Also Fig. 4.10 shows that the CS matching has 13% to 15% error in the bandwidth of interest (i.e., -15dB to -13dB). This error is acceptable since even in the worst case scenario, S_{11} is still below -9dB, therefore satisfying the multi-band input matching requirements. Table 4.1 shows a comparison of the S-parameters of CheII-hourglass, chevII-Elliptic and ChevII-butterworth circuits. As mentioned, the ChevII BPF has been finally chosen. Note that the S_{22} parameter is almost independent on the input matching, so it was not included in the simulations.

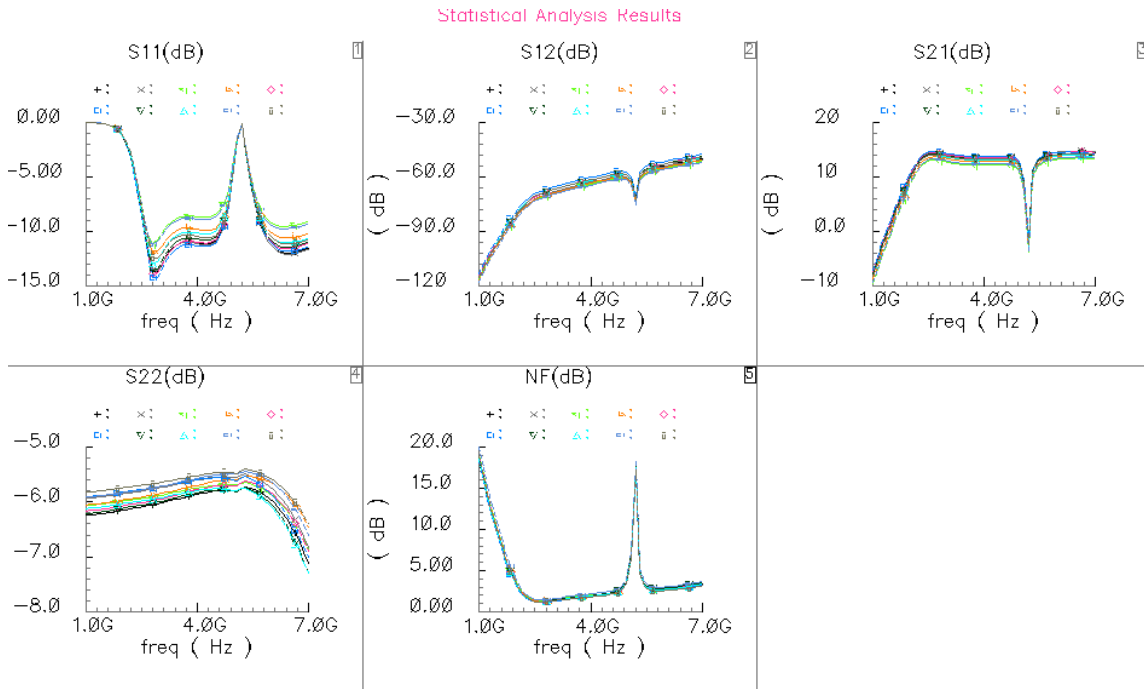

Fig. 4.10: Monte-Carlo MB-UWB-LNA with ChevII-Hourglass: a) S-parameters and b) noise figure

Table 4.1: MB-UWB-LNA parameters for
BW1: 3-5 GHz, BW2: 5-6 GHz, BW3: 6-7GHz

	ChevII-Hourglass			ChevII-Elliptic		
	BW1	BW2	BW3	BW1	BW2	BW3
S_{11} (dB)	10-11.3	0-6	10-10.7	5-15	1-1.5	3-7
S_{21} (dB)	11.6-13.4	6-8	7.8-13.7	13-13.4	8.6-14	14-14.1
S_{12} (dB)	66-68	58-86	56-58	66-68	58-89	56-58
NF (dB)	1.4-5	4.3-25	4-4.6	1.4-3.3	3.4-17	2.7-3.4
1dB (dBm) @5GHz	<-8	<-8	-8	<-11	-<11	-11

	ChevII-Butterworth		
	BW1	BW2	BW3
S_{11} (dB)	1-11	0.6-1	2-5
S_{21} (dB)	4.1-13.4	4.2-9.1	10-13
S_{12} (dB)	66-67	58-86	50-58
NF (dB)	1.4-9	9-30	7.1-9
1dB (dBm) @5GHz	<-20	<-20	-20

4.4 Proposed MB-UWB-LNA with ChevII-Hourglass

4.4.1 Topology comparison

In this section, we compared the shunt and series topologies of the proposed MB-UWB-LNA circuit while combining the ChevII-Hourglass filters. As shown in Figs. 4.11-4.12, the series topology involves less passive elements than the shunt topology. Also, the input matching in series topology is independent on the output and the isolation but on the other side not only the input/output matching are highly dependent to the biasing but also the gain frequency response is limited by the parallel resonance of the output tank. This resonance caused a lower power gain at some particular frequencies. To mitigate this issue, increasing the circuit (filter) inductance could be the solution but this will imply higher power consumption [8]. In conclusion the parallel hourglass SBF fails by default.

4.4.2 Input matching (S_{11})

Figure 4.13 shows a comparison of the desired input matching vs. the input/output performance of series/parallel hourglass SBFs while used in the MB-UWB-LNA. As shown, the shunt/series topology with an hourglass stop-band connected between the cascade network and the buffer presents an excellent matching response not only in the whole desired bandwidth but also in the undesired bandwidth. It is interesting to note that the excellent matching in the undesired bandwidth does not affect its power gain.

4.4.3 Gain

Figure 4.14 illustrates the SB-hourglass performance with series and shunt/series topologies. For the input SB series, the gain has better frequency response, higher SBW and lower passive elements size. Also, in the shunt/series topology, Fig. 4.12, the inductor size is almost 15nH, making its layout implementation unrealistic.

On the other hand, the parallel/series has lower gain in the desired bandwidth even with higher order (parallel) or higher element size. Note that we assumed a stop band rejection of -15dB for all topologies.

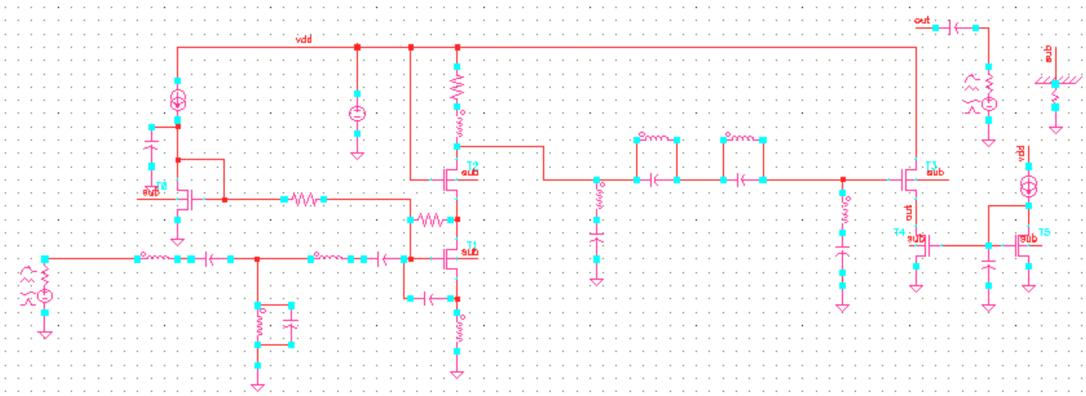

Fig. 4.11: MB-UWB-LNA with the ChevII/Hourglass shunt-out structure

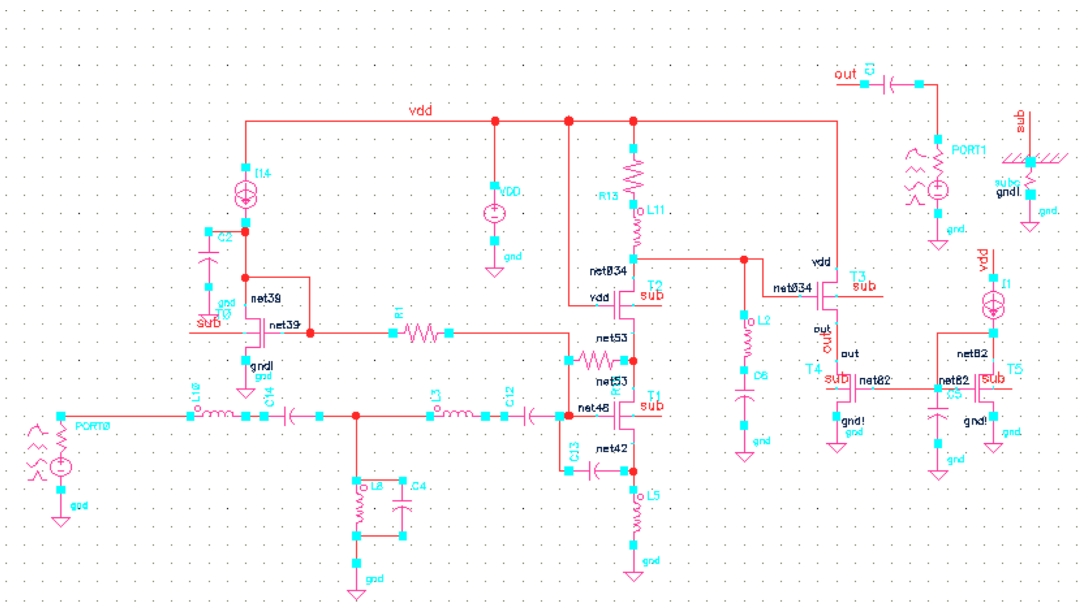

Fig. 4.12: MB-UWB-LNA with the ChevII/Hourglass series topology

4.4.4 Isolation

As well-known, the isolation due to a cascade configuration is not a significant issue but we confirmed that through simulations. As shown in Fig. 4.15, there is more isolation with the hourglass (series topology) especially in the undesired frequency bandwidth (5-

6GHz), which confirms the advantage of this topology (input series) compared to the SB series/ parallel output configuration.

Also, as expected, there is no significant change in the undesired bandwidth for the parallel/series topology, thus exhibiting a relatively constant isolation in the whole bandwidth. On the other hand, the input SB series has higher isolation, thus agreeing with the specifications.

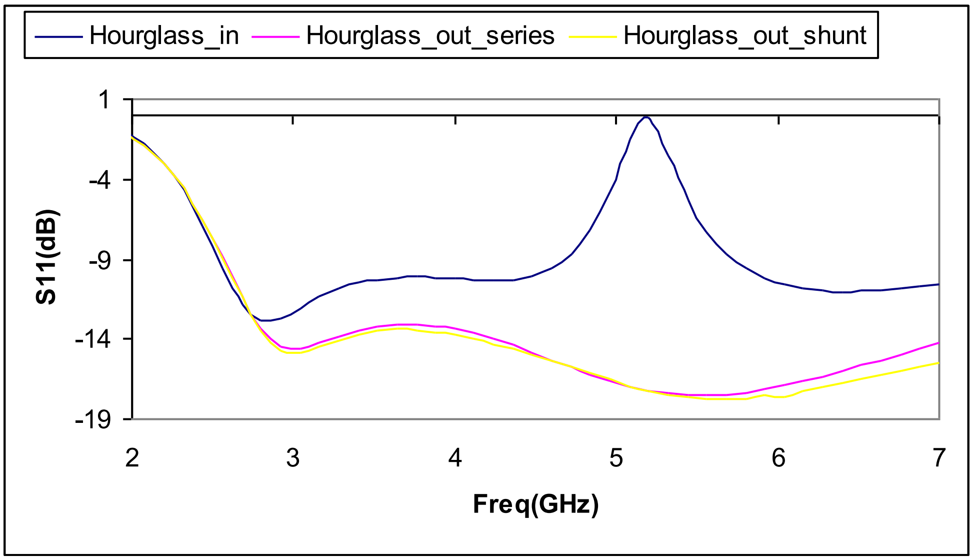

Fig. 4.13: MB-UWB-LNA input matching in series and shunt/series topology.

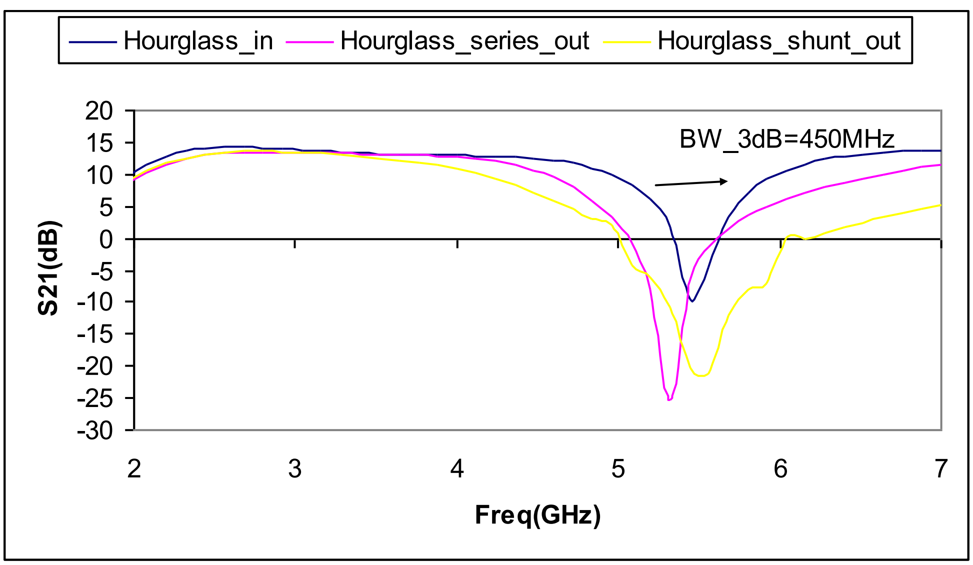

Fig. 4.14: MB-UWB-LNA gain in series and shunt/series topology.

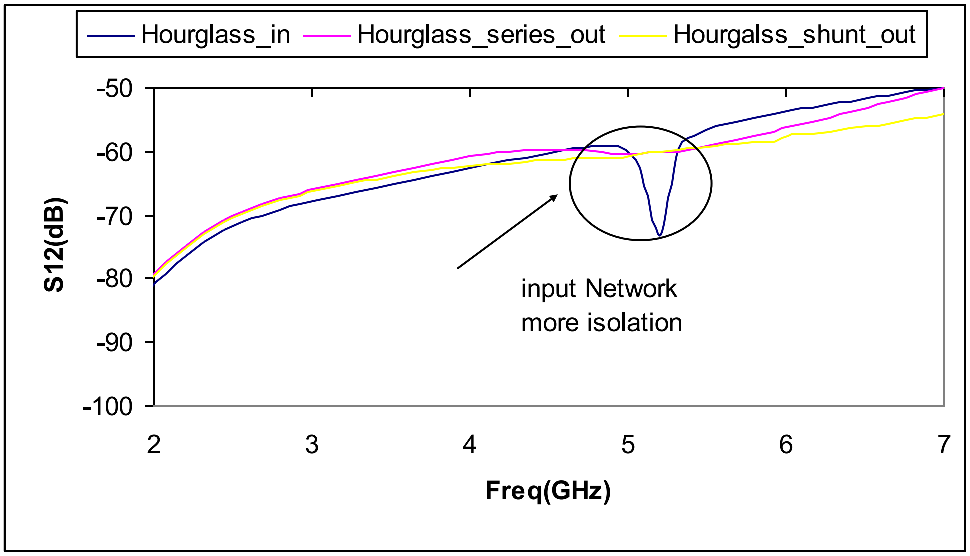

Fig. 4.15: MB-UWB-LNA isolation in series and shunt/series topology.

4.4.5 Noise figure

Figure 4.16 shows that the hourglass output series topology exhibits lower noise figure (NF<1.9-3.3dB). On the other side, the input series topology has a reasonable noise figure (1.6<NF<4.5dB).

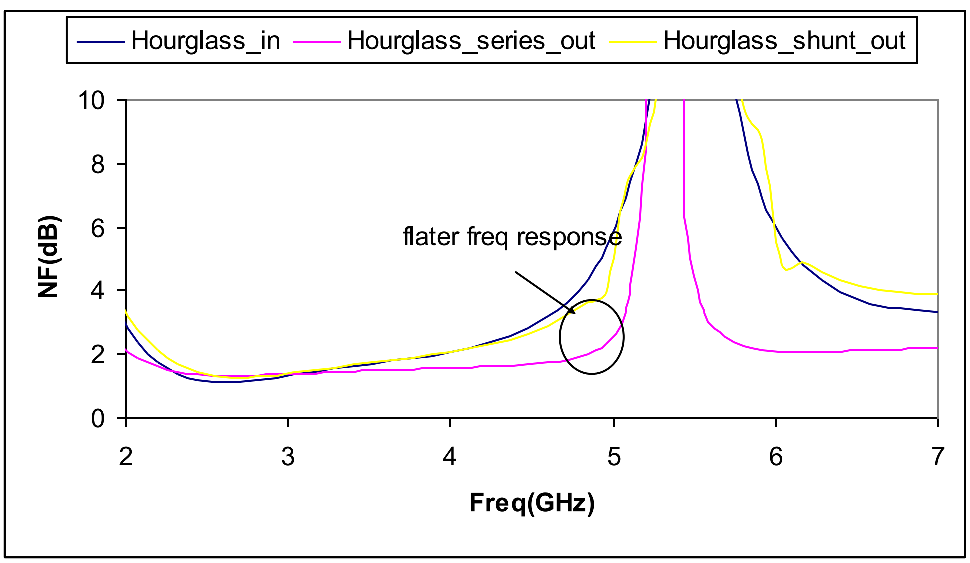

Fig. 4.16: MB-UWB-LNA noise figure in series and shunt/series topology.

4.4.6 Linearity

Figure 4.17 clearly shows that the input series matching decreases the linearity. The reason may be because of the effect of the first stage (C_{gs}).

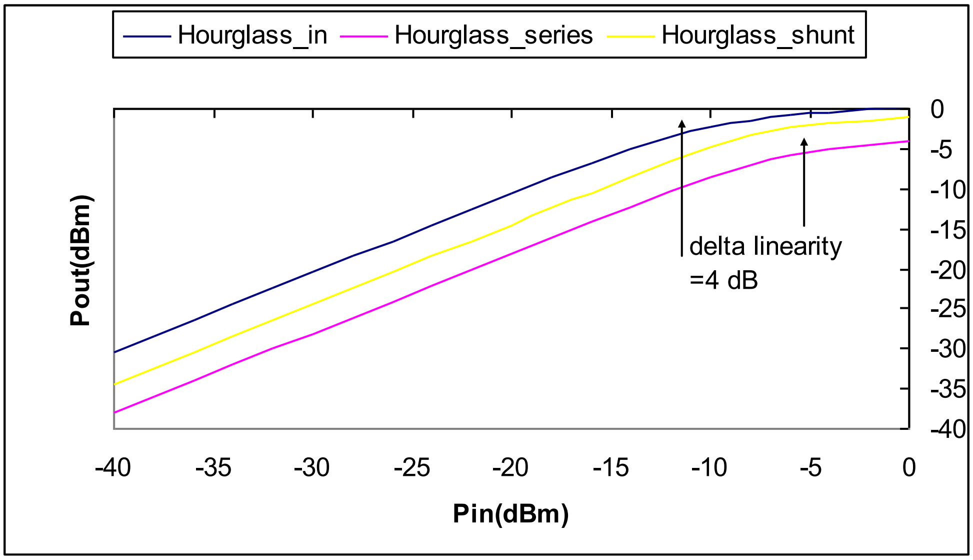

Fig. 4.17: MB-UWB-LNA linearity in series and shunt/series topology.

4.4.7 Monte-Carlo simulation

As illustrated in Fig. 4.18, the circuit presents excellent performance in terms of gain, isolation, and noise figure even with 20% passive parameters tolerances. Note that even if the noise figure varies by almost 15%, it is still within the desired specifications.

Table 4.2 shows a comparison between the proposed circuit and existing MB configurations. To summarize, we can conclude that:

- NF: the proposed topology has the lowest NF in the desired bandwidths (3-5GHz and 6-7GHz).
- S_{11}: the proposed circuit not only satisfy the input matching requirement (<-10dB) but also presents the lowest power consumption. Only the designs published in [1] and [4] have better performance but at the price of higher power consumption (at least five times higher).

- S_{21}: again by considering the power consumption, the proposed design has the best power gain with only 1dB difference in the whole bandwidth while other designs have 5-10dB gain difference.
- Linearity: The proposed design exhibits an IIP3 of +2dB, far better than other designs.

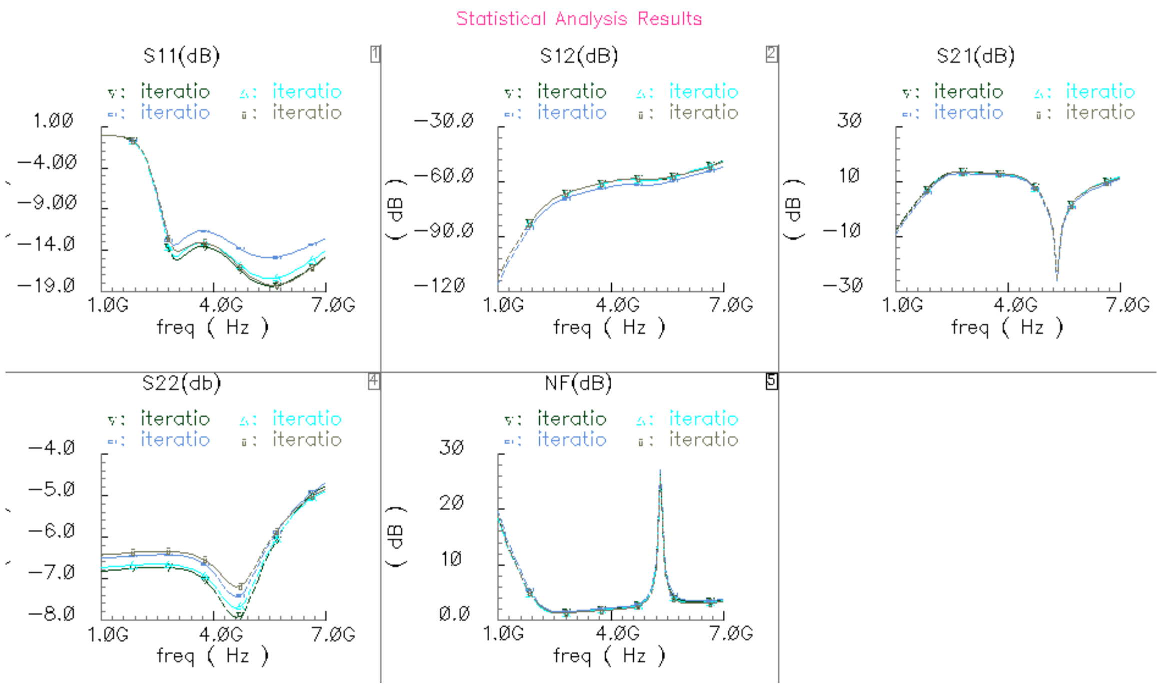

Fig. 4.18: Monte-Carlo MB-UWB ChevII-Hourglass output series: S-parameters and NF.

4.5 Conclusion

In this chapter, an efficient MB-UWB-LNA circuit has been designed with an input series ChevII-hourglass SBF. Note that the series output topology not only has an unacceptable large inductor but also has limited voltage room, leading to lower linearity. Similarly, the parallel hourglass topology contains more passive elements with lower linearity. Some other UWB-LNA design for NBI cancellation have been investigated, [11]-[13], and not retained due to our particular design targets namely, topology simplicity and power consumption consideration.

The next step is to further investigate the constraints designers should consider while dealing with UWB systems.

Beside the RF part, the signal characteristics (shape, duration, delay, …) as well as the channel properties, the noise environment, …, should be considered.

Table 4.2. Performance Comparison of MB-UWB-LNA

Ref.	NF (dB)	S_{11} (dB)	S_{21} (dB)	BW (GHz)	IIP3 (dBm) @ 5GHz	Topology	P_{dc} (mW)
[1]^{m}	3-8	14-20	9-13	3-10	N/A	Notch filter	36mw
[4]^{m}	5-7.2	6-16	20-22	3-8	-3 to -3.3	Double-band (tank)	20mw
[9]^{s}	7.5	< -10	10-15	3.1 – 4.8	-3	CS LC Ladder	30mw
[10]^{s}	4.2-7.7	8-16	15-24	3-10	-3.1	Double-band (tank)	9mw
[2]^{m}	2.5-5	<-7.5	17	2-5	-3	Shunt feedback	18mw
Proposed design^{s}	**1.4-5**	**10-11.3**	**11.6-13.4**	**3 -7**	**+2 @ 5GHz**	**CS_MB_LC-Feedback**	**6.5mw**

m: measured data, s: simulated data

Note that, cadence IBM-130nm processing kits has accurate kits but with limited passive components libraries, e.g., low values of carbon resistors are not available, so parallel high resistance method to get low desired value has to be used. This issue is also valid for for M-cap capacities as well.

References

[1] K.A. Townsend, L. Belostotski, J.W. Haslett, J. Nielsen, "Ultra-wideband front-end with tunable notch filter," *IEEE North-East Workshop on Circuits and Systems,* pp. 177-180, 2006.

[2] K.W. Wong, A. Arasu, W. Chan, "A 90-nm CMOS LNA for MB-OFDM UWB in QFN package" *IEEE Radio Frequency Integrated Circuits Symp.*, pp. 497-500, 2008.

[3] S. Bagga, S.A.P. Haddad, K. Van Hartingsveldt, "An interference rejection filter for an ultra-wideband quadrature downconversion autocorrelation receiver," *IEEE Int. Symp. on Circuits and Systems,* pp. 5357-5360, 2004.

[4] G. Cusmai, M. Brandolini, P. Rossi, F. Svelto, "An interference robust 0.18μm CMOS 3.1-8GHz receiver front-end for UWB radio" *IEEE Custom Integrated Circuits Conf.,* pp. 157-160, 2004.

[5] M. Anis, S. Tontisirin, R. Tielert, N. Wehn, "A 3mW 1GHz ultra-wide-bandpass super-regenerative filter" , *IEEE Radio and Wireless Symp.,* pp. 455-458, 2008.

[6] B. Razavi, T. Aytur, C. Lam, F.R. Yang, "Multiband UWB transceivers," *IEEE Custom Integrated Circuits Conf.,*pp. 141-148, 2006.

[7] R. Roovers, D.M.W. Leenaerts, J. Bergervoet, K.S. Harish, "An interference-robust receiver for ultra-wideband radio in SiGe BiCMOS technology," *J. IEEE solid-State Circuit,* pp. 2563-2572, 2004.

[8] A. Safarian, Z. Lei, P. Heydari, "A Distributed RF Front-End for UWB Receivers," *IEEE Custom Integrated Circuits Conf.,* pp. 805-808, 2007.

[9] J. Bergervoet, K. Harish, G. van Der Weide, "An interference robust receive chain for UWB Radio in SiGe BiCMOS," *Solid-State Circuits Conf.,* pp. 200-593, 2004.

[10] G. Cusmai, M. Brandolini, P. Rossi, F. Svelto, "A 0.18-μm CMOS selective receiver front-end for UWB applications," *J. IEEE Solid-State Circuits,* pp. 1764-1771, 2006.

[11] H. Khatri, P.S. Gudem, L.E. Larson, “Integrated RF interference suppression filter design using bond-wire inductors,” *IEEE Trans. Microwave Theory Tech.,* pp. 1024-1034, 2008.

[12] M. Rahnama, Y.M. Gilmalek, A.M. Kordalivand, “Ultra wide-band LNA using RFCMOS technology and tunability band with neural network,” *IEEE Control and System Graduate Research Colloquium*, pp. 75-79, 2010.

[13] T.W. Fischer, B. Kelleci, S. Kai, A.I. Karsilayan, E. Serpedin, “An Analog Approach to Suppressing In-Band Narrow-Band Interference in UWB Receivers,” *IEEE Trans. Circuits and Systems*, pp. 941-950, 2007.

Chapter 5 IR-UWB System Background

5.1 Introduction

UWB receiver design is more complicated than other narrowband systems, and thus requires receiver design techniques to recover the low power signal from noise. UWB systems may be divided into impulse radio (IR) and multi-band systems.

The goal of this chapter is to provide the reader with some important aspects associated with IR-UWB receiver multipath combination methods like rake receiver and general matched filter (GMF) [1]. Also, the characteristics of an UWB transmitted signal with different pulse shapes and modulation schemes, as well as the characteristics of a typical indoor radio channel and its effects on the UWB transmitted signal will be discussed.

5.2 UWB transmitted signal and modulation schemes

Many different pulse generation techniques may be used to satisfy the requirement of an UWB signal [2], [3]. UWB systems are based on impulse radio concepts. Any given pulse will have very low energy because of the very low power levels permitted for typical UWB transmissions. Therefore, many pulses are combined to carry the information for one bit. The most common modulation schemes are based on time-hopping pulse position modulation (TH-PPM), direct sequence pulse amplitude modulation (DS-PAM) and multiband UWB [4].

5.2.1 TH-UWB signals

An UWB signal can be generated using the setup shown in Fig. 5.1. The quantities in the figure will be explained sequentially.

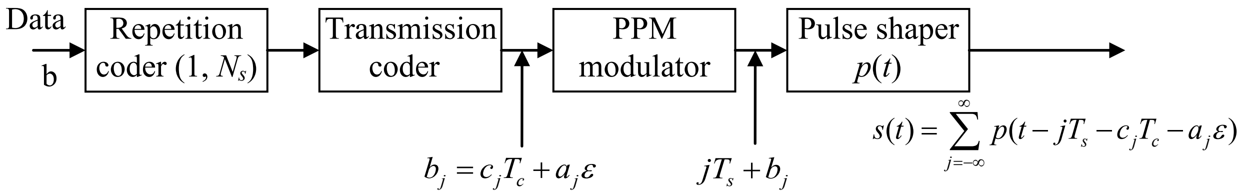

a)

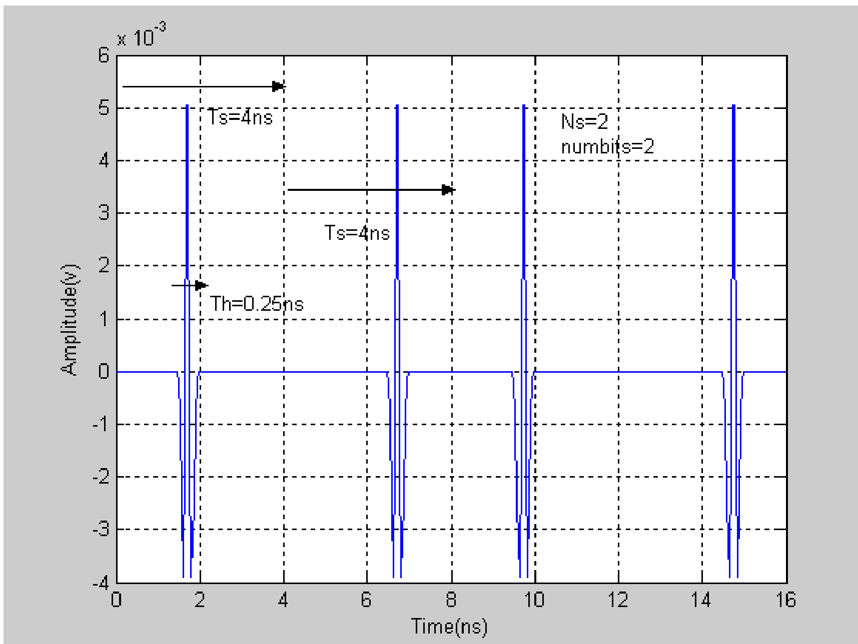

b)

Fig. 5.1: Transmission scheme for a PPM-TH-UWB signal. a) block diagram
b) signal waveform of s(t)

Data are binary sequence to be transmitted. They are generated at a rate of R_b = 1/T_b bit/s. The first system block will repeat the data sequence N_s times (number of pulses per bit) and generate the new binary sequence at the rate of R_{cb} = N_s/T_b. With T_b = N_s T_s, the new coding rate will be R_{cb} = 1/T_s bit/s, T_s being the frame (symbol) period.

A second block generates a new sequence represented by $b_j = c_jT_c + a_j\varepsilon$, where T_c is the chip time, c_jT_c the pseudo random code in chip duration, ε the time shift associated with the TH-PPM while a_j is depend on *j*. The chip time interval T_c represents only one pulse in the time frame period. Note that $a_j\varepsilon + T_h < T_c$, with T_h the pulse period. The real-valued b sequence enters to the modulation system block, which generates a sequence of pulses at the rate of $R_s = 1/T_s$ pulse/s.

These pulses are located at the time $jT_s + b_j$ and are therefore shifted from the nominal position jT_s by b_j. Pulses occur at times ($jT_s + c_jT_c + a_j\varepsilon$). The last block in the UWB transmitted system is the pulse shaper filter with an impulse response $p(t)$. The transmitted signal is given by (5.1) and its simulation shown in Fig. 5.2, [2].

$$s(t) = \sum_{j=-\infty}^{\infty} p(t - jT_s - c_jT_c - a_j\varepsilon) \tag{5.1}$$

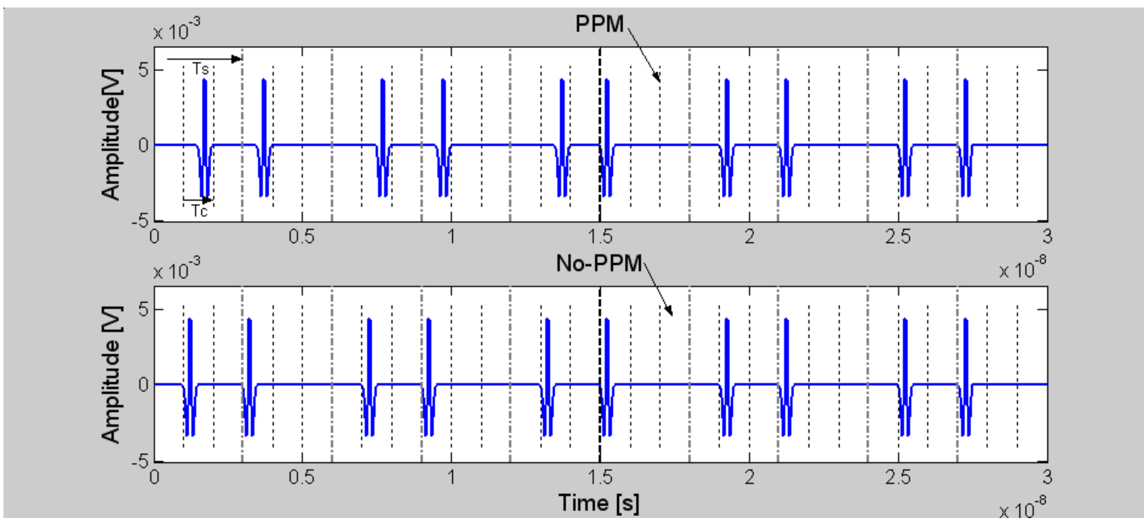

Fig. 5.2: signal generated by the PPM and non-PPM TH-UWB transmitter with $P_{tr} = -25dBm$, Numbits = 2, N_s (pulse/bit) = 5, T_s (frame time) = 3ns, T_c (chip time) = 1ns, T_h (pulse duration) = 0.25ns

5.2.2 DS-UWB signals

Direct-sequence spread (DS-SS) is a well-known modulation technique [4]. Figure 5.3 shows the direct sequence spread-PAM in a UWB transmitted block system.

Note that DS, TH, and OFDM are transmission techniques applied to modulation schemes such as DS-PPM or TH-PAM. The advantages and disadvantages in using TH or DS transmission have been discussed in [1], [4].

TH-PPM is more popular and simpler compared to other modulation schemes. This simplicity is based on power efficiency, spectral lines, implementation, fading margin and performance, while M-ary PAM (M-PAM) requires more bandwidth.

In Fig. 5.3, the first block repeats each bit N_s times and the second block transforms this binary sequence into a positive and negative value sequence, $(d_j = 2a_j - 1) \qquad -\infty < j < +\infty)$

The transmission coder applies a binary code composed of '±1' and generates new sequence. The new data sequence enters the PAM modulation block, which generates the Dirac pulses at rate of $R_s = \frac{N_s}{T_b} = \frac{1}{T_s}$ pulses/s.

These pulses are located at jT_s, same as in TH-PPM modulation schemes. Finally, the last block is a pulse shaping filter with the impulse response of $p(t)$. The output signal S_{PAM} is shown in Fig. 5.4.

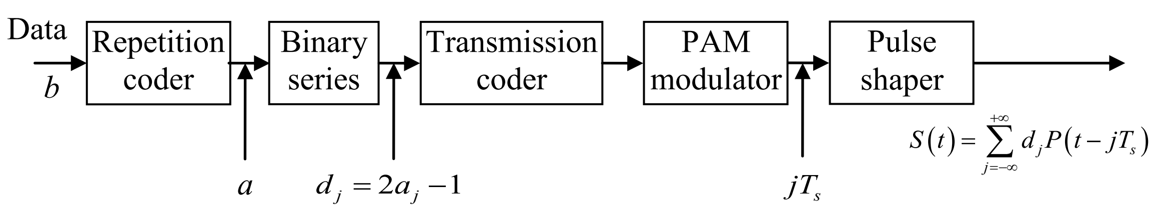

Fig. 5.3: DS-PAM-UWB transmission system

5.3 UWB pulse shapes

5.3.1 Gaussian Pulse-Shape

A typical UWB pulse shape, also known as Gaussian pulse, is often used in UWB systems [4]. Generating pulses with nanosecond duration is possible with an inexpensive CMOS technology. A Gaussian pulse that is described by [3]

$$p(t) = \pm \frac{1}{\sqrt{2\pi\sigma^2}} e^{\left(-\frac{t^2}{2\sigma^2}\right)} = \pm \frac{\sqrt{2}}{\beta} e^{-\frac{2\pi t^2}{\beta^2}} \tag{5.2}$$

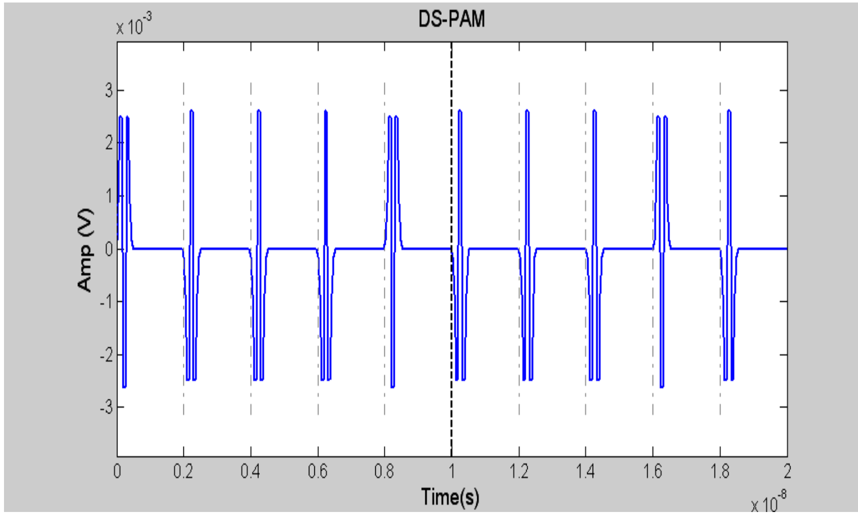

Fig. 5.4: Signal in PAM-DS-UWB:
$P_{tr} = -25dBm$, Numbits = 2, $N_s = 5$, $T_s = 2$ns, $T_h = 0.5$ns

where $\beta = 4\pi\sigma^2$ is the shape factor and σ^2 the variance. The relation between variance and pulse width is given by $\sigma = \dfrac{T_h}{2\pi}$. Figure 5.5 shows the Gaussian waveform.

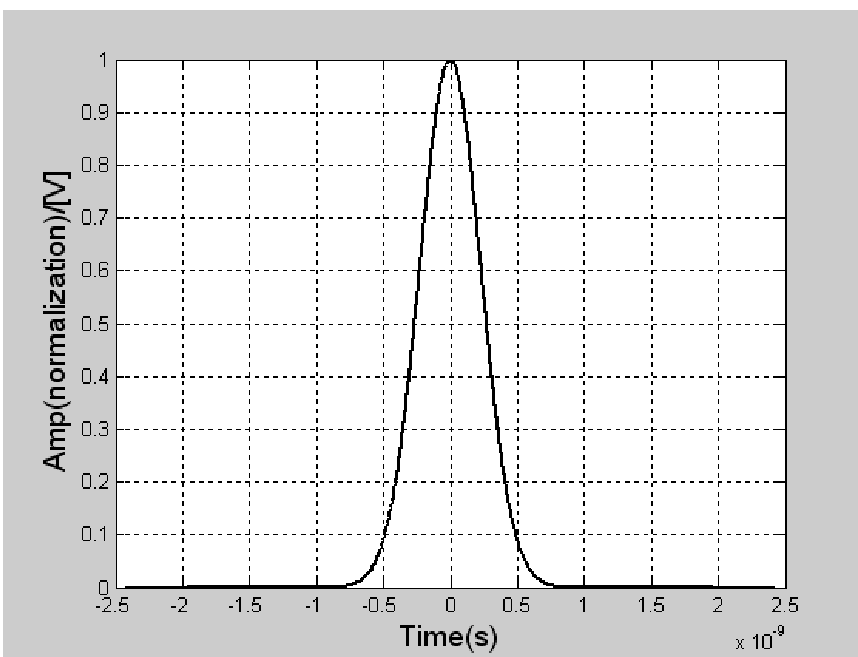

Fig. 5.5: Gaussian pulse wave form, $\beta = 0.81ns$

Several pulse waveforms might be considered such as the Hermite pulse shapes (Multi-user), but the Gaussian derivatives are more suitable [5].

5.3.2 Hermite based orthogonal pulses (multiband user)

The system of sine and cosine has been known historically as orthogonal functions in communication systems. In recent years, other kinds of orthogonal functions have been used for theoretical investigations as well as for equipment design. The use of modified Hermite polynomials to create orthogonal transform, and even to create orthogonal wavelets for multi-carrier data transmission over high-rate digital subscriber loops, has been proposed. Again Hermite pulses have been found suitable for multi-users [2]. The Hermite polynomial can be defined by [3]

$$p_{e_n}(t) = (-\tau)^n e^{\frac{t^2}{4\tau^2}} \tau^2 \frac{d^n}{dt^n}\left(e^{-\frac{t^2}{2\tau^2}}\right) \tag{5.3}$$

where $n = 0, 1, 2, \ldots, -\infty < t < +\infty$ and τ is the time-scaling factor (pulse width regular element). The result is a set of orthogonal functions $p_{e_n}(t)$, which can be easily derived for all values of n. In a multi-user system, the orthogonal pulses can be assigned to different users in order to decrease the co-channel interference (CCI), also known as crosstalk, the inter-symbol interference (ISI) and to reduce the bit-error rate (BER) [5]. The Hermite pulses have the following properties [2]

- The pulse duration and bandwidth are almost the same for all n.
- The pulses are mutually orthogonal.
- The pulses have non-zero DC components and in fact, the low frequency components of the pulses are relatively significant.

Note that Gaussian pulses also have the advantage that by increasing the pulse order and decreasing the pulse width, the bit error rate decreased. In the case of multiple users, Hermite pulses have better performance, but their generation is more difficult.

5.4 UWB indoor channel modeling

The propagation of UWB signals in indoor-outdoor environments is the most important issue. If the channel is well characterized, the effect of disturbances can be reduced by proper design of the transmitter and receiver.

One important aspect of any radio channel-modeling activity is the investigation of the distribution function of channel parameters. Typically, these distributions are obtained from measurements/simulations based on descriptions of the environment. The multipath propagation can be represented conveniently and mathematically by following the discrete impulse response of the channel [7].

$$h(t) = \sum_{n=1}^{N} a_n(t)\,\delta\big(t - \tau_n(t)\big) \tag{5.4}$$

where a_n and τ_n are the n^{th} path channel gain and delay, respectively, measured at time t and N the total number of paths. This model assumes that all channel parameters are random variables with specific distributions. Statistical information is required regarding the distribution of channel gain, a_n, pulse arrival time τ_n, and number of paths, N.

According to [8] and [9], the primary parameters that characterize the indoor channel include the following:

- Number of multipath components: it is important since it determines the design of the rake receiver which collects the receiver pulse energies,
- Average delay: it describes the mean travel time of a signal from transmitter to receiver,
- Delay spread: it is a metric of how much that signal is diluted in time,
- Total delay spread: it indicates the largest delay due to the multi-path,
- Doppler spread: it is related to the coherence time of the channel,
- Amplitude fading distribution or power delay profile,
- Multi-path arrival time: a simple statistical model for arrival times of the paths, since multipath propagation is caused by randomly located objects.

5.5 Rake receiver

The receiver signal energy can be improved in a multipath fading channel by utilizing diversity techniques, such as the rake receiver. Rake receivers combine different signal components that have propagated through the channel via different paths.

The combination of different signal components will increase the signal-noise ratio, signal-to-noise ratio (SNR), and thus improve the system performance [10].

Figure 5.6 consists of a parallel bank of N_R correlators, followed by a combiner that determines the variable to be used for the decision on the transmitter symbol. m_j is the correlator mask and τ_j the propagation delay related to the j^{th} path. The output of the bank of correlators feeds to combiner.

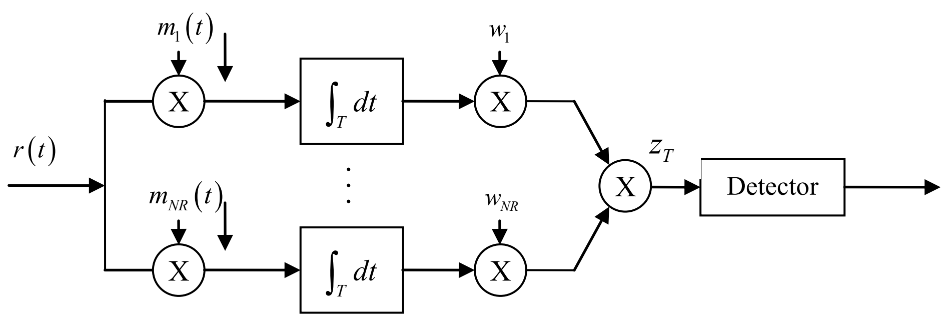

Fig. 5.6: Rake receiver with N_R parallel correlators and time delay

There are three main types of rake receivers:

- Ideal rake receiver, IRAKE, which captures the entire receiver signal power by having the number of fingers equals to the number of multi-path components.
- Selective rake receiver, SRAKE, which only uses the strongest propagation paths. In this case, channel information from the impulse response is required.
- Partial rake receiver, PRAKE, which is a simplified approximation to the SRAKE. The PRAKE involves combining the first propagation paths [11]. The principle behind this approach is that the first multipath components will typically be the strongest and contain the most of the receiver signal power. The

disadvantage is that the multipath components that the PRAKE receiver combines are not necessarily the strongest multipath components, especially in case of extremely NLOS. As a result, optimum performance will not be achieved. Therefore, we need other techniques, such as filter banks, to increase the SNR and system performance.

5.5.1 Multipath combining methods

Signal processing techniques are designed to combine the diversity receptions in some way, and thus they can be referred to, in general, as combining techniques [12] like:

- Equal gain combining (EGC) uses equal weights to combine the multipath components.
- Selective diversity (SD) uses diversity path where the highest SNR is chosen.
- Maximum ratio combining (MRC) combines the components relatively to their signal amplitudes.

MRC is essentially a matched filter (MF) assuming that the receiver signal is being sampled at the Nyquist sampling rate and there are an infinite number of fingers. When the noise is additive white Gaussian noise (AWGN), the MRC diversity achieves maximum SNR at the output of combiner and hence is considered as the optimum technique. However, if we assume color noise, the GMF will be used to weight the signal amplitude harmonics.

5.5.2 General matched filter

The general matched filter **(**GMF) is used when the noise correlation matrix is non-diagonal. However, in many situations the noise is more accurately modeled by a correlated Gaussian noise with zero mean and covariance matrix Q_c [1]. The noise process models any source of interference signal that affects the receiver. Hence, the covariance matrix will generally be a combination of the interfering signals and the channel AWGN.

A GMF maximizes the probability of detection of a known signal in Gaussian noise, subject to a given probability of false alarm.

Let $X = [x_1, x_2, ... \ x_{N-1}]$ denote the observed data samples at the receiver and $s = [s_1, s_2, ... \ s_{N-1}]$ the transmitted pulse samples. The detection process consists to distinguish between the two hypotheses:

$$\begin{aligned} &H_0 : X = W \\ &H_1 : X = s + W \end{aligned} \tag{5.5}$$

where H_0 is the null hypothesis and corresponds to *no pulse* transmitted and H_1 is the alternate hypothesis corresponding to the case where the transmitter sends a pulse. W is a noise. The Neyman-Pearson detector then selects H_1 if the log-likelihood ratio exceeds a threshold, that is:

$$L(X) = \ln\left[\frac{p(x; H_1)}{p(x; H_0)}\right] > \lambda \tag{5.6}$$

where λ is the threshold, $p(x; H_1)$ and $p(x; H_0)$ are the conditional probability density functions, given by, [1]

$$\begin{aligned} p(x; H_1) &= \frac{1}{(2\pi)^{\frac{N}{2}} \sqrt{|Q_c|}} e^{-\frac{1}{2}(X-s)^T Q_c^{-1}(X-s)} \\ p(x; H_0) &= \frac{1}{(2\pi)^{\frac{N}{2}} \sqrt{|Q_c|}} e^{-\frac{1}{2}(X)^T Q_c^{-1}(X)} \end{aligned} \tag{5.7}$$

Finally, the decision test statistic is given by [1], [10]:

$$T(X) = X^T Q_c^{-1} s \tag{5.8}$$

By letting $F = Q_c^{-1} s$ be the filter weights vector, the GMF output is the test statistic, $T(X) = X^T F$. While the filter weights in a MF are directly obtained from the channel impulse response, the GMF weight is obtained by inverting the noise covariance matrix and multiplying it with the channel impulse response.

In this case, the GMF requires the knowledge of both channel impulse response and noise covariance matrix to determine its filter weights for optimum combining.

When the noise is uncorrelated Gaussian, $|Q_c| = \sigma_n^2$, a GMF simply reduces to a MF. Hence, it can be concluded that for operating the GMF, the receiver must know the channel impulse response, the noise covariance matrix, Q_c, and be in perfect synchronization with the transmitter. Note that both GMF and MF processing are coherent techniques and assume that the receiver sampling clock is perfectly aligned with that of the transmitter.

5.6 Conclusion

In this chapter, we showed that IR-UWB transmitters allow simple recovering of low-power UWB signals from noise and take advantage of frequency selective fading.

Two of the most popular UWB transmission models based on the concept of time hopping spread spectrum (TH) and direct sequence spread spectrum (DS) were described. Also general pulse shape (1^{st} Gaussian), modulation schemes, and UWB indoor channel modeling for accurate transceiver modeling investigation were discussed. To take advantage of frequency selective fading, which is part of wideband wireless characteristics, the concepts of rake receiver and multipath combination methods such as General matched filter (GMF), equal gain combining (EGC), selective diversity, (SD), and maximum ratio combining (MRC) in the presence of multipath, were presented.

References

[1] O. Abedi, M.C.E. Yagoub "Efficient narrowband interference cancellation in UWB RAKE receivers", submitted to *IET J. communications*, March 2012.

[2] M. Ghavami, L. B. Michael, R. Kohno, *Ultra Wideband Signals and Systems in Communication Engineering*, J. Wiley, Chichester, England, 2004.

[3] W. Gao, R. Venkatesan, C. Li, A Pulse shape design method for ultra-wideband communications," *IEEE Conf. Wireless Communications and Networking,* pp. 2800-2805, 2007.

[4] O. Abedi, J. Nielsen, "UWB data rate and channel capacity in modulation schemes," *IEEE Conf. Electrical and Computer Engineering,* pp. 1809-1816, 2006.

[5] B. Hu, N.C. Beaulieu, "*Pulse shaping in UWB communication systems", IEEE Conf. Vehicular Technology,* pp. 5175-5179, 2004.

[6] A. Taha, K.M. Chugg, "A theoretical study on the effects of interference UWB multiple access impulse radio," *Conf. Signals, Systems and Computers,* pp. 728-732, 2002.

[7] R. Saadane, A. Khafaji, M. Wahbi, B. El Bhiri, D. Aboutajdine, "Ultra wide bandwidth radio channel indoor propagation and path loss analysis based on measurements," *Conf. Multimedia Computing and Systems*, pp. 259-263, 2009.

[8] A. Barbieri, F. Pancaldi, G.M. Vitetta, "Compressed channel estimation and data detection algorithms for IR-UWB," *Conf. Ultra-Wideband,* pp. 360-364, 2011.

[9] I.Z. Nikookar, H. Janssen, "An overview of ultra wide band indoor channel measurements and modeling," *IEEE J. Microwave Wireless Components Lett.,* pp. 386-388, 2004.

[10] O. Abedi, J. Nielsen, N. Fallah, "Narrowband interference cancellation in an UWB filter bank receiver," *IEEE Conf. Vehicular Technology*, pp. 1-6, 2006.

[11] D. Cassioli, M.Z. Win, F. Vatalaro, A.F. Molisch, "Performance of low-complexity RAKE reception in a realistic UWB channel", *IEEE Conf. ICC*, pp. 763-767, 2002.

[12] M. Renzo, D. Leonardis, F. Graziosi, F. Santucci, "Performance analysis and optimization of Tc-DTR IR-UWB receivers over multipath fading channels with tone interference," *IEEE J. Vehicular Technology,* pp. 3076-3095, 2011.

Chapter 6 UWB Pulse Modulation Schemes

6.1 Introduction

In ultra wide-band (UWB) system design there are always trade-offs between maximum transmit distance, data rate, transmit power, and system complexity. Different data modulation schemes such as pulse-position modulation (PPM), pulse-amplitude modulation (PAM), phase-shift keying (PSK), or on-off keying (OOK) have been used in UWB communications with relative success depending on the targeted application [1], [2]. In fact, their performance can significantly vary according to which system parameters are considered such as narrowband interference (NBI) robustness, symbol error rate (SER), system complexity, data rate, or maximum transmit power with respect to transceiver distance and channel capacity. For instance, if minimum complexity is important, then OOK modulation would be the best choice. However, it is very sensitive to noise. On the other side, if interference robustness and power efficiency are the parameters to consider, Binary PSK (BPSK) and M-ary PPM (M-PPM) can be the best candidates. Nevertheless, M-PPM deals with multi-dimensional signals, whereas M-PAM has only one dimension [3], [4]. This topic has been widely discussed in the last decade but most of published works [4] did not efficiently include all tradeoffs, such as comparison of bit error rate (BER), modulation level, channel capacity and complexity. In fact, even if several technical papers have already discussed this issue, they mainly investigated the modulation performance for specific applications or system requirements and thus, to the best of our knowledge, did not cover the whole comparison spectrum [5].

The aim of this chapter is indeed to evaluate all these parameters and their impact on each scheme performance. For this comparison, we considered the PPM in time-hopping mode (TH-mode), the OOK in direct-sequence mode (DS-mode), and the Binary PAM (BPAM) in both TH- and DS-modes. The channel model is the UWB IEEE 802.15.3a multipath indoor channel model under Additive White Gaussian Noise (AWGN) [6].

Note that the white noise channel model is largely used in the literature due to its relative simplicity. Because the target here is to compare the performance of different UWB pulse modulation schemes under the same channel model, a relatively simple model can be the best candidate. Note also that this channel model can be specified for different propagation scenarios, such as extremely indoor Non-Line-of-Sight (ENLOS) or outdoor Line-of-Sight (LOS). In this work, we focused on the indoor propagation channel model to take advantage of the UWB frequency selective fading.

Also, the transmit power was evaluated by integrating the fifth derivative of the power spectrum density (PSD) of the Gaussian pulse over the whole bandwidth. Note that, the third pulse derivative module has been effectively used because the transceiver antenna acts as a second derivative.

6.2 Modulation schemes

6.2.1 M-PAM

In pulse-amplitude modulation, the same waveform is sent with different amplitudes corresponding to different data being transmitted. The BPAM can be presented using antipodal, monocyclic, or Gaussian pulses. The transmitted signal for M-PAM can be expressed as [7]:

$$S_{PAM}(t) = \sum_{j=-\infty}^{\infty} \sum_{m=1}^{M} \delta_m(j) d_m P(t - jT_s) \tag{6.1}$$

where $\delta(j) = [\delta_1(j), \delta_2(j) ..., \delta_M(j)]$ is an indicator transmitter pulse vector, *i.e.,* for each j (known as unit impulse), only one element of the vector is equal to unity otherwise zero. T_s is the pulse symbol period, M the modulation level, and P the pulse shape impulse response. For multi-user case, d_m is the amplitude of independent and identically distributed (IID) random signals according to an equiprobable distribution.

The related PSD can be formulated as [4]

$$S_{PAM}(f) = S_{CPAM}(f) + S_{dPAM}(f), \tag{6.2}$$

where $S_{CPAM}(f)$ and $S_{dPAM}(f)$ are respectively the desired continuous part (non-periodic) and the undesired discrete part (periodic), which induces more spectral lines and lower mutual information [4]. For real data with equal probability of occurrence, $S_{PAM}(f)$ becomes [6], [7]:

$$S_{PAM}(f) = \frac{\sigma_d^2}{T_S}\left|P(f)\right|^2 + \frac{\mu_d^2}{T_S^2}\sum_{j=-\infty}^{\infty}\left|P\left(\frac{j}{T_S}\right)\right|^2 \delta\left(f - \frac{j}{T_S}\right) \tag{6.3}$$

where σ_d^2 and μ_d are the variance and mean of the random data sequence, respectively. In case of repetition pulse coding [6], [15], each random data contain number of pulses with various amplitude (PAM case) that indicate just one bit of data. Let us consider the symbol period limited by trade of data rate and pulse numbers. For instance, for wider T_s, the data rate is indeed lower but does have better performance with higher pulse repetition coding (increasing pulse numbers), and inversely. On the other hand, if a time-hopping PAM (TH-PAM) is considered, they are dependent on frequency, which is not the case in this study.

In narrow-band, using a filter bank receiver or a mixer bank receiver can mitigate the narrowband interference while splitting the UWB bandwidth to the narrowband. Thus, the average power or variance of the UWB signals can be calculated by integrating the PSD in frequency domain [8], [9]

$$\begin{aligned} Var\left(S_{PAM}(t)\right) &= \int_{-\infty}^{+\infty} S_{PAM}(f)\,df = \int_{-\infty}^{+\infty}\left[\frac{\sigma_d^2}{T_S}\left|P(f)\right|^2 + \frac{\mu_d^2}{T_S^2}\sum_{j=-\infty}^{\infty}\left|P\left(\frac{j}{T_S}\right)\right|^2 \delta\left(f - \frac{j}{T_S}\right)\right]df \\ &= \frac{\sigma_d^2}{T_S}\int_{-\infty}^{+\infty}\left|P(f)\right|^2 df + \frac{\mu_d^2}{T_S^2}\sum_{j=-\infty}^{\infty}\left|P\left(\frac{j}{T_S}\right)\right|^2 \end{aligned} \tag{6.4}$$

Assuming the carrier frequency of the receiver is f_{c0} and the bandwidth of the bandpass filter is B, the UWB interference power can be expressed as [9]

$$P_I = \frac{\sigma_d^2}{T_S}\int_{-\infty}^{+\infty}\left|P(f)H_T(f)\right|^2 df + \frac{\mu_d^2}{T_S^2}\sum_{\frac{j}{T}\pm f_{c0}\in[-B/2\ B/2]}\left|P\left(\frac{j}{T_S}\right)H_T\left(\frac{j}{T_s}\right)\right|^2 \tag{6.5}$$

with $H_T(f) = H_{ch}(f)H_B(f)$, where $H_B(f)$ and $H_{ch}(f)$ are the Fourier transform for the filter and the channel impulse response, respectively. For an ideal band-pass filter, the above equation can be reformulated as [9]

$$P_I = \frac{2\sigma_d^2}{T_S}\int_{f_{c0}-B/2}^{f_{c0}+B/2}\left|P(f)\right|^2 df + \frac{2\mu_d^2}{T_S^2}\sum_{\frac{j}{T}+f_{c0}\in[-B/2\ B/2]}\left|P\left(\frac{j}{T_S}\right)\right|^2 \tag{6.6}$$

Therefore, the interference power can be affected by the following factors:

- The symbol period ($1/T_s$); in fact, increasing T_s will both increase the pulse repetition frequency and decrease the energy spectral density, while the corresponding continuous component of the power spectral density remains unchanged. So the pulse repetition leads to a discrete line spectrum. The line spectral density is composed of the delta function and separated by the pulse repetition frequency.
- The energy spectral density (ESD) of the pulse waveform, $\left|P(f)\right|^2$.
- The power spectral density (PSD) of the UWB chip sequence $S_{PAM}(f)$ determined by σ_d^2 and μ_d for real and mutually uncorrelated sequences. Therefore, a proper pseudo-random (PR) code, directly related to the pulse repetition frequency and corresponding PSD, could be selected to reduce the discrete spectral components. If the mean μ_d is not zero, discrete components (spectral lines) will appear in $S_{PAM}(f)$. However, for a sequence of ± 1, these components will disappear. On the other hand, if the UWB pulse train is

modulated by an all 'one' sequence ($\sigma_d^2 = 0, \mu_d = 1$), the PSD of $S_{PAM}(f)$ will be composed only of discrete components. Thus, if these components, which generally have a stronger PSD than continuous ones [2], [5], are in the band of narrowband systems, they will have a bigger effect on the performance of the victim receiver.

An alternative is to send alternating positive and negative pulses, [2], [8]. This line coding scheme is often called Alternate Mark Inversion (AMI). Following [9], it has been demonstrated that with equal probable binary elements, the PSD is given by

$$S_{AMI}(f) = \frac{1}{2T_s}|P(f)|^2\left[1-\cos(2\pi f T_s)\right] \tag{6.7}$$

which shows there are no spectral lines, and thus, the bipolar PAM signal has a lower bit error rate (BER) compared to the non-bipolar PAM signal, which suffers from the presence of more spectral lines, Fig. 6.1.

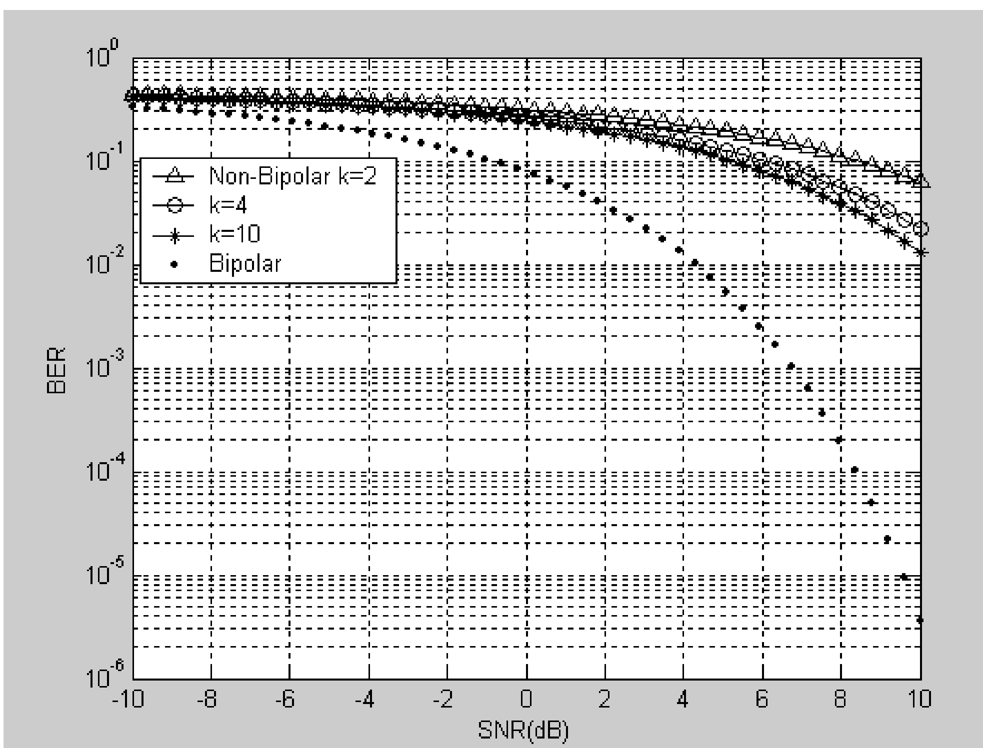

Fig. 6.1: BER AWGN channel Comparison with various polarization, k.

6.2.2 OOK

Compared to others, OOK can be seen as the simplest scheme. In this technique, sending a pulse corresponds to bit '1' and no pulse means '0'.

Therefore, because of the equal probability of either symbols, $\sigma_d^2 = 0.25$, $\mu_d = 0.5$, and the PSD becomes, [6],[9]:

$$S_{OOK}(f) = \frac{1}{4T_S}\left|P(f)\right|^2 + \frac{1}{4T_S^2}\sum_{j=-\infty}^{\infty}\left|P\left(\frac{j}{T}\right)\right|^2 \delta\left(f - \frac{j}{T_S}\right) \tag{6.8}$$

In a variant (Antipodal signals), the transmitter sends a pulse of duration T_p much higher than the bit time T_b to indicate bit '1' and the negative of this pulse for '0'. Therefore, with equiprobable elements, we have $\sigma_d^2 = 1$, $\mu_d = 0$ and thus, a PSD of [9]

$$S_{ant}(f) = \frac{1}{T_S}\left|P(f)\right|^2 \tag{6.9}$$

showing that the PSD of antipodal does not have any spectral lines or discrete components. Note that OOK and binary-PPM are similar. Therefore, only 2-PPM performance was evaluated to avoid duplication.

6.2.3 M-PPM

In M-PPM, the chosen bit to be transmitted influences the position of the UWB pulses. The signal at the output of the transmitter cascade, $s(t)$, can be expressed as [1], [2], [6]:

$$S_{PPM}(t) = \sum_{j=-\infty}^{\infty}\sum_{m=1}^{M} P\left(t - jT_s - c_m T_C - a_m \varepsilon\right) \tag{6.10}$$

where j is the number of transmitted bits and c_m the time-hopping code. The chip time interval T_c represents only one pulse in the time frame period. Note that $a_m\varepsilon + T_p < T_c$ with T_p the pulse period.

The Fourier transform of the PSD of M-PAM can be expressed as [11]

$$S_{PPM}(f) = \int_{-\infty}^{+\infty} S_{PPM}(t) e^{-j2\pi ft} dt \tag{6.11}$$

Leading to the following PSD, expressed in terms of continuous and discrete parts

$$PS_{PPM}(f) = PS_{CPPM}(f) + PS_{dPPM}(f) \tag{6.12}$$

with

$$PS_{CPPM}(f) = \frac{|P(f)|^2}{T_S}\left[1 - \left(\frac{1}{M}\frac{\sin(\pi fT)}{\sin\left(\frac{\pi fT}{M}\right)}\right)^2\right]$$

$$PS_{dPPM}(f) = \frac{|P(f)|^2}{T_S^2}\left(\frac{1}{M}\frac{\sin(\pi fT)}{\sin\left(\frac{\pi fT}{M}\right)}\right)^2\left[\sum_{j=-\infty}^{\infty}\delta\left(f - \frac{j}{T_S}\right)\right] \tag{6.13}$$

which can be simplified to, [6], [11]

$$PS_{PPM}(t) = \frac{1}{T_S^2}\sum_{j=-\infty}^{\infty}\sum_{m=1}^{M}\left|P\left(\frac{jM}{T_S}\right)\right|^2 \delta\left(f - \frac{jM}{T_S}\right) \tag{6.14}$$

showing a smother PSD than of PAM, leading to less narrowband interference. The single pulse of the UWB signal is placed into one of $N=T_{sym}/T_h$ slots, where N is the number of slots per symbol, T_h the pulse width and T_{sym} the symbol time. The number of bits per one PPM symbol is equal to $\log_2^N$.

Note that by increasing M (modulation level) the data rate will increase as well. Furthermore, the average transmitted power will be increased by a factor of M.

In this case, the N slots are divided into L groups. Each group includes N/L slots with a single pulse. With this, the average bit number will be [11]

$$N_b^{'} = \log_2^{\left(\frac{N}{L}\right)^L} = L\left(\log_2^N - \log_2^L\right) \qquad N >> L \text{ and } N_b^{'} = L\log_2^N = N_b \tag{6.15}$$

Thus, modifying the bit rate can improve the throughput of number of pulses per N slots, but it will raise another issue:

- A larger bandwidth requirement, as the number of pulses per symbol interval increases.
- Pulse width relaxation will be limited.
- All symbols can be orthogonal. To solve this for large *N*, one can use predefined pulse arrangement such that no-pulse is put in the same position. In other words, to avoid pulse inter-path interference (IPI) or pulse jamming, we should decrease the pulse period or increase the chip period.

Note that more information on PSK modulation can be found in [4], [6]. Because of its complexity, it has been introduced here mainly for comparison.

6.3 AWGN Channels

Under AWGN UWB channel models expressed by the IEEE 802.15.3a standard, symbol- or bit-error rates can be easily expressed, leading to an optimum receiver [6], [7], consisting on an optimum demodulator (coherent demodulator).

First, let us assume a zero system margin (no power loss between equipment connections), i.e., $M_s = 0$. For any binary modulation, the BER can be calculated using the distance between two symbols as [6]

$$P_b = Q\left(\sqrt{\frac{d}{2N_0}}\right) \tag{6.16}$$

This distance is different for each modulation scheme

$$d_{PPM} = \sqrt{2\gamma_b};\ d_{PSK} = 2\sqrt{\gamma_b}\ ;\ d_{OOK} = \sqrt{2\gamma_b};d_{PAM} < \sqrt{2\gamma_b} \tag{6.17}$$

$\gamma_b = \dfrac{E_{Rx}}{N_0} = N_S \gamma_p$, is the average bit energy in the receiver and γ_p its average pulse energy. Table 6.1 summarizes the BER and SER performance for different modulation schemes.

For simplicity, let us assume $N_s = 1$ with a normalized pulse energy. From theory, and as shown in Fig.2, binary PAM has 3dB more power efficiency than PPM. As M is increasing, the performance of M-PPM also increases.

This is due to space dimensionality that makes more noise orthogonal and causes the elements of the covariance noise matrix, Q_c, to be almost zero [8], [12]. Since the signal-to-noise ratio (SNR) is given by $SNR_r = S^T Q_c^{-1} S$, it will also increase. Also, M-PPM requires lower transmission power in high modulation levels.

On the other hand, the performance of M-PAM becomes worse due to decreased symbol distance and as a result, $|Q_c|$ will increase leading to more interference at narrowband.

Thus, by increasing the modulation level, the M-PPM will exhibit better performance. Note that (17) confirms what was mentioned above, i.e., simulating 2-PPM and OOK parameters leads to similar performance. Therefore, we just simulated and compared the M-PAM and the M-PPM in terms of BER versus SNR while a comparison between OOK and PPM is not necessary.

Table 6.2 summarizes the comparison between the different modulations schemes in terms of noise interference, spectral lines, transceiver complexity, pulse energy variance, and bandwidths.

As shown, the candidate pulse modulation is strongly related to the application. In fact, if simplicity is considered, the repeat pulse coding or OOK modulation will be the good option but in case of NBI the 4-PPM should be chosen to satisfy all spectrum requirements.

Table 6.1. BER and SER in AWGN channel for different UWB modulations.

TH-BPPM	Orthogonal single pulse (Ns=1) $\Pr_b = Q\left(\sqrt{N_s\gamma_b}\right),\ Q(x) = \frac{1}{2}erfc\left(\frac{x}{\sqrt{2}}\right)$ $s_m = \begin{cases} s_0 = +\sqrt{p_{Tx}}\left[1-R_0(m)\right], \\ s_1 = -\sqrt{p_{Tx}}\left[1-R_0(m)\right] \end{cases}$ where $R_j(\varepsilon)$ is autocorrelation of the pulse S_m. orthogonal multi-pulse signal with TH coding: $\Pr_b = Q\left(\sqrt{N_s\gamma_b\left(1-R_0(m)\right)}\right)$
BPAM/BPSK	$P_b = Q\left(\sqrt{2\gamma_b}\right)$
M-PPM	$P_M = \frac{1}{\sqrt{2\pi}}\int_{-\infty}^{\infty}\left[1-\left(\frac{1}{\sqrt{2\pi}}\int_{-\infty}^{y} e^{-x^2/2}dx\right)^{M-1}\right]\ldots$ $\ldots\exp\left[\frac{-1}{2}\left(y-\sqrt{2\gamma_s}\right)^2\right]dy$ $P_b = \frac{2^{k-1}}{2^k-1}P_M \approx \frac{1}{2}P_M$
M-PAM	$P_M = \frac{2(M-1)}{M}Q\left(\sqrt{\frac{6\log_2(M)\gamma_b}{M^2-1}}\right)$ $P_b = \frac{1}{k}P_M$ $\gamma_s = \log_2(M)\gamma_b$ $\gamma_b = N_s\frac{\xi_b}{N_0}$

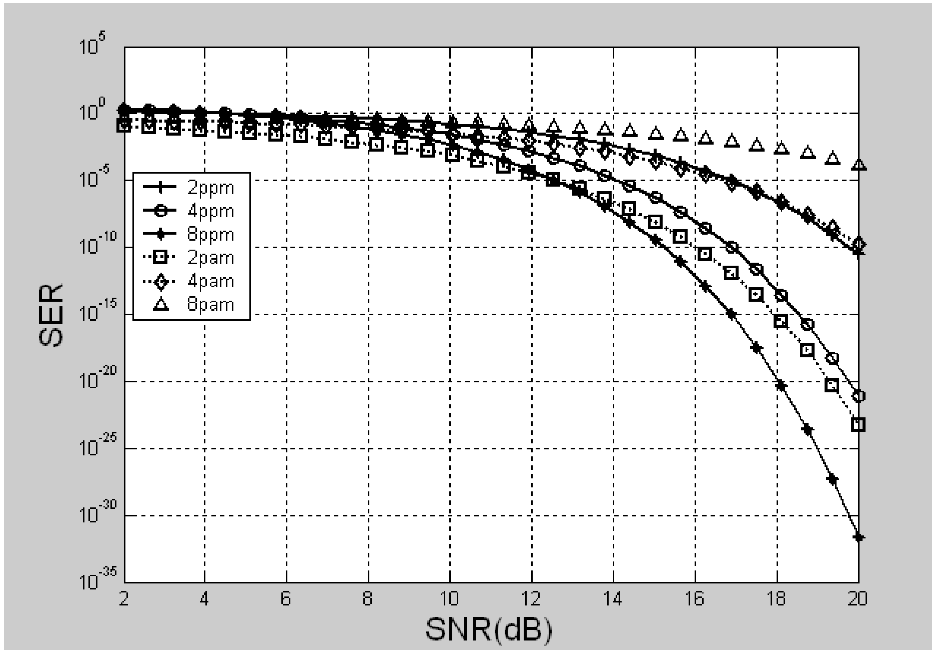

Fig. 6.2: Symbol error rate for different M levels of M-PAM and M-PPM ($N_s = 1$)

Table 6.2. Comparison of various pulse modulation techniques in terms of bandwidth, spectral line, noise sensitivity, transceiver complexity, and pulse energy variance.

	Bandwidth requirement (normalized)	Power requirement (normalized)	Noise sensitively	Spectral line power distortion	Transceiver complexity	Pulse Energy variance
PAM	1	1	Highest (1 dimension)	Yes	Low	$\left(\frac{M^2-1}{6}\right)\frac{1}{\gamma_s}$
PPM	$\left(\frac{M}{\log_2 M}\right)\left(\frac{\tau}{T_s}\right)$	$\sqrt{\frac{2}{M\log_2 M}}$	Lowest (M dimensions)	Yes (lower)	Highest (by M)	$\frac{1}{\gamma_s}$
OOK	1	1	Very high	Yes high	Lowest	$\frac{1}{\gamma_s}$
BPSK	$\frac{\tau}{T_s}$	1.12	Lower (M/2 dimensions)	No	High (by M/2)	$\frac{1}{\gamma_s}$

6.4 Data Rate and Maximum Distance

To further investigate the modulation scheme performance, let us assume that the signal propagation occurs over free space. Thus the free-space attenuation A_m can be expressed as [13], [6]

$$A_m = \frac{4\pi D^2 L}{G_T S_R} \tag{6.18}$$

with D the distance of propagation, S_R the antenna effective area, L the system hardware loss, and G_T the transmitter antenna gain. In this section, we assumed $L = 1$ (no losses in the system hardware).

The pulse waveform is the 5th derivative of a monocyclic Gaussian pulse and its PSD is given by [13]

$$P_s(f) = A_{\max} \frac{(2\pi f \delta)^{2n} e^{-(2\pi f \delta)^2}}{n^n e^{-n}}; A_m = 10^{-13.125}; \delta = 51ps \tag{6.19}$$

leading to the following receiving signal power

$$P_r = \frac{M_s SNR_{spec} N_0}{2} \tag{6.20}$$

where N_0 is the thermal noise power, SNR_{spec} the system requirement SNR, and $H(f)$ the frequency response of the indoor channel, which can be expressed as [13]

$$\left|H(f)\right| = \sqrt{\frac{1}{A_m(f)} R(f)} \tag{6.21}$$

where $R(f)$ is the shadowing parameter that depends on the geography of the propagating environment (usually assumed to be 6dB). The system margin M_s is assumed to be 1dB.

From this, the distance can be reformulated as:

$$D^2 = \frac{\dfrac{G_T G_R c^2}{(4\pi)^2 R_b} 2\displaystyle\int_{fL}^{fH} \frac{P_s(f)}{f^2} df}{M_s SNR_{spec} \dfrac{1}{2} N_0} \qquad N_0 = kT_n(f) = k\left(T_A + \left(F(f) - 1\right) T_0\right) \tag{6.22}$$

where T_n is the noise temperature at the receiver, T_A the receiver antenna temperature, T_0 the room temperature (usually T_0 = 300°K), k the Boltzmann constant, $F(f)$ the noise factor of the receiving device and R_b the data rate. Given a specific SNR (i.e., the SER of a specific modulation scheme), one can evaluate the maximum transmit distance. Figure 6.3 shows the maximum distance as function of data rate for PAM and PPM modulation schemes. The following assumptions have been made

- SER is lower than 10^{-5} ($N_s = 1,\ T_s = 3ns$)
- No fading margin required and PSD of noise is constant (E_b/N_0)

It is observed that BPAM (BPSK) has the best data rate over short distances with respect to complexity. However, by increasing the modulation level M, the M-PPM data rate can be improved ($SER_{8PPM} < SER_{4PPM} < SER_{2PPM}$) while the opposite occurs for M-PAM.

6.5 Channel Capacity

A channel with M-ary PPM/PAM modulation has discrete-valued inputs and continuous valued outputs, which imposes an additional capacity calculation. Let s_m be the encoded M-ary PPM/PAM signal vector input to the channel, and r_i the i^{th} diversity channel output vector corrupted by the AWGN noise vector, w_i, an M-dimensional Gaussian vector with zero mean and variance, $\delta_w^2 = \frac{N_0}{2}$ along each real direction (multi-path).

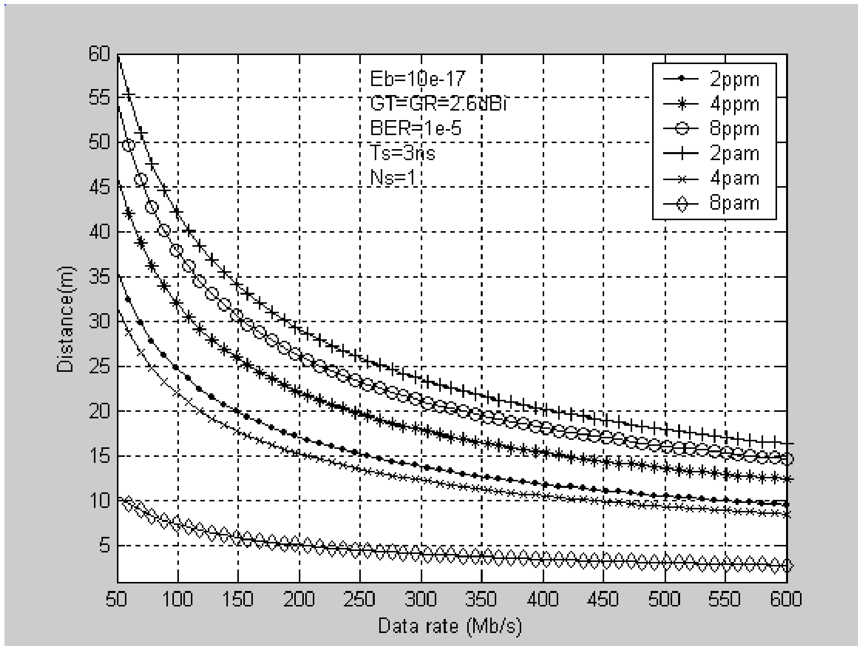

Fig. 6.3: M-PAM and M-PPM signals data rate for short distances and un-coded systems

This output vector is given by

$$r_i = s_m + w_i \quad 1 \le i \le L \tag{6.23}$$

where L is the number of multipaths. The channel capacity (Bits/channel) with input signals restricted to an equiprobable M-ary signal constellation and with no restrictions on the channel output, can be written as [14]

$$C = \log_2(M) - \frac{1}{M}\sum_{m=1}^{M}\int P(r/s_m)\log_2\left(\frac{\sum_{k=1}^{M}P(r/s_k)}{P(r/s_m)}\right)dy$$

$$P(r/s_m) = \prod_{i=1}^{L}\left[\left(\frac{1}{\pi N_0}\right)e^{\frac{-\left(ri-\sqrt{E}\right)^2}{N_0}}\right] \tag{6.24}$$

with P the probability of receiving a signal from the transmitter and N_0 the PSD of white noise.

For M-PAM over an AWGN channel, we obtain

$$C = \log_2(M) - \frac{1}{M}\sum_{k=0}^{M-1}\left\langle\left\{\log_2 \sum_{p=0}^{M-1}\exp\left(\sum_{i=1}^{L}\frac{\left|w_i\right|^2 - \left|s_k + w_i - s_p\right|^2}{N_0}\right)\right\}\right\rangle \tag{6.25}$$

where s_p is one of the M-ary PAM signals. For M-PPM, the probability of receiving a signal is [7], [8], [14]

$$P\left(r / s_m\right) = \prod_{i=1}^{L}\left[\left(\frac{1}{\pi N_0}\right)^{M/2}\left(\prod_{j=1}^{M} e^{-r_{ij}^2/2\sigma_T^{\,2}}\right)e^{-\left(r_{ij}-\sqrt{E_g}\right)^2/N_0}\right] \qquad r_{ij} = \sqrt{E_g} + w_{ij} \tag{6.26}$$

$$\sigma_T^{\,2}\left(n\right) = \sigma_{pre}^{\,2}(n) + \sigma_{post}^{\,2}(n) + \sigma_w^{\,2}$$

$$\sigma_{pre}^2(n) = \frac{1}{N}\sum_{k=-\infty}^{-1} h^2\left(n-k\right)$$

$$\sigma_{post}^2(n) = \frac{1}{N}\sum_{k=1}^{n} h^2\left(n-k\right) \quad \text{for n > 0}$$

where σ_T^2 is the total noise variance, E_g the signal energy, M the signal dimension, $\sigma_{pre}^2(n)$ the variance of the noise pulses preceding the present signal pulse at time n, $\sigma_{post}^2(n)$ the variance of the noise of the pulses following the present signal, and $h(n)$ the discrete channel response.

Giving the following channel capacity model for symmetric channel (Fig. 6.4), [8], [10], [12].

$$C_{M\_PPM} = \frac{1}{M}\sum_{i=0}^{M-1}\sum_{j=0, j\neq i}^{M-1}\frac{P_e}{M-1}\log\left[\frac{\frac{P_e}{M-1}}{\frac{1}{M}}\right] + \frac{1}{M}\sum_{i=0}^{M-1}\sum_{j=0, j\neq 0}^{M-1} P_{cm}\log\left[\frac{P_{cm}}{\frac{1}{M}}\right]$$

$$C_{M-PPM} = \log_2\left(M\right) + P_{cm}\ \log_2\left(P_{cm}\right) + (1-P_{cm})\log_2\left(\frac{1-P_{cm}}{M-1}\right) \tag{6.27}$$

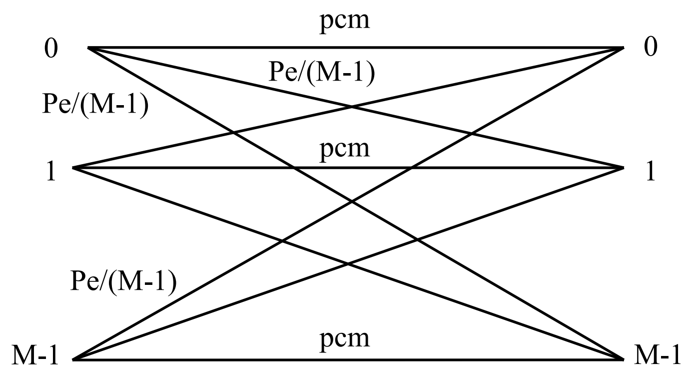

Fig. 6.4 : Channel capacity model for M-ary

Figures 6.5 and 6.6 show the channel capacity of various modulation schemes. From these figures, the capacity can be improved by increasing the modulation level for M-PPM, M-PAM and M-PSK. It shows that binary PAM-PSK requires lower SNR (4dB less) for a fixed channel capacity, which demonstrates its lower system sensitivity. But by increasing the modulation level, as expected due to orthogonally, the M-PPM capacity rapidly increases making it a good candidate compared to the complex PSK modulation. Note that the theory details about this comparison are expressed in Table 6.2.

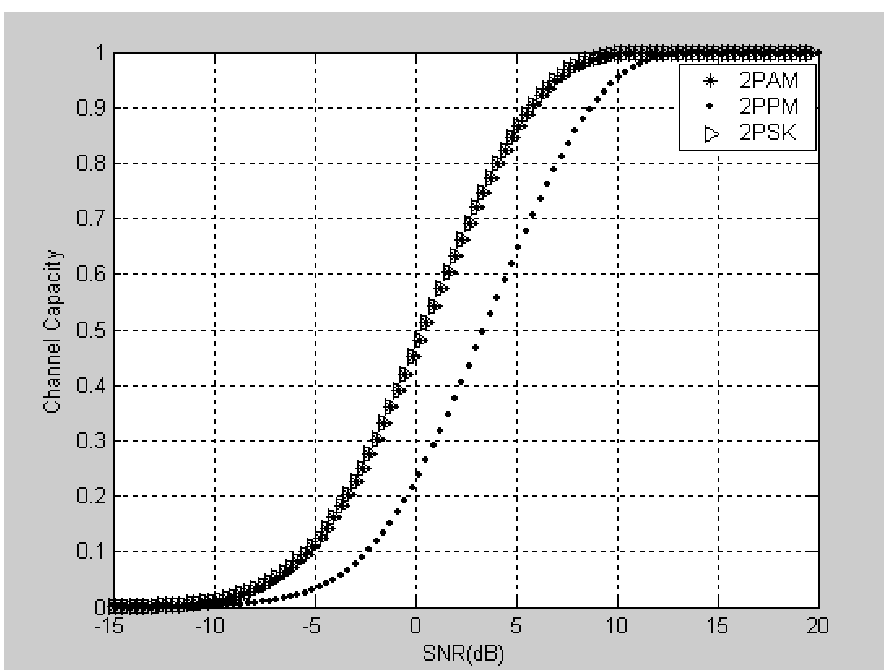

(a)

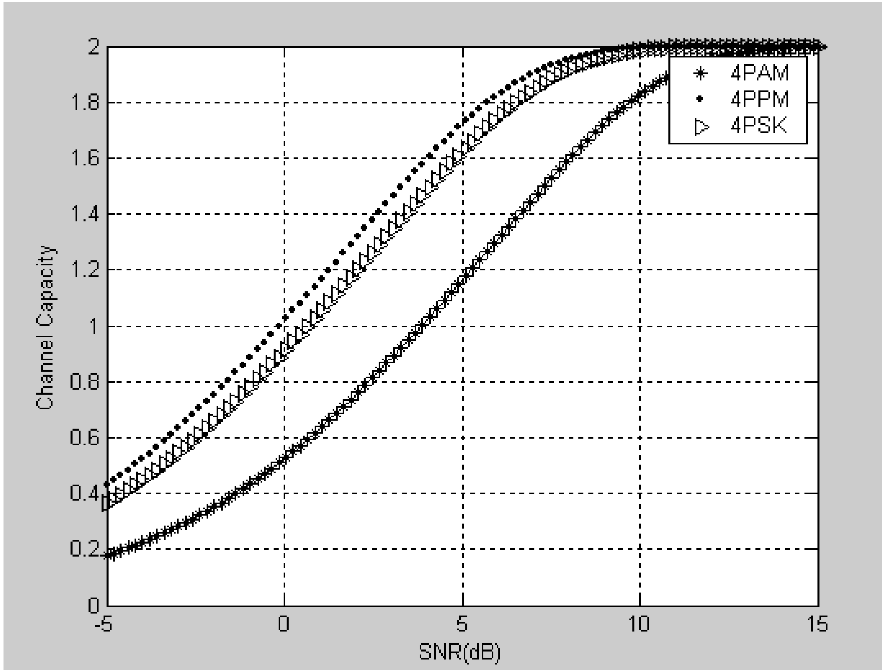

(b)

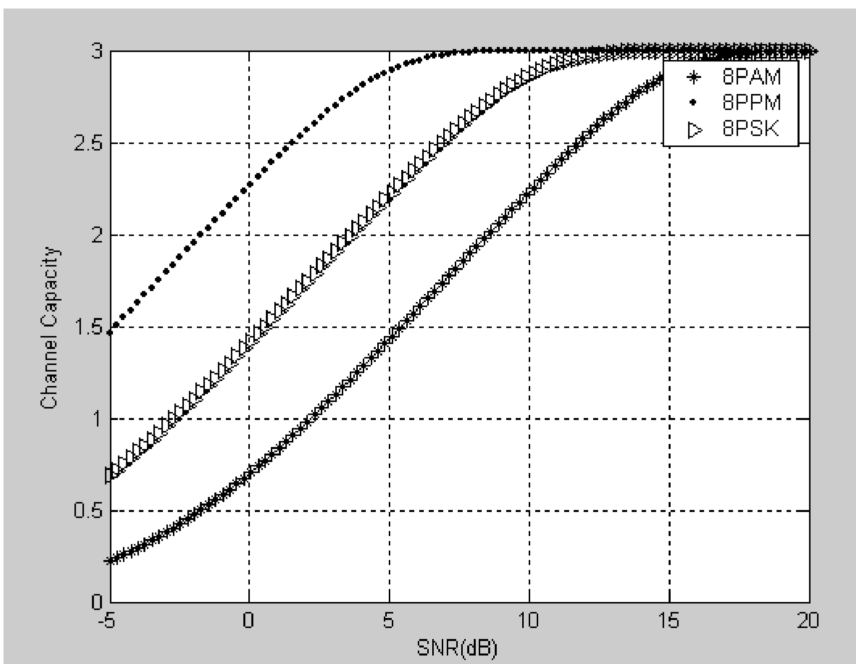

(c)

Fig.6.5: Channel capacity comparison of PAM, PPM, and PSK in various modulation levels.

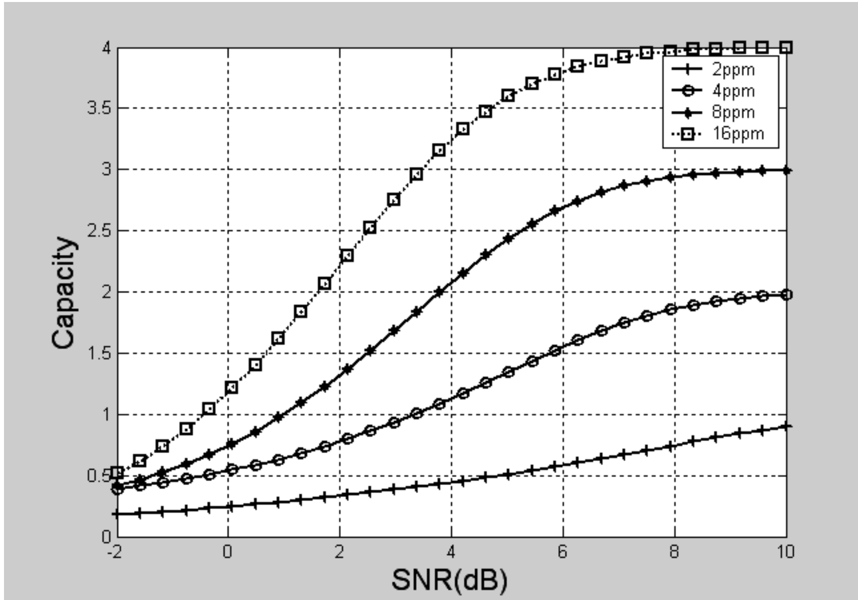

Capacity
SNR(dB)
2ppm
4ppm
8ppm
16ppm

(a)

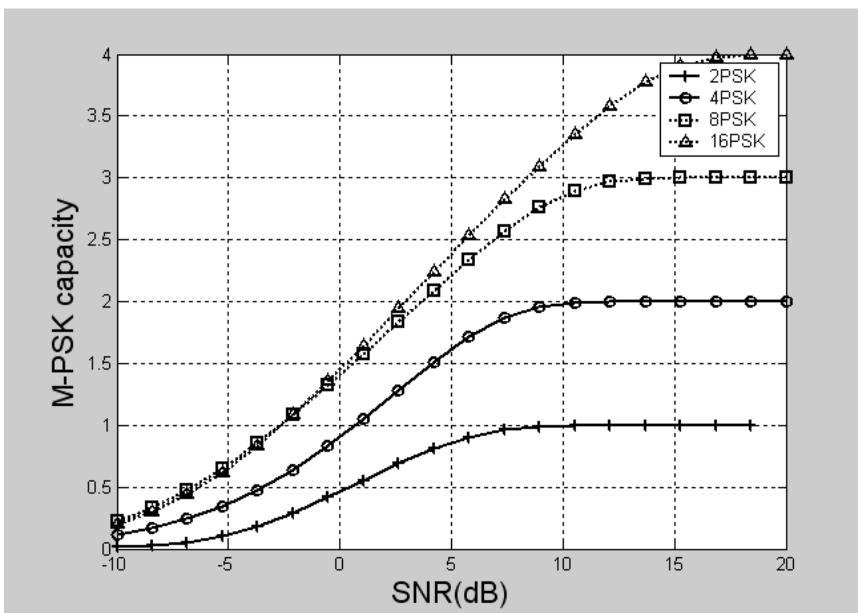

M-PSK capacity
SNR(dB)
2PSK
4PSK
8PSK
16PSK

(b)

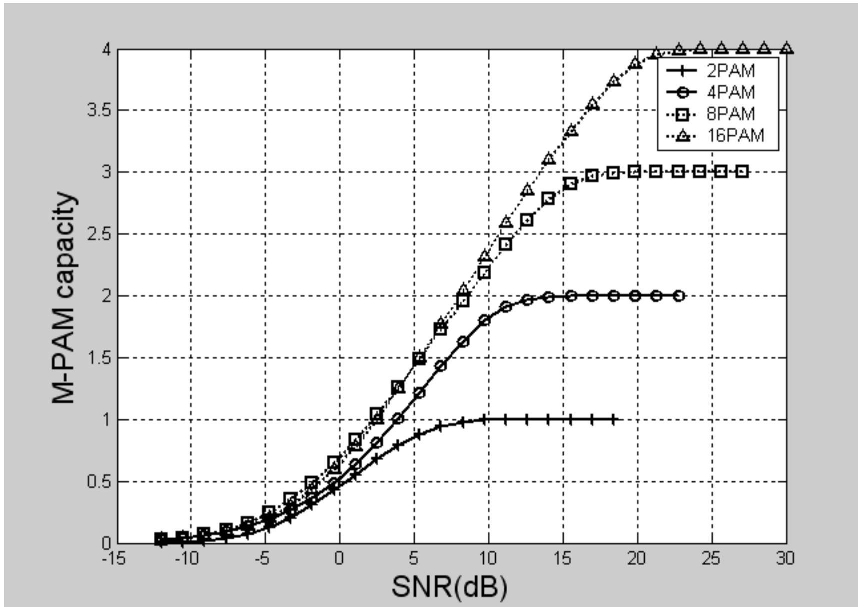

(c)

Fig. 6.6: Channel capacity of (a) M-PPM, (b) M-PSK, and (c) M-PAM modulations.

6.6 Maximum Transfer Power

From a communication theory perspective, the most important characteristic of UWB systems is the power-limited regime operation. Following standards and regulations, there is a maximum allowed transmit power P_t. This limitation has a direct impact on the maximum transmit distance and data rate, [15], [16].

$$\frac{P_t}{P_r}(dB) = C_0 + 10\chi \log_{10}\left(\frac{\lambda}{4\pi d}\right) + X_R(dB) \tag{6.28}$$

$$p_t(dB) = 10l\,og_{10}\left(\frac{M_s R_b E_b^0}{G_T G_R}\left(\frac{4\pi}{\lambda}\right)^2 d^2\right) \tag{6.29}$$

In the above equations, X_R is the average shadowing system, χ the path-loss component, and C_0 the maximum UWB pulse power, assumed to be -41.42dBm [15]. E_b^0 is the energy per bit (1.82. 10^{-19} W) for a specified BER of 5.10^{-5}.

In Fig. 6.7, we compared the transfer power for different modulation levels at a fixed data rate (200MHz) and as function of maximum transmitter power and distance. It can be seen that BPSK-soft decision has a higher maximum distance compared to other modulation schemes.

By increasing the modulation level *M*, M-PPM will be improved but M-PAM and M-PSK will exhibit a lower performance, due to more noise interference (noise dimensionality). Then again M-PPM has better narrowband interference robustness in terms of required less transmit power with respect to system complexity. Furthermore, the 4-PPM has an optimum modulation level which covers all tradeoff as sorted by table 6.2.

In Figure 6.8, we compared the 4-PPM in various data rates using the same transmitter and channel propagation scenario as in Fig. 6.7 for different modulation levels. As expected, by increasing distance, the data rate will decrease, requiring higher transmitter power. Also, for short distance applications (<10m), the data rate cannot exceed 200Mb/s even with an LOS scenario and AWGN channel assumption.

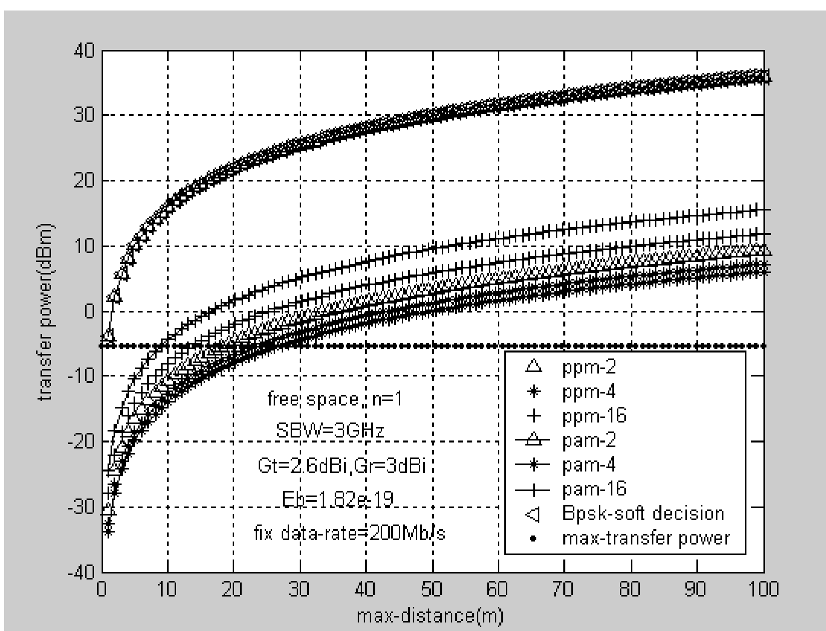

Fig. 6.7: Maximum transfer power for M-PAM-M-PPM, BPSK for a fixed data rate of 200Mb/s. The horizontal line (close to – 5dBm) represents the maximum transmit power specified by FCC regulations.

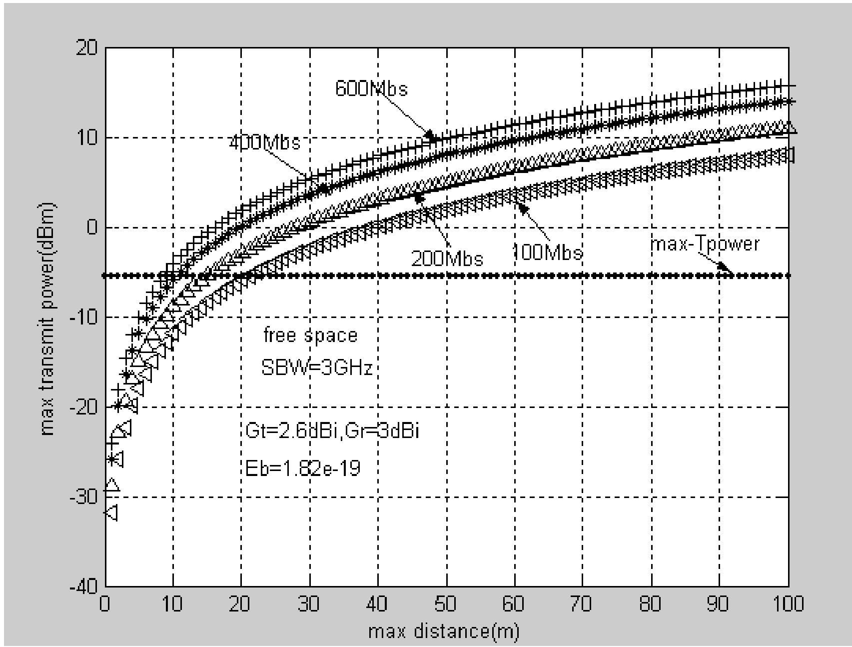

Fig. 6.8: Maximum transfer power for 4-PPM with various data rate. The horizontal line (close to – 5dBm) represents the maximum transmit power specified by FCC regulations.

This demonstrated that the UWB technology cannot practically provide the expected high data rate (>400-600Mb/s) unless a pulse coding is considered. In fact, with more complexity and higher modulation levels, the data rate can be significantly improved but with the cost of higher transmitter power.

6.7 Conclusion

Various UWB pulse modulation schemes were evaluated in this chapter and their performance compared in terms of narrowband interference robustness, symbol error rate, system complexity, data rate, and maximum transmit power with respect to transceiver distance and channel capacity.

It appears that the BPAM has the highest data rate in terms of maximum distance and transmit power. However, M-PPM has better power efficiency and channel capacity, at the expense of increased complexity and bandwidth.

If bandwidth is not an issue, the M-PPM is the best option, due to lower spectral lines (smoother PSD), higher dimensionality (orthogonally of noise) and narrowband interference robustness. However, if the UWB receiver is single band, the M-PPM is not the optimum option in terms of bandwidth.

If the system complexity and bandwidth are the limiting factors, OOK is the best choice, but has more spectral lines and higher probability of error which leads to higher risk of interference. Finally, because of signal orthogonally and lower spectral lines (smoother PSD), the 4-PPM (optimum modulation level) can be the best candidate for NBI robustness and can be used for unique UWB rake filter bank receiver design.

References

[1] A. Naanaa, S. Belghith, "Performance enhancement of a time hopping - pulse position modulation ultra-wide-band system using guided local search" *IET J. Communications,* Vol. 5, 2011, pp. 2212-2220.

[2] Q. Zhu, Z. Jia, C. Zou, "On the performance of different modulation schemes for UWB systems in a multipath channel," *IET Int. Conf. on Wireless, Mobile and Multimedia Networks,* 2006, pp. 1-4.

[3] R. Hidayat, Y. Miyanaga, "IR-UWB Pulse Position Modulation and Pulse Shape Modulation Through S-V Channel Model" *Int. Conf. on Communication Software and Networks,* 2010, pp. 214–217.

[4] A. Al Zaman, N. Islam, "Modulation schemes and pulse shaping in ultra-wideband " *IEEE. Southeast Conf.*, 2008, pp. 142 -146

[5] N. Chiu, B. Dagnachew, "Analysis of UWB Modulation Techniques" *Int. Conf. on Wireless Networks*, 2003, pp. 646-652

[6] M.G. Di Benedetto, G. Giancola, *Understanding Ultra Wide-Band Radio Fundamentals,* Prentice Hall, 2004.

[7] M. Ghavami, L.B. Michael, R. Kohno, *UWB Signals and Systems in Communication Engineering*, 2nd Ed., J. Wiley & Sons, 2007.

[8] M. Wang. T. Chang, "Performance Analysis and simulation of UWB-PAM communications in AWGN Channel" *Int. Conf. on Microwave and Millimeter Wave Technology,* 2004. pp. 830-833.

[9] Y. Zhenzhen, "Power spectral density and in-band interference power of UWB signals at narrowband systems," *IEEE Communications*, 2004, pp. 3561-3565.

[10] R. Passand, "Capacity of PPM ultra-wideband communications with inter pulse interference" *IEEE Canadian Conf. on Electrical and Computer Engineering,*, 2004, pp. 2355-2358.

[11] J. Nielsen, S. Zwierzchowski, "Power spectral density of a UWB signal with discrete quantized pulse positions", *IEEE Canadian Conf. on Electrical and Computer Engineering,* 2003, pp. 3-4.

[12] P.E. McIllree, “Calculation of channel capacity for M-ary digital modulation signal sets,” *IEEE Singapore Int. Conf. on Networks*, 1993, pp. 639-643.

[13] S.S. Mo, “On the power spectral density of UWB signals in IEEE 802.15.3a” *IEEE Conf. on Wireless Communications and Networking,* 2004, pp. 999-1003.

[14] L. Zhao, A.M. Haimovich, “Capacity of M-ary PPM ultra-wideband communications over AWGN channels”, *IEEE Vehicular* Vol. 2, 2001, pp. 1191-1195.

[15] H. Sheng, “On the spectral and power requirements for ultra-wideband transmission” *IEEE Communications*, 2003, pp. 738-742.

[16] S. Mayazulu, V. Srinivasa “Design challenges for very high data rate UWB systems”, *Int. Conf. on Signals, Systems and Computers*, 2002, pp. 717-721.

Chapter 7 UWB Pulse Shape Effects

7.1 Introduction

Impulse-radio ultra-wideband (IR-UWB) systems transit information using extremely short pulses that spread the energy from near DC to a few gigahertz without using a frequency carrier. This carrier-less technique greatly reduces the transceiver complexity and cost [1] but makes the UWB system performance strongly dependent on the pulse shape [2]-[4]. In fact, this later can significantly degrade the UWB system performance in terms of power spectrum density (PSD), BER, bandwidth and NBI cancellation. It is desirable for UWB signals to spread the energy as widely over the frequency band as possible to minimize the power spectral density (PSD), and hence the potential of interference to other user systems [4], [5], such as narrow-band systems like WLAN.

A variety of pulse shapes have been proposed for UWB impulse radio systems [4], which approach ideal transmitter power spectrum, avoiding DC components.

In this chapter, we evaluated different pulse shapes such as Gaussian monocycle (first derivative), Gaussian doublet (second derivative), their combination (linear, random, and LSE), as well as Hermite pulses. In addition, orthogonal pulses based on modified hermite polynomials were considered [6]. The target is to design optimal pulse waveforms that have the following properties:

- The pulse spectrum should be contained in the desired frequency band to satisfy the Federal Communications Committee (FCC) recommendations [1].
- The pulse should be limited to short duration with energy concentration.
- The pulse set is preferred to be orthogonal [6], [7].
- The pulse set is preferred to be flexibly combinable or extendible to fit any further spectral mask change in FCC requirements as well as any other regional regulatory committee around the world [2], [8].

7.2 Power limits and emission mask

The effective isotropic radiate power (EIRP) is defined as the highest signal strength measured in any direction and at any operating frequency from a radiating device. It is defined as, [8]

$$EIRP = P_{tx}G_{tx} \quad \rightarrow \quad EIRP = \frac{V_s^2}{377}4\pi D^2 \tag{7.1}$$

where P_{tx} is the maximum power at the input of the transmitter antenna, G_{tx} the transmitter antenna gain, and V_s the free space voltage (with impedance $Z_{fs} = 377\Omega$).

In UWB systems, the average power levels are shown in Fig. 7.1-7.2 and summarized in Tables 7.1-7.2 for indoor/outdoor propagation environment, indicating a radiated power of $200\mu v/m$ or $-49.18dBm/m$ [9]. Another important parameter to consider is the peak level of emission within a 50MHz bandwidth centered on a frequency f_m. For instance the quantity -43dBm/50MHz is the power limited to -43dBm over a frequency range of 50MHz around f_m.

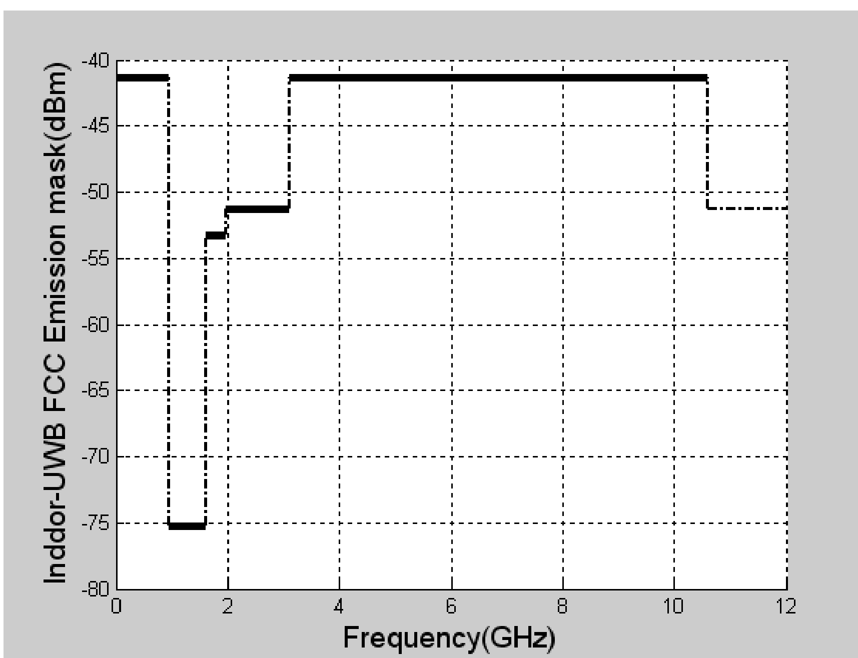

Fig. 7.1: UWB indoor emission mask [1], [9].

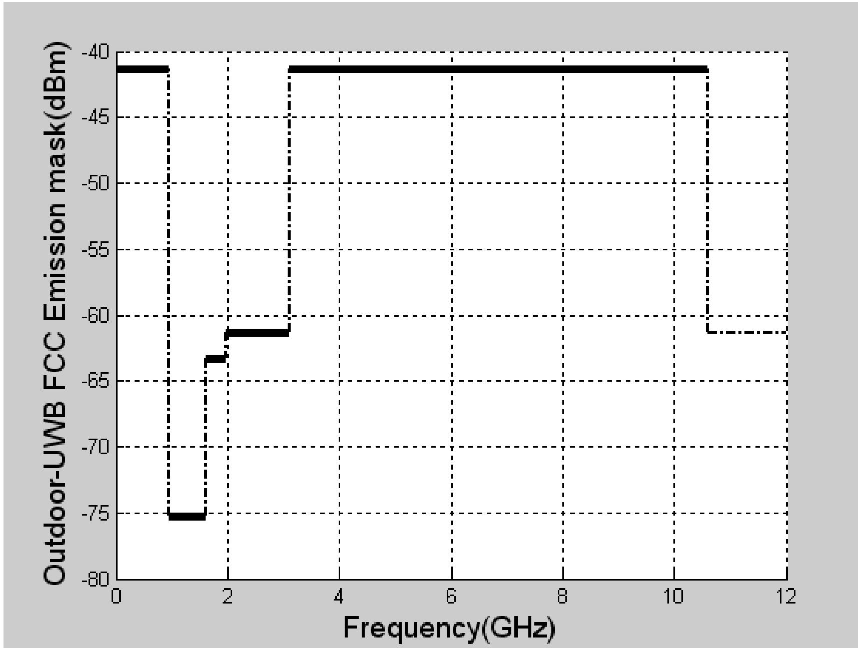

Fig. 7.2: Outdoor FCC UWB masks

TABLE 7.1: Indoor FCC-UWB average power limits

Frequency (GHz)	EIRP (dBm)
0-0.96	-41.3
0.96-1.61	-75.3
1.61-1.99	-53.3
1.99-3.1	-51.3
3.1-10.6	-41.3
Above 10.6	-51.3

TABLE 7.2: Outdoor FCC-UWB average power limits

Frequency (GHz)	EIRP (dBm)
0-0.96	-41.3
0.96-1.61	-75.3
1.61-1.99	-63.3
1.99-3.1	-61.3
3.1-10.6	-41.3
Above 10.6	-61.3

The maximum allowed total power, $P_{\max}$, for a signal of bandwidth $BW\,(f_l, f_H)$ is

$$P_{\max} = \int_{f_l}^{f_H} P_{tx}(f)df \quad f_l = 3.1GHz, f_H = 10.6GHz$$
$$P_{\max} \cong \frac{V_s}{377} 4\pi D^2 \frac{BW}{MB} \tag{7.2}$$

where MB is the measured bandwidth centered around the given frequency. The above equation can be reformulated as

$$P_{\max} = EIRP_{MB} \frac{\left(10.6\times10^9 - 3.1\times10^9\right)}{MB}$$
$$\rightarrow \quad 10\log_{10}\left(P_{\max}\right) = -41.3 + 10\log_{10}\left(7.5\times10^3\right) \cong -2.8dBm \tag{7.3}$$

where $EIRP_{MB}$ ($EIRP = EIRP_{MB}\dfrac{BW}{MB}$) is the maximum EIRP within the measured bandwidth MB and signal bandwidth BW. Note that the maximum allowed EPIR is equal to the sum of the $EIRP_{MB}$ values provided by the FCC emission mask corresponding to the frequency range occupied by the signal. For example, for a signal of BW=700MHz located within the UWB frequency range, 3.1GHz-10.6GHz, $P_{\max}$ is equal to

$$P_{\max} \cong \frac{V_s}{377} 4\pi(3)^2 \frac{700MHz}{1MHz} = -12.8dBm$$

7.3 General IR Transceiver model

The impulse radiated transmitted pulse can be expressed as [11]

$$p_{tx}(t) = m(t) * p(t) * a_{tx}(t) \tag{7.4}$$

where $m(t)$ is the modulating signal, $p(t)$ the pulse shape before the transmit antenna and $a_{tx}(t)$ the impulse response of the transmit antenna.

Thus the receive pulse can be expressed as:

$$p_{rx}(t) = p_{tx}(t) * h_{ch}(t) * a_{rx}(t) \tag{7.5}$$

where $h_{ch}(t)$ and $a_{rx}(t)$ are the impulse responses of the channel and the receiver antenna, respectively. By expressing the Fourier transform of (7.5), the frequency response of the pulse shape before radiation is derived as:

$$p_{tx}(f) = \frac{p_{rx}(f)}{A_{rx}(f)A_{tx}(f)H_{ch}(f)} \tag{7.6}$$

According to (7.5) and (7.6), the PSD of the transmitted signal is related to the pulse shape and modulation scheme.

7.4 Gaussian Pulse-Shape

The Gaussian pulse is often used in UWB systems because its shape can be easily generated [8]. It is simply a square pulse shaped by the limited rise and fall times of the pulse and the filtering effects of the transmitter and receiver antennas [12]. In this section, we analyze the effect of the pulse width (Pulse factor) variations and the pulse shape differentials on the system response, and then the effect of combining different waveforms that comply within the power limitations as set by the FCC emission masks.

The pulse shape that can be generated by a pulse generator has a bell shape (Equation (2.11)). Figure 7.3 shows the Gaussian waveform and its corresponding PSD with a fixed shape factor (β) or pulse duration.

Several pulse waveforms might be considered but the Gaussian derivatives are more suitable. As illustration, the one related to the second derivative of the Gaussian function can be expressed as

$$\frac{\partial^2 p(t)}{\partial t^2} = \left(1 - 4\pi \frac{t^2}{\beta^2}\right) e^{-\frac{2\pi t^2}{\beta^2}} \tag{7.7}$$

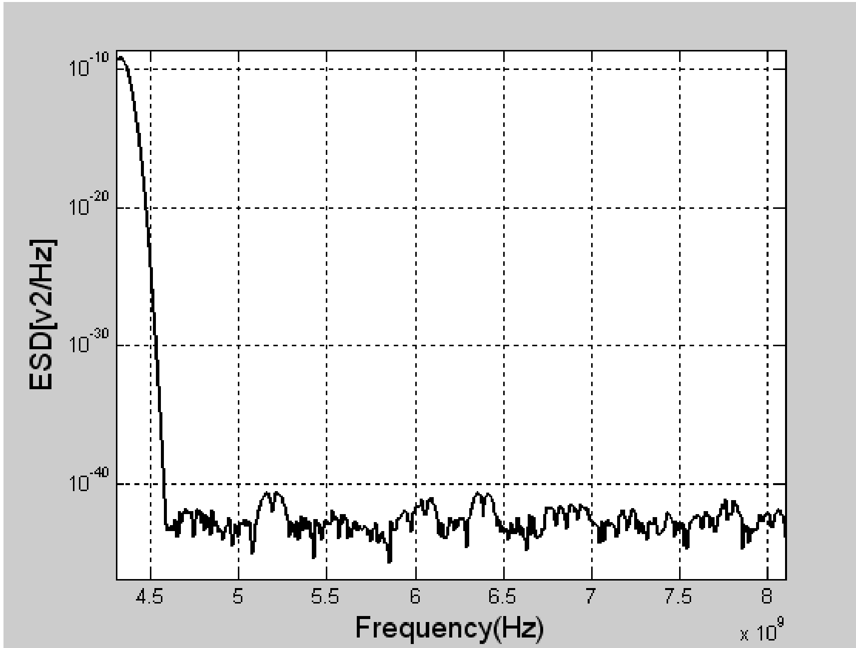

Fig. 7.3: Energy spectral density (ESD) of a Gaussian pulse.

Note that the second derivative of the Gaussian pulse is usually referred as "the pulse at the receiver". In other words, the second derivative will be obtained at the output of transmitting antenna if the antenna is fed with the first derivative of a Gaussian waveform.

7.4.1 PSD-Pulse width variation and differentiation

As illustrated in Fig. 7.4, the pulse width is related to the shape factor. Reducing the value of β will cause a shorter pulse and thus, increase the signal bandwidth. Therefore, we simulated the same waveform (Gaussian, 1st derivative) with a different shape factor.

As shown in Fig. 7.5, by increasing the shape factor the power will be shifted to a lower frequency and the pulse magnitude will decrease in frequency domain. Note that we cannot excessively increase the pulse duration (T_h) since that will result in inter-symbol interference (ISI). Differentiation of the Gaussian pulse also influences the PSD and it is possible to find a relation between the frequency, the order of differentiation (n), and the shape factor (β or T_h).

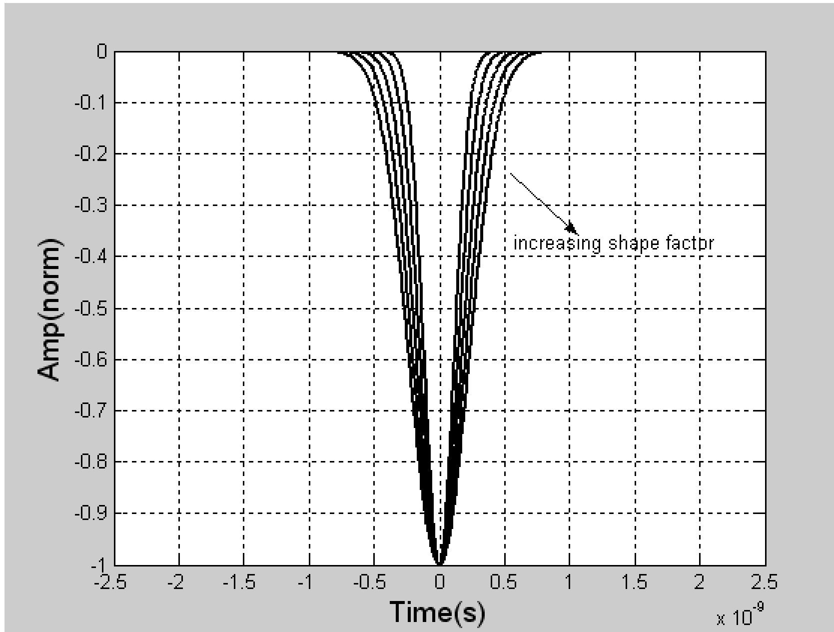

Fig. 7.4: Gaussian pulse in different pulse shape factor
$\beta = [0.3, 0.4, ...\ 0.8] \times 10^{-9}$

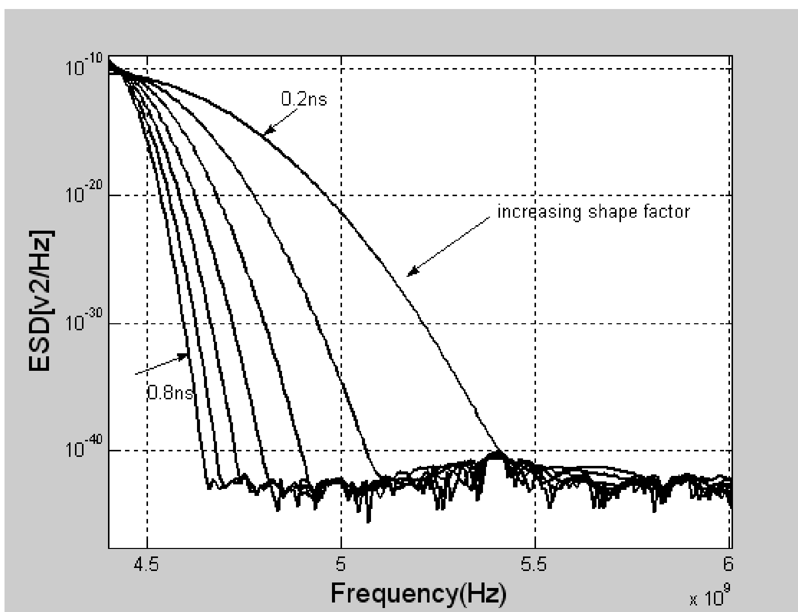

Fig. 7.5: ESD of Gaussian pulse in different shape factor (β)

To approach this matter, it is necessary to consider the Fourier transform of the n^{th} derivative of pulses, which has the following property [3]

$$P_n(f) \propto f^n e^{-\frac{\pi f^2 \beta^2}{2}} \qquad\qquad f = \sqrt{n}\,\frac{1}{\beta\sqrt{\pi}} \qquad (7.8)$$

This equation shows that increasing the order number will increase frequency. In other words, a higher differentiation will move energy to higher frequency bands, thus causing higher power efficiency and lower margin fading in particular frequency bands. Figure 7.6 shows the first ten derivatives of the Gaussian pulse as function of the shape factor. To further evaluate the effect of the differentiation order on the PSD, we determined the derivate waveforms (Fig. 7.7).

We limited the waveforms to the 4th order since higher orders are not practical. In fact, even in theory the Gaussian pulse can be infinitely differentiated, it is usually limited to 4 or maximum 5 derivatives.

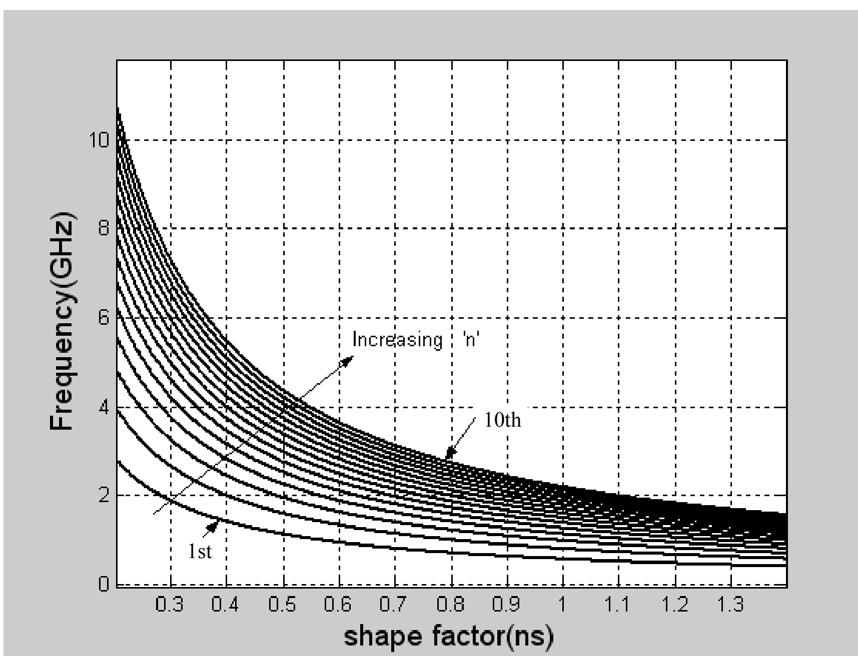

Fig. 7.6: Frequency function of the shape factor for the first ten derivatives of the Gaussian pulse.

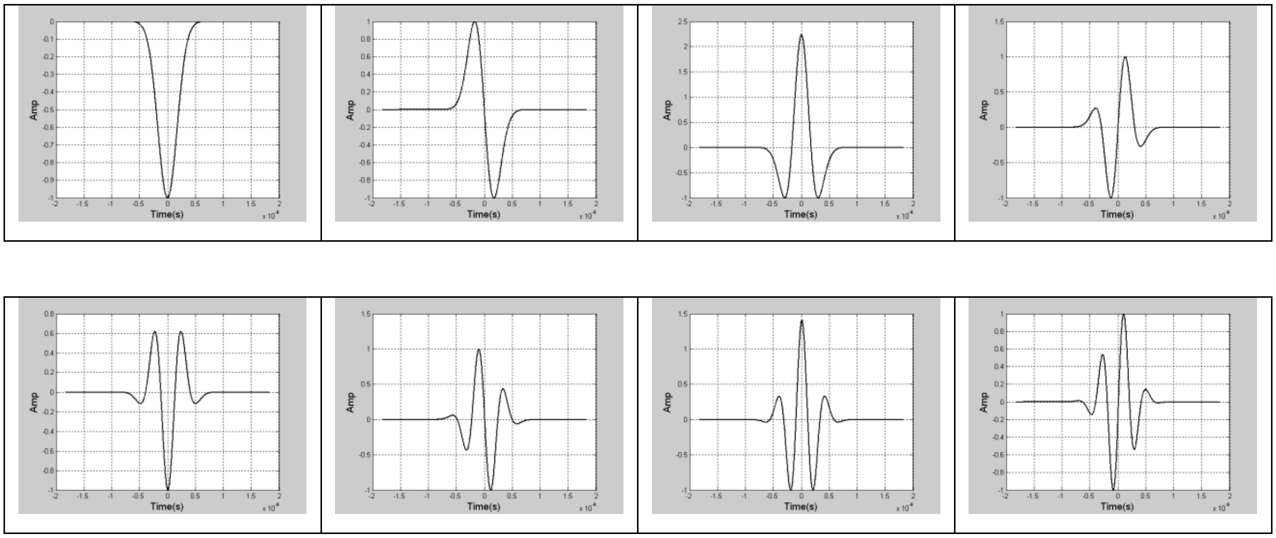

Fig. 7.7: waveform of the Gaussian pulse and its first 7th derivatives.

Therefore, let us consider the following equations by deriving the 1st Gaussian pulse shape equation.

$$
\begin{aligned}
p^{(1)}(t) &= \frac{\sqrt{2}}{\beta} e^{-\frac{2\pi t^2}{\beta^2}} \\
p^{(2)}(t) &= \frac{-4\sqrt{2}\pi t}{\beta^3} e^{-\frac{2\pi t^2}{\beta^2}} \\
p^{(3)}(t) &= \frac{-4\sqrt{2}\pi}{\beta^3} e^{-\frac{2\pi t^2}{\beta^2}} + \frac{16\sqrt{2}\pi^2 t^2}{\beta^5} e^{-\frac{2\pi t^2}{\beta^2}} \\
p^{(4)}(t) &= \frac{48\sqrt{2}\pi^2 t}{\beta^5} e^{-\frac{2\pi t^2}{\beta^2}} - \frac{64\sqrt{2}\pi^3 t^3}{\beta^7} e^{-\frac{2\pi t^2}{\beta^2}} \\
p^{(5)}(t) &= \frac{48\sqrt{2}\pi^2 t}{\beta^5} e^{-\frac{2\pi t^2}{\beta^2}} - \frac{384\sqrt{2}\pi^3 t^2}{\beta^7} e^{-\frac{2\pi t^2}{\beta^2}} + \frac{256\sqrt{2}\pi^4 t^4}{\beta^9} e^{-\frac{2\pi t^2}{\beta^2}}
\end{aligned}
\tag{7.9}
$$

Figure 7.8 shows the effect of the differentiation order on the pulse waveform and the Electrostatic discharge (ESD). Note that ESD is directly related to the PSD of pulse shape, i.e., by increasing the ESD, the PSD will be increase. As expected from (7.8), the simulations show that higher derivatives cause the ESD to move to higher frequencies.

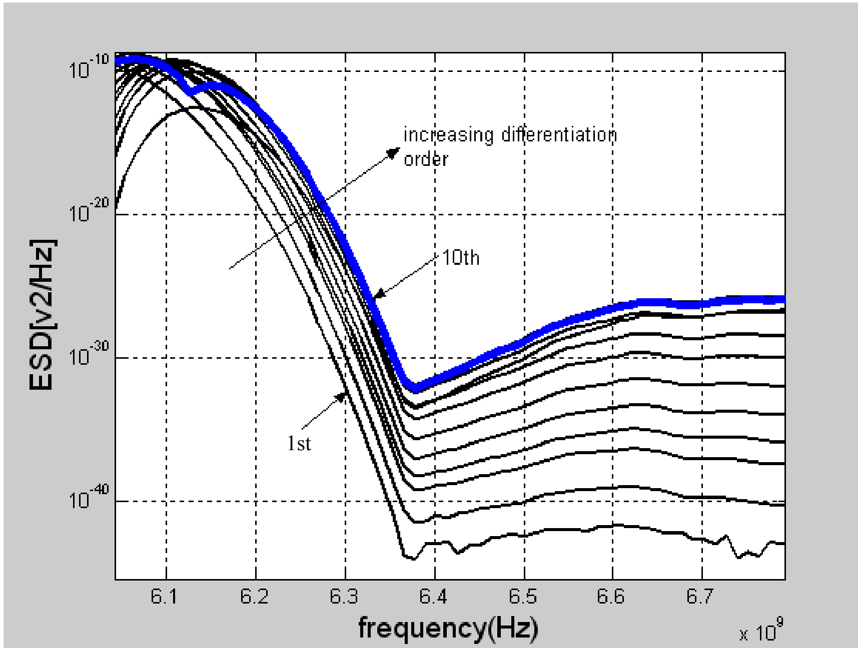

Fig. 7.8: ESD of the ten first derivatives of the Gaussian pulse with β =0.61

7.4.2 Gaussian pulse BER

The bit error rate in a white channel can be expressed as, [12]

$$\Pr_b = Q\left(\sqrt{\gamma_b\left(1 - R_0\left(\varepsilon\right)\right)}\right) \tag{7.10}$$

where $R_j\left(\varepsilon\right)$ is the autocorrelation of the pulse $p_j\left(t\right)$. If $R_0\left(\varepsilon\right)$ is positive, the receiver experiences a loss in performance, i.e., an increased signal energy will be required to achieve the same error probability. If $R_0\left(\varepsilon\right)$ is negative, the performance will be improved, showing the role of the PPM shift, ε, in the design of a PPM modulator. Figure 7.9 shows this improvement in terms of pulse autocorrelation for various order numbers. The optimum PPM shift, ε_{opt}, is the ε value that satisfies the following condition:

$$R_0\left(\varepsilon_{opt}\right) \le R_0\left(\varepsilon\right) \tag{7.11}$$

Thus, the bit error rate can be reduced by increasing the pulse duration, Fig. 7.10.

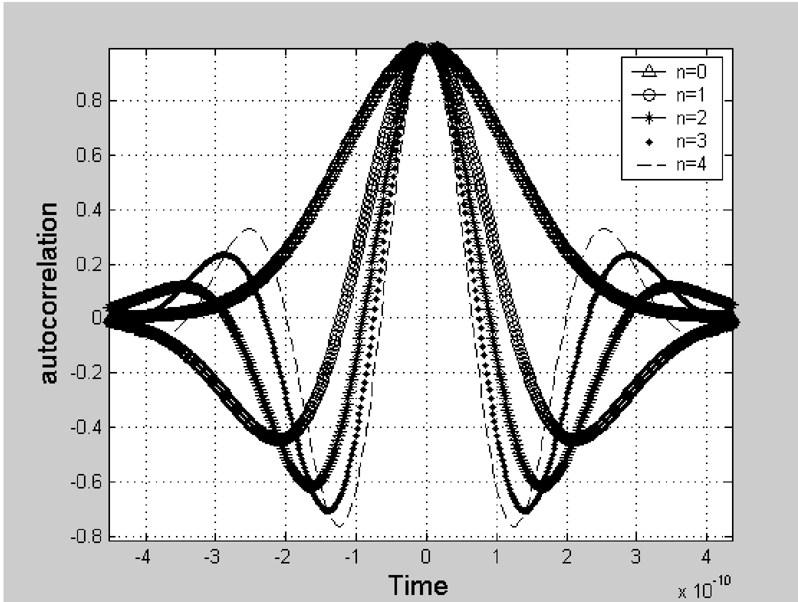

Fig. 7.9: autocorrelation of Gaussian pulses for different order numbers (derivations)

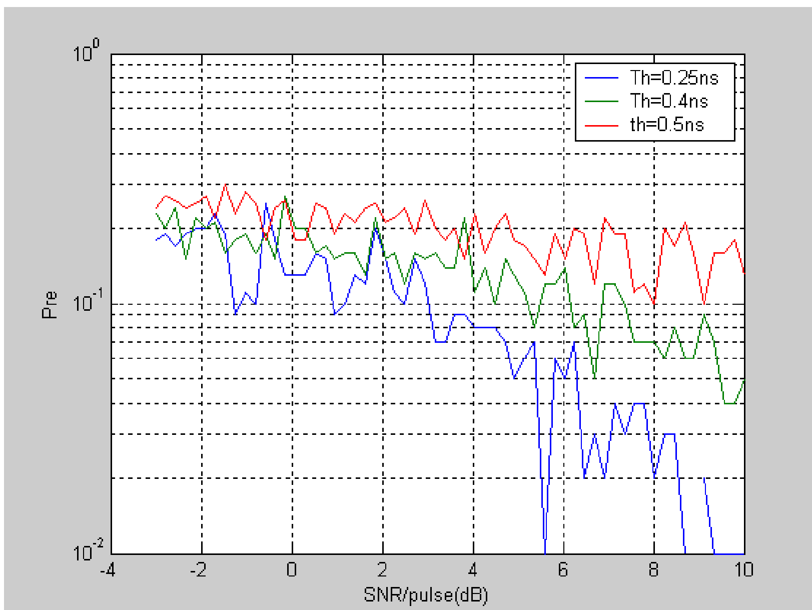

Fig. 7.10: BER in TH-PPM for different pulse durations
(Conditions: Multi-path channel, perfect synchronization, Monte-Carlo simulation)

This can be attributed to the following:

- By decreasing the pulse duration, the inter path/pulse interference (IPI) and the inter symbol interference (ISI) will be reduced (lower overlapping) and thus the BER performance will be improved. If the number of chip/frame ($N_c = \frac{T_s}{T_c}$) is close to the number of multi-paths N_r, the effect of IPI and ISI can be ignored and a better channel impulse response (CIR) is obtained, especially in an ENLOS case which deals with high multi-path numbers. By decreasing T_h it is possible to decrease T_c and thus, N_c will increase. Note that in multi-user case, reduction of T_h will be more effective and important.
- By decreasing T_h, the signal power moves to the desired frequency (3.1-10.6GHz), and the receiver captures more signal energy and thus increases the SNR. However, the synchronization will be complicated by reducing T_h ($T_h \prec$).

7.5 PSD of pulse derivation, pulse combination, and pulse period

It has been shown that both differentiation and pulse width variation affect the ESD of the Gaussian pulse. Meeting emission masks set by the regulation authorities is a typical task required from UWB designers. For this purpose, we analyzed the possibility of tuning the PSD by combining a single reference pulse and its derivatives (e.g., a Gaussian pulse and its derivatives).

For simplicity, we assumed that this combination is linear and that the generated waveform can be assimilated to one pulse instead of several. To adjust the ESD to satisfy the FCC masks, using a high number of Gaussian pulse derivatives and very narrow-band pulses (lower than T_h) should be avoided. Improved solutions will involve a combination of pulses that includes the following:

- Modified combination: combine the Gaussian derivatives either by using a same shape factor (Linear combination) or by choosing different β values for different derivatives, thus providing a high degree of flexibility while generating the pulse waveforms.

- Least square error (LSE) combination.

For each approach, we considered two cases: the first allows different β values for derivatives. However, this may require a higher number of iterations to guarantee the requested link. While in the second, all derivatives have the same β value.

Figure 7.11 shows a comparison between the required emission mask and the PSD of different Gaussian derivatives and the modified combination when the same pulse shape β=0.614ns is applied.

For the second case, the results in Fig. 7.12 show that we have a better approximation of the mask than in the first case, thanks to the increased bandwidth of the higher derivatives. However, the implementation of the modified (Random) combination will be easier than the higher pulse derivatives [3].

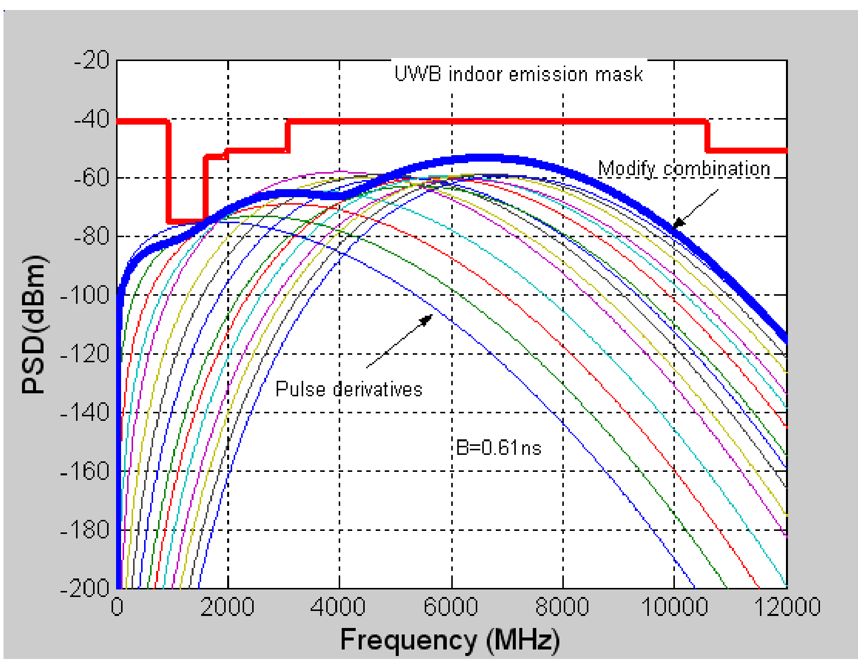

Fig. 7.11: PSD of the Gaussian pulse derivatives and the modified combined waveforms with the emission mask. β=0.614ns

As in Fig. 7.13, the PSD of the modified combination will move to lower frequency band by reducing the pulse period T_s. But in practice, it is not recommended to change T_s, since increasing T_s results in low data rate and decreasing T_s is limited by channel delay.

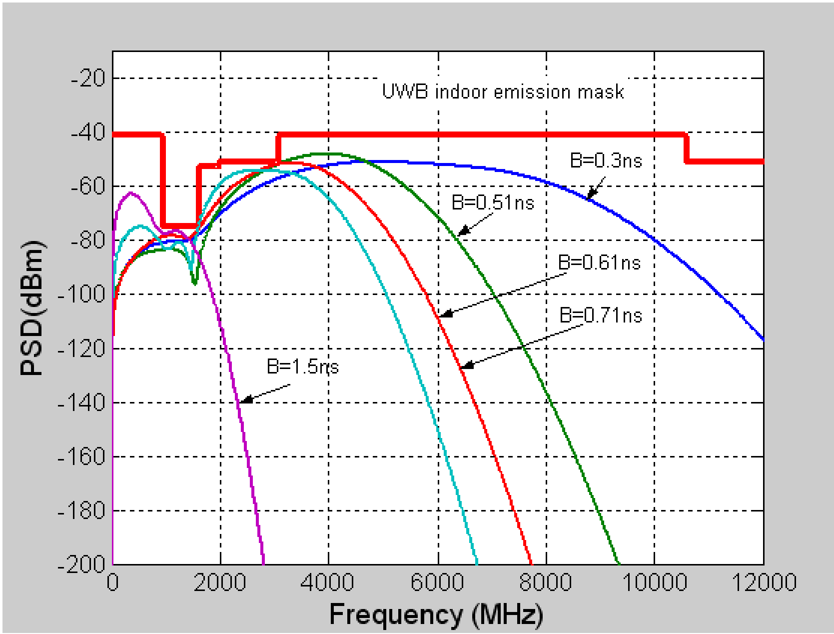

Fig. 7.12: PSD of the modified combined waveform with different β.

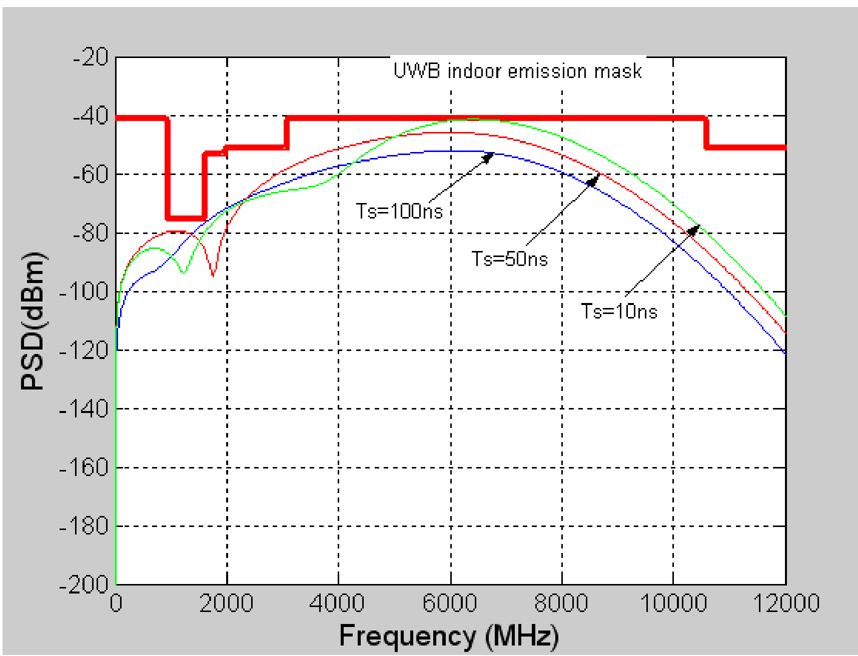

Fig. 7.13: PSD of the modified combination for different pulse periods.

A more systematic way of selecting such coefficients is to apply standard procedures for error minimization such as the least square error (LSE), in which the following error function must be minimized [8]

$$e = \int_{-\infty}^{+\infty} \left| P_M(f) - F(f) \right|^2 df \qquad (7.12)$$

where $P_M(f)$ represents the emission mask and $F(f)$ the PSD of the linear combination (Modified combination with same shape factor).

The PSD envelope is mainly determined by the Fourier transform of the impulse response $P(f)$ of the pulse shape. Using $P(f)$ in place of the exact PSD simplifies the optimization problem while computing the voltage $v(t)$ representing the mask bound in time-domain. The targeted emission voltage mask can be obtained by dividing the power emission mask, normalized by $1/T_s$, by the free space impedance, taking the square root, and applying the Fourier transform. In this case, the error can be defined as:

$$e = \int_{-\infty}^{+\infty} \left| v(t) - \sum_{n=1}^{N} a_n f_n(t) \right|^2 dt \qquad (7.13)$$

As a general remark, the LSE method cannot guarantee by itself compliance with the emission mask. The optimization procedure is based on an average quadratic distance and does not impose bounds on a frequency-by-frequency basis. In order to guarantee compliance with mask for each frequency, error minimization should be performed. Compared to linear combination, the LSE method has a better power efficiency, Fig. 7.14.

Figure 7.15 compares the PSD of the LSE and the linear combination for different pulse shapes. As expected, decreasing the pulse width moves the power to the high frequency bound and causes high power efficiency as well as lower bit error rate. Note that by increasing T_s or decreasing the PSD of the linear combination, the LSE could be fixed to the Emission mask, Fig. 7.15-b.

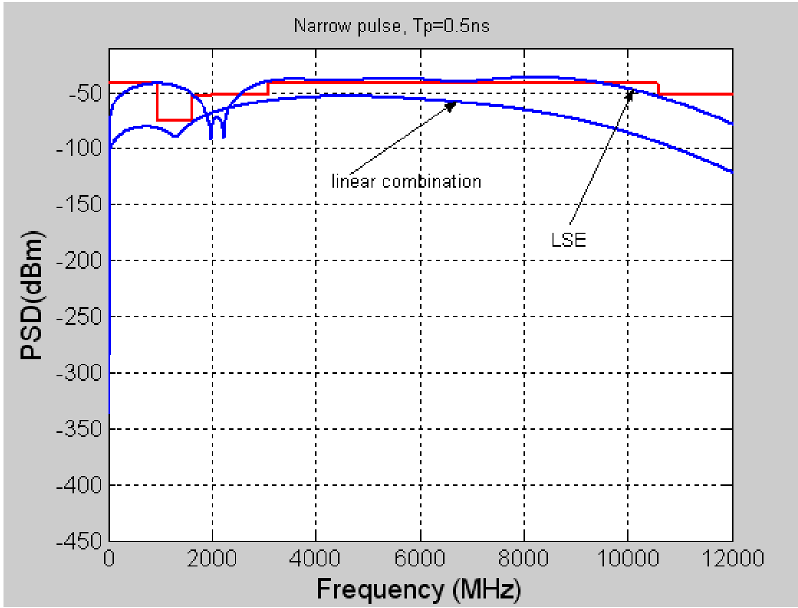

Fig. 7.14: Comparison of the PSD of LSE and linear combination ($\beta = 0.31$, $T_s = 10^{-8}$)

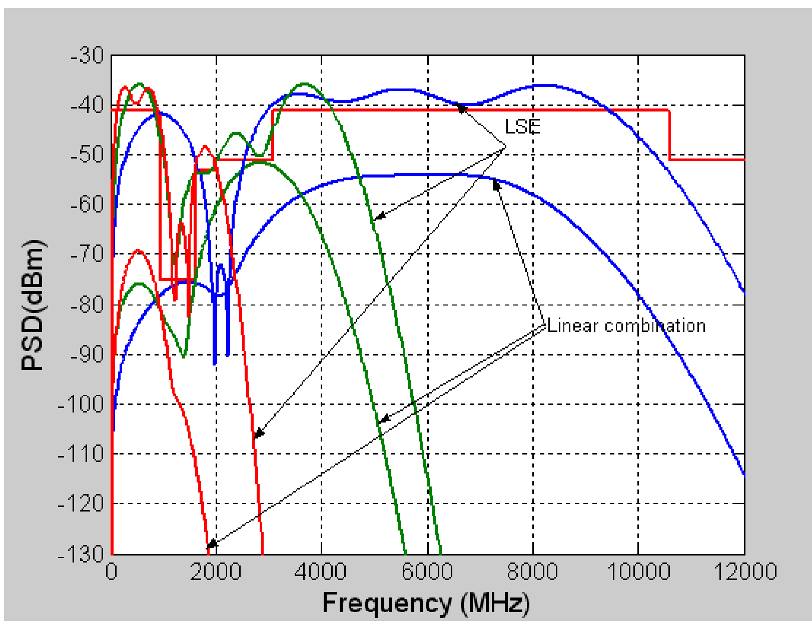

a)

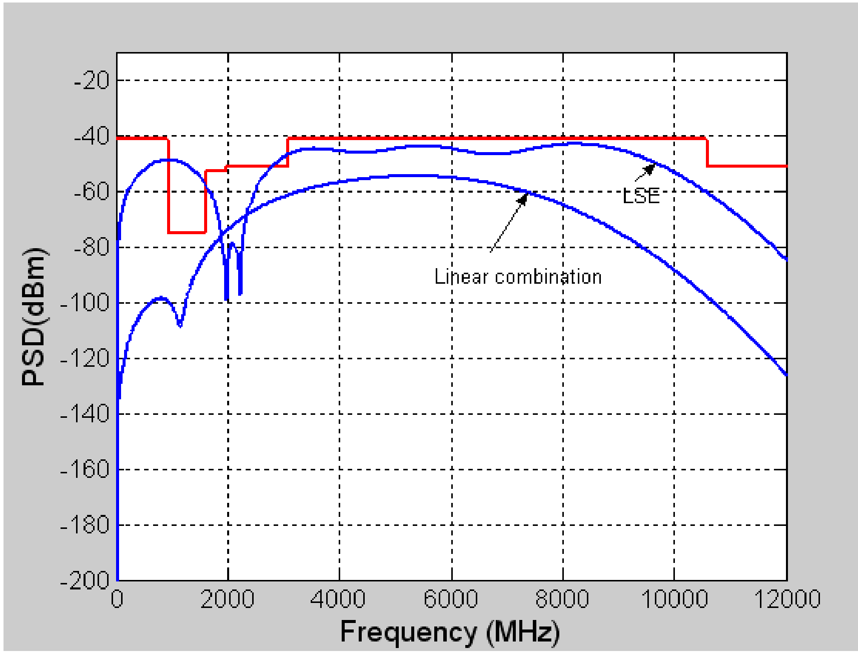

b)

Fig. 7.15: a) Comparison of the PSD of LSE and linear combination for different pulse factors, $T_s = 10^{-8}$, b) Lower PSD of linear combination.

7.6 Hermite-Based Orthogonal Pulses

The *sine and cosine* system is known historically as a set of orthogonal functions in communication systems. In recent years, other complete systems of orthogonal functions have been used for theoretical investigations as well as for equipment design. The use of modified Hermite polynomials to create an orthogonal transform or even to create orthogonal wavelets for multi-carrier data transmission over high-rate digital subscriber loops has been proposed [13]. The Hermite polynomial is defined by [6], [13]

$$p_{e_n}(t) = (-\tau)^n e^{\frac{t^2}{2\tau^2}} \frac{d^n}{dt^n}\left(e^{-\frac{t^2}{2\tau^2}}\right) \qquad (7.14)$$

where $n = 0, 1, 2, \ldots$, $-\infty < t < +\infty$ and τ is the time-scaling factor (pulse width regular element).

By expanding the equation (3.16), we obtain

$$p_{e_{n+1}}(t)=\frac{t}{\tau}p_{e_n}(t)-\tau\frac{d}{dt}\left(p_{e_n}(t)\right)\qquad \frac{d}{dt}\left(p_{e_n}(t)\right)=\frac{n}{\tau}p_{e_{n-1}}(t) \tag{7.15}$$

As shown, the Hermite polynomials are not orthogonal; however, they can be modified to become orthogonal as follows

$$p_{e_n}(t)=(-\tau)^n e^{\frac{t^2}{4\tau^2}}\tau^2\frac{d^n}{dt^n}\left(e^{-\frac{t^2}{2\tau^2}}\right) \tag{7.16}$$

The result is a set of orthogonal functions $p_{e_n}(t)$ which can be easily derived for all values of *n*, Fig. 7.16. It has been proven that different orders of modified Hermite pulses have lower SER than conventional pulses [11]. In addition, in a multi-user system, the orthogonal pulses can be assigned to different users to decrease the co-channel ISI and BER, [11], [13].

Based on simulations, we achieved the following:

- The pulse duration and the bandwidth are almost the same for all values of *n*.
- The pulses are mutually orthogonal.
- The pulses have non-zero DC components (n =0), and in fact, the low frequency components of the pulses are relatively significant, Fig. 7.17.

The autocorrelation of the modified Hermite pulses for different *n*, displayed in Fig. 7.18, shows that the width of the main peak becomes narrower as the order increases.

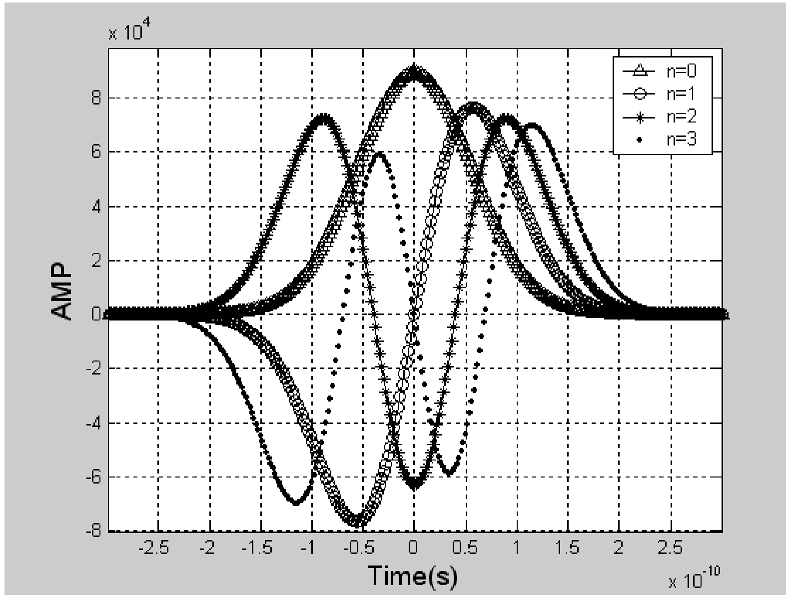

Fig. 7.16: Waveform of Hermite orthogonal pulses for different orders

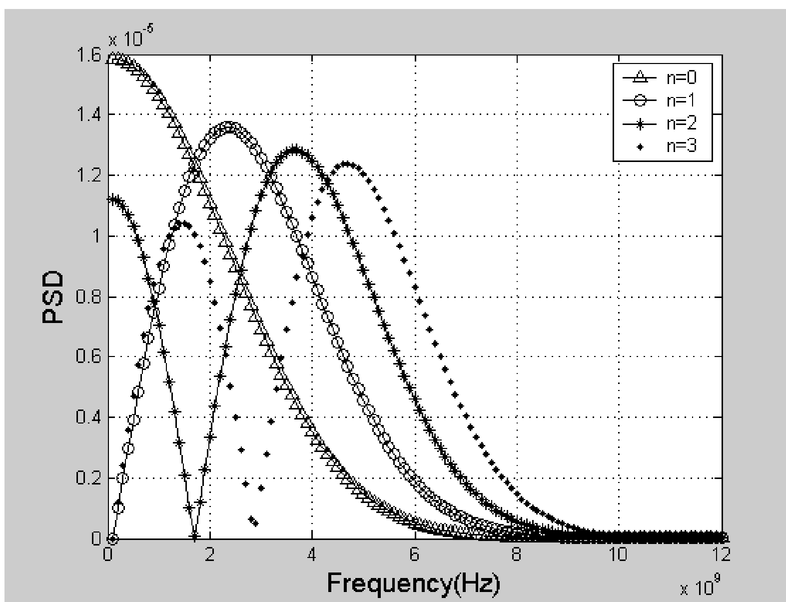

Fig. 7.17: PSD of the Hermite orthogonal pulses for different orders

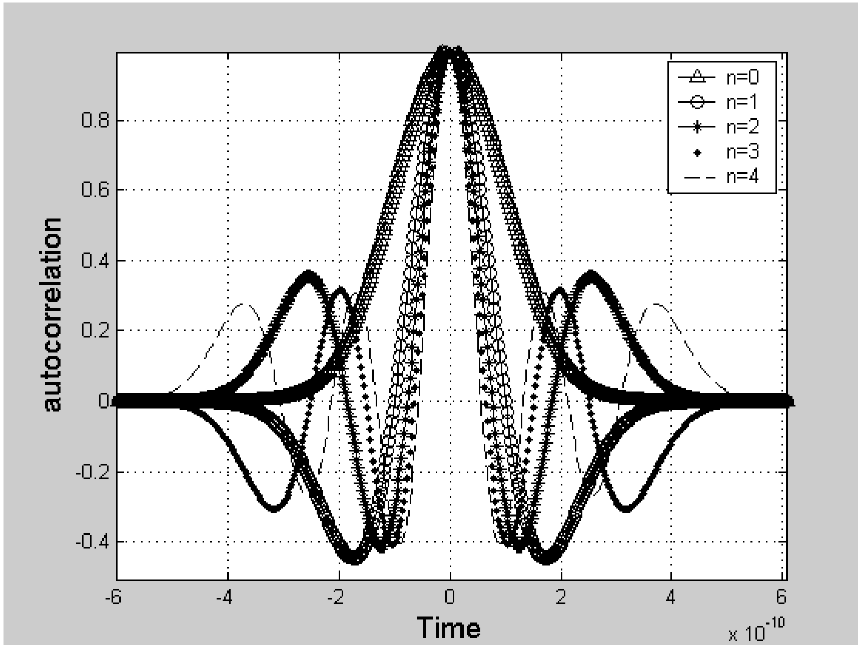

Fig. 7.18: Autocorrelation of the modified Hermite pulses for different orders.

7.7 Conclusion

In this chapter, we demonstrated that both differentiation and pulses width variation affect the PSD of a Gaussian pulse and can be used to shape the transmitted waveform. According to FCC specifications on UWB radio frequency constraints, a pulse shape for indoor UWB devices should be strictly limited in time to remove interference while at the same time, should have its power distribution inside the 3.1-10.6GHz frequency band. To maintain this wide bandwidth, improved performance and avoid complexity, the fifth-order derivative was found to be good candidate for indoor systems. By increasing the shape factor and decreasing the differentiation order, the power will be spread over a smaller bandwidth. This can be used to occupy different bandwidths by adjusting the shape factor.

Finally, the Gaussian pulse has been chosen due to its simple circuitry. On the other hand, other pulse shapes and corresponding derivation levels exhibit slightly better performance but they add more complicity to the transmitter section, therefore limiting significantly their usage.

References

[1] M.G. Di Benedetto, G. Giancola, "Understanding ultra wide-band radio Fundamentals" Prentice-Hall, *chaps. 2, 6, and 8*, 2004.

[2] K. Fan, S. Zhang, X. Liu, "A UWB pulse shapes modulation scheme based on modified Hermite polynomials" *Int. Conf. Wireless Communications, Networking and Mobile Computing*, 2008.

[3] W. Li, P. Wu, X. dong, J. Zhang, "Improved UWB pulse shaping method based on Gaussian derivatives," *Int. J. Wireless Mobile and Computing*, pp. 438-442, 2011.

[4] S. Mo, "On the power spectral density of UWB signals in IEEE 802.15.3a" *IEEE Wireless Communications and Networking Conf.,* pp. 999-1003, 2004.

[5] B. Hu, N.C. Beaulieu, "Pulse shaping in UWB communication systems", *IEEE Vehicular Technology Conf.*, pp. 5175-5179, 2004.

[6] D. Abreu, G. Thadeu, "Jitter-robust orthogonal Hermite pulses for ultra-wideband impulse radio communications", *J. Applied Signal Processing*, pp. 369-381, 2005.

[7] M. Ghavami, L.B. Michael, "A novel UWB pulse shape modulation system", *Wireless Personal Communications*, Vol. 23, pp. 105-120, 2002.

[8] H. Ling, H.X. Zhang, Y.H. Lu, "A novel method to generate UWB shaping pulses based on chip pulse," *Int. Conf. on ITS Telecommunications,* pp. 290-293, 2006.

[9] M.-G. Di Benedetto, B.R. Vojcic, "UWB wireless communication tutorial", *J. Communication* Vol. 5, pp. 290-302, 2003.

[10] X. Chen, S. Kiaei, "Monocycle shapes for ultra wideband system," *IEEE Int. Symp. on Circuits and Systems*, pp. I/597-I/600, 2002.

[11] W. Hu, G. Zheng, "Orthogonal Hermite pulses used for UWB M-ary communication" *Int. Conf. on Information Tech.: Coding and Computing,* 2005.

[12] J.T. Conroy, J.L. Lo Cicero, D.R. Ucci, "Communication techniques using monopulse waveforms", *IEEE Military Communications Conf.*, pp. 1181-1185, 1999.

[13] C. Mitchell, R. Kohno, "High data rate transmissions using orthogonal modified Hermite pulses in UWB communications", *Int. Conf. Telecommunications,* pp.1278-1283, 2003.

Chapter 8 NBI Cancellation in UWB RAKE Receivers

8.1 Introduction

Ultra wide-band (UWB) communication systems have been extensively studied in the recent few years due to their wide potential applications, particularly in short-range access wireless communications. However, some key UWB receiver parameters, such as narrowband interference (NBI), still need more investigation for optimum performance, especially in the presence of color noise. In fact, NBI plays a crucial rule in UWB receiver performance since it reduces the receiver signal-to-noise ratio (SNR), thus directly affecting the probability of error and consequently, the system capacity [1].

Though UWB pulses propagating through obstacles can be scattered, creating multipath pulses that remove energy from the primary pulse, UWB technology allows the separation of the direct pulse [2]. One of the solutions for increasing the receiver SNR is to use a RAKE receiver, which takes the advantage of UWB selective frequency fading to combine energy from multipath pulses. However, in case of extreme non-line-of-sight (ENLOS) and channel delay, the rake receiver requires more correlators, thus leading to higher circuit complexity [3].

An ideal RAKE receiver (IRAKE), expected to capture all multipath energy, can be used as reference. But in practice, a partial RAKE (PRAKE) or selective RAKE (SRAKE) receiver is more suitable [4]. In this work, a simple PRAKE receiver structure is proposed, which combines the number of selective paths (LP) and the first arrival path out of the total multipath (LI) components [5]. To reach such target, we analyzed the performance of PRAKE while optimizing the number of fingers of the filter bank (FB), its stepped impedance resonator (SIR), and the symbol error rate (SER) [6]. We also assumed a causal, statistical channel including interference noise (color noise), tones and narrowband noise.

In terms of pulse modulation, M-pulse position modulation (M-PPM) and M-pulse amplitude modulation (M-PAM) were considered. As for the shape, we assumed up to the fifth derivative of a Gaussian pulse [7].

We also used the indoor UWB IEEE channel model [8], which considers statistical path loss for ENLOS and the effects of pulse shape and distribution in different environments to efficiently predict the overall performance of UWB systems.

8.2 Pulse Modulation for NBI Cancellation

In narrowband cancellation, the first step is to select the most suitable modulation type and level that allow both circuit simplicity and efficient SER performance. To achieve that, different pulse modulation receiver schemes such as the M-PAM and the M-PPM were first evaluated with additive white Gaussian noise (AWGN) channel model [6]. Then, other types of noises were considered.

8.2.1 IR-UWB Receiver

This section analyzes the receiving signal after propagating over the radio channel. We first assumed perfect synchronization between transmitter and receiver (in real case, due to the very short pulse duration, receiver performance is sensitive to synchronization error [2]).

The UWB radio signal is ideally composed of a sequence of pulses that do not overlap in time. While ISI among pulses is ideally absent in the transmitted signal, it might not be the case after the signal has traveled through a real channel. For example, the pulses might be differently delayed, and replicas of pulses due to multi-path may cause ISI.

At the receiver, the reference signal is corrupted by two main noise components [6]. The first group is the narrow-band noise that can be represented by a white Gaussian random process. The second noise source is the tone/multi-tone noise.

In continuous transmission, multi-path causes rapid fluctuations in the receiver signal envelope, thus severely degrading the receiver performance. On the other side, in the IR-UWB case, multi-path reflections result in a sequence of delayed and attenuated replicas of the transmitted pulse. Therefore, by combining the multi-path pulses, the energy used in the decision process can be increased.

8.2.2 UWB receiver in multi-path-free AWGN channel

Let $r_u(t)$ be the useful signal at the receiver. This signal could be corrupted by additive thermal noise $n(t)$, assumed to be a stochastic Gaussian process with a two sided PSD $\frac{N_0}{2}$. The total receiver signal can be expressed by [2]:

$$r(t) = r_u(t) + n(t) \tag{8.1}$$

$$r_u(t) = h(t) * S(t) \tag{8.2}$$

where $S(t)$ is transmitter signal, $h(t)$ is channel impulse response and $r_u(t)$ is an attenuated and delayed version of the transmitted signal(receiver signal), with different modulation schemes.

$$r_u(t) = \chi S(t-\tau) \tag{8.3}$$

In this equation, the channel gain (attenuation) χ and the delay τ depend on the propagation distance *D* between the transmitter and the receiver. τ can be obtained from $\tau = \frac{D}{C}$ where *C* is the speed of light. An optimum receiver for an AWGN channel is composed of two blocks: the correlator and the detector. The role of the correlator is to convert the receiver signal into a set *Z* of decision variables, while the role of the detector is to decide which signal waveform was transmitted. Assuming that the transmitter sends information using different waveforms, $S_m(t)$, within a symbol interval, T_{sym}, $S_m(t)$ can be generated by N orthogonal basis functions, written as [9]:

$$S_m(t) = \sum_{k=0}^{N-1} S_{mk} \Psi_k(t) \tag{8.4}$$

with

$$S_{mk} = \int_0^T S_m(t)\Psi_k(t)\,dt \tag{8.5}$$

After substitution the receiver signal can be rewritten as

$$r(t) = \sum_{k=0}^{N-1} \chi S_{mk}\Psi_k(t-\tau) + n(t) \tag{8.6}$$

The output decision variable Z_k of the correlator receiver for $r(t)$ (Fig. 8.1) can be expressed as

$$Z_k = \int_{\tau}^{T_{sym}+\tau} r(t)\Psi_k(t-\tau)\,dt = \chi S_{mk} + n_k \qquad n_k = \int_{\tau}^{T_{sym}+\tau} n(t)\Psi_k(t-\tau)\,dt \tag{8.7}$$
$$k = 0,\ldots..N-1$$

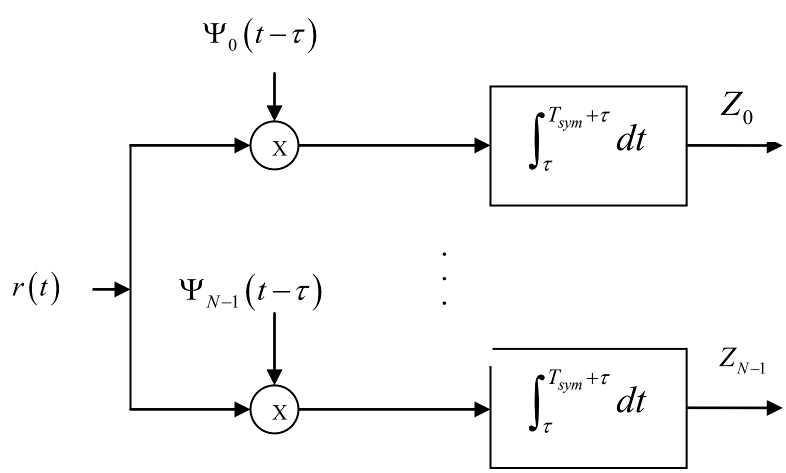

Fig. 8.1: Structure of the receiver signal correlator

Let the noise components, n_k, be uncorrelated Gaussian variables with $\mu = 0,\ \sigma^2 = \frac{N_0}{2}$. The Maximum likelihood (ML) criterion was applied to optimum detection of the signal. It selects among the *M* possible transmitted waveforms. Figure 8.2 shows the optimum receiver for AWGN channel based on the ML criterion.

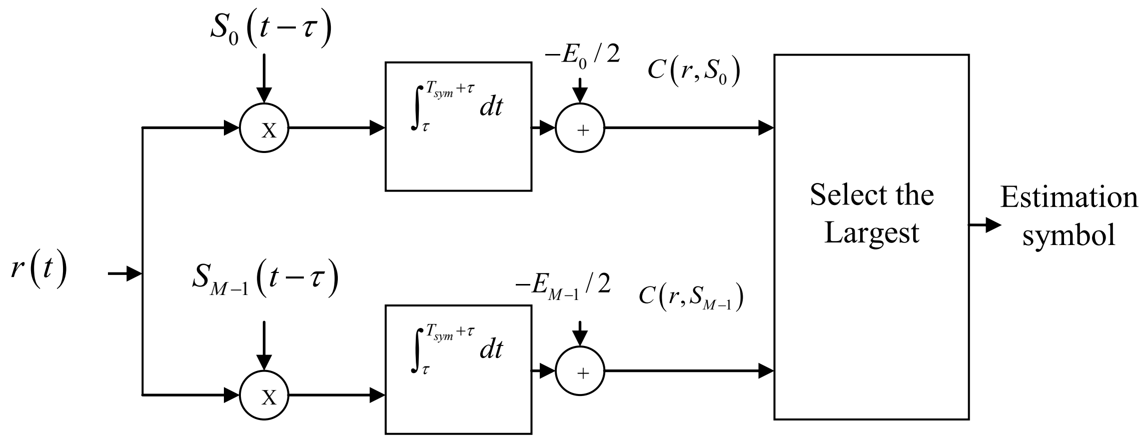

Fig. 8.2: Optimum receiver for AWGN channel.

8.3 Mathematical approach for PPM receiver

8.3.1 Receiver for binary orthogonal PPM

Binary orthogonal PPM transmitted signals can be expressed as [1]

$$S_m(t) = \begin{cases} \sqrt{E_{Tx}}\, p_o(t) \\ \sqrt{E_{Tx}}\, p_1(t) \ where\ p_1 = p_0(t-\varepsilon) \end{cases} \tag{8.8}$$

where E_{Tx} is the transmitted energy per pulse $p_0(t)$. These pulses will be orthogonal if ε is greater than the pulse duration T_h ($\varepsilon > T_h$). If we assumed a Gaussian random noise with $\mu = 0,\ \sigma^2 = \dfrac{N_0}{2}$, the average bit error rate probability for a binary orthogonal PPM signal is

$$\Pr_b = Q\left(\sqrt{\frac{E_{Rx}}{N_0}}\right) \tag{8.9}$$

where $E_{Rx} = \chi^2 E_{Tx}$ is the received energy per pulse. Note that the transmitted bits are assumed independent and equally probable.

8.3.2 Receiver for non-orthogonal binary PPM

The receiver structure for orthogonal and non-orthogonal PPM is the same, except that for the later, the PPM time shift ε is smaller than the pulse duration ($\varepsilon \prec$). Hence, the signal coming out from the correlator is

$$s_m = \begin{cases} s_0 = +\sqrt{E_{Tx}}\left[1 - R_0(\varepsilon)\right] \\ s_1 = -\sqrt{E_{Tx}}\left[1 - R_0(\varepsilon)\right] \end{cases} \tag{8.10}$$

where $R_0(t)$ is the autocorrelation of the pulse $p_0(t)$. The average bit error rate probability in this case is:

$$\Pr_b = Q\left(\sqrt{\frac{E_{Rx}\left(1 - R_0(\varepsilon)\right)}{N_0}}\right) \tag{8.11}$$

8.3.3 Receiver for orthogonal M-PPM

M-PPM can be considered as an extension of B-PPM where ε should be larger than pulse duration in order to maintain orthogonality. Figure 8.3 shows the optimum receiver for M-PPM.

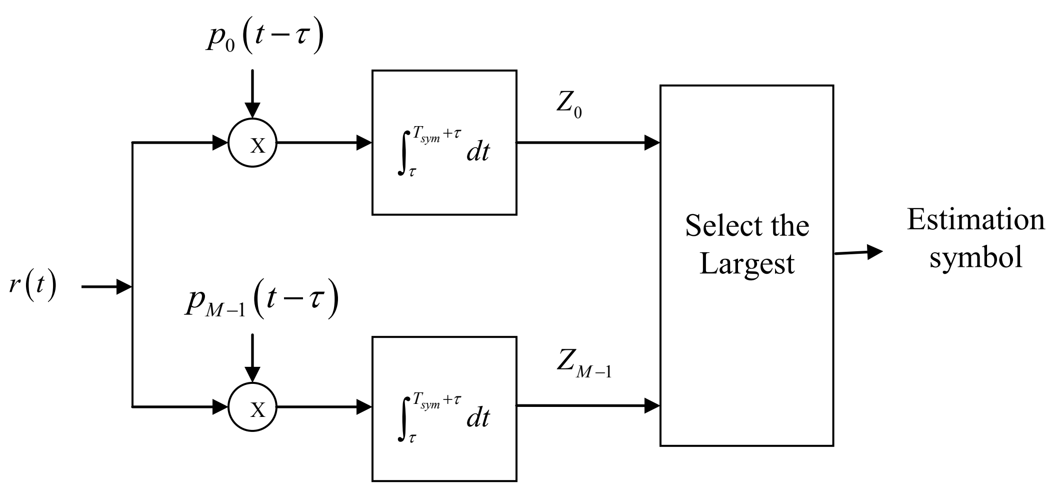

Fig. 8.3: Optimum receiver for orthogonal TH-M-PPM.

The decision variables at the output of the correlator are expressed as [10]:

$$\begin{Bmatrix} Z_0 = \chi s_{m0} + n_0 \\ Z_{M-1} = \chi s_{m(M-1)} + n_{M-1} \end{Bmatrix} \tag{8.12}$$

with

$$s_{mj} = \sqrt{E_{Tx}} \int_0^{T_s} p_0\left(t - m\varepsilon\right) p_0\left(t - j\varepsilon\right) dt \,.$$

The M possible generated waveforms are assumed having equal probability of $1/M$. Thus, the average error probability on the symbol, $\Pr_s$ is the probability of misdetection on one of the symbols and is presented as [11]

$$\begin{aligned} \Pr_s &= \frac{1}{\sqrt{2\pi}} \int_{-\infty}^{\infty} \left[1 - \left(\frac{1}{\sqrt{2\pi}} \int_{-\infty}^{y} e^{-x^2/2} dx \right)^{M-1} \right] \ldots \\ &\ldots \exp\left[\frac{-1}{2} \left(y - \sqrt{2\gamma_s} \right)^2 \right] dy \end{aligned} \tag{8.13}$$

8.4 Mathematical approach for PAM receiver

8.4.1 TH-BPAM-antipodal

In this case, two possible signals are generated by the transmitter [1]:

$$S_m\left(t\right) = \begin{cases} \sqrt{E_{Tx}}\, p_o\left(t\right) \\ \sqrt{E_{Tx}}\, p_1\left(t\right) = -\sqrt{E_{Tx}}\, p_0\left(t\right) \end{cases} \tag{8.14}$$

The optimum receiver is thus composed of one correlator as shown in Fig. 8.4. In this figure, the correlator output is $Z = \chi s_m + n$, with n a Gaussian random variable with $\mu = 0,\ \sigma^2 = \dfrac{N_0}{2}$.

8.4.2 DS-BPAM-antipodal

The scheme shown in Fig. 8.5 is a modification of that in Fig. 8.4, highlighting the c_j term that indicates the j^{th} binary antipodal coefficient of the DS code assigned to the user under examination and $m(t) = c_j p_0(t-\tau)$ the correlation mask of the correlator.

The bit error rate is expressed as

$$\Pr_b = Q\left(\sqrt{\frac{2E_{Rx}}{N_0}}\right).$$

Note that the binary antipodal PAM requires half energy compared to BPPM to achieve the same bit error.

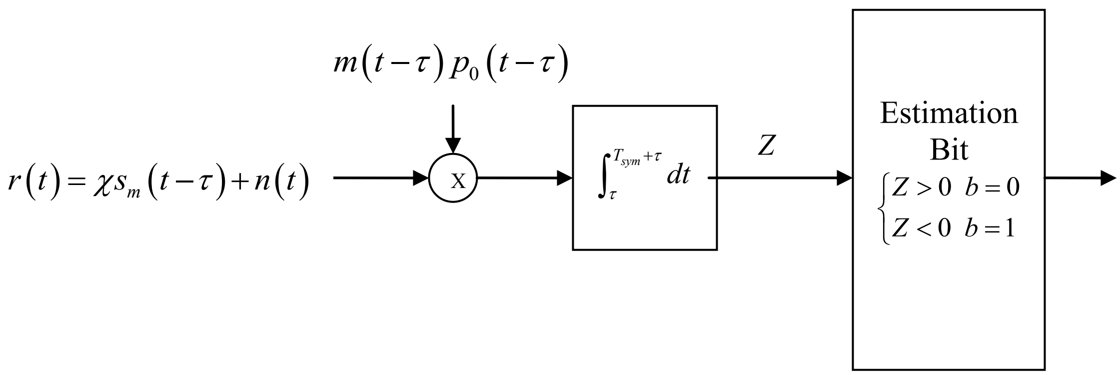

Fig. 8.4: optimum receiver for antipodal TH- BPAM

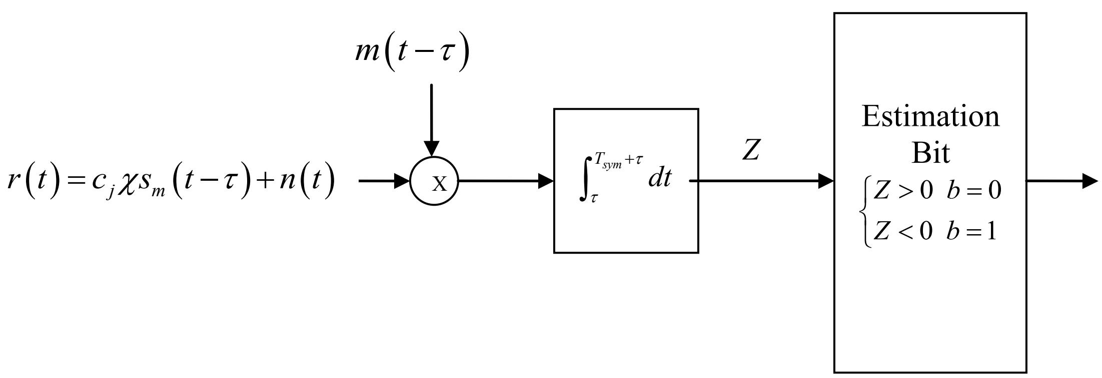

Fig. 8.5: optimum receiver for antipodal DS-BPAM

8.4.3 Optimum Receiver for M-PAM

The received signal of M-PAM can be expressed as [1]

$$r(t) = s_m(t-\tau) + n(t).$$

where

$$s_m(t) = A_m\sqrt{E_{Rx}}\,p_0(t) \qquad A_m = \frac{2m-M+1}{2},\ \ m = 0,.....M-1 \tag{8.15}$$

Its optimum receiver has shown by Fig. 8.6.

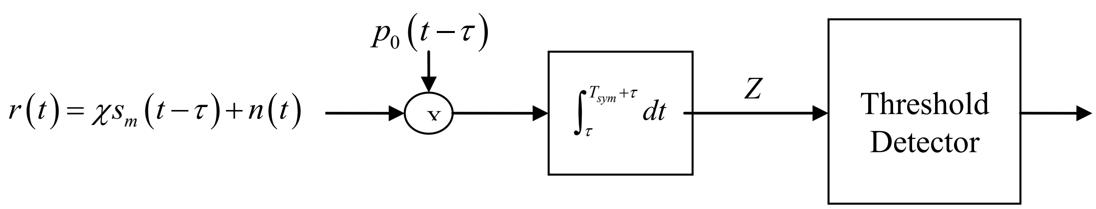

Fig. 8.6: optimum receiver and equivalent for M-PAM

The average symbol error will be expressed as [1], [2], [6]:

$$\Pr_s = \frac{2(M-1)}{M} Q\left(\sqrt{\frac{6\log_2(M)E'_{Rx}}{\left(M^2-1\right)N_0}}\right) \tag{8.16}$$

with

$$E_m = \left(A_m\right)^2 E_{Rx} = \left(\frac{2m-M+1}{2}\right)^2 E_{Rx} \tag{8.17}$$

Note that E'_{Rx} has a different meaning from E_{Rx}. In M-PAM case, E'_{Rx} is the received energy in a pulse and does not coincide with the average receiver energy per pulse E_{Rx}; however, assuming A_m=1, they will be equal.

8.5 Indoor UWB Channel Model

Accurate channel characterization allows correct evaluation of key parameters like frequency spectrum and transmitted power.

In narrowband systems, multipath propagation leads to multipath fading, while in UWB systems, monocycles commonly do not overlap because the pulse width is smaller than the channel propagation delay. However, only limited work has been achieved on UWB channel modeling. Parameters to be involved in such models include signal characteristics, delay distribution, and pulse shape distortion distribution.

8.5.1 IEEE 802.15.3a UWB Indoor Channel Model

Several works have been done to model indoor/outdoor LOS/NLOS scenarios [2], [3], [7]. However, in case of extremely NLOS environments (ENLOS), the above parameters have to be carefully evaluated [12]. Therefore, we introduced a new expression for the impulse response in an IEEE 802.15.3a UWB indoor channel model as

$$h(t) = G\sum_{n=1}^{N}\sum_{k=1}^{K}\alpha_{nk}\delta\left(t - T_n - \tau_{nk}\right) \tag{8.18}$$

G is a log-normal random variable representing the magnitude of the channel gain; N is the number of clusters and K the number of multi-paths for a particular cluster. $a_{nk} = \beta_{nk}e^{-\theta_{nk}}$ is the number of multi-path complex random variables per cluster, β_{nk} is a statistically independent random variable with Raleigh distribution, and θ_{nk} a statistically independent random variable with uniform distribution representing the pulse multi-path inversion. T_n is the time arrival for n^{th} cluster and τ_{nk} the multi-path delay, for a particular cluster distribution. To avoid complexity, the average cluster delay used in the valuation was defined as

$$\tau_{rms} = \sqrt{\sum_{n=1}^{N}\tau_n{}^2 a_n{}^2 / G - \left(\sum_{n=1}^{N}\tau_n a_n{}^2 / G\right)^2} \tag{8.19}$$

The proposed expression that expresses the IEEE indoor channel (equation (8.18)) covers not only the pulse amplitude distortion per cluster but also the pulse shape/phase distortion as well.

8.5.2 Random channel

As stated above, the IEEE model assumes that all channel parameters are time-dependent. This approach is accurate but not practical, especially for indoor channels. We thus investigated for a simpler model which can reduce the simulation time. The impulse response of a random channel is defined as [7]

$$h(t) = \sum_{n=1}^{N} a_n \delta(t - n\tau_n) \tag{8.20}$$

In this equation, there is no assumption for pulse shape distortion or channel propagation. Therefore, it presents a major drawback when applied to impulse ratio technique (IR) and does not account for the pulse shape variation due to reflection or penetrations through material. Also, the angle of pulse arrival distribution is neglected, the gain attenuation distribution is uniform and the attenuation decay has a same rate, implying low complexity receiver design and thus, higher probability of error. Note that in the proposed channel model we covered most channel characteristics such as pulse shape distortion, multipath delay as well as various attenuation scenarios (referring to 8.18).

8.6 UWB Noise Modeling

For accurate noise modeling, three different noises were considered namely, AWGN, narrowband interference noise (based on the autocorrelation function), and tone/multi-tone noise. Figure 8.7 is a schematic representation of the equivalent noise filter with $d_k(n)$ the discrete impulse response of the i^{th} filter and $e_k(n) = h(n) + w(n)$ the template receiver signal, n being the discrete time sampling. $h(n)$ is the channel impulse response and $w(n)$ the total noise while $<y(i)\ y(j)>$ represents the noise autocorrelation matrix.

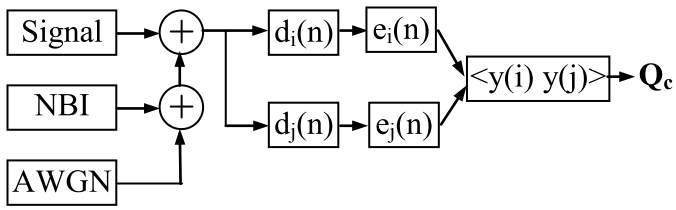

Fig.8.7. Equivalent receiver with various noises.

8.6.1 AWGN

Let $w(n) = f\left(0, \sigma_w{}^2\right)$, with f a Gaussian noise distribution function that passes through the filter with zero mean and covariance $\sigma_w{}^2$. The output noise autocorrelation can be expressed as [6]

$$R_x(m) = \langle x(n)\, x(n+m) \rangle = \sigma_w{}^2 \delta(m)$$

$$R_y(m) = \langle y(n)\, y(n+m) \rangle = \sigma_w{}^2 \sum_{\tau=0}^{\infty} h(\tau) h(\tau+m) \quad \rightarrow \quad R_y(m) = \sigma_w{}^2 \frac{n^m(1-n)}{1+n} \quad (8.21)$$

where m and n are discrete time sampling. $x(n)$ the input noise and $y(n)$ the output noise after passing the filter/channel which impulse response is denoted $h(t)$. If only AWGN channel is assumed, the noise average distribution is zero, and thus, the sum of filter bandwidths will be the same as the overall UWB bandwidth. So, with a white noise assumption, there is no point to split the bandwidth to narrowband using filter band approach or NBI mitigation.

8.6.2 Narrow-Band Noise

The desired deterministic narrow-band noise $Z(n)$ and its autocorrelation $R_z(m)$ can be defined as [4]

$$Z(n) = y_c(n)\cos(2\pi v n) + y_s(n)\cos(2\pi v n)$$

$$R_z(m) = R_y(m)\cos(2\pi v n) = \sigma^2 \frac{a(1-a)^m}{2-a}\cos(2\pi v n) \quad (8.22)$$

$y_c(n)$ and $y_s(n)$ represent the output sinusoid noise autocorrelation at frequency v and a the channel coefficient. $R_y(m)$ is the autocorrelation of the total interference noise while σ^2 is the noise variance.

8.6.3 Single Tone Interference with Filter bank

Thus, we added to the AWGN a single tone interference with center frequency f_I and magnitude A_I. Let us split the desired bandwidth (3.1-10.6 GHz) using a number of band-pass filters, $N_f \leq N_{fmax}$. The related noise covariance matrix $\mathbf{Q_c}$ is given by:

$$Q_c = \sigma_w^2 I_{N_f} + \sigma_I^2 \overline{HH^T} \tag{8.23}$$

with

$$\overline{H} = \left[DE_1(f_I), DE_2(f_I), ...DE_{N_f}(f_I)\right]^T \tag{8.24}$$

where $DE_i(f_I)$ is the Fourier transform of the channel parameter $de_i(n)$ and $\sigma_I^2 = \left|\overline{A_I^2}\right|$ the variance interference. The eigenvectors of $\mathbf{Q_c}$ span the signal space into N_f dimensions. Under tone noise, the eigenvalues can be formulated as, [6]

$$\lambda_i = \begin{cases} \sigma_w^2 + \sigma_I^2 \sum_{i=1}^{N_{f\max}} \left|DE_i(f_1)\right|^2 \\ \sigma_w^2 \quad if \quad \sigma_I^2 = 0 \end{cases} \tag{8.25}$$

Thus, the average receiver SNR output can be obtained as:

$$\overline{SNR_z} = \frac{E}{N_{f_{\max}}} \sum_{i=1}^{N_{f\max}} \lambda_i^{-1} = \frac{E_0}{\sigma_w^2} \frac{N_{f_{\max}} - 1}{N_{f_{\max}}} + \frac{E_o}{N_{f_{\max}}} \frac{1}{\sigma_w^2 + \sigma_I^2 \sum_{i=1}^{N_{f\max}} \left|DE_i(f_{1)}\right|^2} \tag{8.26}$$

$$\rightarrow \quad \overline{SNR_z} = \frac{E_0}{\sigma_w^2} \left[1 - \frac{1}{N_{f_{\max}}} \left[1 - \frac{\sigma_w^2}{\sigma_w^2 + \sigma_I^2 \sum_{i=1}^{N_{f\max}} \left|DE_i(f_{1)}\right|^2}\right]\right] < \frac{E_0}{\sigma_w^2} \tag{8.27}$$

Without interference noise, the above equations can be reformulated as

$$\overline{SNR_z} = \frac{E_0}{\sigma_w^2}$$

for $\sigma_I^2 = 0$, while with the interference, σ_I^2 increases and thus, $\overline{SNR_z}$ will decrease within the following range

$$\frac{N_{f_{\max}} - 1}{N_{f_{\max}}} \frac{E_0}{\sigma_w^2} < \overline{SNR_z} < \frac{E_0}{\sigma_w^2} \tag{8.28}$$

Actually the tone noise model investigation represents here the multi-carrier receiver ($DE_1(f_I), DE_2(f_I), \ldots.$) that will be matched to the filter bank with different filter number N_f. Note that with an UWB noisy environment, we cannot avoid complexity; so most of designers assumed a white noise (AWGN). However this assumption is not accurate, especially when dealing with weak UWB receiver signals. Therefore, the filter order is a key design parameter in presence of strong NBI noise (color noise).

8.6.4 Multi-Tone Interference (Filter bank Case)

At this stage and for simplicity let us assume independent N_I tones with random magnitude and equal variance. Also, let the number of distinct interference tones be N_I with equal variance and independent. The noise covariance matrix with N_I interference frequencies $f_1 \ldots f_{NI}$ can be expressed as, [13]

$$\mathbf{Q_c} = \sigma_w^2 I_{N_f} + \overline{H} \left\langle \overline{D_I}\,\overline{D_I}^T \right\rangle \overline{H}^T \tag{8.29}$$

where $\overline{D_I} = \left[A_1 \ldots A_{N_I}\right]^T$ with A_i the interference tone coefficients (N_I Gaussian random variables). Also,

$$\mathbf{H} = \begin{bmatrix} H_1(f_1) \ldots H_1(f_{N_1}) \\ \ldots \quad \ldots \quad \ldots \\ H_{N_f}(f_1) \ldots H_{N_f}(f_{N_I}) \end{bmatrix}; \qquad \mathbf{H_i(f_j)} = DE_i(f_j);\; Q_I = \left\langle \overline{D_I}\,\overline{D_I}^T \right\rangle = \begin{bmatrix} \sigma_1^2 \ \ldots \ 0 \\ \ldots \ldots \ \ldots \\ 0 \ \ldots \ \sigma_{N_I}^2 \end{bmatrix}$$

while the matrix eigenvalues can be determined from [13] as

$$\left(\boldsymbol{\lambda}\text{-}\sigma_w^2\right)^{N_f-N_I}\left|\left(\boldsymbol{\lambda}\text{-}\sigma_w^2\right)I_{N_I}-\sqrt{Q_I}^T\,\overline{H}^T\,\overline{H}\sqrt{Q_I}\right|=0 \tag{8.30}$$

If we assume that the interference frequencies are sufficiently separated then,

$$\sqrt{\mathbf{Q_I}}^T\,\overline{\mathbf{H}}^T\,\overline{\mathbf{H}}\sqrt{\mathbf{Q_I}}=\begin{bmatrix}\sigma_1^2\sum_{k1}^{N_f}\left|H_k\left(f_1\right)\right|^2 & \ldots & 0\\ \ldots & \ldots & \ldots\\ 0 & \ldots & \sigma_{N_I}^2\sum_{k1}^{N_f}\left|H_k\left(f_{N_f}\right)\right|^2\end{bmatrix} \tag{8.31}$$

and

$$\lambda_i=\begin{cases}\sigma_w^2+\sigma_i^2\sum_{k=1}^{N_f}\left|DE_k\left(f_i\right)\right| & i=1,2,\ldots.N_I\\ \sigma_w^2 & N_I<i<N_f\end{cases}$$

The average output SNR can be thus obtained as

$$\left\langle SNR_Z\right\rangle=\frac{E_0}{N_f}\sum_{i=1}^{N_f}\boldsymbol{\lambda}_{\mathbf{i}}^{\mathbf{-1}}=\frac{E_0}{\sigma_w^2}\frac{N_f-N_I}{N_f}+\frac{E_0}{N_f}\sum_{i=1}^{N_I}\frac{1}{\sigma_w^2+\sigma_i^2\sum_{k=1}^{N_f}\left|DE_k\left(f_i\right)\right|} \tag{8.32}$$

Note that

$$\frac{N_f-N_I}{N_f}\frac{E_0}{\sigma_w^2}<\left\langle SNR_Z\right\rangle<\frac{E_0}{\sigma_w^2} \tag{8.33}$$

So it is clear that compared to single tone, multi-tone SNR is worse since reduced by a factor of $-10\log\left(\frac{N_f-N_I}{N_f}\right)$.

So the solution will be to increase N_f. In practice an optimal correlator can be set to $N_{f_{\max}}$ = 10, making the interference noise negligible. For such value, the BER is very low and thus, we used this number for further simulations.

8.6.5 Correlated Multi-Tone Interference Noise

Let us consider now a more general case with closer multi-tone frequencies and correlated interference signals at the filter output [13]. The eigenvalues can be stated as

$$\left(\lambda\text{-}\sigma_w^2\right)^{N_f}\prod_{k=1}^{\min(N_f,N_I)}\left(1-\frac{\sigma_I^2}{\left(\lambda-\sigma_w^2\right)}\lambda_{Hk}\right)=0 \tag{8.34}$$

where λ_{Hk} are the eigenvalues of **H**. Thus, we can easily extract the single tone case

$$\left(\lambda\text{-}\sigma_w^2\right)^{N_f-1}\prod_{k=1}^{1}\left(\lambda_1-\sigma_w^2-\sigma_I^2\lambda^2{}_{H1}\right)=\left(\lambda-\sigma_w^2\right)^{N_f-1}\left(\lambda-\sigma_w^2-\sigma_I^2\lambda_{H1}^2\right)$$

with

$$\lambda_i=\left\{\begin{matrix}\sigma_w^2+\sigma_I^2\lambda_{Hi}^2 & & i=1\\ \sigma_w^2 & & 1<i<N_f\end{matrix}\right\} \tag{8.35}$$

A similar procedure can be used to extract the independent multi-tone noise eigenvalues from this general case.

8.7 Theory and Performance of Various Rake Receivers

8.7.1 Rake Receiver Theory

A received multi-path signal $r(t)$ consists on the superposition of several attenuated, delayed and eventually distorted replicas of a transmitted waveform [4]. The typical time-hopping transmitted output signal used by an impulse radio is, [6], [13]

$$s_{tr}^{(k)}\left(t^{(k)}\right)=\sum_{j=-\infty}^{\infty}P_{tr}\left(t^{(k)}-jT_s-c_j^{(k)}T_c-a_j^{(k)}\varepsilon\right) \tag{8.36}$$

Here $t^{(k)}$ is the k^{th} transmitter clock time, T_c the M-chip time, and T_s the pulse repetition time. P_{tr} is the transmitted pulse waveform assumed monocycle. $c_j^{(k)}$ is the time-hopping, or pseudo-random sequence (integer value, periodic), that provides additional shift of the pulse train $c_j^{(k)} T_c$. $a_j^{(k)} \varepsilon$ is the data sequence modeled as a stationary random process. If propagation fluctuations within an observation time $T >> T_b$ (bit period) and path-dependent distortions can be neglected, the receiver signal can be written as

$$r(t) = X\sqrt{E_{TX}} \sum_{j} \sum_{n=1}^{N} \sum_{k=1}^{k(n)} \alpha_{nk} a_j p_{tr} \left(t - jT_s - \varphi_j - \tau_{nk}\right) + n_{total}(t) \tag{8.37}$$

Here X is the log-normal distributed channel gain, E_{TX} the transmitted energy per pulse, N the number of clusters, k the number of multi-paths, α_{nk} the channel coefficient, a_j the j^{th} pulse magnitude, φ_j the time dithering associated to the j^{th} pulse, and τ_{nk} the delay correlated to the k^{th} path and the n^{th} cluster.

There are different strategies for exploiting diversity that can be adopted by a receiver, such as Selection diversity (SD), equal gain combining (EGC) and maximal ratio combining (MRC) methods [4]. In MRC, the different contributions are weighted and the weights are determined to maximize the SNR before the decision processes. The optimal receiver matched to a single waveform corresponds to the first correlator. In the rake receiver case, the optimum correlator must include additional correlators associated with the different replicas of the transmitted waveform [2], [12] (also known as correlation mask $m(t)$ as shown in Fig. 8.8).

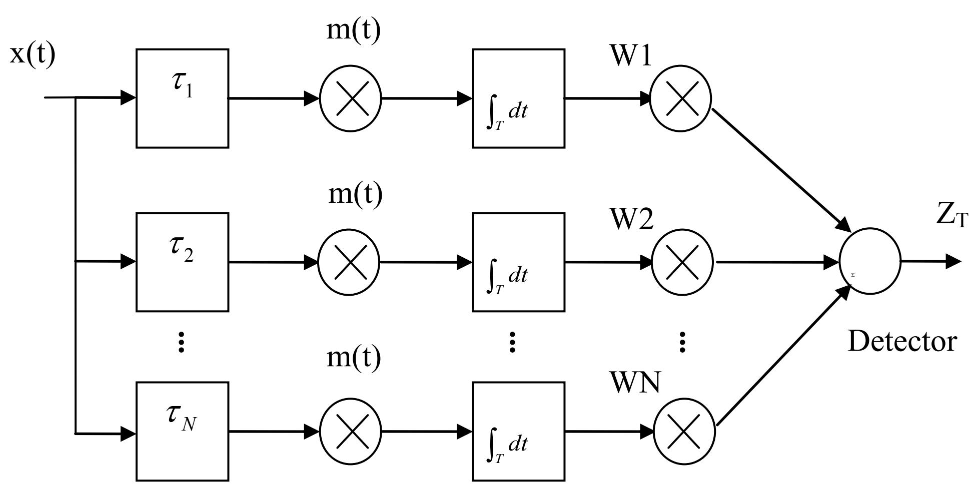

Fig. 8.8. Rake Receiver with N_f parallel correlators and time delays τ_i ([10])

From Fig. 8.8 Z_T is the sum of the weighted signals

$$Z_T = \sum_{j=1}^{N_T} w_j \int_{T_L} r(t) m(t-\tau_j)\, dt \tag{8.38}$$

which can be also expressed as

$$Z_T = \int_{T_L} r(t) m_R(t)\, dt \qquad m_R(t) = \sum_{j=1}^{N_T} w_j m(t-\tau_j) \tag{8.39}$$

T_L is the observation time and τ_i the propagation delay corresponding to the j^{th} path. By simplifying (35), we can draw the equivalent rake receiver structure shown in Fig. 8.9.

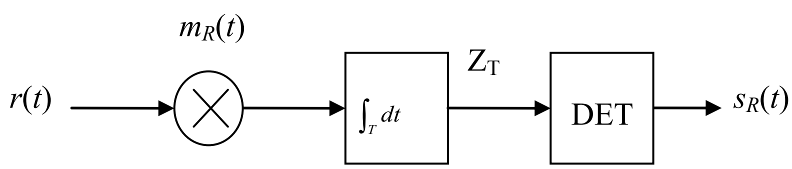

Fig. 8.9. Equivalent Rake Receiver Structure, DET= $\overline{Z_T}$

The output of the bank of correlators feeds the combiner, which is function of the diversity and the set of weights.

8.7.2 Rake Receiver Capacity

If we assume that the source has a Gaussian distribution, the capacity of IRAKE receivers is equal to [5].

$$C = I_{\max}(x,y) = \log_2(M) - \frac{1}{M}\sum_{m=1}^{M}\int p(y/x_m)\log_2\left(\frac{\sum_{k=1}^{M} P(y/x_k)}{P(y/x_m)}\right)dy \tag{8.40}$$

where $p(y/x_m)$ is the probability of data variable x sitting in the y channel area (time/frequency domain).

Let us consider the following equations to reach the final capacity definition, [5]

$$\left|\mathbf{S}^{\mathbf{T}}\mathbf{S}\right|\left|\mathbf{I}+\mathbf{Q}_{C}^{-1}\mathbf{S}\mathbf{S}^{\mathbf{T}}\right|=\left|\mathbf{S}\mathbf{S}^{\mathbf{T}}\right|\left|\mathbf{I}+\mathbf{Q}_{C}^{-1}\mathbf{S}\mathbf{S}^{\mathbf{T}}\right|$$
$$\mathbf{S}\left|\mathbf{I}+\mathbf{Q}_{C}^{-1}\mathbf{S}\mathbf{S}^{\mathbf{T}}\right|=\left|\mathbf{S}\mathbf{S}^{\mathbf{T}}\left(\mathbf{I}+\mathbf{Q}_{C}^{-1}\mathbf{S}\mathbf{S}^{\mathbf{T}}\right)\right| \tag{8.41}$$

where S is the UWB transmitted signal. We thus obtain

$$\mathbf{S}\left|\mathbf{I}+\mathbf{Q}_{C}^{-1}\mathbf{S}\mathbf{S}^{\mathbf{T}}\right|=\left|\mathbf{S}^{\mathbf{T}}\mathbf{S}+\mathbf{S}\mathbf{Q}_{C}^{-1}\mathbf{S}\mathbf{S}^{\mathbf{T}}\mathbf{S}\right|=\left|\mathbf{S}+\mathbf{S}^{\mathbf{T}}\mathbf{Q}_{C}^{-1}\mathbf{S}\mathbf{S}\right| \tag{8.42}$$

leading to

$$C=\frac{1}{2}\log_2\left(\frac{\left|\mathbf{S}\mathbf{S}^{\mathbf{T}}+\mathbf{Q}_{\mathbf{C}}\right|}{\left|\mathbf{Q}_{\mathbf{C}}\right|}\right)=\frac{1}{2}\log_2\left(1+\mathbf{S}^{\mathbf{T}}\mathbf{Q}_{C}^{-1}\mathbf{S}\right)$$

8.7.3 Results

The rake receiver performance is generally evaluated knowing the coefficients of the channel impulse response. A receiver with good tradeoff between complexity and performance is a PRAKE. Since we used ENLOS as opposed to LOS, we should increase the number of fingers to get the same performance. Note that the number of fingers also depends on the tradeoff between the transfer signal parameters and the receiver design [6]. Table 8.1 summarized the transmitter signal and channel parameters in LOS/ENLOS scenarios. As shown, the ELNOS scenario has higher delay and distortion.

The minimum SNR of the filter bank with general match filter (GMF) is smoothly better even at lower bound and independent of any interference magnitude as shown in Fig. 8.10.

Table 8.1. Transfer Signal Parameters.

P_t = -30dBm	Channel LOS	Channel ENLOS
N_s = 10, Tau = 0.25ns	A_0 = 47dB	A_0 = 51dB
T_s = 10ns, T_m = 0.5ns	X=240*10^{-6}	X=72*10^{-6}
F_c = 20GHz, TPPM = 0.5ns	RMS = 6.3ns	RMS = 22ns

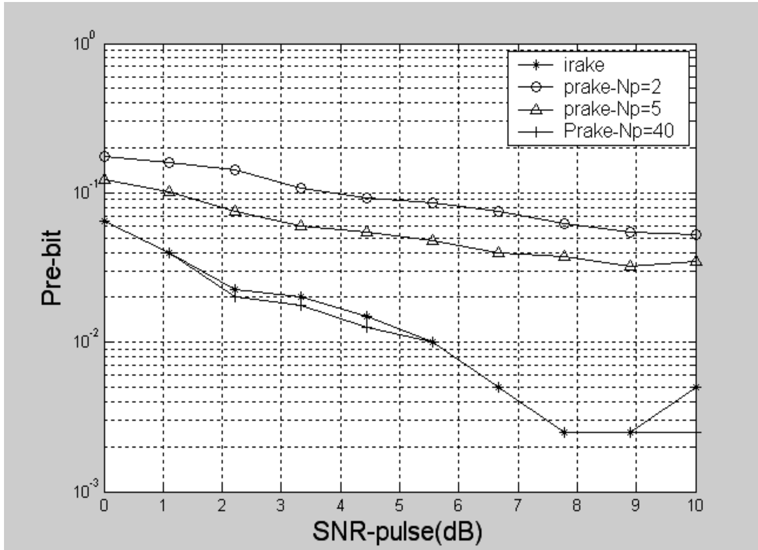

Fig. 8.10. BER of IRAKE and PRAKE receivers without filter bank

8.8 Proposed NBI Cancellation Method

Using a filter bank can reduce the effect of narrowband interference and inter pulse interference (IPI) [5], [9], [14]. Figure 8.11 shows the receiver design model with the filter bank. The response of the filter bank impulse shown in Fig. 8.11 is displayed in Fig. 8.12. It uses ten filters to remove the effect of tone noise. However, our purpose is to take advantage of inter symbol interference (ISI) and inter pulse interference (IPI).

Let us assume a number of band-pass filters (BPFs) uniformly spaced with lower and higher corner cut-off frequencies f_L = 3.1GHz and f_H = 10.6GHz, respectively. Let us also assume that SNR with white noise is independent of the number of filters.

The following equation shows that there is no benefit to use filter bank if the noise is assumed white (which noise PSD is constant):

$$SNR_{AWGN} = \frac{\sum_{0}^{Nh} h_{ch}^2}{\delta^2} \;,\quad SNR = \frac{S_r BW_{ch}}{N_0\left(B_{f1} + B_{f2} + ...\right)} = \frac{S_r BW_{ch}}{N_0 BW_{ch}} = \frac{S_r}{N_0} \qquad (8.43)$$

with h_{ch} the channel impulse response, S_r the receiver signal, BW_{ch} the desired bandwidth, and N_o the noise power. B_{f_n} is the bandwidth of the n^{th} BPF filter.

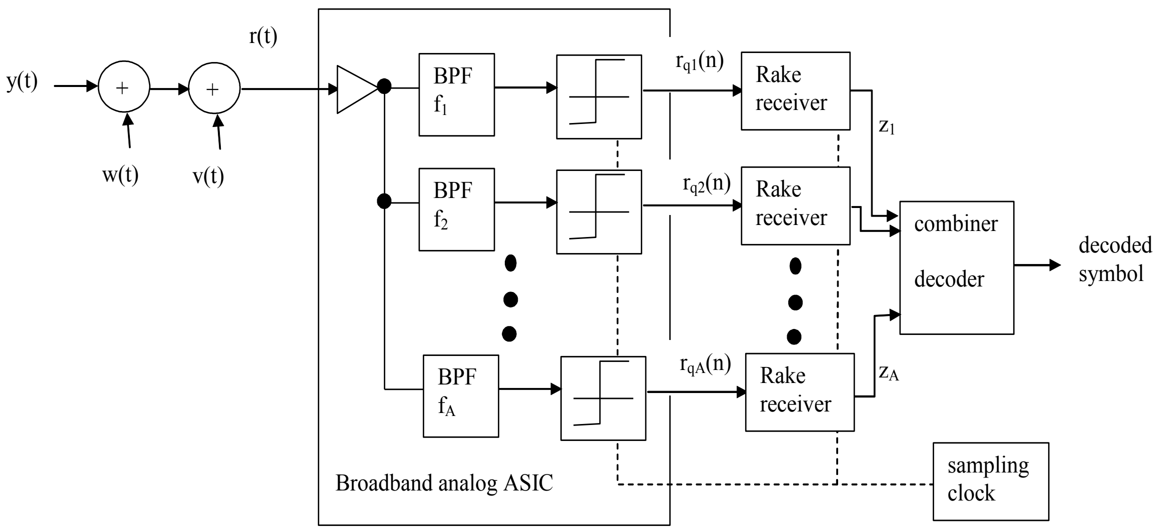

Fig. 8.11. Receiver with the filter bank diagram (From [6])

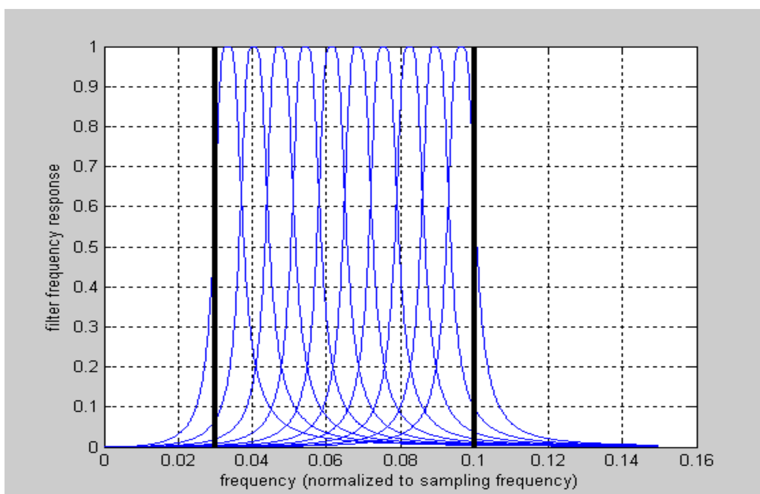

Fig. 8.12. 2nd order Butterworth filter with ten filters

By adding the tone noise, the scenario becomes different. In fact, even with only two filters, the capacity and BER becomes strongly dependent on the interference due to the leakage of the second filter (Figs. 8.12 and 8.13). As illustrated in Fig. 8.12 and 8.13, the BER and channel capacity are improved by applying filter bank. This is due to the dimensionality of the noise subspace being reduced to a single dimension, while the filter bank is dependent on F_N.

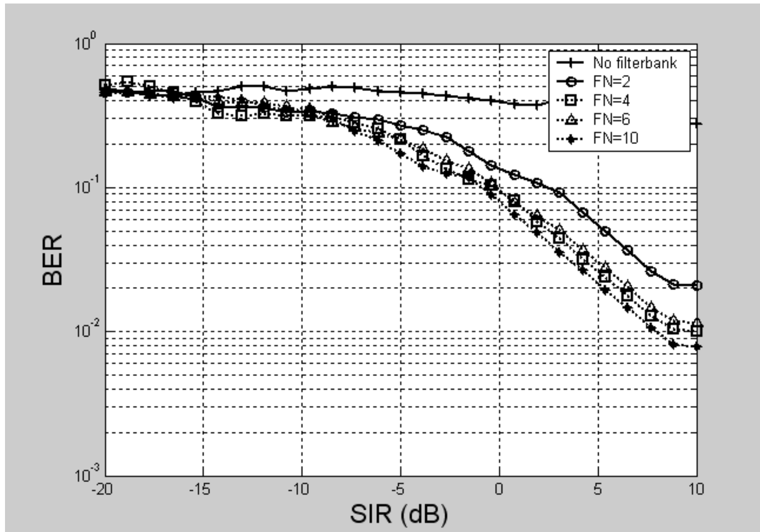

Fig. 8.13. BER comparison without filter bank and for various filter numbers (Low receiver SNR)

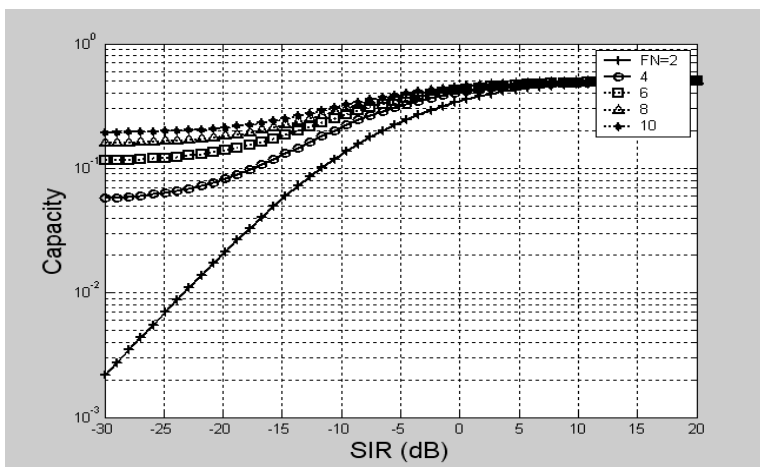

Fig. 8.14. Capacity for various filter numbers (Low receiver SNR)

8.8.1 Filter bank Specifications

The second order biquad section is modeled after the analog band-pass filter with Quality factor Q and center frequency w_c [14] (Fig. 8.12)

$$H(s) = \frac{\frac{\mathrm{wc}}{\mathrm{Q}} s}{s^2 + \frac{\mathrm{wc}}{\mathrm{Q}} s + wc^2} \tag{8.44}$$

with

$$Q = \sqrt{\frac{1-B}{B}} \frac{Awc}{\left|wc^2 - A^2\right|}$$

$$A = wc + \pi B_{fn} \qquad \mathrm{B} = \left| \frac{\frac{\mathrm{wc}}{\mathrm{Q}} A}{-A^2 + j\frac{\mathrm{wc}}{\mathrm{Q}} A + wc^2} \right|^2 = \frac{\left(\frac{\mathrm{wc}}{\mathrm{Q}} A\right)^2}{\left(wc^2 - A^2\right)^2 + \frac{\mathrm{wc}^2 \mathrm{A}^2}{\mathrm{Q}^2}}$$

Note that the energy per channel filter can be expressed as, [1], [9]

$$E_{ch_j} = \sum_{i=1}^{length(h_{ch})} \left| h_{ch_{ji}} \right|^2 \tag{8.45}$$

This energy varies significantly for each channel impulse response $h_{ch}(n)$ that is randomly determined. The signal outputs have to be generated for each band-pass filter. In each case, we correlated the output of each filter with the matched filter weights applied to the correlator following each of the BPFs is a rake receiver. The outputs of the N_f rakes are then combined according to the GMF weighting algorithm [9].

The weighting coefficients are determined by $\mathbf{W} = \mathbf{Q}_\mathbf{C}^{-1}\mathbf{S}$ and the related noise covariance matrix is defined by

$$\mathbf{Q}_{\mathbf{C}_{\mathbf{ij}}} = \left\langle \left(\mathbf{h}_{\mathbf{e}_\mathbf{i}} * \mathbf{w}\right)\left(\mathbf{h}_{\mathbf{e}_\mathbf{j}} * \mathbf{w}\right) \right\rangle$$

$$\mathbf{Q}_{\mathbf{C}_{\mathbf{ij}}} = \left\langle y_i y_j \right\rangle = \sum_{k=0}^{\infty} \sum_{k'=0}^{\infty} h_{e_i}(t) h_{e_j}(t') R_w(t - t') \tag{8.46}$$

Here R_w is the autocorrelation of the IRAKE weighting coefficients. Finally, the SNR output decision variable was calculated using the model shown in Fig. 8.11.

$$\sigma_Z^2 = \left\langle \mathbf{Z}^2 \right\rangle - \left\langle \mathbf{Z} \right\rangle^2 = \mathbf{S}^\mathbf{T}\mathbf{Q}_\mathbf{C}^{-1}\mathbf{S} \quad ; \qquad \mathbf{SNR}_\mathbf{Z} = \mathbf{S}^\mathbf{T}\mathbf{Q}_\mathbf{C}^{-1}\mathbf{S}$$

With low receiver SNR, Fig. 8.13 shows a BER comparison without filter bank and for various filter numbers, while Fig. 8.14 shows the capacity performance vs. the filter number.

As illustrated, by using filter banks, both BER and capacity have been improved even with strong interference. It also shows that with higher SIR (lower interference), the performance with lower number of filters number is similar to that with higher number. Therefore, a maximum number can be practically set as $N_{f_{\max}} < 6$.

8.8.2 Channel Estimation

Note that we assumed that the proposed channel model is stationary since the channel variable rate is much smaller than the pulse rate. In ENLOS case, the effect of the transmitted energy time dispersion is more evident than in LOS case. In fact, as shown in Figs. 8.15 and 8.16, all over 50GHz (corresponding to 50GHz/100GHz = 0.5 as normalized frequency) and considerate receive energy even after 130-150ns. Compared to the LOS case, this will increase the pulse period and the channel impulse response components will be more spread over the frequency domain (almost 3 to 4 times as in Fig. 8.17), which indicates more multipath and channel attenuation.

Even if the existing IEEE model is relatively efficient [3], it needs more fingers (correlator numbers) to capture more pulse energy leading to more complexity in the receiver design. On the other hand, increasing the receive pulse energy spread in time interval, causes higher RMS and higher pulse period (T_s) and consequently, lower data rate and lower performances. Therefore, a new approach to capture more pulse energy and reduce the number of receiver correlators should be investigated.

As shown in Figs. 8.18, 8.19, and 8.20, in LOS case, accurate channel estimation is not necessary and thus random channel modeling will be enough. In fact, in the presence of a strong receiver signal (negligible NBI), the channel delay and distortion will be ignored and the random channel estimation will be enough (for example if there is no tone noise or WLAN in the receiver environment). On the other hand in the ENLOS case, the IEEE channel estimation becomes more accurate due to multipath (weakest receiver signal) and NBI as shows in Figs. 8.21, 8.22, and 8.23.

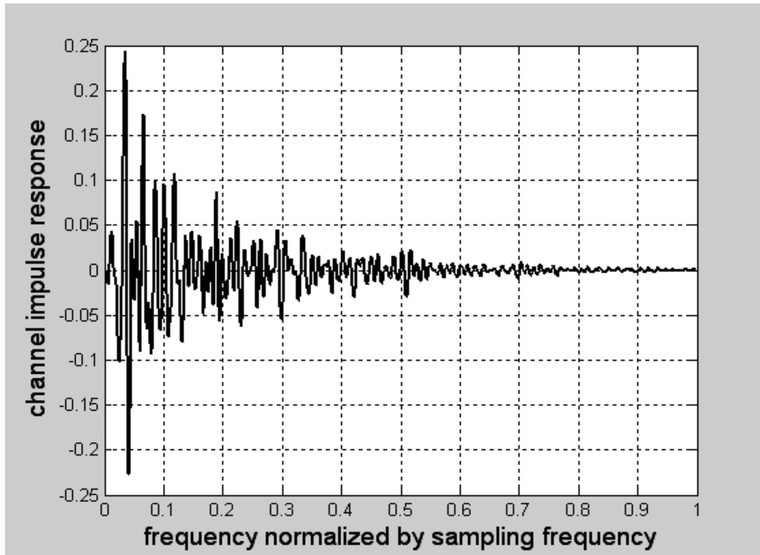

Fig. 8.15. Random channel impulse response.

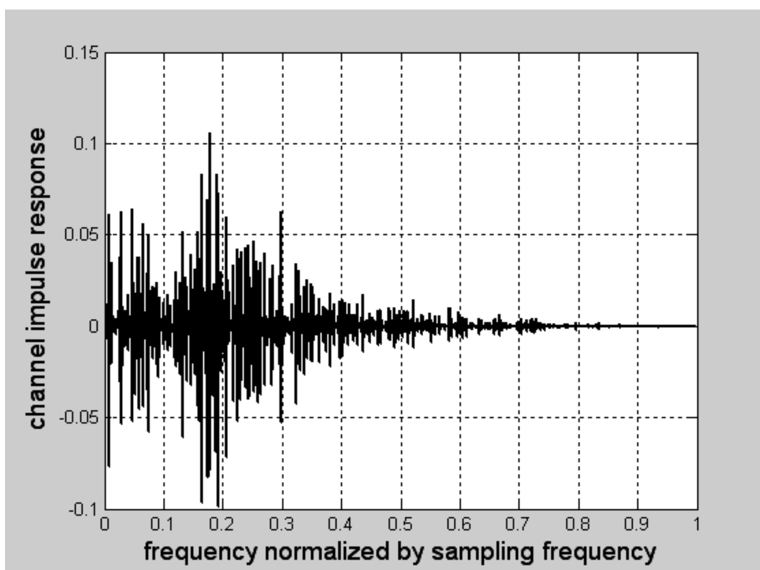

Fig. 8.16. IEEE channel impulse response (ENLOS case)

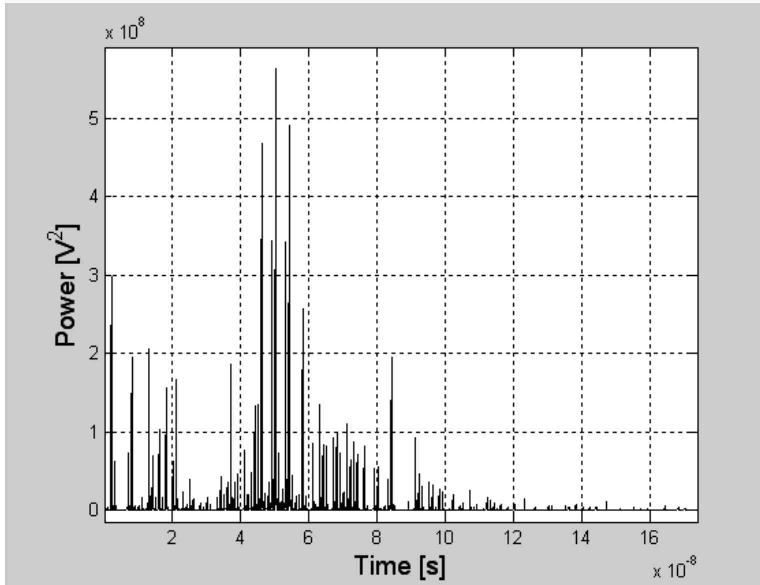

Fig. 8.17. PDP of the IEEE channel (ENLOS case)

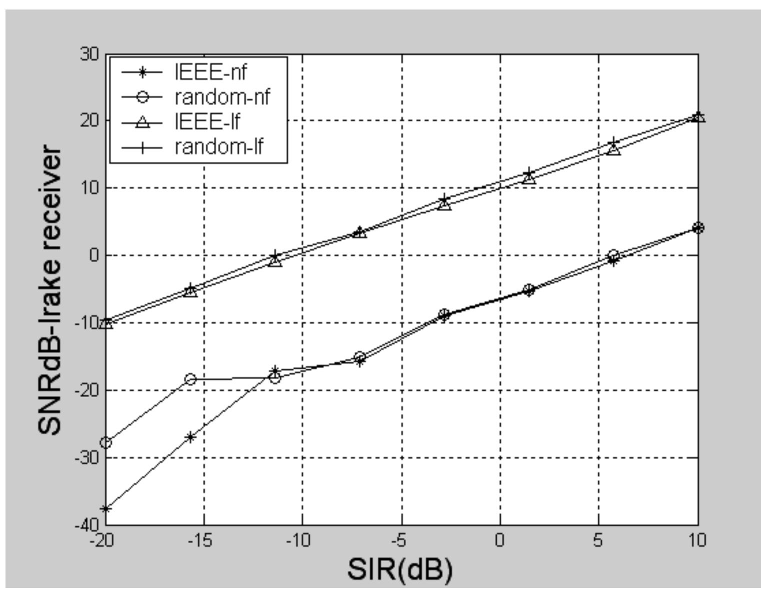

Fig. 8.18. SNR and SIR of the IRAKE receiver (LOS case)

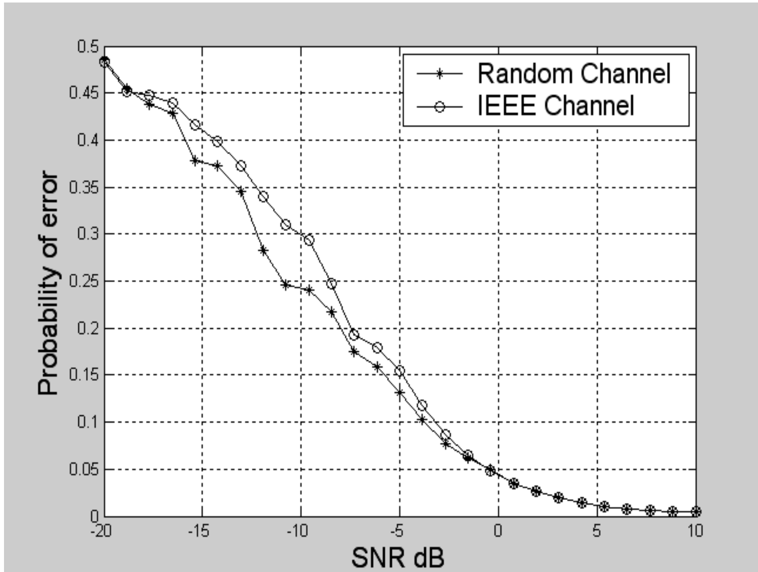

Fig. 8.19. BER of random and IEEE channels (with and without filter bank) – LOS case.

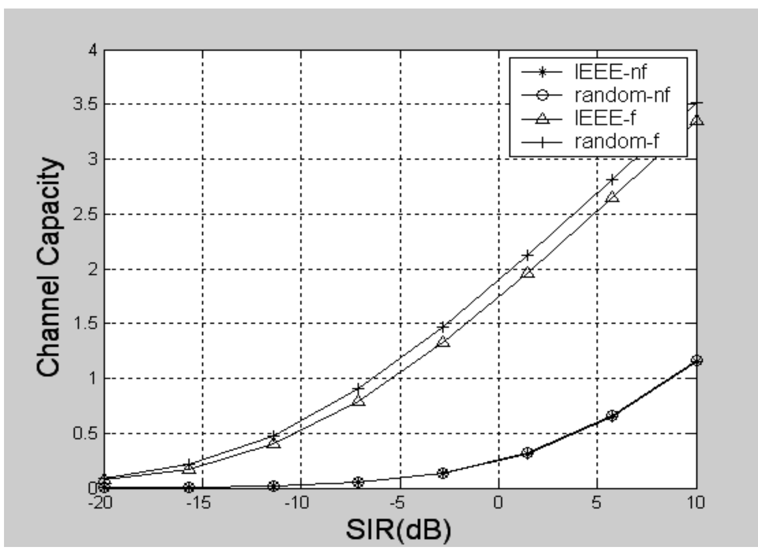

Fig. 8.20. Channel capacity of random and IEEE channels (LOS case)

In Fig. 21, we can see that by using filter banks, SNR requirements are the same for both IEEE and random channels, which demonstrates that accurate channel estimation is not required in the presence of filter banks. Similar conclusions can be achieved for BER and channel capacity tests (Figs. 8.22 and 8.23). Indeed, filter bank took advantage from the UWB frequency fading [7], [9].

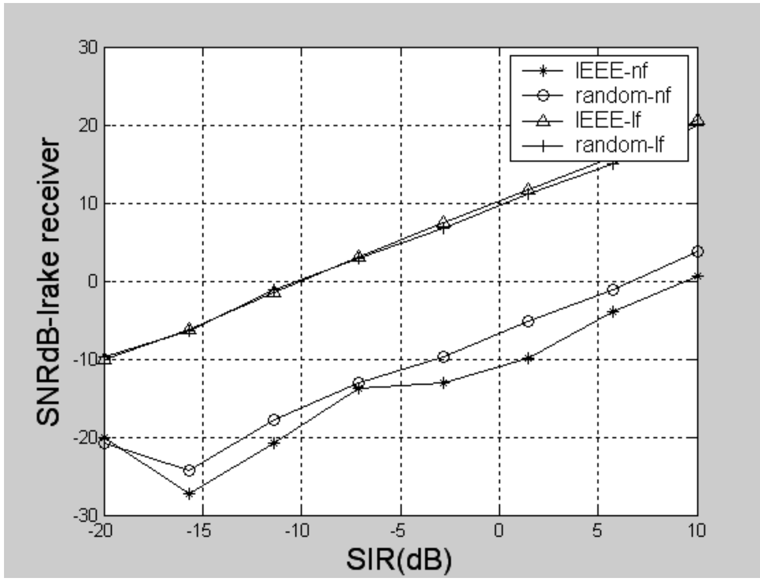

Fig. 8.21. SNR and SIR of the IRAKE receiver (ENLOS case)

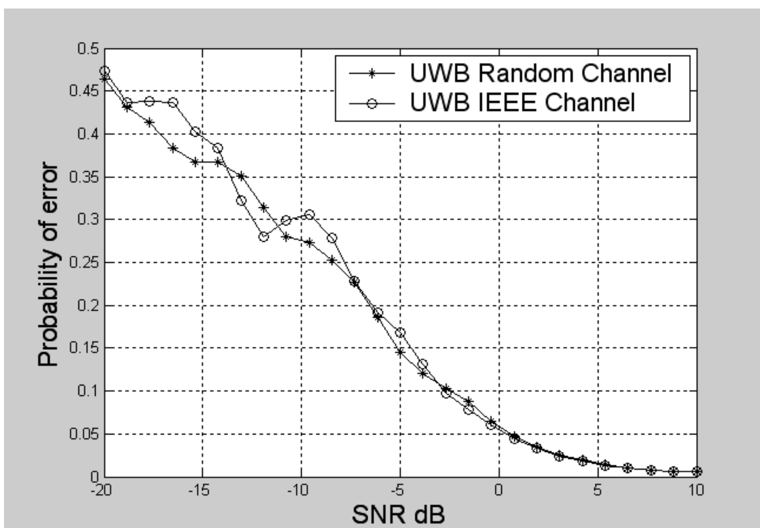

Fig. 8.22. BER of random and IEEE channels (with and without filter bank) – ENLOS case.

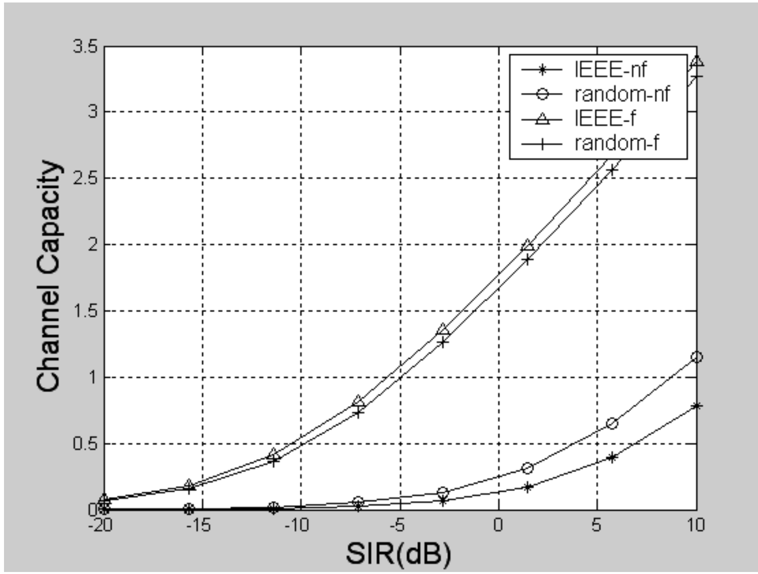

Fig. 8.23. Channel capacity of random and IEEE channels (ENLOS case)

8.9 Performance Evaluation

We performed Monte-Carlo simulations to evaluate the IRAKE/PRAKE receiver performance with filter bank (Figs. 8.24 and 8.25). In this simulation, we swept over the SIR and at each simulation point, noisy samples were generated and GMF weights determined for the two cases namely, with and without filter bank and single bit rake. We also assumed Rayleigh fading instead of Nakagami fading [2].

Figure 8.24 shows the Monte-carlo IRAKE receiver BER comparison with/without FB and with single bit rake receiver, (SBR). As shown, without FB, SBR and IRAKE receiver have almost same performance but with FB the improvement is significant.

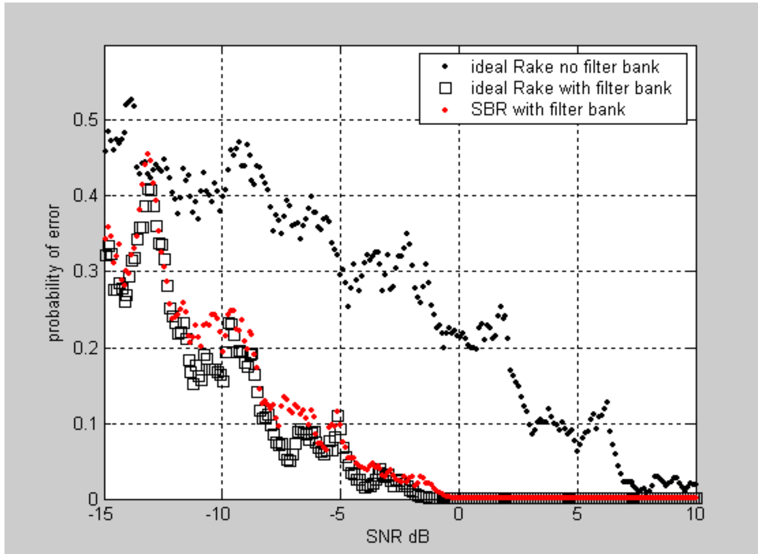

Fig. 8.24. Monte-Carlo simulation with/without filter bank and single bit rake in terms of BER.(NF=50, $N_f = 10$)

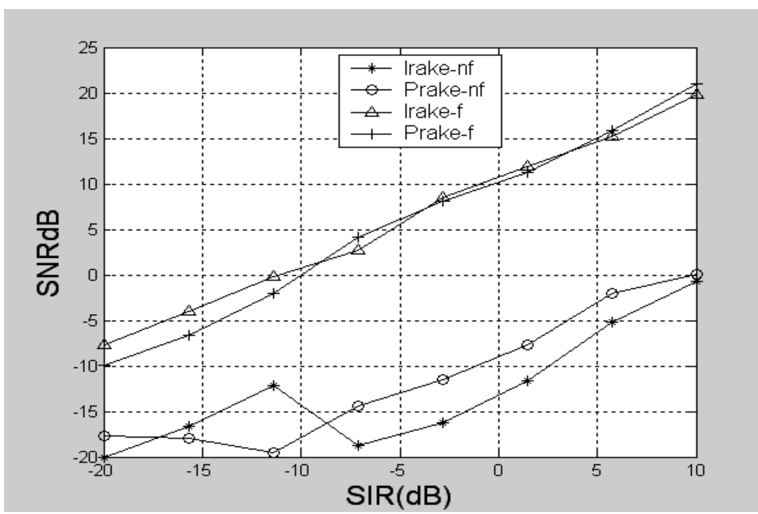

Fig. 8.25. Comparison of SNR with and without filter bank using the same number of fingers (NF=50, $N_f = 10$)

These Monte-Carlo simulations have been set with 100 iterations with 10% channel propagation parameter tolerances in ENLOS case. Note that in order to reduce the CPU time, time channel parameters have been set independent to each other.

Figure 8.25 also shows improvement with the filter bank while comparing the requirement SNR (receiver sensitivity) of PRAKE and IRAKE receivers with and without a filter bank, in the ENLOS case. It has been then demonstrated that, by using filter bank, the IRAKE and PRAKE receiver performances become quite similar with NF=50, $N_f = 10$.

Figures 8.26 and 8.27 show BER and channel capacity for IRAKE/PRAKE receiver in terms of SNR requirement, when ISI, tone and AWGN noises were added to the pulse signals, highlighting a 10dB SNR improvement with the filter bank. This result clearly highlights the importance of using the suitable UWB fading model. Also, in a noisy and higher interference environment where the average channel delay is high (high RMS [10]-[12]), the effect of filter banks is much more significant as the filter banks take advantage of overlapping signals. Hence by using filter banks, the number of fingers can be reduced to capture the same amount of signal energy.

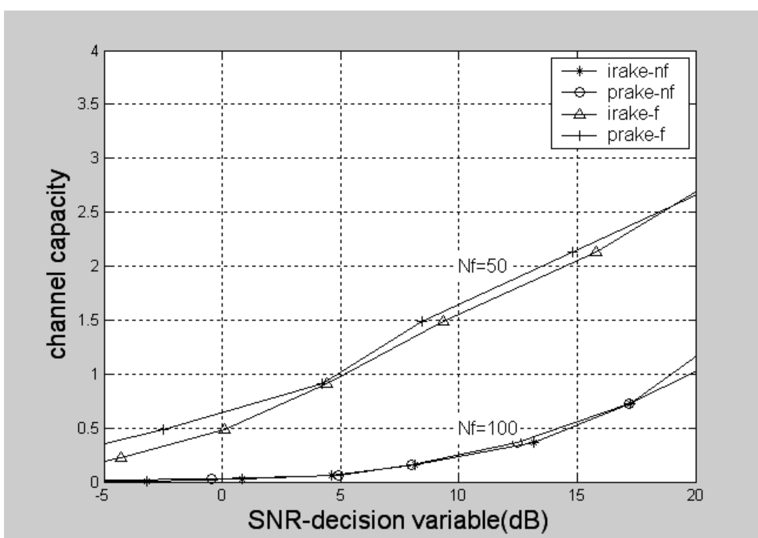

Fig. 8.26. Channel capacity with and without filter bank for different numbers of fingers

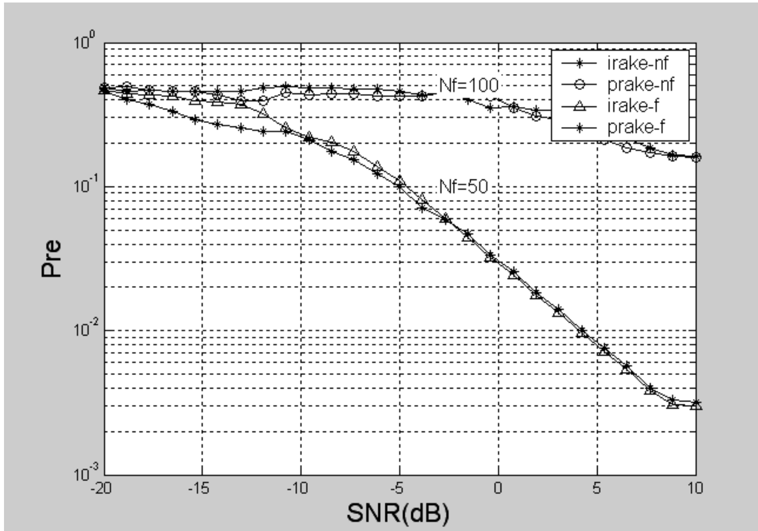

Fig. 8.27: Number of Fingers with and without a Filter bank (ENLOS)

The above figures also show that we need at least twice the number of fingers (NF) to achieve comparable results without the filter bank. In fact, including filter banks improved receiver sensitivity (lower SNR) but other parameters as well such as IEEE/random channel capacity and BER while dealing with color noises (i.e., when the noise PSD is function of frequency).

8.10 Conclusion

A new NBI cancellation method for UWB systems has been proposed. It provides effective suppression of narrowband interference based on filter bank consisting of low Q analog band-pass filters easily implementable in monolithic circuits. The analog filter bank is obtained by a combination of IRAKE and GMF processing. First, the type of modulation and level suitable for NBI has been evaluated, considering an UWB indoor channel. The 4-PPM transmitter signal has been selected due to its noise orthogonally and required lower bandwidth that corresponds to the higher modulation level. As demonstrated, with an optimized number of ten BPF filters covering the entire UWB spectrum, the suppression of almost 10dB of narrow band noise is possible (noise BW=50MHz).

In addition, the SIR level is negligible regardless of the number of filter banks. Increasing the number of filters even with low SIR will increase the SNR out of the GMF. In fact, the determinant of the noise covariance matrix will be close to zero; hence the filter bank output becomes linearly dependent.

Also the performance of the PRAKE receiver has been compared with the IRAKE receiver with the filter bank and combining the GMF, based on the number of fingers (correlators). With the filter bank, the required number of fingers was decreased, while the channel capacity increased and the bit error probability decreased. The reason is the output SNR of the GMF will be increased by reducing the total noise power, especially in the presence of strong/correlated multi tone noise.

Even if UWB receivers look simpler compared to narrowband systems, we demonstrated that with strong NBI (color noise/undesired UWB signal), this simplicity is quite difficult to achieve even with taking advantage of wideband frequency selective fading.

Thus, we proposed an original NBI cancellation method for UWB systems which provides effective suppression of narrowband interference based on filter bank or channel dimensionality.

References

[1] O. Abedi, J. Nielsen, R. Passand, “UWB data rate and channel capacity in modulation schemes,” *IEEE Canadian Conf. on Electrical and Computer Engineering*, Ottawa, Canada, 2006, pp. 1809-1816.

[2] M.G. Di Benedetto, B.R. Vojcic, “UWB wireless communication tutorial,” *J. Communications and Networks*, vol. 5, Dec. 2003, pp. 290-302.

[3] J.D. Choi, W.E. Stark, “Performance analysis of RAKE receivers for ultra-wideband communications with PPM and OOK in multi-path channels,” *IEEE Int. Conf. on Communications,* New-York, NY, 2002, pp. 1969-1973.

[4] O. Abedi, J. Neilsen, “UWB Channel Models Apply Ideal Rake Receiver Filter Bank”, TR-Lab internal report, *University of Calgary*, Calgary, Canada, 2008.

[5] H. Niu, J.A. Ritcey, H. Liu, “Performance of UWB RAKE receivers with imperfect tap weights**”** *Int. Conf. Acoustics, Speech, and Signal Processing,* Hong Kong, Hong Kong, 2003.

[6] R. Pasand, J. Nielsen, A. Sesay,” UWB receiver based on filter bank architecture for suppression of narrowband interference noise,” *IEEE Military Communications Conf.*, Monterey, CA, 2004.

[7] M.G. Di Benedetto, G. Giancola, *Understanding Ultra Wide-Band Radio Fundamentals*, Prentice-Hall, Ch. 2, Ch. 6, Ch. 8, Upper Saddle River, NJ, 2004.

[8] V. Lottici, A. Andrea, U. Mengali, “Channel estimation for ultra-wideband communication,” *IEEE J. on selected area in communication*, vol. 20, pp. 1638-1645, 2002.

[9] P.P Vaidyanathan *Multi-rate Systems and Filter Bank*, Ch. 10, Prentice-Hall, Englewood Cliffs, NJ, 1993.

[10] S. Haykin, *Communication System*, 4th Ed., Ch. 9, J. Wiley & Sons, 2001.

[11] V. Lottici, A. D'Andrea, U. Mengali, “Channel estimation for ultra-wideband communication,” *IEEE J. Select. Areas. Commun.*, vol. 20, pp. 1638-1645.

[12] S. Chen, B. Mulgrew, P.M. Grant, “A clustering technique for digital communications channel equalization using radial basis function networks,” *IEEE Trans. Neural Networks*, vol. 4, pp. 570–578, 1993.

[13] D. Cassioli, M.Z. Win, F. Vatalaro, A.F. Molisch, “Performance of low-complexity RAKE reception in a Realistic UWB channel” *IEEE Int. Conf. on Communications,* New-York, NY, 2002, pp. 763-768.

[14] O. Abedi, M.C.E. Yagoub, A. Abedi, “Enhanced UWB CS-LNA with inverse filter and shunt feedback resistor in 130nm CMOS,” *IEEE Int. Conf. on Signals, Circuits and Systems*, Jerba, Tunisia, 2009, pp. 1-6.

Chapter 9 Conclusions and Perspectives

9.1 Conclusions

In any selective UWB channel, especially when narrowband interference cancellation has to be considered, filter design plays a key role in the overall communication system performance. For this aim, different filter parameters were investigated under strict specifications to get the most suitable band-pass and stop-band filters for UWB applications. However, since in this work filter sharpness and size are the most significant parameters to consider, the Hourglass and the Type II Chebyshev filters have been retained.

Further, we investigated the performance of UWB-LNA circuits, highlighting the fact that the CG-UWB-LNA input matching not only depends on the LNA circuit biasing but also still needs to approach the minimum UWB-LNA requirements. In fact, even if theoretically, CG matching is independent on frequency, we demonstrated that its input matching requires an input matching network leading to high sensitivity to noise and biasing. For accurate evaluation, Cadence IBM-130nm processing and real active-passive components were used as well as some considerations about layout limitations.

In addition, it is very difficult to boost the gain while maintaining a reasonable noise figure. Also the biasing increases the core-LNA transistor parasitic capacitors, thus reducing the gain and increasing the noise figure even without further layout considerations. To solve this issue, some boosting techniques were considered and the CG-CS-UWB-LNA configuration was evaluated, with the conclusion that this configuration is not suitable in our case. Also, its gain is lower compared to the CS-UWB-LNA and needs some boosting techniques, implying even higher noise figure. In addition, the linearity was not significantly improved with the CG-CS-UWB-LNA because the first linearity stage is low and the second stage gain is not so high. Therefore, the CS-UWB-LNA with the ChevII BPF has been finally retained.

Then, an efficient MB-UWB-LNA circuit for double band issues to mitigate WLAN interference, has been designed with an input series ChevII-hourglass SBF.

Different series and parallel topologies (BPF, SBF and their combination) were added to the main circuit to select/mitigate desired/undesired frequency bands.

Next, different UWB pulse modulation schemes were evaluated and their performance compared in terms of narrowband interference robustness, BER/SER, simplicity, data rate, and maximum transmit power with respect to transceiver distance and channel capacity. This demonstrated that B-PAM has the highest data rate in terms of maximum distance and transmit power. However, M-PPM has better power efficiency and channel capacity, at the expense of increased complexity and bandwidth. If bandwidth is not an issue, the M-PPM is the best candidate, due to lower spectral lines which indicate smoother PSD, higher orthogonally of noise and narrowband interference robustness.

Finally, because of signal orthogonally and lower spectral lines while considering tradeoffs between receiver complexity and optimum performance, the 4-PPM can be the best candidate.

By investigating the pulse shape characteristics, we showed that both differentiation order and pulses width variation affect the PSD of the Gaussian pulse and thus can be used to shape the transmitted waveform. According to the FCC specifications on UWB radio frequency constraints, a fifth-order derivative pulse shape for indoor UWB systems can be designed to efficiently remove interference while still containing its power distribution inside the 3.1-10.6GHz UWB frequency band. Even if Gaussian pulses were considered due to their easy generation, other pulse shapes and derivation level can lead to slightly better performance but will add more complexity to the transmitter section.

In the last part of this work, an original NBI cancellation method for UWB systems has been proposed. It provides effective suppression of narrowband interference based on filter bank or channel dimensionality. An analog filter bank was obtained by a combination of IRAKE, PRAKE and GMF processing. As demonstrated, an optimum number of filters can be deduced for maximum performance.

Also the performance of the PRAKE receiver has been compared with the IRAKE receiver by using filter banks and combining the GMF, based on the number of fingers (correlators). With this option, the required number of fingers was decreased, while the channel capacity increased and the bit error probability decreased.

Finally, by adding filter banks, the sampling rate issue can be solved and can be matched with existing commercial analog-digital converters that not require high sampling rate.

9.2 Perspectives and Future Works

In this research, many important issues have not been considered or have been considered with simplified assumptions. There are many areas that can be extended, including:

- Evaluate various types of filters in terms of higher stop-band attenuation, SBA, and stop-band width (SBW) with respect to the filter order and complexity. Higher SBA is indeed necessary for some applications such as sound and video applications.
- Investigate advanced CG-UWB-LNA input-matching techniques especially for emergent communication bands like the unlicensed 60GHz band, to take advantage of the cut-off frequency independency in the high frequency spectrum part.
- Improve current-mirror circuit performance to mitigate shot noise. In fact, the most important source of shot noise for the bias and buffer sections is the current mirror with frequency response limitation. Differential current mirror configurations can improve the buffer gain especially in high frequency applications (e.g., 60 GHz).
- Reduce the number of inductances in the circuit using methods like zigzag LC ladder. This evaluation could be based on capacitance layout issue and power gain reduction.
- Improve the UWB filter-bank model. In the present work, we assumed perfect filter impulse response and synchronization. It will be more realistic if the analog filter bank (AFB) model is implemented.

- Compare the performance of other NBI cancellation receiver techniques based on complexity and channel capacity. Instead of using the AFB in the analog section, it may be possible to use a mixer with a bank of low pass filters.
- Evaluate the performance of other multi-user transmission methods such as OFDM.
- Investigate techniques for multi-user detection (MUD) in UWB systems. In the present work we used single user detectors.
- Simplify the receiver demodulator block by exploring some equalization techniques of the transmitted signal.
- Characterize the outdoor channel estimation. This area requires deep research in terms of channel parameters based on the purpose of interference.
- Consider multi-antenna systems (MAS), which have some benefits for wireless communication systems. They could be useful in the presence of obstacles in the wireless link (by combining narrow-band and UWB systems to take advantage of fading).